Dissertation

submitted to the

Combined Faculty of Mathematics, Engineering and Natural Sciences

of Heidelberg University, Germany

for the degree of

Doctor of Natural Sciences

Put forward by

Markus Wiesinger

born in: Rohrbach in Oberösterreich

Oral examination: 26.7.2023

Sympathetic Cooling of a Single Individually-Trapped Proton in a Cryogenic Penning Trap

Abstract

A method to prepare arbitrary stored ions with low energy in the mK range would improve many high-precision Penning trap experiments and is essential for high-precision measurements of the antiproton and proton g-factors. In this thesis, we investigate sympathetic cooling of a single individually-trapped proton by laser-cooled $^9\mathrm{Be}^+$ ions stored in a separate trap. Both ions are coupled by image currents induced in a common electrode and the coupling is enhanced by a connected cryogenic superconducting radio-frequency RLC oscillator. The image-current based coupling makes the technique applicable to arbitrary ions. We describe the new experimental setup, based on a significant modification of the previous proton g-factor experiment, and the installation and optimization of new image-current detectors. We further describe the development and characterization of a single-photon sensitive fluorescence detection system based on silicon photomultipliers integrated into the cryogenic Penning trap. We demonstrate laser-cooling of the $^9\mathrm{Be}^+$ ions and measure their temperature to $1.1(2)\,\mathrm{mK}$ using fluorescence detection. The simultaneous detection of fluorescence photons and image currents of laser-cooled $^9\mathrm{Be}^+$ ions enables a measurement of the laser-induced damping. We further demonstrate sympathetic cooling of the axial mode of a single proton to $2.6(2.5)\,\mathrm{K}$, limited by the applied temperature measurement method. With a newly developed temperature measurement trap, we improve this value to $160(30)\,\mathrm{mK}$, almost two orders of magnitude below the environment temperature. Finally, we argue that the technique can be optimized to reach temperatures in the low double-digit mK range, which would enable a future generation of antiproton and proton g-factor measurements with an order of magnitude improved precision. For other high-precision Penning trap experiments, the method will be an attractive tool to prepare arbitrary ions for measurement.

Zusammenfassung

Eine Methode zur Präparation beliebiger gespeicherter Ionen mit Energien im mK-Bereich würde viele hochpräzise Penningfallen-Experimente weiter verbessern und ist für hochpräzise Messungen des g-Faktors von Antiprotonen und Protonen unerlässlich. In dieser Arbeit untersuchen wir die sympathische Kühlung eines einzelnen gefangenen Protons durch lasergekühlte ^{9}Be$^+$-Ionen, die in einer separaten Falle gespeichert sind. Beide Ionen werden durch in einer gemeinsamen Elektrode induzierte Bildströme gekoppelt und die Kopplung wird durch einen angeschlossenen kryogenen supraleitenden Radiofrequenz-RLC-Schwingkreis verstärkt. Die bildstrombasierte Kopplung macht die Technik auf beliebige Ionen anwendbar. Wir beschreiben den neuen Versuchsaufbau, der auf einer wesentlichen Modifikation des vorherigen Proton-g-Faktor-Experiments basiert, sowie die Installation und Optimierung neuer Bildstromdetektoren. Wir beschreiben weiter die Entwicklung und Charakterisierung eines einzelphotonenempfindlichen Fluoreszenzdetektionssystems auf Basis von Silizium-Photomultipliern, die in die kryogene Penning-Falle integriert sind. Wir demonstrieren die Laserkühlung der ^{9}Be$^+$-Ionen und messen ihre Temperatur zu $1.1(2)$ mK mittels Fluoreszenzdetektion. Die gleichzeitige Detektion von Fluoreszenzphotonen und Bildströmen lasergekühlter ^{9}Be$^+$-Ionen ermöglicht eine Messung der laserinduzierten Dämpfung. Wir demonstrieren außerdem die sympathische Kühlung der Axialmode eines einzelnen Protons auf $2.6(2.5)$ K, begrenzt durch die angewandte Temperaturmessmethode. Mit einer neu entwickelten Temperaturmessfalle verbessern wir diesen Wert auf $160(30)$ mK, fast zwei Größenordnungen unter der Umgebungstemperatur. Abschließend argumentieren wir, dass die Technik optimiert werden kann um Temperaturen im niedrigen zweistelligen mK-Bereich zu erreichen, was eine zukünftige Generation von g-Faktor Messungen an Antiprotonen und Protonen mit um eine Größenordnung verbesserter Präzision ermöglichen würde. Für andere hochpräzise Penningfallen-Experimente wird die Methode ein attraktives Werkzeug sein um beliebige Ionen für die Messung vorzubereiten.

Contents

Chapter 1

Introduction

The origin of the observed matter-antimatter asymmetry in the universe is one of the big open questions in cosmology and particle physics [1, 2]. Matter-antimatter asymmetry is the absence of equal amounts of antimatter, compared to matter, in the universe. In fact, there is lots of antimatter in the universe, e.g. in form of positrons [3] or antiprotons [4], but not in form of heavy antinuclei [4] or antistars [5], and nowhere near the amount of matter in the universe. This is puzzling, because the Standard Model of particle physics contains a matter-antimatter symmetry and treats matter and antimatter on an equal footing. Ultimately, this symmetry is based on the fundamental assumption of charge parity time (CPT) symmetry in the Standard Model.

In principle, CP symmetry violation together with other conditions could explain a finite matter-antimatter asymmetry via baryogenesis. However, in the Standard Model these contributions are far to small to explain the observations [6, 1].

Another option that would create a matter-antimatter asymmetry would be CPT violation [7, 8]. On the one hand, this has been disregarded on theoretical grounds because CPT symmetry is a fundamental ingredient of self-consistent quantum field theories [9, 10]. On the other hand, so far many symmetries thought to be fundamental have turned out to be violated, e.g. parity symmetry [11], and CP symmetry [12].

To tackle the problem from an experimental side, many CPT tests have been performed on the most fundamental particles in the Standard Model. These CPT tests utilizing the fundamental building blocks of matter may provide information about the origin of matter-antimatter asymmetry. Unfortunately it is unclear in which sector CPT violation may arise, such that searches in all sectors are meaningful. In the baryon sector the BASE collaboration provides currently the most precise CPT tests which are based on comparison of antiproton and proton charge-to-mass ratios on the one hand [13], and on the comparison of antiproton and proton g-factors on the other hand [14, 15].

One specialty of these experiments on protons and antiprotons is the extremely low energy of the transitions under investigation. On an absolute energy scale, the

1

CPT tests of BASE reach 2×10^{-27} GeV, the smallest energy scale of all CPT tests performed directly on antimatter particles. This is advantageous e.g. in constraining coefficients of the Standard Model Extension (SME) [16, 17].

Another big open question of physics is the origin of dark matter. So far no particle has been identified as the source of dark matter. In the context of dark matter searches, interactions of antimatter particles with dark matter could be different from interactions of matter particles with dark matter. Therefore, searches for dark matter using antimatter sensors, as performed by the BASE collaboration [18], are well motivated. Anomalous interaction of antimatter with dark matter might even provide an answer to both open questions.

Finally, the gravitational interaction of antimatter with matter has been a field of interest for a long time. Especially because an antiatom, freely falling in the gravitational potential of the earth is not the CPT symmetric counterpart of a matter atom freely falling in the gravitational potential of the earth. Anomalous gravity therefore would not immediately violate the CPT symmetry. Here, experiments on single antiprotons, when compared with protons [13], can provide important input that is complementary to free-fall experiments currently under preparation [19, 20, 21].

All these experiments aim to set the most stringent limits practically achievable, so more precise measurements allow more stringent tests of symmetries, immediately rule out additional parameter space, or – in case the null hypothesis is rejected – provide considerable room for discovery of new physics. Therefore it is crucial to identify the limits precluding improved precision and ways to eliminate them.

In the current generation of antiproton and proton g-factor and q/m measurements, the particle temperature is identified as one of the sources that limits precision, on the one hand via temperature-dependent detection fidelity [22, 23, 24] which impacts statistical uncertainty, and on the other hand via temperature dependent systematic frequency shifts. Currently resistive cooling to liquid helium temperatures (4 K) is the state-of-the-art in these experiments. In combination with electronic feedback cooling the temperature can be reduced to 1 K at the cost of longer thermalization time constants. It is therefore very desirable to cool single protons and antiprotons to lower temperatures, or even to the ground state.

For selected ions, laser cooling using basic techniques such as Doppler cooling allows to reach temperatures in the range of mK, and with more advanced techniques, e.g. electromagnetically induced transparency (EIT) cooling [25, 26, 27], or sideband cooling [28, 29], the ions can be cooled to the ground state of motion.

In this thesis, we investigate the applicability of laser cooling to single protons focusing on techniques which immediately would allow us to extend these techniques to antiprotons also. The general idea is to sympathetically cool a single proton individually trapped in one Penning trap with a laser-cooled ion stored in another

trap. A crucial aspect is to cool only a single proton which is individually trapped, as the techniques used for g-factor measurements crucially rely on the condition that only a single particle is stored in the spin-state analysis trap. Another crucial aspect is the coupling which has to happen between particles stored in different traps, potentially over large distances (several cm) such that direct Coulomb coupling becomes unfeasible. We rely on a technique proposed in [30] where the coupling between the two traps is mediated by the capacitance of a common electrode. This capacitance does not need not be a capacitor, but might be an effective capacitance such as presented by an RLC circuit off resonance. To jump ahead: we successfully implemented a variant of this technique and were able to cool a single proton to a temperature about two orders of magnitude below the temperature reached in the state-of-the-art experiments, see also [31].

The remaining part of this thesis is structured as follows: In chapter 2 we provide a short overview of relevant Penning-trap physics. In chapter 3 we discuss the recently-performed most-precise measurement of the proton g-factor [15, 32], its limitations, and a concept for an improved measurement. In chapter 4 we describe the multi-Penning-trap apparatus which is designed for an improved proton g-factor measurement and which has been set up over the course of this work. Further, we describe some of the most commonly used experimental methods. In chapter 5 and 6 we describe the image-current-based and the newly-developed fluorescence-based detection methods used throughout this work. In chapter 7 we discuss laser cooling, the level structure of the laser-cooled ^{9}Be$^+$ ion, and some peculiarities of laser cooling in Penning traps. In chapter 8 we focus on sympathetic cooling and temperature measurements of radio-frequency (RF) resonators coupled to laser-cooled ^{9}Be$^+$ ions. In chapter 9 we discuss mode coupling in the Penning trap. And in chapter 10 we summarize the results on sympathetic cooling of a single individually-trapped proton by laser-cooled ^{9}Be$^+$ ions stored in a separate trap and remotely coupled by a common RF resonator, relying on the results presented in chapters 5 to 8. Finally, we conclude the thesis with a comparison of the presented cooling technique to the previous state-of-the-art and a discussion of avenues for potential improvement in chapter 11.

Note that parts of this thesis have been published in several progress reports of the EU-funded initial training network AVA (Marie Skłodowska-Curie grant agreement No 721559). In addition, chapter 6 has been prepared for submission to Review of Scientific Instruments. There is also some overlap with PhD theses [31] and [33] as they were conducted in parallel with this thesis.

Chapter 2

Penning-Trap Physics

Charged particles are confined in the Penning trap by a superposition of a static homogeneous magnetic field

$$\vec{B}(x, y, z) = B_0 \vec{e}_z \tag{2.1}$$

for confinement in radial direction (perpendicular to the magnetic field) and a static electric quadrupole field

$$\vec{E}(x, y, z) = V_0 C_2 \left(x \vec{e}_x + y \vec{e}_y - 2z \vec{e}_z \right) \tag{2.2}$$

for confinement in axial direction (parallel to the magnetic field), with C_2 being a negative constant of dimension m^{-2}. The former is usually created inside of a superconducting magnet operated in persistent mode with typical field strength in the range of $2\,\mathrm{T}$ to $7\,\mathrm{T}$. The latter is created by a voltage applied to an electrode geometry as shown in figure 2.1a which consists of a ring electrode held at the trap voltage V_0 and end electrodes held at ground. Two additional correction electrodes allow anharmonic terms of the trapping potential to be tuned to zero.

In absence of the electric field the charged particle would perform a circular motion in the radial plane with a frequency given by the free cyclotron frequency

$$\omega_c = 2\pi\nu_c = \frac{q}{m} B_0 \tag{2.3}$$

and would be unbound in the axial direction.

2.1 The Ideal Penning Trap

The motion in the ideal Penning trap is treated e.g. in [34, 35] under the assumption that there are no deviations from the ideal fields given in equations (2.1) and (2.2). Then the equation of motion of the position $\vec{x}$ of a charged particle of mass m and
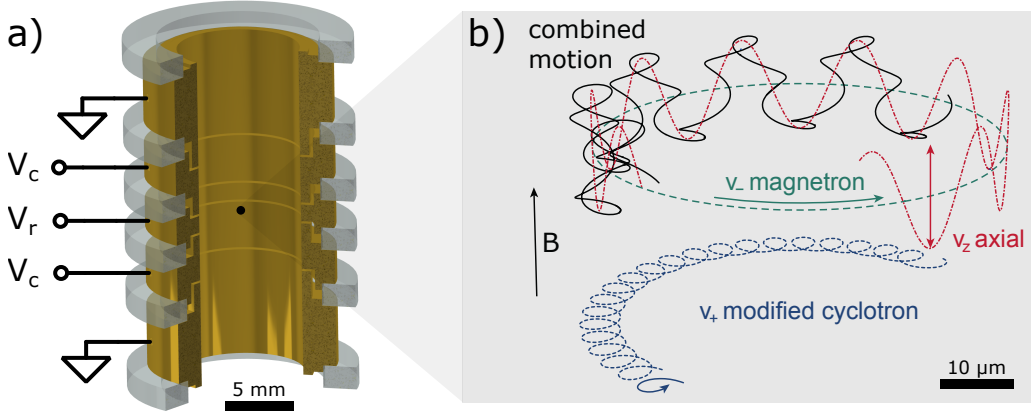
Figure 2.1: (a) Trap electrodes of a cylindrical open-endcap 5-electrode Penning trap. The voltage applied to the ring electrode is $V_r = V_0$ and the voltage applied to the correction electrodes is $V_c = TR \times V_0$, where TR is the tuning ratio. The end electrodes are held at ground. (b) Characteristic motion of a charged particle in an ideal Penning trap. The subfigure (b) is adapted from [32].

charge q in the ideal Penning trap is

$$m\ddot{\vec{x}} = q\vec{E} + q(\dot{\vec{x}} \times \vec{B}) \tag{2.4}$$

which is separable into an axial and a radial component.

The equation of motion for the axial component is

$$m\ddot{z} = -qV_0 C_2 2z \tag{2.5}$$

with a solution that is a harmonic motion with amplitude a in axial direction

$$z(t) = a\cos(\omega_z t + \phi_z). \tag{2.6}$$

The equations of motion for the radial part are

$$m\begin{pmatrix} \ddot{x} \\ \ddot{y} \end{pmatrix} = qV_0 C_2 \begin{pmatrix} x \\ y \end{pmatrix} + qB_0 \begin{pmatrix} 0 & 1 \\ -1 & 0 \end{pmatrix} \begin{pmatrix} \dot{x} \\ \dot{y} \end{pmatrix} \tag{2.7}$$

with solutions that are two independent circular motions with radii r_+ and r_- in the radial plane

$$\begin{pmatrix} x(t) \\ y(t) \end{pmatrix} = r_+ \begin{pmatrix} \cos(\omega_+ t + \phi_+) \\ \sin(\omega_+ t + \phi_+) \end{pmatrix} + r_- \begin{pmatrix} \cos(\omega_- t + \phi_-) \\ \sin(\omega_- t + \phi_-) \end{pmatrix}. \tag{2.8}$$

Consequently, in the combined electric and magnetic field of the ideal Penning trap, the motion of the charged particle is composed of three independent motional modes: the harmonic axial mode, and the circular magnetron and modified-cyclotron modes, as shown in figure 2.1b. The eigenfrequencies of the axial, modified-

5

cyclotron, and magnetron modes are

$$\omega_z = 2\pi\nu_z = \sqrt{\frac{q}{m}2V_0C_2} \tag{2.9}$$

$$\omega_+ = 2\pi\nu_+ = \frac{1}{2}\left(\omega_c + \sqrt{\omega_c^2 - 2\omega_z^2}\right) \tag{2.10}$$

$$\omega_- = 2\pi\nu_- = \frac{1}{2}\left(\omega_c - \sqrt{\omega_c^2 - 2\omega_z^2}\right). \tag{2.11}$$

There are two trapping conditions that need to be fulfilled for the motion to be bound: The first one is that the root in equation (2.9) must be real leading to

$$qV_0 \leq 0 \tag{2.12}$$

when taking into account that C_2 is negative. A consequence of this condition is that only particles of the same charge can be trapped in a given trapping potential. The second trapping condition arises from the requirement that the roots in equations (2.10) and (2.11) must be real leading to

$$\omega_c^2 \geq 2\omega_z^2. \tag{2.13}$$

This condition allows the Penning trap to be used as mass filter.

For typical parameters used in Penning-trap experiments the eigenfrequencies follow the order $\omega_- \ll \omega_z \ll \omega_+ < \omega_c$ but ω_z can in principle be as large as $\omega_c/\sqrt{2}$. Important relations between the eigenfrequencies are

$$\omega_c = \omega_+ + \omega_- \tag{2.14}$$

$$\omega_z^2 = 2\omega_+\omega_- \tag{2.15}$$

$$\omega_c^2 = \omega_+^2 + \omega_z^2 + \omega_-^2 \tag{2.16}$$

where the last relation also holds for certain imperfections in real Penning traps and is called the Brown-Gabrielse invariance theorem [36].

2.2 Effects of Electric Field Anharmonicities and Magnetic Field Inhomogeneities

Deviations from the ideal fields given in equations (2.1) and (2.2) occur due to the finite size of the used superconducting magnet and trap electrodes. In addition, the trap-electrode geometry of cylindrical traps only provides an approximation to the ideal electric field near the center of the trap. Further causes of deviations from the ideal fields arise from manufacturing tolerances, misalignment, etc. The main effect of these deviations are amplitude-dependent frequency shifts of the eigenfrequencies

of the motional modes [35]. This can also be interpreted as a form of coupling between the eigenmodes [37]. The most important deviations are characterized by the coefficients C_4 and B_2 as described below.

Electric field imperfections, which occur in any real Penning trap, are characterized by performing a multipole expansion of the trapping potential Φ. Near the center of the trap the electric potential can be expanded in spherical harmonics where each term satisfies the Laplace equation independently [35]. The potential then becomes

$$\Phi(x, y, z) = V_0 \sum_{k=0}^{\infty} C_k r^k P_k(\cos(\theta)) \tag{2.17}$$

$$= V_0 \left(C_0 + C_1 z + C_2 \left(z^2 - \rho^2/2 \right) + ... \right) \tag{2.18}$$

where $P_k(x)$ are the Legendre polynomials. This multipole expansion has the convenient characteristic that on axis, where $\rho = 0$, it simplifies to a polynomial expansion in z. Note that here and in the following we use Cartesian coordinates (x, y, z), cylindrical coordinates (ρ, φ, z) and spherical coordinates (r, θ, φ) interchangeably. For the ideal Penning trap all coefficients C_k are zero except for C_2 and the potential describes the electric field given in equation (2.2). Therefore, all coefficients other than C_2 are considered electric field imperfections. The most important anharmonic term is the electric octupole term

$$\Phi(x, y, z) = V_0 C_4 \left(z^4 - 3z^2 \rho^2 + \frac{3}{8} \rho^4 \right) \tag{2.19}$$

which leads to frequency shifts given by

$$\begin{pmatrix} \Delta\omega_z/\omega_z \\ \Delta\omega_+/\omega_+ \\ \Delta\omega_-/\omega_- \end{pmatrix} = \frac{3C_4}{qV_0 C_2^2} \begin{pmatrix} \frac{1}{4} & -\frac{1}{2}(\omega_z/\omega_+)^2 & 1 \\ -\frac{1}{2}(\omega_z/\omega_+)^2 & \frac{1}{4}(\omega_z/\omega_+)^4 & -(\omega_z/\omega_+)^2 \\ 1 & -(\omega_z/\omega_+)^2 & 1 \end{pmatrix} \begin{pmatrix} E_z \\ E_+ \\ E_- \end{pmatrix}. \tag{2.20}$$

Magnetic field imperfections are any deviations from the perfectly homogeneous magnetic field given in equation (2.1). Again, a multipole expansion around the trap center can be performed

$$\vec{B}(x, y, z) = \sum_{l=0}^{\infty} B_l r^l \left(P_l(\cos(\theta))\vec{e}_z - \frac{1}{l+1} P_l^1(\cos(\theta))\vec{e}_\rho \right) \tag{2.21}$$

where $P_l^1(x)$ are the associated Legendre polynomials of order 1 [35] . The lowest multipole term, except for B_0, that does not average out during the particle motion is the magnetic hexapole term

$$\vec{B}(x, y, z) = B_2(z^2 - \rho^2/2)\vec{e}_z - B_2 z\rho\vec{e}_\rho. \tag{2.22}$$

It leads to frequency shifts of

$$
\begin{pmatrix} \Delta\omega_z/\omega_z \\ \Delta\omega_+/\omega_+ \\ \Delta\omega_-/\omega_- \end{pmatrix} = \frac{B_2}{qV_0 B_0 2C_2} \begin{pmatrix} 0 & 1 & -1 \\ 1 & -(\omega_z/\omega_+)^2 & 2 \\ -1 & 2 & -2 \end{pmatrix} \begin{pmatrix} E_z \\ E_+ \\ E_- \end{pmatrix} . \tag{2.23}
$$

Note that both matrices in equations (2.20) and (2.23) are symmetric. As a consequence, the relative frequency shift of mode i due to energy in mode j is equal to the relative frequency shift of mode j due to energy in mode i, where $i, j \in \{z, +, -\}$.

2.3   Quantum Mechanical Description

The quantum mechanical description is treated e.g. in [34, 35] (see also references therein). The motion of the trapped charged particle in the Penning trap is described by the Hamiltonian

$$
H = \frac{1}{2m}\left(p_x^2 + p_y^2\right) + \frac{m}{8}\left(\omega_c^2 - 2\omega_z^2\right)\left(x^2 + y^2\right) - \frac{\omega_c}{2}L_z \tag{2.24}
$$

$$
+ \frac{1}{2m}p_z^2 + \frac{m}{2}\omega_z^2 z^2 \tag{2.25}
$$

where

$$
L_z = xp_y - yp_x \tag{2.26}
$$

is the axial component of the angular momentum operator. Here, x, y, z and p_x, p_y, p_z are operators.

With the introduction of appropriate creation and annihilation operators [34], the Hamiltonian can be expressed as

$$
H = (N_z + 1/2)\hbar\omega_z + (N_+ + 1/2)\hbar\omega_+ - (N_- + 1/2)\hbar\omega_- + m_s\hbar\omega_L \tag{2.27}
$$

where N_z, N_+, N_- are number operators with eigenvalues n_z, n_+, n_-. In the last term we have additionally introduced the spin with quantum number $m_s = \pm 1/2$ and the Larmor frequency ω_L. The first three terms in equation (2.27) are the Hamiltonian of three simple harmonic oscillators with the distinction that the energy levels of the magnetron oscillator are inverted with more negative energy for higher quantum number. The last term is the Hamiltonian of a quantum mechanical two-level system. The complete set of eigenstates is given by

$$
|n_z, n_+, n_-, m_s\rangle = |n_z\rangle \otimes |n_+\rangle \otimes |n_-\rangle \otimes |m_s\rangle . \tag{2.28}
$$

The charged particle bound to the trap forms an artificial atom with level structure

given by the eigenvalues of equation (2.27).

Electric field anharmonicities and magnetic field inhomogeneities such as the ones given in equations (2.17) and (2.21) contain terms proportional to mixed products of the operators x, y, and z. Their effects can be described via interaction Hamiltonians

$$H_{int} \propto xz, H_{int} \propto xy, \text{ or } H_{int} \propto yz \tag{2.29}$$

which lead to coupling between the eigenmotions facilitating energy exchange between the eigenmotions near resonance [30].

2.4   Manipulation of Particle Motion

For some experiments it is desirable to manipulate the motion of the charged particle in the Penning trap. For this purpose, time dependent electric fields with well-defined geometry and frequency ω_{RF} are used [38, 39, 40].

For resonant excitation of a motional mode, a drive with an electric dipole field in direction of the motion and oscillating at the frequency $\omega_{RF} = \omega_z$, ω_+, or ω_- is used. This type of excitation preserves the phase space distribution of identically prepared particles from before the excitation and only shifts it in phase space. It can be used to excite the motion to a well-defined amplitude and phase.

Parametric excitation of a motional mode is realized by applying a drive with a quadrupole field which is proportional to the trapping potential and oscillating at the frequency $\omega_{RF} = 2\omega_z$, $2\omega_+$, or $2\omega_-$, twice the eigenfrequency of the respective mode. In phase space this type of excitation leads to a squeezing of the initial phase space distribution [41]. In case the axial mode is continuously driven, the axial frequency synchronizes with $\omega_{RF}/2$ and the amplitude is limited by anharmonicities, e.g. the anharmonic term proportional to C_4. Therefore, it can be used to characterize these anharmonic terms [42].

Interconversion of two motional modes is achieved by a drive with an electric quadrupole field derived from a potential which is proportional to the product of both coordinates and which oscillates with the sum or difference frequency of the respective motional modes. Mode coupling and exchange of action is accomplished when $\omega_{RF} = \omega_+ - \omega_z$, $\omega_+ + \omega_-$, or $\omega_z + \omega_-$, the difference frequency of two modes. Note that due to the inverted level structure of the magnetron mode $-\omega_-$ is used instead of ω_- to calculate the frequency difference. In this case the amplitude and phase of both modes are continuously exchanged and can be swapped after application of a π-pulse [43]. This technique is an essential component of a phase-sensitive frequency-measurement method [44]. For example, to couple the axial and cyclotron modes, an electric field derived from a quadrupole potential such as

$$\Phi(x, y, z, t) = xz V_{RF} C_{RF} \cos(\omega_{RF} t + \phi_{RF}) \tag{2.30}$$

is used. C_{RF} is a constant of dimension m^{-2}. Note that, in addition to being time-dependent, this is a different quadrupolar field than the trapping potential. Compared to the term proportional to C_2 in equation (2.17) it is rotated by $\pi/4$ in the xz-plane.

Finally, amplification of two motional modes is possible with a quadrupole drive at the sum frequency, when $\omega_{RF} = \omega_+ + \omega_z$, $\omega_+ - \omega_-$, or $\omega_z - \omega_-$. Here the amplitudes of both motional modes grow exponentially, but their final amplitudes and phases are dependent on the initial amplitude and phase of both modes. This type of excitation is an essential part of another phase-sensitive frequency measurement method [45, 46].

In practice, to apply these fields to the particle, the time-varying potential is added to one of the trap electrodes. An end electrode or correction electrode creates a dipole field in axial direction as well as a quadrupole field proportional to the trapping potential. One segment of a split correction electrode creates an axial-radial quadrupole field and in addition a dipole field in axial direction and a dipole field in radial direction. Finally, one segment of a 4-fold split ring electrode creates a radial quadrupole field in addition to a radial dipole field.

Further discussion of excitation drives in Penning traps is provided e.g. in [40].

2.5   Cooling and Detection

Cooling of particle motion is essential to attain the low mode energies necessary for high-precision measurements. In this work resistive cooling and laser cooling are used to prepare particles with temperatures of a few K or a few mK, respectively. Each cooling method comes with an associated detection method: Image current detection in case of resistive cooling and fluorescence detection in case of laser cooling. Both methods are described in detail in sections 5 and 6 of this thesis. An overview of these and other cooling methods can be found in [47, 48].

In our experiment only the axial mode is cooled directly to an average energy of $\langle E_z \rangle = k_B T_z$ where k_B is the Boltzmann constant and T_z the axial temperature. The other modes are cooled via continuous interconversion of motional modes, as described above. Using this technique, the magnetron mode can be cooled to low energies because the energy of the magnetron mode is $\langle E_- \rangle = \langle E_z \rangle \omega_-/\omega_z$ after interconversion where $\omega_-/\omega_z \ll 1$ typically [35]. This is due to the fact that the classical action is constant during interconversion. In the quantum mechanical picture, the quantum numbers are exchanged. In contrast, the energy of the cyclotron mode is $\langle E_+ \rangle = \langle E_z \rangle \omega_+/\omega_z$ after the interconversion where $\omega_+/\omega_z = \omega_z/2\omega_- \gg 1$.

Chapter 3

Concept of a Next-Generation Proton g-Factor Measurement

In the context of searches for CPT violation in the baryon sector of the Standard Model of particle physics, high-precision measurements of the proton g-factor and the antiproton g-factor are performed within the BASE collaboration. The proton g-factor has been measured in Mainz with a relative uncertainty of 3.0×10^{-10} (68% CL) [15] and the antiproton g-factor was measured at CERN in a similar experiment with a relative uncertainty of 1.5×10^{-9} (68% CL) [14]. Together these measurements allow a g-factor based CPT test with a relative uncertainty of 1.7×10^{-9} (68% CL) and at an absolute energy scale of 6×10^{-25} GeV [49]. It is expected that an antiproton g-factor measurement with a similar uncertainty than the proton g-factor measurement becomes available soon. This would then allow a CPT test with relative uncertainty down to 3.0×10^{-10}.

To further improve the uncertainty of the g-factor based CPT test beyond the level of 3.0×10^{-10}, the uncertainty of both the proton and the antiproton g-factor measurement needs to be improved. In the following we describe the proton g-factor measurement technique, have a critical look at the factors limiting the precision, and outline important characteristics of an improved experiment. This will inform the steps and developments necessary for even more precise proton and antiproton g-factor measurements.

3.1   (Anti)Proton g-Factor

The (anti)proton g-factor measurement is based on the measurement of the Larmor frequency

$$\omega_L = 2\pi\nu_L = \frac{g}{2}\frac{qB}{m} \tag{3.1}$$

of a single (anti)proton in the homogeneous magnetic field B of a Penning trap located inside of a superconducting magnet. In order to characterize the magnetic

field, the cyclotron frequency ω_c of the single (anti)proton is measured simultaneously. To this end, all three eigenfrequencies ω_+, ω_z, and ω_- are measured and application of the invariance theorem, equation (2.16), determines the cyclotron frequency ω_c. Actually, only ω_+ which contributes most to ω_c is measured simultaneously with ω_L, while ω_z and ω_- are measured before and after the simultaneous measurement and interpolated. Both the cyclotron and Larmor frequency measurements average over the same spatial and temporal variations of the magnetic field in the Penning trap. As a result, the factor qB/m cancels in the ratio of both frequencies and the proton g-factor is given by

$$\frac{g}{2} = \frac{\omega_L}{\omega_c}. \tag{3.2}$$

In practice, the Larmor frequency is not measured directly, but rather probed at frequencies near the expected Larmor frequency. Near the Larmor resonance the (anti)proton spin is flipped with a certain probability. It is this spin-flip probability as a function of the ratio of probe frequency to cyclotron frequency that is actually measured.

Due to the magnetic field dependence of the Larmor frequency, it suffers from the same magnetic field dependent shifts as the cyclotron frequency, compare equation (2.23), but it is unaffected by electric field anharmonicities. E.g., the relative shift in the field of the magnetic hexapole term (B_2) is

$$\frac{\Delta\omega_L}{\omega_L} = \frac{B_2}{qV_0 B_0 2C_2} \left(E_z - \left(\frac{\omega_z}{\omega_+ - \omega_-}\right)^2 E_+ - 2E_- \right) \tag{3.3}$$

where E_z, E_+, and E_- are the energy in the axial, magnetron, and cyclotron mode. In principle, these shifts cancel in the ratio $\omega_L/\omega_c \approx \omega_L/\omega_+$. However, since the axial and cyclotron energies sample a Boltzmann distribution during the measurement, these shifts lead to a broadening of the Larmor resonance. It is therefore desirable to minimize the energy of all motional modes and especially magnetic field inhomogeneities in the g-factor measurement trap.

3.2 Continous Stern-Gerlach Effect

For readout of the proton spin state a certain magnetic field inhomogeneity – the magnetic hexapole term which we will call magnetic bottle from now on – is desirable. In a magnetic bottle the axial frequency is shifted by

$$\frac{\Delta\omega_z}{\omega_z} = \frac{B_2}{qV_0 B_0 2C_2} \left(E_+ - E_- + m_s \hbar \omega_L \right) \tag{3.4}$$

where m_s is the quantum number of the proton spin projection in direction of the magnetic field with eigenvalues of $\pm 1/2$. If the mode energies are expressed in terms of their quantum numbers and the trapping potential in terms of the axial frequency

$$\Delta\omega_z = \frac{B_2 \hbar \omega_+}{B_0 m \omega_z} \left((n_+ + 1/2) + \frac{\omega_-}{\omega_+}(n_- + 1/2) + \frac{g}{2}m_s \right). \tag{3.5}$$

Note that the switch from the minus to the plus sign is due to $E_- = -\hbar\omega_-(n_- + 1/2)$. The axial frequency shift due to the last term in equation (3.5) is advantageous because it couples the spin state of the proton to the frequency of the axial mode. This type of spin motional coupling is also called the continuous Stern-Gerlach effect, its first use for spin-state readout has been in the context of electron g-factor measurements by Dehmelt [50, 51, 52].

However, compared to the free or bound electron, the magnetic moment of the proton, and therefore its Larmor frequency, is smaller by a factor of order m_e/m_p. In addition, the axial frequency shift is inversely proportional to the mass of the particle. These effects make the axial frequency shift of a single proton very small and necessitate the use of very large magnetic bottles. In the current generation of proton g-factor experiments a magnetic bottle with $B_2 = 300\,000\,\mathrm{T\,m^{-2}}$ is used which is already at the technical limit of what is possible [53]. In this magnetic bottle and for an axial frequency of $550\,\mathrm{kHz}$ the axial frequency shifts due to a spin-flip, cyclotron quantum jump, and magnetron quantum jump are $233\,\mathrm{mHz}$, $83\,\mathrm{mHz}$, and $0.039\,\mathrm{mHz}$, respectively. Expressed as function of radial energy the axial frequency shift is $97\,\mathrm{Hz\,K^{-1}}/k_B$. In order to resolve the frequency jumps due to spin-flips, the axial frequency needs to be stabilized to better than 1×10^{-7} and cyclotron quantum jumps need to be avoided. In the state-of-the-art experiments [14, 15] the frequency shift due to a spin-flip is resolved, but the frequency stability is not sufficient to resolve the frequency shift due to single cyclotron quantum jumps. Observation of single cyclotron quantum jumps would only require a factor of 3 better axial frequency stability, but this is challenging to achieve even with the most stable voltage sources, see also figure 4.11.

Furthermore, the axial frequency shift due to the continuous Stern-Gerlach effect, equation (3.5), allows for a very precise measurement of the energy in the radial modes. In case of the cyclotron mode of a single proton the resolution almost allows to resolve the quantized energy levels in this mode.

3.3 Double Penning-Trap Method

Unfortunately, precise Larmor frequency measurements and high-fidelity spin-flip readout have opposing requirements on the magnetic field, and, therefore, they cannot be performed in the same magnetic field. The solution to this problem has

been first presented in context of bound electron g-factor measurements of highly charged ions [54]. The use of two Penning traps, separated by a transport section, allows both requirements to be fulfilled in one trap system. A precision trap (PT) with a homogeneous magnetic field provides the environment for a high-precision measurement of the Larmor frequency, and an analysis trap (AT) with a strong magnetic bottle provides the ability to resolve spin transitions with high fidelity. Both traps need to be separated by a suitable distance in order to avoid residual magnetic field inhomogeneities in the PT originating from the magnetic bottle of the AT. The first application of the double Penning-trap technique for proton spin-state readout was reported in [23].

3.4   The Need for Cooling

It turns out that the spin-state detection fidelity in the large magnetic bottle of the AT strongly depends on the energy in the radial modes, the cyclotron and magnetron modes. This is due to undesired axial frequency fluctuations which are observed to increase with increasing magnetron and cyclotron energy. These axial frequency fluctuations have been attributed to electric field noise $E_n \approx 200\,\mathrm{pV/m}\sqrt{\mathrm{Hz}}$ of unexplained origin which leads to cyclotron quantum transitions and, therefore, to axial frequency fluctuations [55]. The axial frequency fluctuation, characterized by the differential Allan deviation [56], becomes

$$\Xi(\tau) = \mathrm{SD}(\nu_z(t+\tau) - \nu_z(t)) = \sqrt{\frac{dn_+}{dt}\left(\Delta\nu_{z+}\right)^2 \tau} \qquad (3.6)$$

where SD denotes the standard deviation, τ is the time between two measurements, dn_+/dt is the cyclotron transition rate, and $\Delta\nu_{z+} = 83\,\mathrm{mHz}$ is the axial frequency shift due to a cyclotron quantum jump. The axial frequency shift due to magnetron quantum jumps is $\Delta\nu_{z-} = 0.039\,\mathrm{mHz}$ and can be neglected. It has been shown that the transition rate is proportional to the energy in the cyclotron mode [22],

$$\frac{dn_+}{dt} = 0.030\,\mathrm{s}^{-1} \times \frac{E_+}{k_B}\mathrm{K}^{-1} \qquad (3.7)$$

and to the energy in the magnetron mode [55],

$$\frac{dn_+}{dt} = 0.040\,\mathrm{s}^{-1} \times \frac{-E_-}{k_B}\mathrm{K}^{-1}. \qquad (3.8)$$

Consequently, the transition rate can be brought to acceptably low levels by cooling the cyclotron and magnetron modes. While the dependence on the cyclotron and magnetron energy is similar in size, the magnetron mode can be cooled to low energies using interconversion with the axial mode where $\langle E_- \rangle = \langle E_z \rangle \, \omega_-/\omega_z$ with $\omega_-/\omega_z \approx 1/65$. In contrast, after interconversion with the axial mode, the cyclotron
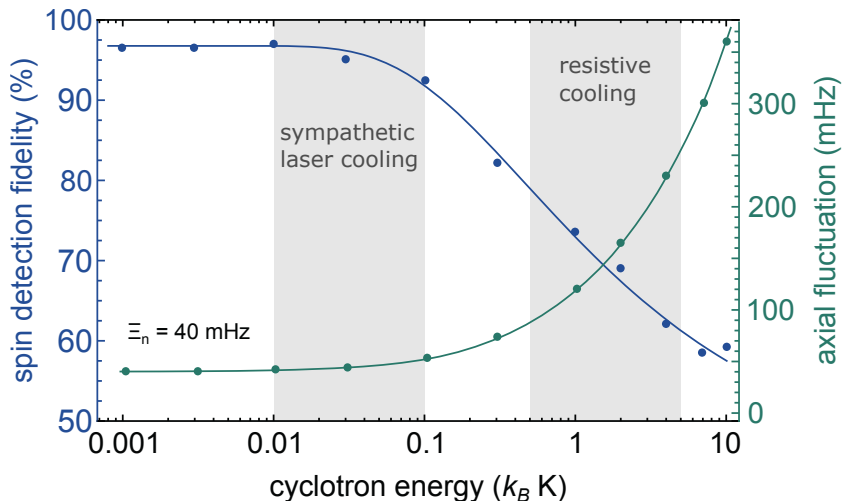
Figure 3.1: Axial frequency fluctuation (right axis) and spin-state detection fidelity (left axis) as a function of cyclotron energy. The spin-state detection fidelity is defined as the fraction of correctly identified spin states. A background fluctuation of 40 mHz is assumed. Adapted from [32].

energy would be $\langle E_+ \rangle = \langle E_z \rangle \, \omega_+/\omega_z$ with $\omega_+/\omega_z \approx 33$, a factor of ≈ 2100 higher than the energy in the magnetron mode. Therefore, the cyclotron mode needs to be cooled differently.

The spin-state detection fidelity as a function of cyclotron energy has been estimated in [32] and is shown in figure 3.1. The spin-state detection fidelity, defined as the fraction of correctly identified spin states, drops with increasing cyclotron energy and reaches 50 % for large cyclotron energies, as expected for the case where the spin-state assignment is random. The cyclotron energy for which the spin-flip fidelity starts to decrease is determined by the size of the axial frequency jump due to a spin-flip $\Delta\nu_{z,SF}$. In our case $\Delta\nu_{z,SF} = 233$ mHz and cyclotron energies above $E_+/k_B \approx 0.6$ K are unusable for spin-state readout.

This situation made it necessary to use an RLC resonator at the cyclotron frequency to directly cool the cyclotron mode. The cooling procedure to prepare a single proton for spin-state readout in the state-of-the-art proton g-factor experiment [15] is as follows: First, in the PT, the cyclotron mode of the proton was thermalized with the RLC resonator with an effective temperature of $T_0 \approx 3.2$ K for a duration of 120 s. Then, the proton was transported to the AT and the energy in the cyclotron mode was measured. This energy is Boltzmann distributed with an average energy of $\langle E_+ \rangle /k_B = T_0$. Only if the energy of the cyclotron mode was below the threshold energy of $E_{th}/k_B = 0.6$ K, leading to a detection fidelity ≥ 75 %, the sequence proceeded to the spin-state readout in the AT. Otherwise the proton was transported back to the PT and thermalized again. The low threshold together with the long thermalization time made this sub-thermal cooling procedure very time consuming which eventually limited the statistical uncertainty of the experiment.

15

An improved experiment would immensely profit from both faster cooling and lower temperatures as becomes obvious from figure 3.1. The goal would be to cool the proton's cyclotron mode to below 100 mK. Cooling to even lower temperatures will lead to diminishing return in terms of the spin-flip fidelity because the axial frequency stability is limited by voltage stability and other effects in this case, as shown in figure 3.1. In case the cyclotron mode is not cooled directly, but by interconversion with the axial mode, the ratio ω_+/ω_z must be taken into account and the axial mode needs to be cooled to temperatures of a few mK.

3.5 Other Limitations

In the following, we discuss the systematic corrections of the previous proton g-factor measurement [15, 32]. The uncertainties of all systematic corrections would in principle allow for more precise proton g-factor measurements.

The largest systematic correction is the image charge shift which affects the magnetron and cyclotron frequencies. This effect enters the proton g-factor with a relative shift of -98×10^{-12} and an uncertainty of 3×10^{-12}. Compared to the measurement in [15, 32], this shift has been reduced by a factor of 2 in the current setup by increasing the trap radius. Together with a more careful characterisation of this effect [57], an uncertainty of 1×10^{-12} should be possible in a future measurement.

The second largest systematic correction is the relativistic shift due to the energy in the cyclotron mode which predominantly affects the cyclotron and Larmor frequencies. This correction enters the proton g-factor with a relative shift of -44×10^{-12} and an uncertainty of 26×10^{-12}. The uncertainty is dominated by an artificially increased uncertainty on the cyclotron energy measurement in order to take into account two conflicting energy measurements differing by about a factor of 2. If this discrepancy can be resolved (see also the discussion in [31]) and the actual uncertainty of the cyclotron energy measurement would be used instead of the artificially increased uncertainty, an uncertainty in the g-factor of 2×10^{-12} should be possible in a future measurement.

The systematic correction with the largest uncertainty is due to the cyclotron frequency measurement. There is no shift, but an uncertainty of 80×10^{-12} which is caused by the used double-dip method relying on the continuous interconversion of the cyclotron and axial mode for detection. Here, the cyclotron frequency is extracted from two dips in the resulting axial spectrum which are fitted with a simplified theoretical lineshape. Evidently, the fit-result frequencies depend on the detuning to the frequency of the RLC resonator with an effect on the g-factor of $21 \times 10^{-12} \, \text{Hz}^{-1}$. A conservative estimate of the detuning of $\pm 2 \, \text{Hz}$ was used to arrive at the stated uncertainty, even though the detuning was measured to $< 1 \, \text{Hz}$. Consequently, using the full lineshape model also taking into account FFT window

functions together with a measurement of the detuning to the frequency of the RLC resonator, an uncertainty of 20×10^{-12} seems possible. Further improvements would be possible by using phase sensitive cyclotron frequency measurement techniques [43, 46] instead of the double-dip method. With that technique an uncertainty much lower than 10×10^{-12} should be possible in a future measurement.

There is a number of other systematic corrections, as discussed detail in [15, 32]. However, all these other systematic corrections are smaller than 10×10^{-12} with uncertainties smaller than 10×10^{-12}.

Another limiting effect is the linewidth of the Larmor resonance which was approximately 2×10^{-9} in the previous proton g-factor measurement [15, 32]. This resulted from the double-dip method where three axial frequency measurements with an uncertainty of $30\,\mathrm{mHz}$ each determine the cyclotron frequency near $29\,\mathrm{MHz}$. It is difficult to improve this method further, however, with a phase-sensitive measurement of the cyclotron frequency the linewidth of the Larmor resonance can be reduced by up to a factor of 10 [46]. Then, the leading contributions to the linewidth of the Larmor resonance would be due to the term $B_2 E_z$ in equation (3.3) and due to cyclotron frequency fluctuations due to magnetic field fluctuations. Steps have been taken to minimize B_2 in the PT by increasing the distance to the AT and by designing superconducting shim coils, to stabilize the environment parameters such as pressure and temperature that influence the magnetic field stability, and to install superconducting self-shielding coils to shield external magnetic field fluctuations, see also chapter 4 and [31].

To summarize, the uncertainty of the previous measurement of 300×10^{-12} could be improved by at least a factor of 10 if a fast cooling method with low final temperatures were available.

3.6   Multi Penning-Trap Methods

There are two avenues for improved cooling that are explored within BASE: The first one, which is a rather conventional approach and which is implemented at the CERN experiment, is the addition of a third dedicated cyclotron-cooling trap to the trap stack. This trap features a split electrode for direct detection and cooling of the cyclotron mode with an RLC resonator at the cyclotron frequency, similar to the PT discussed above. The crucial improvements are a shorter cooling time enabled by a higher quality factor and smaller effective electrode distance and a reduction of the temperature by application of negative feedback [58, 59]. The second avenue, sympathetic cooling by laser-cooled $^9\mathrm{Be}^+$ ions, is developed at the Mainz experiment and is the main topic of this thesis.

The implementation of the sympathetic laser-cooling method requires two more traps in addition to the double Penning trap. These two traps are a cooling trap

(CT) where a single to-be-cooled (anti)proton is trapped individually, and a beryllium trap (BT) which contains a cloud of laser-cooled $^9\mathrm{Be}^+$ ions. Both traps share a common electrode which couples the axial modes of the (anti)proton and the $^9\mathrm{Be}^+$ ion cloud via their image currents induced in this electrode. The concept is based on a proposal by [30] and the first version of this setup was designed in [32] and further discussed in [60].

The idea of this cooling method is to utilize the advances in the field of laser-cooling of trapped ions, and especially the low temperatures reached, for particles without optical transitions, in our case protons and antiprotons. Ion species suitable for laser cooling, e.g. singly charged alkaline-earth ions, have been cooled to the motional ground state in Penning traps using advanced laser-cooling techniques [27, 28, 29]. Using Doppler cooling of $^9\mathrm{Be}^+$ ions, temperatures as low as $0.5\,\mathrm{mK}$ are reached, four orders of magnitude lower compared to the temperatures reached with resistive cooling. To make these low temperatures available for other ions, some kind of coupling to the laser-cooled ions is needed. In this work, we employ the aforementioned common electrode coupling which enables oscillatory exchange of energy between the coupled ions: In the first step, a $^9\mathrm{Be}^+$ ion cloud is Doppler laser-cooled. Afterwards both ions are coupled by setting both axial frequencies equal. After a duration of $t = \pi/\Omega$, where Ω is the Rabi frequency of the coupling, the energy of both axial modes is interchanged. Ideally, the final temperature of the (anti)proton is equal to the initial temperature of the $^9\mathrm{Be}^+$ ion cloud after the cooling procedure.

In contrast to sympathetic cooling of particles stored in the same trapping potential (co-trapped particles) [61, 62], the image-current based interaction allows to cool individually-trapped particles. This is crucial when, as in the (anti)proton g-factor experiments, readout based on the continuous Stern-Gerlach effect is used because the readout method is only applicable when a single particle is individually trapped in the analysis trap. In addition, this allows to cool ion species of opposite charge, e.g. antiprotons, which cannot be stored in the same trapping potential as the laser-cooled ions. Essentially, this cooling technique is applicable to all ions. The distinction between cooling individually-trapped particles and cooling co-trapped particles only arises once a second laser-cooled ion species is introduced. So far, using image current based cooling methods, cooling individually-trapped particles has been the standard, and this distinction did not have to be made.

Compared to sympathetic cooling of individually-trapped particles via Coulomb interaction [63, 64], our method allows to place the involved traps far apart. Consequently, coherent motional coupling is possible over large separations between the involved ions.

For the (anti)proton g-factor experiments, the sympathetically cooled axial mode needs to be transferred to the cyclotron mode via interconversion of modes. This

increases the final temperature of the cyclotron mode by the ratio ω_+/ω_z, typically 50 to 100. Nevertheless, the sympathetic cooling method outlined above should provide individually-trapped protons and antiprotons with cyclotron temperatures below 100 mK. We envision that these final temperatures are low enough such that only a single cooling attempt is necessary to reach acceptable spin-flip detection fidelity. This should speed up the data taking in the (anti)proton g-factor experiments enormously, as the cycle times will be reduced from a few hours to a few minutes. Further, the sympathetic cooling technique will also be useful for future phase sensitive cyclotron-frequency measurements.

Chapter 4

Experimental Apparatus and Methods

The experimental apparatus used in this work is designed for an improved measurement of the proton g-factor, critically relying on the successful implementation of the sympathetic-cooling method described in the previous chapter. To this end, the apparatus used in the previous proton g-factor measurements in 2014 [65, 66] and 2017 [15, 32] has been heavily modified. This apparatus is described in many of the previous PhD theses carried out at the proton g-factor experiment [32, 42, 66, 67, 68, 69]. Essentially, it consists of a cryogenic trap chamber and an electronic section cooled to near 4 K (the 4 K-section) which are located inside the horizontal bore of a warm-bore 1.9 T superconducting magnet. The 4 K-section is cooled independently by being connected to the liquid-helium stage of a bath cryostat via an oxygen-free high-thermal-conductivity (OFHC) copper rod.

What has been retained from the previous apparatus is the cryo-mechanical support structure: This structure provides support for the 4 K-section which is suspended inside an aluminium tube (77 K-section) that is clamped to a horizontal arm consisting of a fiber-glass tube. The horizontal arm is in turn mounted inside of a CF200 6-way cross. The 77 K-section is connected to the liquid nitrogen stage of the bath cryostat via OFHC copper rods and shields the 4 K-section from thermal radiation. Crucial to the design is the balance between sturdy support, high thermal conductivity to the bath cryostat, and low heat load to the cryogenic sections of the setup. The original cryo-mechanical support structure has been set up in 2006 [70] and featured a pulse-tube cryo-cooler. This was later replaced by a bath cryostat in order to solve problems caused by vibrations of the cryo-cooler. A considerable advantage of the cryo-mechanical support structure is that it can be moved out of the horizontal bore of the magnet on rails, facilitating relatively quick upgrades to the cryogenic sections.

Completely new is the 4 K-section of the experiment, see figure 4.1: The electronic section was elongated to allow for a total of three resonators to be imple-
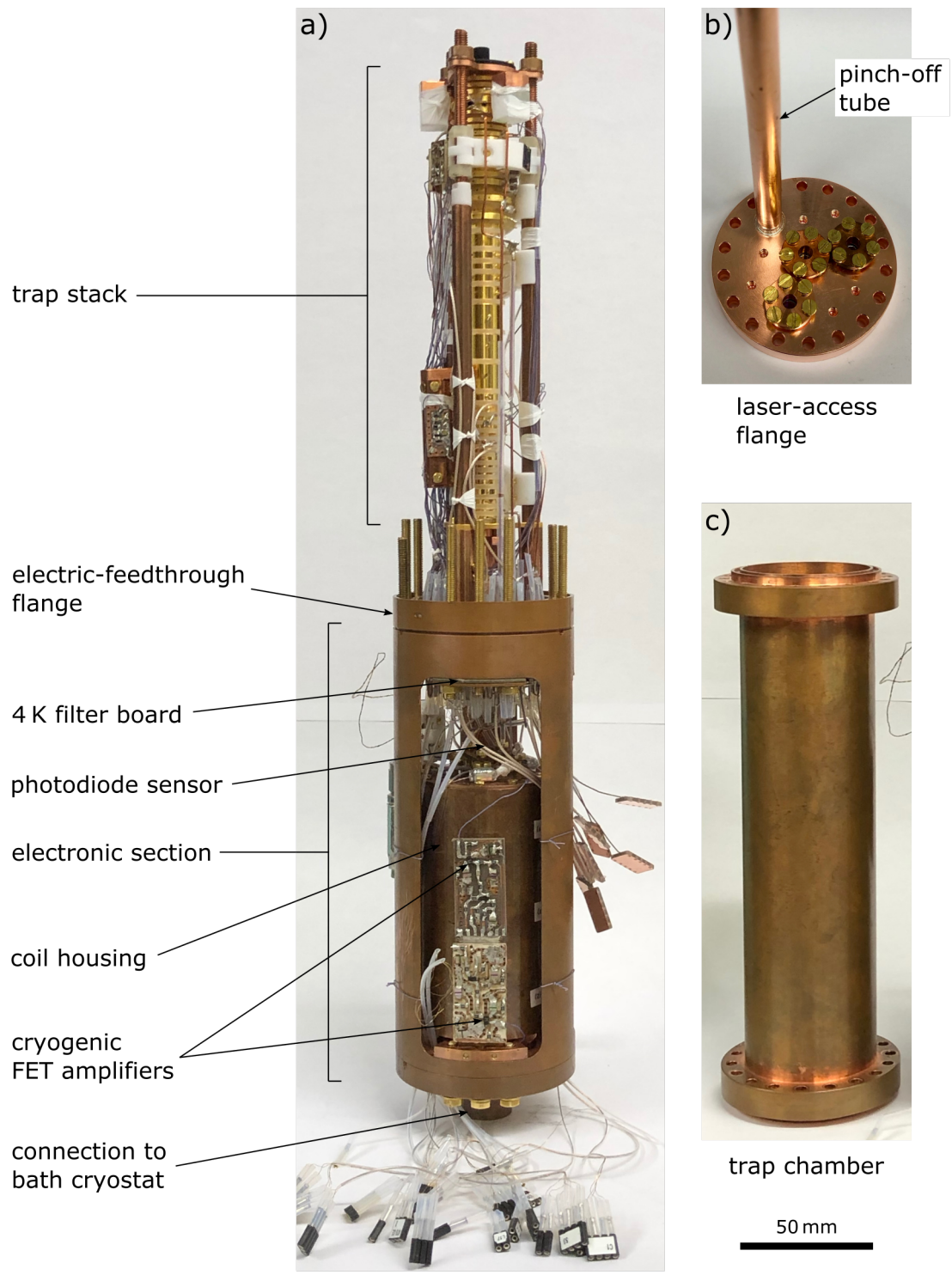
Figure 4.1: 4 K-section of the proton g-factor experiment. (a) trap stack with electronic section, (b) laser-access flange with pinch-off tube, (c) trap chamber.

mented. The electronic section further houses the associated cryogenic amplifiers, and low-pass filters for the bias and excitation lines. The new trap chamber now features two flanges, one with feedthroughs for all electrical connections, and one with three windows for laser access and a pinch-off tube. Inside the trap chamber, the removal of the cyclotron resonator which used up almost half of the available space made way for the new coupling traps and loading trap. The number of electrodes has more than doubled, which made it necessary to renew most electrical connections, as well as the filter boards located at room temperature, in the 77 K-section, and in the 4 K-section. Although, most of the 4 K-section was built from new components, some components such as the AT trap electrodes, the spin-flip coils, and two out of three of the initially-used resonator coils were reused from the previous setup.

The trap chamber is hermetically sealed. To this end, both flanges are mounted to the trap chamber using indium seals. The electrical feedthroughs and the pinch-off tube are hard soldered to the respective flange, while the fused-silica windows are pressed onto indium seals with copper cylinders. Before cool-down, the trap chamber is baked and pumped to a residual gas pressure below 1×10^{-6} mbar. After leak-tightness is assured, the copper pinch-off tube is pinched off which seals the trap chamber. After cool-down, cryo-pumping improves the residual gas pressure typically by more than 11 orders of magnitude to levels below 1×10^{-17} mbar [71]. This extremely low residual gas pressure allows the storage of single protons for many months.

4.1 Multi Penning-Trap System

The multi-Penning-trap system located inside the trap chamber (see figure 4.2) is the heart of the experiment, in its final version it consists of six traps with very different features and purpose. These six traps are described in the following. All traps are stacked along the magnetic field axis, and transport electrodes allow for adiabatic transport of stored ions between the traps. The electrodes are held in place by sapphire rings or, in two instances, quartz rings. The assembled trap stack is sandwiched between two end-plates and compressed by three OFHC copper rods, an assembly that is self-tightening when cooled to 4 K.

4.1.1 Precision Trap (PT) and Analysis Trap (AT)

The PT and AT are designed to implement the double Penning-trap method for magnetic moment measurements according to [23, 54]. Both traps are cylindrical open-endcap traps in compensated, orthogonal design [72]. The PT is located in the center of the magnet at the position of the most homogeneous magnetic field. It is used primarily for precise cyclotron and Larmor frequency measurements. The currently-used PT has an increased diameter of 9.0 mm compared to the 7.0 mm
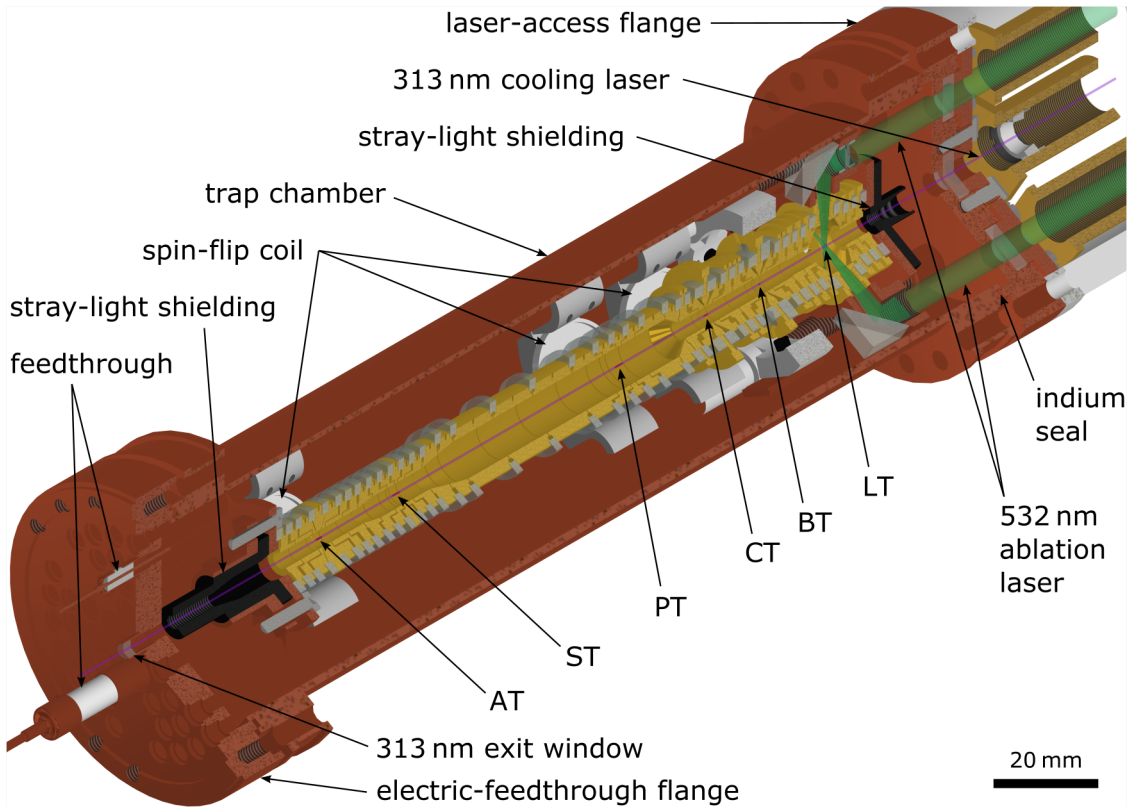
Figure 4.2: Multi-Penning-trap system. For details see text.

diameter used previously [32] in order to reduce the leading systematic effect: Image charge shifts. Previous generations of the experiment used a cyclotron resonator connected to the PT to cool the single proton. This was somewhat inefficient because of the large effective electrode distance in the large-diameter PT. In the new generation of the experiment the cyclotron resonator is no longer needed and the available space previously occupied by the cyclotron resonator is used for the coupling traps and the ion loading trap used for laser cooling.

A self-shielding superconducting solenoid [73] is used to stabilize the magnetic field at the position of the PT. This reduces short term fluctuations of the magnetic field and leads to improved cyclotron frequency stability. Winding of the coil is described in [74]: Superconducting NbTi wire is used to wind a solenoid onto the trap chamber centered around the PT ring electrode. The loop is closed by connecting both ends of the solenoid with a superconducting joint. Consequently, the coil is normally operated in persistent mode. When needed, a resistor mounted next to the superconducting wire serves as heater which allows to quench the coil. A more sophisticated multi-solenoid setup which will also allow to compensate linear and quadratic inhomogeneous terms has been designed [31] and will be implemented in the future.

The AT features a strong magnetic bottle with $B_2 = 300 \, \text{kT} \, \text{m}^{-2}$ in order to allow the detection of single spin flips of a single proton, The design of the trap is described in [53]. The large magnetic bottle term is achieved by using a ring

electrode made from cobalt-iron (CoFe) which has a high saturation magnetization of 2.35 T. Crucially, the inner diameter of this trap is only 3.6 mm in order to increase the magnetic bottle term. Hence, the voltages applied to the trap electrodes are on the order of 0.5 V, which makes this trap very sensitive to patch potentials on the surface of the electrodes. Consequently, the small diameter together with the strong magnetic bottle term makes the AT very difficult to operate. In addition to the small diameter of the electrodes, the ring electrode geometry is optimized to increase the magnetic bottle term. Compared to the previous setup [15, 32], the distance between the PT and the AT was increased to further reduce the influence of the magnetic gradient in the PT caused by the ferromagnetic ring electrode of the AT.

4.1.2 Cooling Trap (CT) and Beryllium Trap (BT)

The CT and BT were designed for sympathetic cooling of a single individually-trapped proton by image-current coupling to laser cooled $^9Be^+$ ions via common electrode [32, 60]. To this end, the proton is stored in the CT and a cloud of laser-cooled $^9Be^+$ ions is stored in the BT. The axial mode of the proton is coupled to the axial center-of-mass mode of the $^9Be^+$ ion cloud via the image currents induced in a common electrode. In the original design, the common electrode is formed by four electrodes, the two correction electrodes and the two end electrodes located between the position of the proton and the $^9Be^+$ ion cloud, which are capacitively connected. This common electrode coupling is enhanced when the capacitance of the common electrode C_T is small and when the effective electrode distances of the proton and $^9Be^+$ ion cloud are small.

The CT and BT are also cylindrical open-endcap traps in compensated, orthogonal design [72]. The small diameter of 4.0 mm provides a small effective electrode distance in order to facilitate fast coupling times. Further, the geometry of the trap electrodes is optimized to reduce the capacitance between the ring electrodes and the adjacent correction electrodes. In addition, the sapphire rings between these electrodes are replaced by quartz rings in order to reduce the permittivity. Altogether, a trap capacitance of 5.6 pF was estimated and 5.5(5) pF was measured in a test setup [32]. Once implemented in the 4 K-section, we measured a common-electrode capacitance of 7.5 pF. The difference is likely due to the stray capacitance of the wires which connect to the electrodes.

As an additional feature, the BT ring electrode is split into six segments. This allows the application of a rotating wall drive to the six segments, which was intended to compress the laser-cooled $^9Be^+$ ion cloud radially. However, we could not get the rotating wall to work reliably and abandoned this concept. Instead a small radial component of the cooling laser was used to compress the $^9Be^+$ ion cloud radially, which worked reliably. The six slits in the BT ring electrode allow fluorescence light to escape the trapping region, enabling fluorescence detection. More details on the

geometry of the BT are provided in chapter 6 in context of fluorescence detection. Further details about the trap design can be found in [32, 60, 33].

Later we realized that the coupling can also be achieved via a common RLC circuit instead of the common electrode, as suggested in [30] and first demonstrated in [75]. Essentially, near resonance the RLC circuit provides a very small effective capacitance, several orders of magnitude smaller than the common electrode capacitance. Therefore, in addition to the common electrode coupling, common-RLC circuit coupling is possible between the CT and BT because they are both connected to the same RLC circuit for image-current detection. Because the other traps are also pairwise connected to an RLC circuit, this common-RLC circuit coupling is also possible between the AT and ST, and the PT and LT.

4.1.3 Storage Trap (ST)

Originally, the ST was used as a trap for production and storage of protons. As all the traps discussed above, the ST is also a cylindrical open-endcap trap with compensated, orthogonal design [72]. The diameter of 5.0 mm is a compromise between small effective electrode distance and convenient trap voltages. To produce protons, an electron beam is emitted from a field-emission tip, passes the ST, and is reflected back by a blocking voltage on the adjacent transport electrode. The electrons undergo multiple reflections and eventually hit the surfaces of the trap where they release hydrogen atoms from the surface which are then ionized in the center of the trap. This loading procedure worked reliably, however the field-emission tip was in the way of the cooling laser beam and led to unacceptably large stray-light intensity. Therefore, proton loading by electron beam was finally replaced by proton loading through laser ablation, see section 4.1.4.

In the final version of the apparatus the ST served an entirely different purpose: radial energy measurements. Making use of the continuous Stern-Gerlach effect [51], equation (3.5), the magnetic bottle used to detect proton spin flips in the AT can also be used to determine the radial energy of the proton. Here, the energy in the radial motional modes is measured via an axial frequency shift. However, due to the large value of the magnetic bottle in the AT, $300 \, \mathrm{kT \, m^{-2}}$, the frequency shift due to typical radial energies is inconveniently large, about $97 \, \mathrm{Hz \, K^{-1}}/k_B$ for protons and $10.8 \, \mathrm{Hz \, K^{-1}}/k_B$ for $^9\mathrm{Be}^+$ ions. During initial experiments to determine the proton temperature in the AT it turned out to be very time consuming to scan the frequency range covered by protons with average cyclotron energies of around $k_B \times 300 \, \mathrm{K}$. A single cyclotron energy measurement under these conditions requires on average 2 hours, and a temperature measurement with 50 data points about 4 days. Because the duration of a temperature measurement is directly proportional to the strength of the magnetic bottle, a reduction speeds up the temperature measurement. Moreover, a lower temperature also speeds up the measurement, but this requires a working
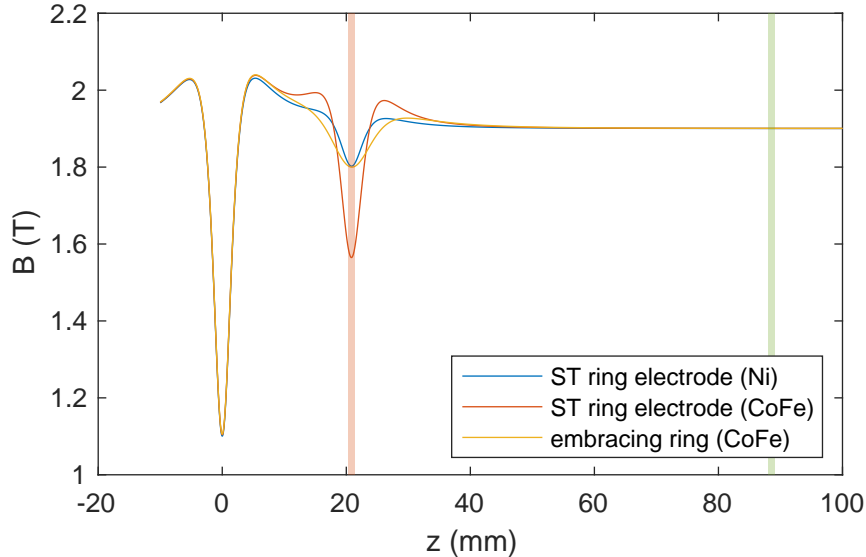
Figure 4.3: Magnetic field along the trap axis for 3 design options to create a magnetic bottle in the ST. The origin is centered at the position of the AT. The red vertical line indicates the position of the ST, the green vertical line the position of the PT.

cyclotron-cooling technique.

Therefore, as part of this thesis, several design options to change the ST into an efficient temperature measurement trap by creating a comparably smaller magnetic bottle have been investigated. These are: a ring electrode made from nickel (Ni) with a saturation magnetization of $0.64\,T$; a ring electrode made from cobalt-iron (CoFe) with a saturation magnetization of $2.35\,T$; and a ring, embracing the ring electrode, made from CoFe. The magnetic fields of each configuration have been simulated with COMSOL. The resulting magnetic field on the trap axis is shown in figure 4.3. The three options lead to magnetic bottle terms of $27.7\,kT\,m^{-2}$, $95\,kT\,m^{-2}$, and $9.1\,kT\,m^{-2}$, respectively. Given the constraints of geometry, manufacturability, and minimal influence at the position of the PT, the best option has been determined to be the ring electrode made from nickel. In addition to the magnetic bottle of $27.7\,kT\,m^{-2}$, the geometry of the ST ring electrode leads to an unavoidable higher order term $B_4 = -3.9\,GT\,m^{-4}$.

Consequently, we modified the ST with a magnetic ring electrode made from nickel. This solution leads to a frequency shift of $5.7\,Hz\,K^{-1}$ for protons and $0.63\,Hz\,K^{-1}$ for $^9Be^+$ ions. Note that the magnetic field at the center of the ST is approximately $1.80\,T$, a factor of 1.5 larger than the magnetic field at the center of the AT, $1.17\,T$. This makes the frequency shift smaller by an additional factor of 1.5. The smaller shift speeds up the temperature measurement for a single proton by a factor of 17, while still maintaining a temperature resolution of better than $10\,mK$. With this modification, the ST is ideally suited for temperature measurements of resistively-cooled, laser-cooled, or sympathetically-cooled protons, where radial temperatures between a few mK and a few K are expected, and also works

well for radial temperatures up to several $100\,\mathrm{K}$. Radial temperature measurements in the ST are at least an order of magnitude faster than in the AT. Only when the ultimate temperature resolution is needed, the AT is preferable.

Detecting the first $^9\mathrm{Be}^+$ ions in the new ST was a matter of minutes, while searches for particles in the AT could last for several weeks. This trap proved to be a cornerstone of the very successful sympathetic cooling experiments described in chapter 10.1.2. Characterisation measurements of the magnetic bottle in the ST have been carried out with a single proton or $^9\mathrm{Be}^+$ ion as magnetic field sensor, they are described in detail in [31]. These measurements resulted in values of $B_0 = 1.798\,917\,\mathrm{T}$, $B_2 = 27.8(7)\,\mathrm{kT\,m^{-2}}$, and $B_4 = -4.4(5)\,\mathrm{GT\,m^{-4}}$. All of these values are in good agreement with the simulated values described above.

4.1.4 Loading Trap (LT)

Originally, $^9\mathrm{Be}^+$ ion production was done in a loading electrode next to the BT. To produce $^9\mathrm{Be}^+$ ions, a $10\,\mathrm{ns}$ pulse from a $532\,\mathrm{nm}$ ablation laser was directed to a target made from beryllium metal. The laser pulse sputters atoms and ions off the target and some of these ions are trapped in the adjacent BT [33]. This production method was associated with several problems: First, the loading electrode design did not allow for storage of ions in this electrode due to the large radial holes of this trap breaking cylindrical symmetry. Consequently, a potential well in the adjacent BT was used to trap the produced ions. Second, the use of relatively large pulse powers in the range of $3\,\mathrm{mJ}$ were necessary in order to trap some $^9\mathrm{Be}^+$ ions in the BT. Third, there was a direct line of sight from the beryllium target to the trap electrodes of the BT. Ablated atoms were able to travel to the BT electrodes and got stuck on the surfaces. This led to a change of trapping potentials in the BT after each applied ablation laser shot. In addition, after several shots the axial frequency of the ions stored in the BT showed excessive frequency instability, essentially rendering the BT unusable. However, the potentials could be reset by warming up the apparatus to room temperature, an expected behaviour for surface charges.

A dedicated loading trap (LT) was designed to mitigate the most pressing of these problems. In designing the loading trap, the first challenge is presented by the required radial access to the trapping region, necessary to bring the ablation laser beam to the target. The generally used cylindrical open-endcap Penning-trap design [72] features a very short ring electrode, which makes it difficult to implement holes in radial direction for the target and the ablation laser. In contrast, the cylindrical flat-endcap Penning-trap design [72] features a comparably long ring electrode with ample space to implement radial holes. However, the cylindrical cavity of this design is closed in all directions. Inspired by these designs, we investigated the geometry shown in figure 4.4a. This geometry has features of both designs discussed above. It features a rotationally-symmetric barrel-shaped cavity with large
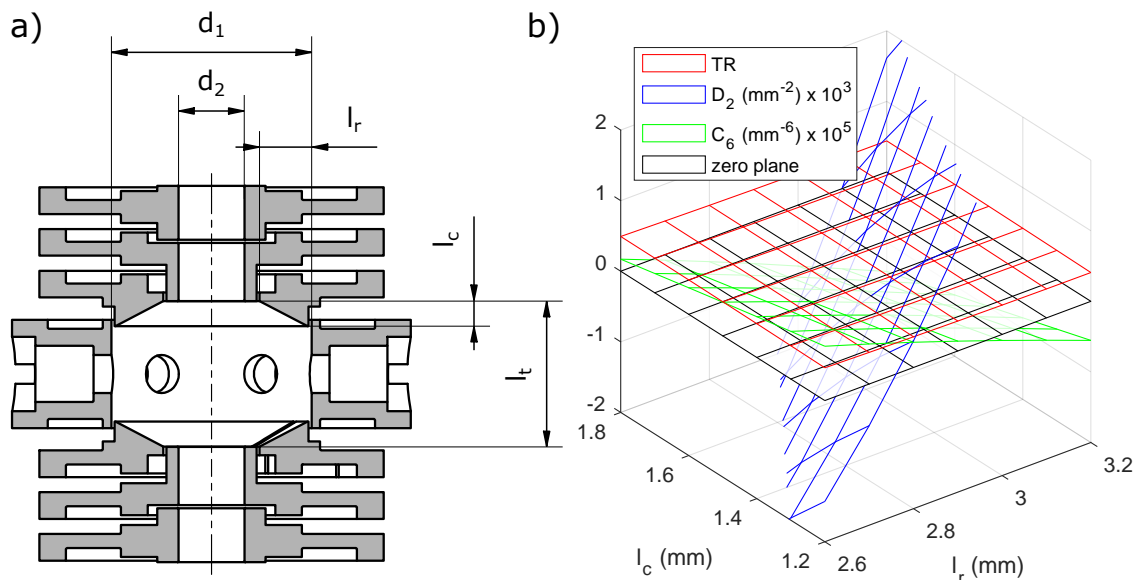
Figure 4.4: Loading trap: (a) definition of LT dimensions. (b) potential coefficients as function of LT dimensions.

diameter and a long ring electrode. In addition, the endcaps are open and allow the transport of ions into and out of the trap. Crucially, the correction electrodes feature a chamfer. In contrast to a cylindrical shape ($l_r = 0$), this shape allows for a compensated and orthogonal design. The long ring electrode provides ample space for radial holes for the target and the ablation laser beam. We chose a six-fold symmetry of these radial holes for two reasons: First, because this eliminates trap ellipticity, as the first non-vanishing potential perturbations are of high order. And second, because this allows for more than one target and ablation laser beam path to be implemented. We decided to implement two separate targets for production of $^9\mathrm{Be}^+$ ions and protons, respectively. In the remaining third slot we implemented a silicon photomultiplier (SiPM) for fluorescence detection, see figure 4.5.

In defining the LT geometry we start with a judicious choice of the diameters $d_1 = 11.0\,\mathrm{mm}$ and $d_2 = 3.6\,\mathrm{mm}$. The diameter of the ring electrode d_1 defines the C_2 of the trap, and we were aiming for a C_2 in between the values for the PT, $C_2 = -18\,510\,\mathrm{m}^{-2}$, and the ST, $C_2 = -59\,900\,\mathrm{m}^{-2}$. The diameter of the end electrodes d_2 was chosen smaller than the diameter of the adjacent BT and CT, such that ions escaping from the ablation region would rather hit the end electrodes than the BT and CT electrodes. The values of the other dimensions, the length of the trap l_t, the length of the correction electrode l_c, and the length of the chamfer in radial direction l_r, are optimized by numerical simulations of the trapping potential in order to assure a compensated and orthogonal design [72]. The gaps between electrodes are $0.140\,\mathrm{mm}$ wide.

The trapping potential is the superposition of the potential due to the voltage $V_r = V_0$ applied to the ring electrode and the potential due to the voltage $V_c = V_0 \times TR$ applied to both correction electrodes. Expanding the potential of the ring

a) b)

lens | target | SiPM | lens | ion cloud
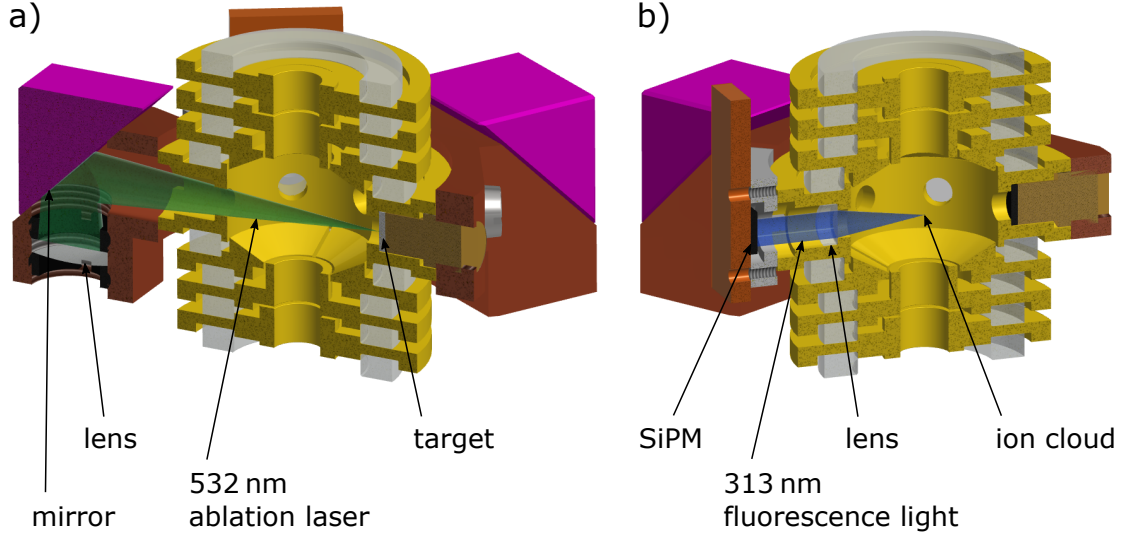mirror | 532 nm ablation laser | | 313 nm fluorescence light |

Figure 4.5: Loading trap: (a) ablation laser beam path and p/Be target. (b) fluorescence readout with SiPM. Holders for the mirrors, targets, and the SiPM are mounted radially to the ring electrode.

electrode as in equation (2.17) and denoting the coefficients E_k, as well as expanding the potential of both correction electrodes and denoting the coefficients D_k leads to

$$C_k = E_k + D_k \times TR. \tag{4.1}$$

In this formalism compensation is characterized by

$$C_4 = E_4 + D_4 \times TR \overset{!}{=} 0 \text{ and} \tag{4.2}$$

$$C_6 = E_6 + D_6 \times TR \overset{!}{=} 0 \tag{4.3}$$

and orthogonality by

$$D_2 \overset{!}{=} 0. \tag{4.4}$$

The optimisation procedure to achieve orthogonality and compensation simultaneously is as follows: As a function of trap dimensions, we calculate the potentials with COMSOL and extract the E_n and D_n coefficients by fitting the on-axis potential in the region $\pm 2\,\text{mm}$ around the trap center with a polynomial function. In the next step we calculate the tuning ratio by setting $TR = -E_4/D_4$. Using this value for TR we calculate $C_6 = E_6 + D_6 \times TR$. Next, we plot D_2 and C_6 as a function of trap dimensions, see figure 4.4b. The resulting surfaces have a zero-crossing for compensation and orthogonality, respectively. The parameter region for $D_2 = 0$ and $C_6 = 0$ is plotted in figure 4.6. At the point where both surfaces have a zero-crossing, compensation and orthogonality is fulfilled simultaneously. Reading off the trap dimensions with $1\,\text{µm}$ accuracy is sufficient, as the manufacturing tolerances will be typically several µm. This procedure is repeated for a few values of the trap length l_t. In the end, a trap length of $l_t = 8.000\,\text{mm}$ was chosen because
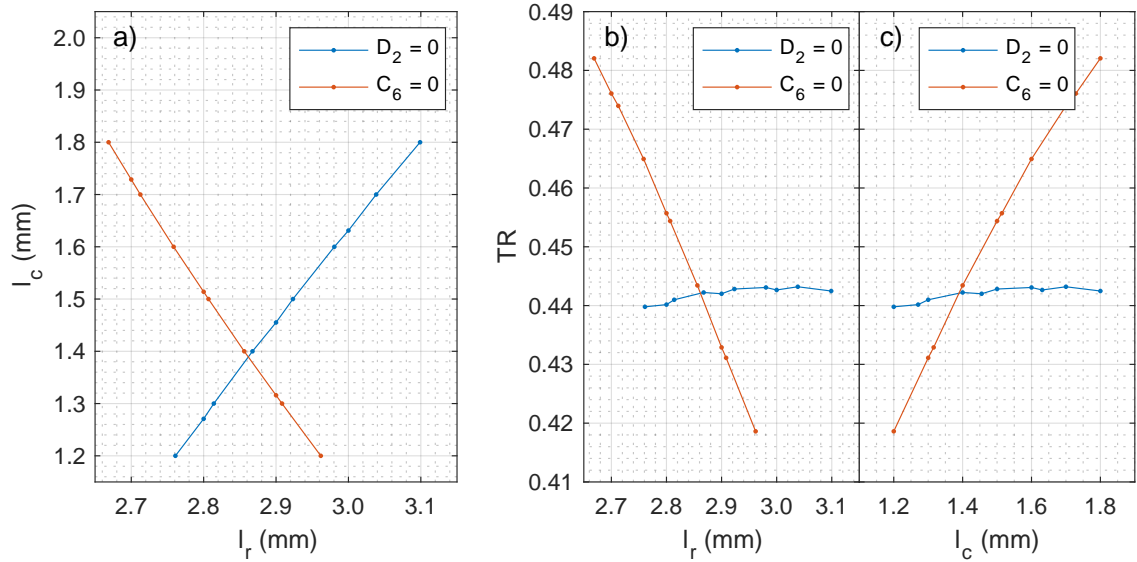
Figure 4.6: Parameter region where $D_2 = 0$ and $C_6 = 0$ for $l_t = 8.000\,\text{mm}$: in (a) as a function of trap dimensions l_r and l_c, in (b) as a function of l_r and TR, and in (c) as a function of l_c and TR.

quantity	value
d_1	11.000 mm
d_2	3.600 mm
l_t	8.000 mm
l_r	2.862 mm
l_c	1.389 mm
TR	0.442
C_2	$-29\,471\,\text{m}^{-2}$
D_4	$-1.76 \times 10^9\,\text{m}^{-4}$
D_c	14.4 mm
D_e	18.1 mm
D_{c+e}	8.0 mm

Table 4.1: Loading trap (LT) dimensions and parameters.

this value maximized the length of the ring electrode $l_t - 2l_c$ while keeping l_r small enough to be manufactureable. The dimensions of the final design are summarized in table 4.1. In addition, the values of the parameters C_2 and D_4 are listed, as well as the effective electrode distances of the correction electrode D_c, the end electrode D_e, and the combination of correction electrode and end electrode D_{c+e}.

The final design of the LT, shown in figure 4.5, eliminates the problems discussed above. Ions can be stored directly at the production site. As a result, much less laser power should be needed to load ions. Further, a direct line of sight from the target to the trap surfaces of the BT and CT is not present. This mitigates contamination of the BT and CT electrodes by atoms. Contamination by ions is avoided due to a small diameter of the end electrodes of the LT. Ions on large magnetron or cyclotron radii would rather strike the end electrodes of the LT than the trap electrodes in the BT and CT. In addition, the possibility to include multiple targets is a considerable
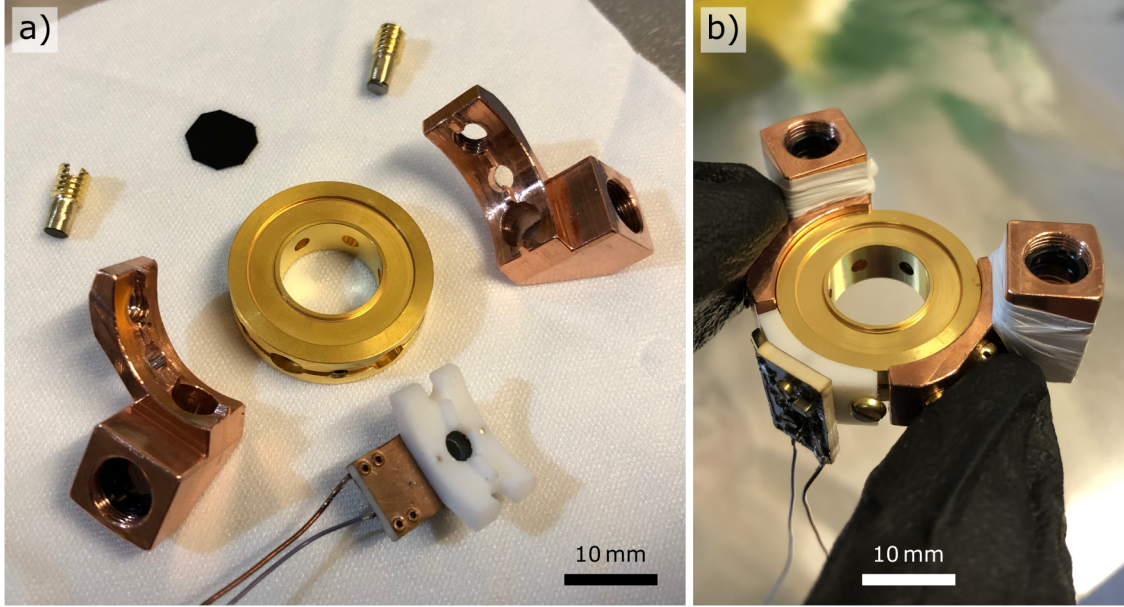
Figure 4.7: LT ring electrode: (a) components before assembly. (b) fully assembled LT ring electrode.

upside of the design. Also, the LT features a split correction electrode for application of a quadrupole excitation. The two halves of the electrode are fixed in place by sapphire balls assuring a uniform gap.

After manufacturing and gold plating of the electrodes, the trap was assembled and integrated into the trap stack. Photographs of the ring electrode before and after assembly are shown in figure 4.7. The ring electrode is the most complicated part of the LT, as it features two targets, two mirrors, and a SiPM mounted via holders that are bolted radially to the ring electrode.

In a first run we chose a beryllium foil as target to produce $^9\text{Be}^+$ and a polyethylene (PE) target to produce protons. While the beryllium foil worked very well, the protons from the PE target were contaminated by a large number of other low-mass ions. In a second run we replaced the PE target with a tantalum (Ta) target [76], which worked very well as a source for protons. A contamination by relatively high-mass Ta^+ ions is easy to remove.

We characterized the LT with $^9\text{Be}^+$ ion clouds and measured the trap parameters C_2, D_4, and TR. All of them are consistent with the simulated values listed in table 4.1. During operation we found that much lower laser power, typically $0.22\,\text{mJ}$, is necessary to effectively load $^9\text{Be}^+$ ions in the LT. This greatly reduces the problem of coating the trap surfaces, but does not avoid it completely. We found that after each loading the trap parameters of the LT change slightly, as expected. However, the trapping parameters of the other traps, especially the BT and CT, still change slightly after loading. In a future upgrade the LT would ideally feature a movable electrode such that the LT can be closed off from the rest of the trap stack during loading. Hopefully, this would avoid the trapping potential changes introduced by

ion loading completely.

In practice, the small potential changes in the LT caused by loading ions did not prevent us from operating this trap successfully. The LT was used e.g. in the sympathetic cooling experiments described in chapter 10. Furthermore, the design allows for fluorescence detection to be performed in this trap. Fluorescence detection is discussed in more detail in chapter 6 using ions stored in the BT, but it is routinely performed in the LT as well.

4.2   Evolution of the Trap Stack

Several configurations of the trap stack have been used throughout this work, they are compared in figure 4.8. For reference, the trap stack used in the previous proton g-factor measurement [15, 32] is shown on the right. Over the years, several changes and improvements have been implemented, which are described in the following.

The first version of the trap stack designed for sympathetic cooling was set up in 2017. It featured the configuration described in [32] and [60], consisting of the ST, AT, PT, CT, and BT, in this order. We used this setup to characterize the loading procedures, the transport between all traps, and demonstrated image-current detection and cooling of the axial modes, as well as cooling of the radial modes with sideband coupling. We successfully loaded protons in the ST using a reflected electron beam, in contrast to the electron beam that passes through the complete trap stack used previously. We further demonstrated $^9\mathrm{Be}^+$ ion loading by laser ablation, after switching from a fiber-based beam delivery to a free-space beam. While proton loading in the ST using the reflected electron beam worked well, see also the description in [74], $^9\mathrm{Be}^+$ loading by laser ablation in the loading electrode presented several problems, as discussed in the previous sections. We also performed a first experiment on laser-$^9\mathrm{Be}^+$ interaction read out by image-current detectors. In this case we heated the $^9\mathrm{Be}^+$ ions with a low-power blue detuned laser. With the fluorescence readout not yet available, we used image-current detection to record the signal of the heated $^9\mathrm{Be}^+$ ions, see section 7.3. Also, without a technique for direct cooling of the cyclotron mode, T_+ was approximately $300\,\mathrm{K}$ after sideband cooling and made the temperature measurements in the AT time consuming.

In 2018 we moved the ST in between the BT and the $^9\mathrm{Be}^+$ loading electrode. This was intended to shield the BT and CT from the loading section. The change was necessary because ablated atoms and ions coated the trap surfaces of the BT and CT in the previous configuration, where, after a few shots of the ablation laser, the CT and BT were unusable and the experiment had to be warmed up to reset the surface contamination. With the modified setup we observed that the loading problem had improved; The trap voltage in the trap next to the loading section (ST) would still increase after each loading, however the changes in the BT and CT
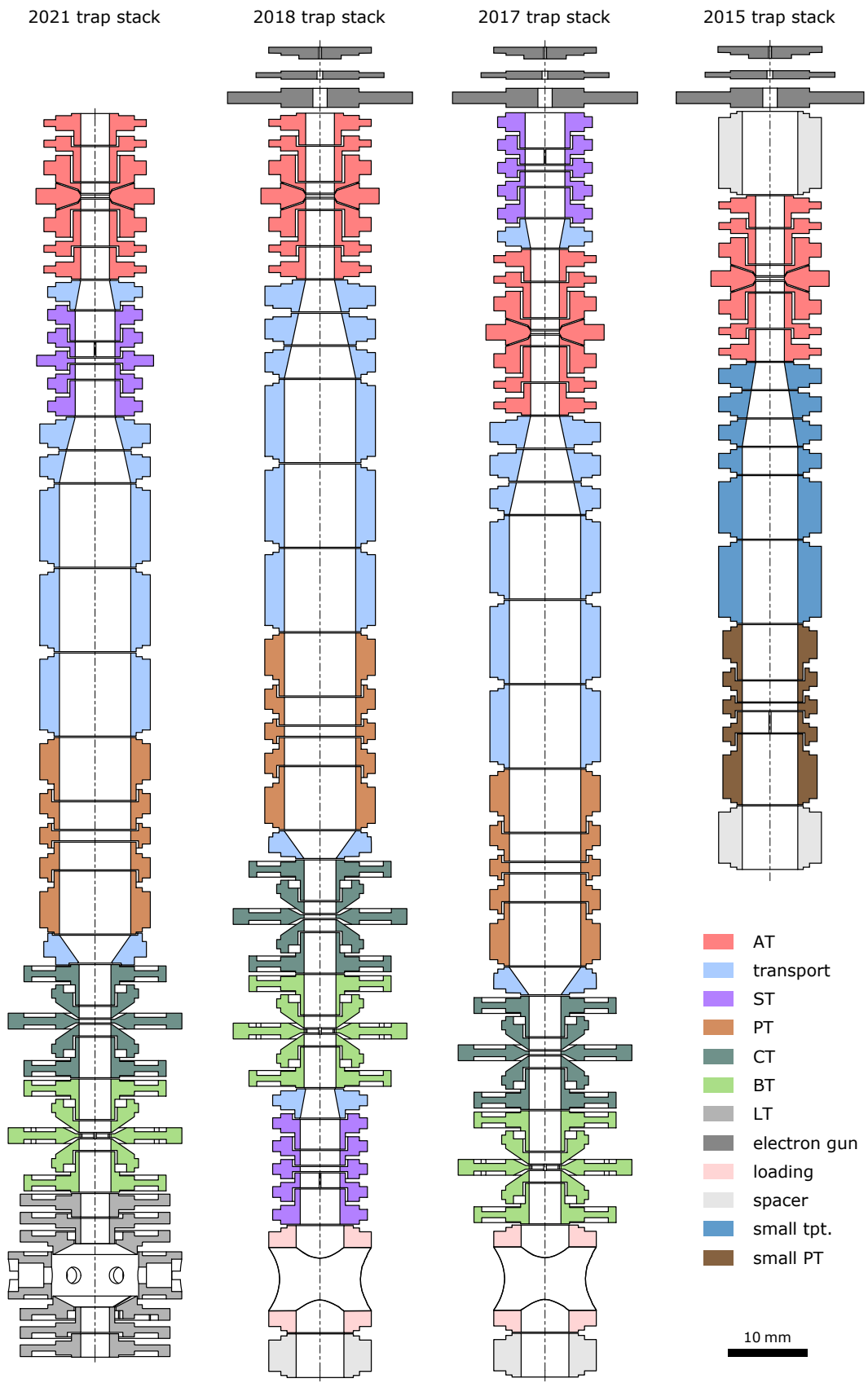
Figure 4.8: Comparison of trap stack configurations. tpt.: transport.

were manageable. In the beginning, we used the electron beam to load protons, but later had to switch to ablation loading from the beryllium foil. Here we simply increased the energy of the ablation laser pulses until protons would be produced, likely from rest gas frozen out on the beryllium target. However, this is not recommended in case the trapping potential changes after loading are to be minimized. We further switched from a fiber-based beam delivery to a free-space beam for the cooling laser also, as this gave us control over the beam position and angle, see also section 7.6. With this improvement we were able to successfully laser-cool ^{9}Be$^+$ ions in the BT. We also succeeded with fluorescence detection after the readout was changed to the single photon sensitive readout described in chapter 6. With this new detection method available, we demonstrated for the first time simultaneous detection of fluorescence and image currents of laser-cooled ^{9}Be$^+$ ions in this setup, see section 8.3. Fluorescence detection was, however, plagued by stray light e.g. from the field emission tip of the electron gun. An attempt to measure the radial energy of ^{9}Be$^+$ ions in the AT after laser cooling was thwarted by resonance effects, as further discussed in chapter 9. Lastly, using this configuration we first succeeded in sympathetic cooling of a single proton. Here, the proton was stored in the PT and the ^{9}Be$^+$ ion cloud in the ST, with the ion motion coupled via the RLC resonator connected to both traps, as described in chapter 10.

Finally, in 2021 we implemented the new loading trap (LT) and also replaced the trap electrodes of the AT, BT and CT with newly manufactured ones. The ST, now placed between the AT and PT, was equipped with a magnetic bottle. Loading both protons and ^{9}Be$^+$ ions in the LT by laser ablation allowed us to remove the electron gun including the field emission tip, which resulted in an unblocked beam path for the cooling laser along the trap axis. In addition, stray light shielding was installed, as shown in figure 4.2. This configuration led to a much lower stray light level compared to previous versions. Also, the loading problems were largely eliminated. Using this configuration, we performed a second run of the experiments on simultaneous detection of image currents and fluorescence, see chapter 6 and section 8.3. Here, a crucial improvement was the control of the cooling laser beam position and angle with motorized mirrors. Initially, we suffered from low Q-factors of the image-current detectors because some of the newly installed components led to increased loss in the RLC circuits, see section 5.8.4. However, after thorough optimisation work to improve the Q-factors, we achieved Q-factors above 10 000 for the first time for all three image-current detectors simultaneously. Lastly, this configuration was used successfully for sympathetic cooling of a single proton stored in the PT, with the ^{9}Be$^+$ ion cloud stored in the LT, combined with a precise temperature measurement in the ST. This measurement is summarized in chapter 10.

In total we had 6 cool-downs with the 2017 configuration, 4 cool-downs with the 2018 configuration, and so far 3 cool-downs with the 2021 configuration.

4.3 Laser Access

Originally it was foreseen to deliver both the cooling laser light and the ablation laser light to the cryogenic trap chamber via optical fiber. However, in case of the cooling laser, this meant that the position and angle of the cooling laser was fixed. This turned out to be a major obstacle for laser cooling, as the ability to successfully laser-cool the stored ^{9}Be$^+$ ions critically depends on optimized beam position and angle. In case of the ablation laser, it was difficult to deliver enough laser power without damaging the fiber. Later, delivery through fibers was abandoned and free-space laser beams were used to deliver the laser light to the trap chamber.

Three windows in the laser-access flange allow for laser access into the trap chamber: The on-axis window, featuring an anti-reflective coating in the ultraviolet (UV), allows for access of the 313 nm cooling laser to the traps used for ^{9}Be$^+$ ion cooling. Two off-axis windows, featuring an anti-reflective coating optimized for 532 nm, allow for access of the ablation laser to the solid beryllium target used to produce ^{9}Be$^+$ ions and to the tantalum (Ta) target used to produce protons. To assure leak-tightness of the flange, the fused-silica windows are pressed onto an indium seal by copper cylinders. Discs made from aluminum foil are used as spacers to avoid cracking of the windows under uneven load. The holders for the fiber mounts have been repurposed as apertures that help with alignment of the free-space beams, see also figure 4.2.

One disadvantage of the use of free-space laser beams is that a direct line of sight from room temperature to the 4 K-stage is necessary. In a cryogenic experiment, this leads to a significantly increased heat load to the 4 K-stage and decreases the standing time of the bath cryostat.

Another important aspect is the beam dump of the cooling laser: A window in the electrical-feedthrough flange allows the cooling laser beam to exit the trap chamber again. The beam is mostly absorbed by a diode located in the electronic section which is used to monitor the laser intensity. Care is taken to mount both the exit window and the diode under an angle, in order to avoid that reflected light enters the trap chamber again. Inside the trap chamber the reflection of the exit window is absorbed by stray light shielding, see figure 4.2.

4.4 Electrode Manufacturing

All electrodes, with two exceptions[1], are made from OFHC copper. They are manufactured to a precision of a few µm. After manufacturing in the workshops[2], the electrodes are carefully polished on the inner surfaces to smooth out even micro-

---

[1] The AT ring electrode is made from CoFe and the ST ring electrode is made from Ni.

[2] We thank the workshop at the Institute of Physics at the University of Mainz and the workshop at the Max-Planck-Institut für Kernphysik in Heidelberg.

scopic groves remaining from the turning. In order to contact the electrodes, OFHC copper wires have been soldered into holes drilled radially into the electrodes. This should be replaced with a different process in the future, as the solder introduces unexpected problems, see section 5.8.4. Before and after soldering, the electrodes are carefully cleaned with acetone in an ultrasonic bath. The electrodes are then gold plated: First, a 7 µm thick diffusion barrier of silver is applied and afterwards a 8 µm thick layer of gold[3].

Finally, the electrodes are cleaned again and assembled into the trap stack. In the trap stack, the electrodes are separated by sapphire rings, and in two cases by quartz rings[4]. The assembled trap stack is placed between two end plates and compressed by OFHC copper rods.

4.5   Trap Biasing

To bias the trap electrodes, extremely stable voltages are necessary, as the axial frequency stability

$$\frac{\delta\nu_z}{\nu_z} = \frac{1}{2}\frac{\delta V_0}{V_0} \tag{4.5}$$

is directly related to the stability of the trap voltage $\delta V_0/V_0$. In addition, low noise on the output voltage is required in order to avoid exciting the ion motion.

As an example, the circuit diagram for biasing of the ST electrodes is shown in figure 4.9. The static bias voltages are applied via several low-pass filter stages. One at room temperature, one at the 77 K-section, and one at the 4 K-section. A capacitive voltage divider at the 4 K-section allows to add an alternating voltage to the electrodes used for excitation. In the ST we use the S1 electrode to apply an axial dipole field and the split S2 electrode to apply a quadrupole drive for sideband coupling.

The biasing circuits are implemented on milled circuit boards. The traces are milled into copper-plated boards in-house using a ProtoMat S63 circuit board plotter from *LPKF*. The board material FR4 is used for room temperature applications, and the low-loss PTFE-based board material RO4300 from *Rogers* is used for cryogenic and RF applications . Resistors and capacitors are implemented using SMD components. We use exclusively metal film resistors due to their excellent noise properties. We use ceramic capacitors for capacitances in the pF range and ECHU foil capacitors for capacitances in the nF range. At room temperature, coaxial cables with SMA connectors are used where possible. The static voltages are routed to the cryogenic section via small-diameter manganin wire and the alternating voltages via cryo-coax cables. Inside the trap chamber, care is taken to only use non-magnetic

---

[3]Gold plating was performed at *Drollinger GmbH*.
[4]The ring electrode of the BT and CT are separated from the common-endcap electrodes by quartz rings.
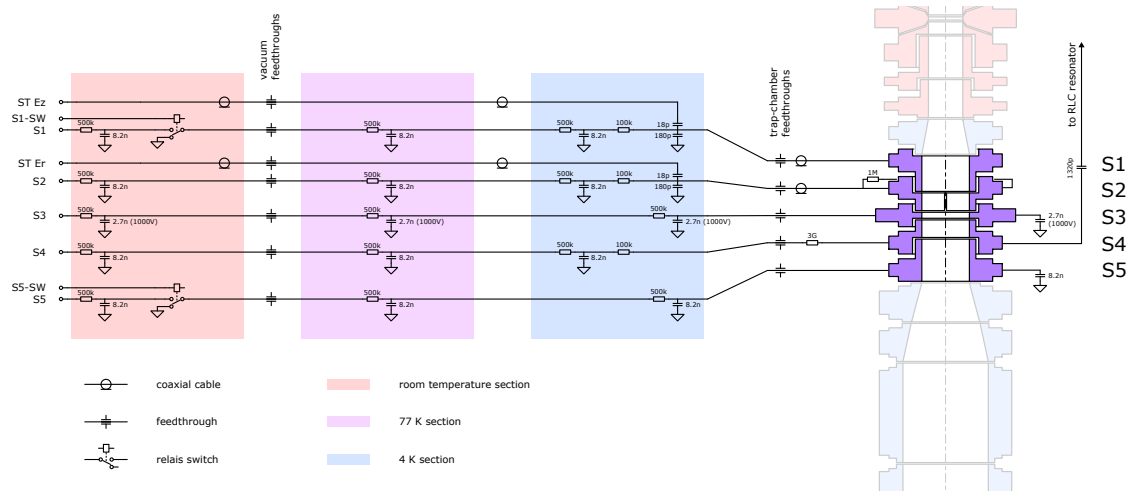
Figure 4.9: Wiring diagram of the storage trap (ST).

cables.

For static voltages we used three different types of precision voltage source: Our standard device is the UM 1-14-LN ultra high precision voltage source from *Stahl Electronics* which features three precision voltage channels with a range of $-14\,\text{V}$ to $0\,\text{V}$ with 25 bit resolution. In addition, ten auxiliary voltage channels are available with a range of $-14\,\text{V}$ to $14\,\text{V}$, 16 bit resolution, and reduced stability. These are used to bias the electrodes during transport. The second device used is the StaReP [77] built by the electronics workshop of the MPIK. It features ten channels, each with two 16 bit digital-to-analog converters (DAC) for coarse and fine adjustment of the voltage, and a range of $-100\,\text{V}$ to $0\,\text{V}$. For our purposes, six channels have been modified to provide a range of $-20\,\text{V}$ to $0\,\text{V}$. The third device used is a self-made prototype based on the LTZ1000 ultra precision reference and the AD5791 20-bit DAC, both from *Analog Devices*. The device has one channel with a range of $-10\,\text{V}$ to $10\,\text{V}$.

For oscillating voltages, we use function generators and arbitrary waveform generators from *Keysight* and *Rhode&Schwarz*. All of these devices are locked to a FS725 $10\,\text{MHz}$ rubidium frequency standard from *SRS* and are controlled by the experiment PC via USB or GPIB interface.

For transport of ions through the trap stack, the electrodes are switched from the precision voltage channels to the auxiliary voltage channels of the UM 1-14-LN. These can be ramped and allow to move the potential well along the trap stack from one trap to another. With a trap stack featuring six traps, programming and testing the transport routines have become quiet complex.

4.6 Ion Loading, Cleaning and Cooling

Protons and $^9\text{Be}^+$ ions are loaded by electron beam or laser ablation, as discussed above. After loading the trap typically also contains unwanted ion species. There-

fore, several cleaning techniques are applied to get rid of these contaminants.

- Initial cooling: After loading, particles might be located at large amplitudes and consequently have shifted axial frequencies due to higher order potential terms. Thus, the trap voltage is ramped from $5\,\%$ to $-5\,\%$ of the nominal value several times to bring these particles in resonance with the axial resonator for resistive cooling. We found that this procedure cools particles at high initial amplitudes very effectively.

- High-voltage ramps: The trapping condition of equation (2.13) means that the Penning trap can be used as mass filter. All ions with q/m smaller than $4C_2V_0/B_0^2$ are expelled from the trap. To achieve this, the trapping potential needs to be ramped to relatively high voltages. Therefore, the AT, ST, and LT are equipped with ring electrodes that are compatible with these voltages. This type of cleaning is especially useful to prepare a cloud of protons, as all unwanted ions have smaller q/m.

- Resonant magnetron excitation: The magnetron frequencies of all ion species are typically contained in a narrow range. Sweeping a drive across these frequencies while simultaneously cooling the magnetron mode of the desired ion species, e.g. by a second drive leading to interconversion of the axial and mangnetron mode, provides an efficient cleaning method. After excitation these ions are expelled from the trap by lowering the trapping potential.

- Transport cleaning: Transporting through or into a trap with small diameter eliminates ions trapped on relatively large radii.

- Separation ramps: Here, the potential well containing the ion or ion cloud is split in two and one of the resulting wells is emptied [78]. If adjusted carefully, the probability of an ion to end up in each well is approximately $50\,\%$. This procedure is used e.g. to reduce an ion cloud to a single particle or to remove contaminating ions from a single particle, as the contaminants are lost with approximately $50\,\%$ probability when the potential well with the desired ion is kept and the other one is discarded.

For maximum effect, these techniques are also applied in combination, and repeated several times if necessary. Verification that only a single particle is present in the trap can be quite tricky. Observables that are necessary, but not sufficient, are: The dip width of the image-current spectrum needs to agree with the prediction for a single particle, the axial frequency stability needs to be in the rage of $30\,\mathrm{mHz}$ when the ion is stored in a harmonic trap, and the Rabi frequency of the magnetron and cyclotron sideband coupling needs to be consistent with a value from a single-particle calibration.

4.7 Trap Optimisation

To achieve the most harmonic electric potential in the trap it is necessary to optimize the voltages applied to the trap electrodes. Typically, the electrodes of a 5-electrode Penning trap such as the ST shown in figure 4.9 are biased as

$$V_{S1} = 0 \tag{4.6}$$
$$V_{S2} = V_0 \times TR + 0.5 \times AS \tag{4.7}$$
$$V_{S3} = V_0 \tag{4.8}$$
$$V_{S4} = V_0 \times TR - 0.5 \times AS \tag{4.9}$$
$$V_{S5} = 0 \tag{4.10}$$

where the end electrodes (S1 and S5) are held at ground. The remaining three voltages applied to the ring electrode (S3) and correction electrodes (S2 and S4) are parameterized with the trap voltage V_0, the tuning ratio TR, and the trap asymmetry AS. The image-current signal of a single ion stored in the trap is then used to optimize these parameters.

The electric potential is characterized by the coefficients E_k and D_k which are combined into the coefficients $C_k = E_k + D_k \times TR$. For an ideal trap $D_2 = 0$, and in addition $C_4 = 0$ and $C_6 = 0$ at the design tuning ratio. For a real trap these coefficients are small but finite, with the exception of C_4 which can be tuned to zero by optimizing the tuning ratio TR. We define the ideal tuning ratio TR_i as the one which achieves $C_4 = E_4 + D_4 \times TR_i = 0$ and express the tuning ratio as

$$TR = TR_i + \Delta TR \tag{4.11}$$

and the C_k-coefficients as

$$C_k = E_k + D_k \times TR_i + D_k \times \Delta TR \tag{4.12}$$

with ΔTR being the deviation of the applied tuning ratio TR from the ideal tuning ratio TR_i.

To find the ideal tuning ratio TR_i in the real trap we use axial energy-dependent axial frequency shifts due to C_4. Combining equations (2.20) and (4.12) we arrive at

$$\Delta\omega_z = \frac{3}{2m\omega_z C_2} C_4 E_z \tag{4.13}$$
$$= \frac{3}{2m\omega_z C_2} (E_4 + D_4 \times TR_i + D_4 \times \Delta TR) E_z \tag{4.14}$$
$$= \frac{3}{2m\omega_z C_2} (D_4 \times \Delta TR) E_z. \tag{4.15}$$

and observe that the axial frequency shift depends on the coefficient D_4, the axial energy E_z, and the deviation from the ideal tuning ratio. For $\Delta TR = 0$, where $TR = TR_i$, the axial frequency shift vanishes. Note that the axial energy E_z samples a Boltzmann distribution characterized by the temperature T_z while the ion is in contact with the axial image-current detector. As a result, the axial frequency shift is also Boltzmann distributed and the line-shape of the single-ion signal is broadened. One method to determine the ideal tuning ratio is measuring this broadening and the accompanying loss in amplitude as a function of TR. At TR_i the broadening vanishes and the amplitude is maximum. Another method is based on changing the axial energy or temperature with electronic feedback. Scanning TR and comparing the axial frequency for two different energies, the axial frequency difference vanishes for $TR = TR_i$.

As a consequence of finite D_2 in the real trap, the axial frequency

$$\omega_z = \sqrt{\frac{q}{m} 2V_0 \left(E_2 + D_2 \times TR_i + D_2 \times \Delta TR\right)} \tag{4.16}$$

is a function of the tuning ratio, which is undesirable. The coefficient D_2 is determined by measuring the axial frequency shift as a function of ΔTR as

$$\Delta\omega_z \approx \frac{\omega_{z,0}}{2C_{2,0}} D_2 \times \Delta TR, \tag{4.17}$$

where $\omega_{z,0}$ is the axial frequency for $\Delta TR = 0$, and $C_{2,0} = m\omega_z^2/q2V_0$, also for $\Delta TR = 0$. The coefficient E_2 is determined by equation (4.12) for $\Delta TR = 0$. With the measured value of D_2, the trap voltage can be adjusted such that ω_z stays constant when TR is changed. This way orthogonality can be achieved in the real trap.

Unfortunately there is no further parameter to compensate C_6. Its finite value in the optimized trap can be characterized by exciting the magnetron mode and measuring the resulting axial frequency shift as function of magnetron radius.

For ion clouds containing hundreds of ions, as needed e.g. for sympathetic cooling, the optimization methods discussed above are not applicable anymore. The reason is that the axial frequency shift, equation (4.13), is too small to broaden the particle signal noticeably. Instead we used a different method based on axial frequency drifts. We noticed that, after the radial modes of the ion cloud are cooled by sideband cooling, the axial frequency starts to drift. The direction and magnitude of this drift depend on the tuning ratio TR, as shown in figure 4.10. At the ideal tuning ratio TR_i the drift vanishes. This effect is likely caused by heating of the ion cloud and an associated expansion in radial direction over time, which in an anharmonic electric potential leads to the observed axial frequency shifts.

The trap asymmetry AS can be used to compensate for asymmetric patch potentials, asymmetric manufacturing errors, or an asymmetric geometry of the trap
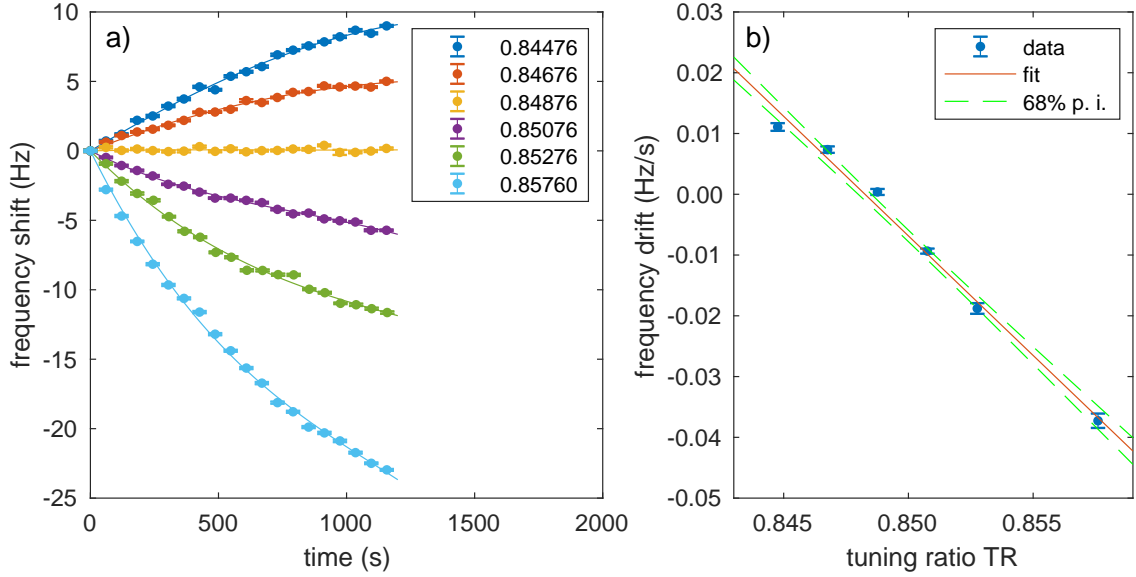
Figure 4.10: Drift-based TR optimization. (a) Axial frequency shift as function of time, for various TR. The starting point is defined as the time when the sideband cooling is stopped. (b) Initial linear drift from polynomial fits to the data in (a) as function of TR. p. i.: prediction interval.

cavity, as is the case e.g. for the CT. Applying a finite asymmetry, the ion is shifted along the trap axis to a location where asymmetric higher order coefficients, e.g C_3, vanish. In practice, the axial frequency is measured as function of AS and the ideal trap asymmetry AS_i is found where the axial frequency is minimum.

4.8   Electric and Magnetic Field Stability

To reach the highest levels of precision in measurements performed in Penning traps, the stability of the magnetic and electric fields that define the motional frequencies is essential.

To generate highly-stable magnetic fields, superconducting magnets operated in persistent mode are utilized. A relative magnetic field stability on the order of 2×10^{-11} per hour has been reached in such magnets [79]. Crucial to the magnetic field stability is also the stabilization of the pressure in the liquid helium and liquid nitrogen reservoirs. In our experiment we actively stabilize the pressure of the liquid helium reservoirs to better than 1×10^{-6} by regulating the flow to the recovery line. The setup is described in detail in [31]. A possible further improvement would be to stabilize the liquid nitrogen reservoirs also. Additionally, temperature stabilisation has been employed during g-factor measurement campaigns. Here, a wooden box was built around the complete experimental setup and the air temperature was regulated by a heater [32]. Finally, to reach the highest levels of stability, the use of self-shielding coils is necessary in order to dampen external magnetic field fluctuations [73, 80].
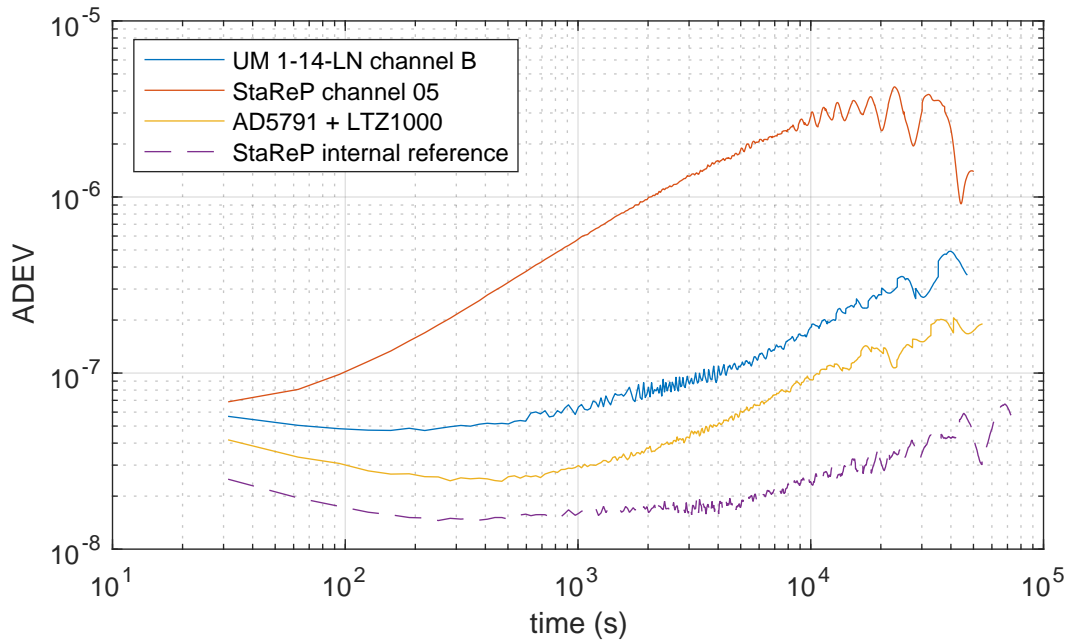
Figure 4.11: Stability of the voltage sources UM 1-14-LN, StaReP, and the AD5791+LTZ1000 prototype. The relative Allan deviation is plotted for one channel of each voltage source. In addition, the internal reference voltage of the StaReP is shown. The stability of the StaReP channels suffered from a grounding issue and might be improved up to the stability of the internal reference.

To generate highly-stable electric fields, high-precision voltage sources are utilized. The devices used in our experiment, the UM 1-14-LN from *Stahl Electronics* and the StaReP, have already been described above. To make use of the full potential of the UM 1-14-LN devices, passive temperature stabilization is applied. To this end, the voltage sources are housed in a massive copper block which dampens external temperature fluctuations. In addition, care is taken to design the circuit boards in a way that minimizes temperature coefficients [81]. A possible future improvement would be to actively stabilize the temperature of the copper housing.

During this work another solution to create even more stable voltages was identified. The prototype is based on the LTZ1000 ultra precision reference in combination with the AD5791 ultra-low-noise high-precision 20-bit DAC from *Analog Devices*. Crucially, both devices feature extremely low temperature coefficients. An Allan deviation plot of the output voltage is shown in figure 4.11 and compared to the devices currently used. The prototype provides the most stable voltage of all three devices. An improvement in axial frequency stability of up to a factor of 2 seems possible if the voltage stability can also be transferred to axial frequency stability. A multi-channel voltage source based on these components is currently in development.

Chapter 5

Image Current Detection

The image current detection method is based on the electromagnetic interaction of the stored ion with an electric resonance circuit connected to one of the Penning-trap electrodes. The mutual interaction between both oscillators relies on the following effects: the stored ion, oscillating in the trap, induces an electric current in the detection electrode; and, at the same time, the oscillating voltage on the detection electrode applies a force to the stored ion. Consequently, the stored ion and the electric resonance circuit form a pair of coupled oscillators, showing typical effects like formation of normal modes, antiresonance, and avoided crossing. For readout, the voltage on the electric resonator is amplified by a cryogenic low-noise transistor amplifier connected to the resonance circuit via an autotransformer and, after further amplification at room temperature, recorded on an FFT analyser. Conversely, the motion of the particle is not directly observed, but manifests itself in a modified lineshape of the electric resonance circuit.

The method was pioneered by Dehmelt [82, 83, 84], was further explored in [85], and has found applications mainly for non-destructive detection of single particles in high-precision mass and g-factor measurements in Penning traps, e.g. [86, 87, 88, 89].

Since it is based on electromagnetic interaction, the image current detection method is applicable to all ions, from electrons to singly-charged ions to highly-charged ions to bare nuclei, of both matter and antimatter. This is in contrast to the fluorescence-based detection method, described in the next chapter, which requires a suitable internal level structure of the trapped ion in order to laser-excite the ion and detect the emitted fluorescence photons.

5.1   The Oscillators

The resonance or RLC circuit is constructed by connecting a superconducting coil in parallel to the detection electrode. Then, the inductance of the coil L together with the capacitance of the detection electrode C_e and the parasitic capacitance of

the coil C_c form the narrow-band electric oscillator. The effective parallel resistance R is determined by losses in the circuit and by the input resistance of the connected amplifier. The equation of motion (EOM) of the RLC circuit is

$$\ddot{\varphi} + \frac{1}{RC}\dot{\varphi} + \frac{1}{LC}\varphi = \frac{1}{C}i \tag{5.1}$$

where $\dot{\varphi}$ is the voltage V on the detection electrode, $C = C_e + C_c$ is the total capacitance, and i is the sum of external currents. The circuit is characterized by its angular resonance frequency ω_0, given by $\omega_0 = 1/\sqrt{LC}$, and the damping factor Γ (in angular frequency), given by $\Gamma = 1/RC$. The quality factor Q is defined as $Q = \omega_0/\Delta\omega$ where $\Delta\omega$ is the full width at half maximum (FWHM) of the power spectrum. It is given by $Q = \omega_0/\Gamma = R\sqrt{C/L}$. Expressed in regular frequency, the resonance frequency and damping factor are $\gamma = \Gamma/2\pi$ and $\nu_0 = \omega_0/2\pi$, respectively.

Normally, the resonance circuit is in thermal equilibrium with the environment at a temperature T. Therefore, the oscillator is excited by thermal noise, also called Johnson-Nyquist noise [90, 91]. Thermal noise can be modelled by a current source in parallel with the resistor with the root mean square (RMS) current given by

$$i_n = \sqrt{\frac{4k_BT\Delta\nu}{R}} \tag{5.2}$$

where k_B is the Boltzmann constant and $\Delta\nu$ the observation bandwidth. Note that the damping factor and the excitation amplitude are not independent, but are related by R, a consequence of the fluctuation-dissipation theorem [91, 92].

The axial motion of the stored ion is described by the equation of motion

$$\ddot{z} + \Gamma_z\dot{z} + \omega_z^2 z = \frac{1}{m}F \tag{5.3}$$

where z is the axial displacement, F is an external force on the ion with mass m, and ω_z is the axial frequency. Since the axial motion of the stored ion forms a very high-Q oscillator, essentially without damping, the ions damping factor Γ_z is neglected until we will introduce damping by laser cooling later. Expressed in regular frequency $\nu_z = \omega_z/2\pi$ and $\gamma_z = \Gamma_z/2\pi$.

In the following, we describe the coupling of the axial motion to the resonance circuit, but the cyclotron motion can be coupled to a resonance circuit in a similar manner, as used e.g. in the previous (anti)proton g-factor experiments for cooling of the cyclotron motion (see section 3.4).

5.2   Coupled Equations of Motion

Viewed individually, both the RLC circuit and the stored ion form a harmonic oscillator, oscillating at their resonance frequencies ω_0 and ω_z, respectively. In order

to include their mutual interaction, the following effects are considered:

The oscillating ion with charge q and velocity $v_z = \dot{z}$ induces a current

$$i_i = \frac{qv_z}{D} \tag{5.4}$$

in the detection electrode, a consequence of the Shockley-Ramo theorem [93, 94]. The factor D is called the effective electrode distance. It is given by

$$\frac{1}{D} = \frac{E_v}{V} \tag{5.5}$$

where E_v is the component of the electric field from the detection electrode in direction of the ion motion, at the instantaneous position of the ion, given a potential V applied to the detection electrode, and under the condition that all other electrodes are grounded. The effective electrode distance is typically on the order of several mm. Values of D for the traps used in our experiment can be found in [32].

The oscillating voltage V on the detection electrode applies a force

$$F = -\frac{qV}{D} \tag{5.6}$$

on the stored ion with charge q. Here, the gradient of the electric potential is expressed as V/D where D is again the effective electrode distance.

Thus, a mutual interaction is established, leading to a coupling of both oscillators. Their coupled equations of motion become

$$\ddot{\varphi} + \Gamma\dot{\varphi} - \frac{q}{CD}\dot{z} + \omega_0^2\varphi = \frac{1}{C}i_n \tag{5.7}$$

$$\ddot{z} + \Gamma_z\dot{z} + \frac{q}{mD}\dot{\varphi} + \omega_z^2 z = 0 \tag{5.8}$$

where $i = i_n + i_i$ and $V = \dot{\varphi}$ has been used. These are the equations of motion of two velocity-coupled harmonic oscillators, one of which is excited by thermal noise i_n. Interestingly, the coupling term does not depend on the oscillating quantity, but its derivative, leading to a damping-like coupling term.

5.3 Frequency Response in Thermal Equilibrium

The frequency response of the coupled oscillator system to excitation by thermal noise is shown in figure 5.1. Examining the amplitudes of the ion displacement and the RLC circuit voltage as a function of frequency, we see that both oscillators show two resonances at the normal-mode frequencies. The resonances are characterized by a peak in amplitude and negative phase shift. In addition, the RLC oscillator, which is driven by thermal noise, shows a pronounced dip in amplitude accompanied by a positive phase shift. In contrast, the ion oscillator, which is not driven, shows
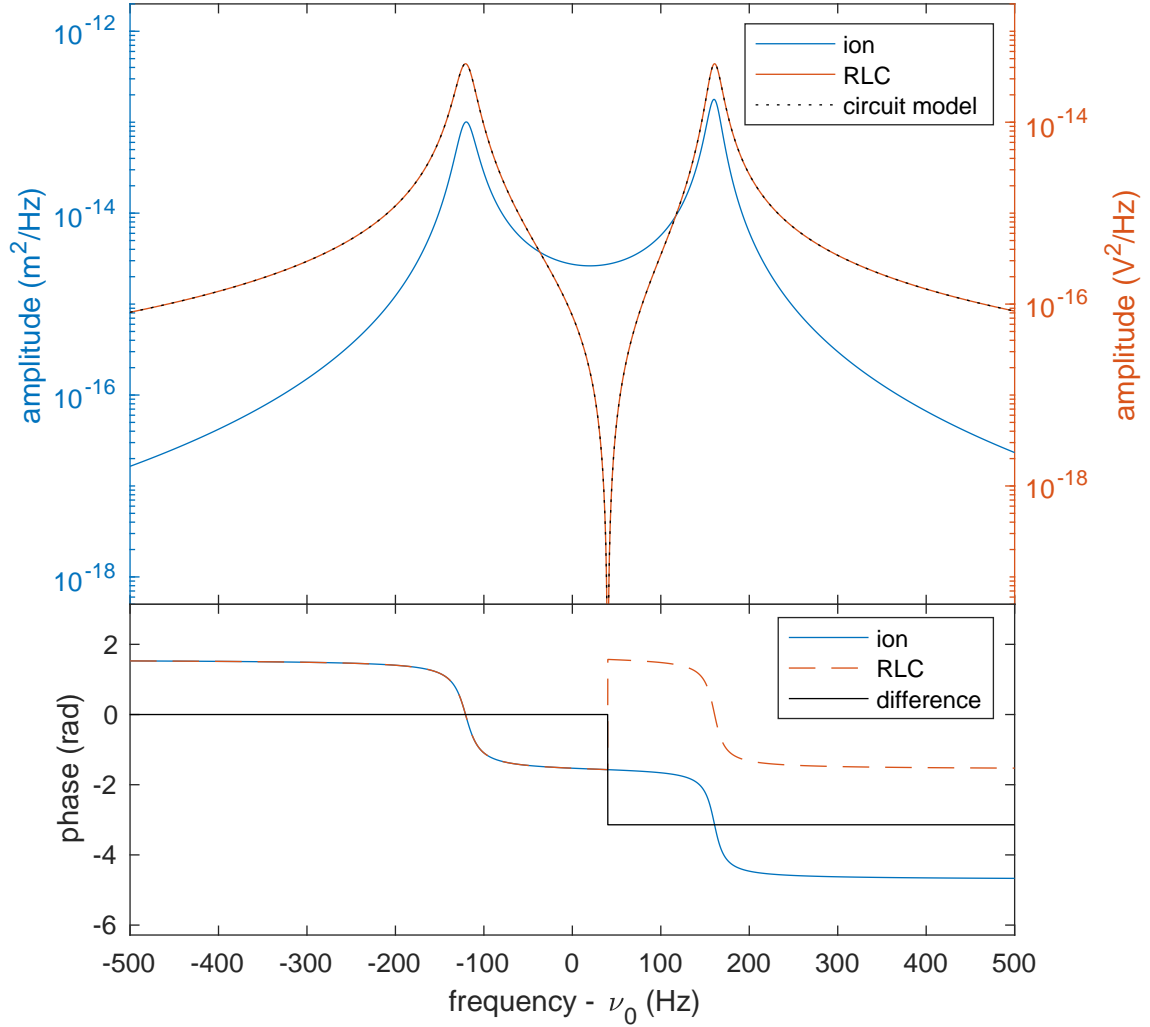
Figure 5.1: Frequency response of the coupled oscillator system consisting of the axial motion of a stored ion and an RLC circuit. Top: Squared amplitudes of the ion and RLC oscillators (from the numerical calculation described in section 5.4) as well as the squared amplitude of the RLC oscillator according to the circuit model described in section 5.6. Bottom: Phase of the ion and RLC oscillators as well as their phase difference. The detuning is $\delta = \nu_z - \nu_0 = 40\,\mathrm{Hz}$. The damping factor is $\Gamma = 2\pi \times 40\,\mathrm{Hz}$ and the coupling coefficient is $\Gamma_i \approx 2\pi \times 1941\,\mathrm{Hz}$.

just a minimum in amplitude with no accompanying phase shift at this frequency.

The pronounced dip in the amplitude of the driven oscillator is a so-called antiresonance. Its frequency depends only on the properties of the undriven oscillator, and is independent of the driven oscillators resonance frequency or damping factor.

Examining the phases of both oscillators, and in particular the phase difference, we observe the formation of two regions with phase difference 0 and π, respectively. We identify these regions as the in-phase and out-of-phase modes of the coupled oscillator system. Naturally, when transitioning between in-phase oscillation and out-of-phase oscillation, the amplitude of at least one of the oscillators must have a zero-crossing. This requirement gives a simple explanation for the appearance of the antiresonance feature, in the Penning-trap community simply called the "dip". For a finite damping factor Γ_z of the ion oscillator, the transition between both regions

is not abrupt but smooth, and the amplitude of the driven oscillator is not zero, but finite.

When the resonance frequency of one oscillator is tuned across the resonance frequency of the other oscillator, the peaks of the normal modes of the driven oscillator are always separated by the antiresonance and, therefore, show an avoided crossing. Note that two normal modes in the undriven oscillator appear only in the case of strong coupling where the coupling coefficient is larger than the damping factor. Otherwise there is only one mode.

Further note that, in the frequency response of the driven oscillator, resonances and antiresonances alternate. More than one antiresonance can be observed when more than one ion is coupled to the RLC circuit or when more than one motional mode of a single ion is coupled to the RLC circuit.

Besides measuring the motional frequencies of stored ions, antiresonance has further interesting applications in characterising complex coupled quantum systems [95].

5.4   Solution of the Coupled EOM

To solve the above equations of motion (EOM) we make use of the fact that they are linear. One consequence of linearity is that the sum of solutions to the EOM is also a solution to the EOM. This allows us to write the solution as the (infinite) sum of the contributions from each frequency.

The first step is to write the thermal noise as an infinite sum of contributions with amplitude i_n, angular frequency ω, and a random phase, which we set to zero. Consequently,

$$i_n(t) = \int i_n(\omega)e^{\imath\omega t}\mathrm{d}\omega \qquad (5.9)$$

where $i_n(\omega) = i_n = \sqrt{4k_BT\Delta\nu/R}$ is the frequency-independent amplitude in the bandwidth $\Delta\nu$. Next, we solve the EOM for each frequency individually using the following ansatz for $z(\omega)$ and $\varphi(\omega)$:

$$z(\omega) = ae^{\imath\omega t} \qquad (5.10)$$

$$\varphi(\omega) = be^{\imath\omega t}. \qquad (5.11)$$

After inserting into the EOM we get a system of linear equations for the complex amplitudes a and b:

$$\left(\omega_0^2 - \omega^2 + \imath\omega\Gamma\right)b - \imath\omega\frac{q}{CD}a = \frac{1}{C}\left|i_n\right| \qquad (5.12\mathrm{a})$$

$$\left(\omega_z^2 - \omega^2 + \imath\omega\Gamma_z\right)a + \imath\omega\frac{q}{mD}b = 0. \qquad (5.12\mathrm{b})$$

This system of linear equations is then solved numerically for each frequency.

The solutions for the amplitudes of the ion displacement and the voltage on the RLC oscillator are $z = a$ and $V = \dot{\varphi} = \imath b \omega$, respectively. The resulting squared amplitudes and phases are shown in figure 5.1. Note that the phases are defined relative to the phase of the exciting noise, which is random, but has been arbitrarily set to zero above. In principle, the solutions for $z(t)$ and $V(t)$ can now be expressed as an integral over $z(\omega)$ and $V(\omega)$, respectively. However, we are only interested in the frequency-dependent quantities. Additional solutions of the coupled EOM for frequently occurring parameters are shown in figure 5.2, e.g. for the limit of weak coupling in figure 5.2a, and for strong coupling in figure 5.2b.

Finally, we would like to note that there is also the possibility to derive lengthy analytic expressions for the amplitudes a and b by using Cramer's rule.

5.5 Dip Width and Mode Separation

To derive an analytic expression for the dip width, we examine the cases of weak and strong coupling. In doing so, we take advantage of the fact that appropriate simplifications can be made in each case.

In the limit of weak coupling, the EOM of both oscillators can be solved independently, neglecting coherent interaction. The response of an RLC circuit to an external current i is given by the impedance of the RLC circuit

$$Z(\omega) = \frac{R}{1 + \imath Q \left(\frac{\omega}{\omega_0} - \frac{\omega_0}{\omega} \right)} \tag{5.13}$$

with resonance frequency $\omega_0 = 1/\sqrt{LC}$ and quality factor $Q = R/\omega_0 L = R\omega_0 C$. When i is set to the induced current of a particle oscillating at $\omega_z = \omega_0$, the voltage V on the detector electrode is

$$V = Z(\omega_0)i = R\frac{q}{D}\dot{z}. \tag{5.14}$$

Using equation (5.6) to calculate the force on the ion due to this voltage, and inserted into the EOM of the stored ion, equation (5.3), we get

$$\ddot{z} + \omega_z^2 z + \frac{q}{mD} R \frac{q}{D} \dot{z} = 0 \tag{5.15}$$

where the intrinsic damping factor Γ_z in equation (5.3) was neglected. We identify the last term on the left in the equation above as a damping term and obtain a damping factor of

$$\Gamma_i = \frac{R}{m} \frac{q^2}{D^2}. \tag{5.16}$$

This damping appears due to the interaction with the RLC circuit. The resulting lineshape of the ion is a Lorentzian peak with a FWHM linewidth Γ_i in the power
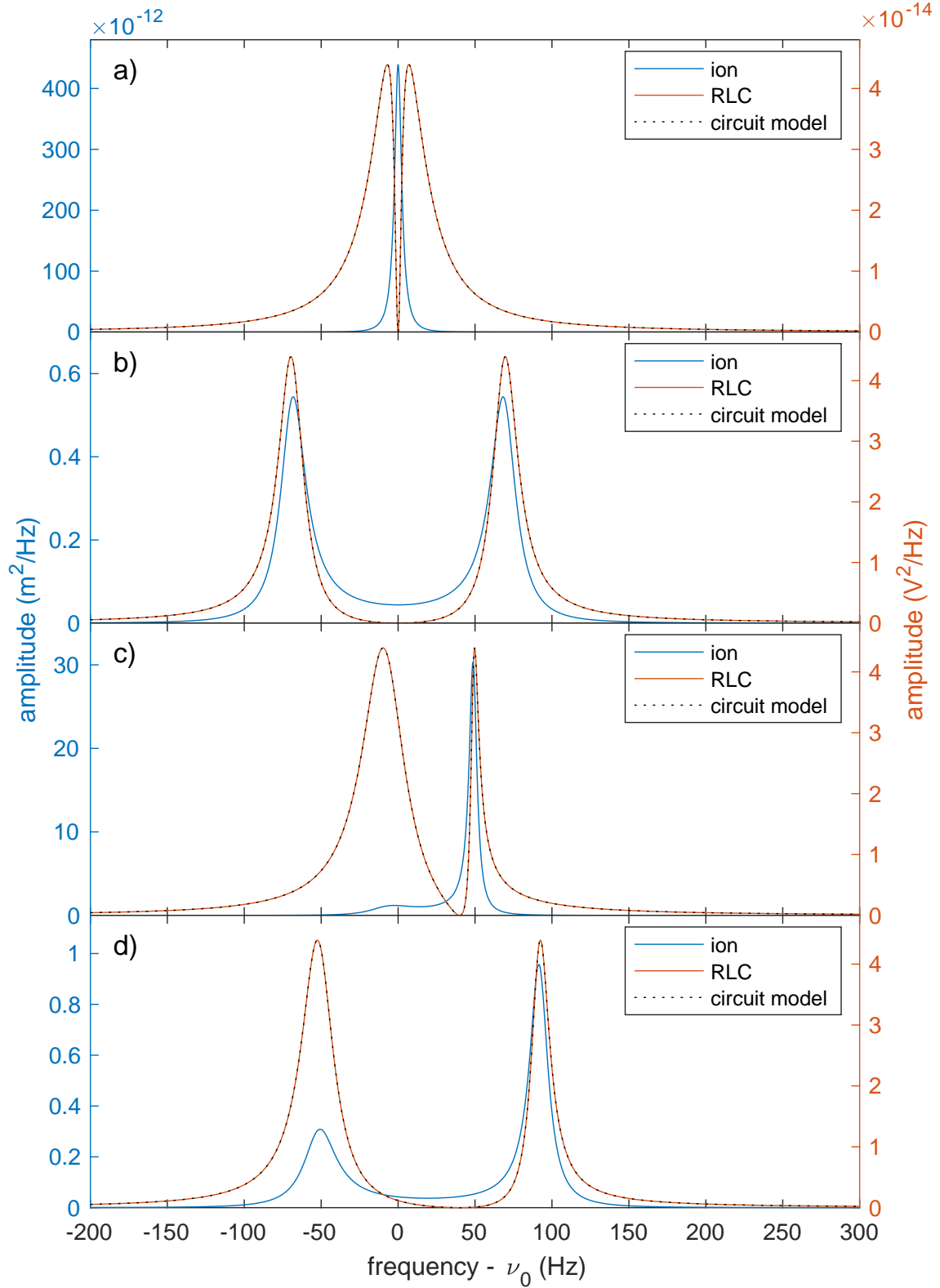
Figure 5.2: Squared amplitudes of the ion and RLC oscillators (from the numerical calculation described in section 5.4) as well as the squared amplitude of the RLC oscillator according to the circuit model described in section 5.6 for various parameters Γ_i and δ where $\delta = \nu_z - \nu_0$. The damping factor is $\Gamma = 2\pi \times 40\,\text{Hz}$. (a) Weak coupling: $\Gamma_i \approx 2\pi \times 4.85\,\text{Hz}$ and $\delta = 0$. (b) Strong coupling: $\Gamma_i \approx 2\pi \times 485\,\text{Hz}$ and $\delta = 0$. (c) Intermediate coupling with detuning: $\Gamma_i \approx 2\pi \times 48.5\,\text{Hz}$ and $\delta = 40\,\text{Hz}$. (d) Strong coupling with detuning: $\Gamma_i = 2\pi \times 485\,\text{Hz}$ and $\delta = 40\,\text{Hz}$.

spectrum, see the blue curve in figure 5.2a. The lineshape of the RLC circuit shows a Lorentzian dip with the same FWHM linewidth Γ_i at the frequency ω_z in the power spectrum of the uncoupled RLC circuit, see the red curve in figure 5.2a. Because we neglected the coherent interaction between the ion oscillator and the RLC oscillator, this derivation is valid only on resonance, when the intrinsic damping of the ion is negligible, and when the coupling is weak such that $\Gamma_i < \Gamma$. However, the parameter Γ_i is a useful quantity for describing the ion-resonator interaction also beyond these limits.

In the limit of strong coupling, the damping terms in equations (5.12) are small and can be neglected. Additionally, the excitation terms are neglected as well. The resulting system of linear equations has solutions when the determinant of the coefficient matrix is zero, resulting in the condition

$$\left(\omega_z^2 - \omega^2\right)\left(\omega_0^2 - \omega^2\right) - \frac{q^2}{mCD^2}\omega^2 = 0 \tag{5.17}$$

with the solution

$$\omega_\pm^2 = \frac{1}{2}\left(\omega_0^2 + \omega_z^2 + \frac{q^2}{mCD^2}\right) \pm \sqrt{\frac{1}{4}\left(\omega_0^2 + \omega_z^2 + \frac{q^2}{mCD^2}\right)^2 - \omega_0^2\omega_z^2}. \tag{5.18}$$

When the ions resonance frequency ω_z is tuned across the RLC oscillators resonance frequency ω_0 the normal-mode frequencies $\omega_\pm$ show an avoided crossing. For $\omega_z = \omega_0$ the normal-mode frequencies can be approximated as

$$\omega_\pm \approx \omega_0 \pm \tilde{\omega}/2 \tag{5.19}$$

with a separation between both modes of

$$\tilde{\omega} = \sqrt{\frac{1}{mC}\frac{q^2}{D^2}}. \tag{5.20}$$

The resulting lineshapes of both the ion and the RLC oscillator show two resonances at the normal mode frequencies, see figure 5.2b. Note that

$$\tilde{\omega}^2 = \Gamma_i\Gamma \tag{5.21}$$

is another useful quantity describing the ion-resonator interaction and is also valid beyond the limit of strong coupling ($\Gamma_i > \Gamma$) for which it was derived.

In case there are N ions stored in the trap, the RLC oscillator couples to the center-of-mass motion of the ion cloud [84]. It can be treated as the motion of a single ion with mass $N \times m$ and charge $N \times q$, resulting in

$$\Gamma_i = N\frac{R}{m}\frac{q^2}{D^2} \tag{5.22}$$

and

$$\tilde{\omega} = \sqrt{\frac{N}{mC}\frac{q^2}{D^2}}. \tag{5.23}$$

5.6 Circuit Model

Another approach to solve the EOM defined above is to write the EOM of the stored ion in terms of its image current [83, 84, 85]. The resulting equation is identified as the equation of a series LC circuit with inductance L_p and capacitance C_p given by

$$L_p = \frac{mD^2}{q^2} \tag{5.24}$$

and

$$C_p = \frac{1}{\omega_z^2 L_p} = \frac{q^2}{\omega_z^2 mD^2} \tag{5.25}$$

where ω_z is the resonance frequency of the ion. This equivalent electric circuit for the ion motion is connected in parallel to the parallel RLC circuit. The combined system is described by the impedance

$$Z(\omega) = \frac{R}{1 + \imath RB(\omega)} \tag{5.26}$$

with a susceptance

$$B(\omega) = \omega C - \frac{1}{\omega L} - \frac{1}{\omega L_p - \frac{1}{\omega C_p}}. \tag{5.27}$$

This impedance describes the interaction of the trapped ion with the RLC circuit in terms of an electric circuit.

The RMS voltage on the resonator is given by

$$V = \sqrt{4k_B T \operatorname{Re}(Z)\Delta\nu} \tag{5.28}$$

with the real part of the impedance

$$\operatorname{Re}(Z) = \frac{R}{1 + R^2 B^2}. \tag{5.29}$$

Using the relations

$$L = R/\omega_0 Q \tag{5.30}$$

$$C = Q/R\omega_0 \tag{5.31}$$

$$L_p = R/\Gamma_i \tag{5.32}$$

$$C_p = \Gamma_i/R\omega_z^2 \tag{5.33}$$

equation (5.27) can be expressed as

$$B = \frac{1}{R}\left(Q\left(\frac{\omega}{\omega_0} - \frac{\omega_0}{\omega}\right) - \frac{\omega\Gamma_i}{\omega^2 - \omega_z^2}\right) \tag{5.34}$$

resulting in

$$V = \sqrt{\frac{4k_BTR\Delta\nu}{1 + \left(Q\left(\frac{\omega}{\omega_0} - \frac{\omega_0}{\omega}\right) - \frac{\omega\Gamma_i}{\omega^2 - \omega_z^2}\right)^2}}. \tag{5.35}$$

This result for the RMS voltage on the RLC oscillator agrees with the numerical solution derived above up to the numerical precision of the used computational method. It is also shown in figure 5.1, plotted on top of the numerical result. For $\Gamma_i \to 0$ we recover the lineshape of the parallel RLC circuit without ions.

It is insightful to write the RMS voltage as

$$V = \sqrt{4k_BTR\chi(\omega)\Delta\nu} \tag{5.36}$$

where all frequency dependence is absorbed in the line-shape parameter $\chi(\omega)$ with a range in the interval $[0, 1]$ and with the integral $\int_0^\infty \chi(\omega)d\omega = \pi\Gamma/2$. The maximum amplitude of the RMS voltage is then solely dependent on the prefactor $4k_BTR\Delta\nu$. This formalism allows to derive analytic lineshapes for commonly used configurations of stored ions coupled to an RLC oscillator. Lineshape parameters $\chi(\omega)$ for various coupled oscillator systems are listed in appendix A.

Note that, the resonator lineshape parameter $\chi(\omega)$ can be expressed as $1/(1+\epsilon^2)$ with $\epsilon = Q(\omega/\omega_0 - \omega_0/\omega)$. Near the resonance frequency, ϵ can be approximated by $\epsilon = (\omega - \omega_0)/\Gamma_i$, which leads to a Lorentzian lineshape. Phase coherent background can be incorporated into the lineshape, in similarity to Fano-lineshapes, by taking $1/(1+\epsilon^2) \to (1+\epsilon r)^2/(1+\epsilon^2)(1+r^2)$ where r is the ratio of background amplitude to oscillator amplitude.

5.7 Experimental Results

In the following, we compare the lineshape of the coupled ion-RLC oscillator system derived above with experimental data. For the ion oscillator we use the axial center-of-mass motion of a cloud of $^9\mathrm{Be}^+$ ions stored in the ST. Here, the version of the ST without magnetic bottle was used. The center-of-mass motion is coupled to the RLC oscillator connected to the correction electrode of this trap with a resonance frequency of $\nu_0 \approx 478.93\,\mathrm{kHz}$ and a Q-factor of $Q \approx 11\,000$. The strength of the coupling to the RLC oscillator is varied by varying the number of ions stored in the trap. Before recording FFT spectra, the $^9\mathrm{Be}^+$ ion cloud is laser cooled to mK temperatures in order to keep the amplitude in all modes other than the axial center-of-mass mode small.

We tune the resonance frequency ν_z of the ion oscillator by adjusting the trap voltage V_0 applied to the ST electrodes in steps of ΔV_0, thereby shifting the resonance frequency by

$$\Delta\nu_z = \frac{\nu_z}{2V_0}\Delta V_0, \tag{5.37}$$

while keeping the resonance frequency ν_0 of the RLC oscillator constant. For each step, an FFT spectrum of the voltage on the RLC oscillator is recorded. The resulting data is shown in figure 5.3a as a function of the trap voltage. Selected FFT spectra at three specific trap voltages are shown in figure 5.4.

We observe the formation of two normal modes in the FFT spectra. When the detuning $\delta = \nu_z - \nu_0$ is small, the frequency of both modes is shifted from the unperturbed resonance frequencies of the oscillators. This is the avoided crossing, which is characteristic of coupled oscillators. The maxima of both modes follow the relationship derived in equation (5.18). Both modes are separated by the antiresonance or dip feature at all times, and the antiresonance frequency coincides with the resonance frequency ν_z of the unperturbed ion oscillator. For $\delta = 0$, both normal modes have equal components of voltage amplitude[1] and it is possible to detect them simultaneously. As the detuning from the unperturbed resonance frequency of the RLC oscillator becomes large, the normal mode appears narrower because in this situation this normal mode is composed mostly of ion displacement amplitude and less of voltage amplitude, but only the voltage amplitude is detected. For the data shown in figure 5.3, the ratio of ion-resonator coupling to resonator damping is $\gamma_i/\gamma \approx 1.5$, which is already in the strong coupling regime. In this situation, also the ion displacement amplitude is composed of two modes, as shown in figure 5.2b, but the ion displacement amplitude is undetected.

We fit the FFT spectra at each individual trap voltage setting with the lineshape derived above. As the data is recorded as power spectral density (PSD), we make

---

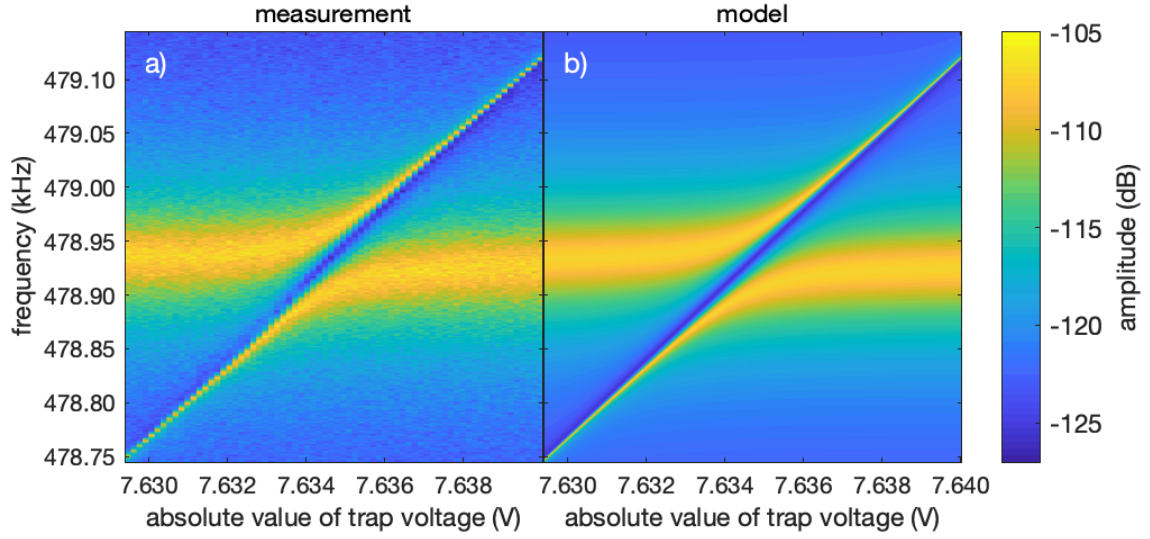[1]We denote the amplitude of the voltage on the RLC oscillator as "voltage amplitude" in the following.

Figure 5.3: Voltage amplitude of the coupled ion-RLC oscillator system as function of frequency and trap voltage. The ion number is chosen such that $\gamma_i/\gamma \approx 1.5$. (a) measurement, (b) model.
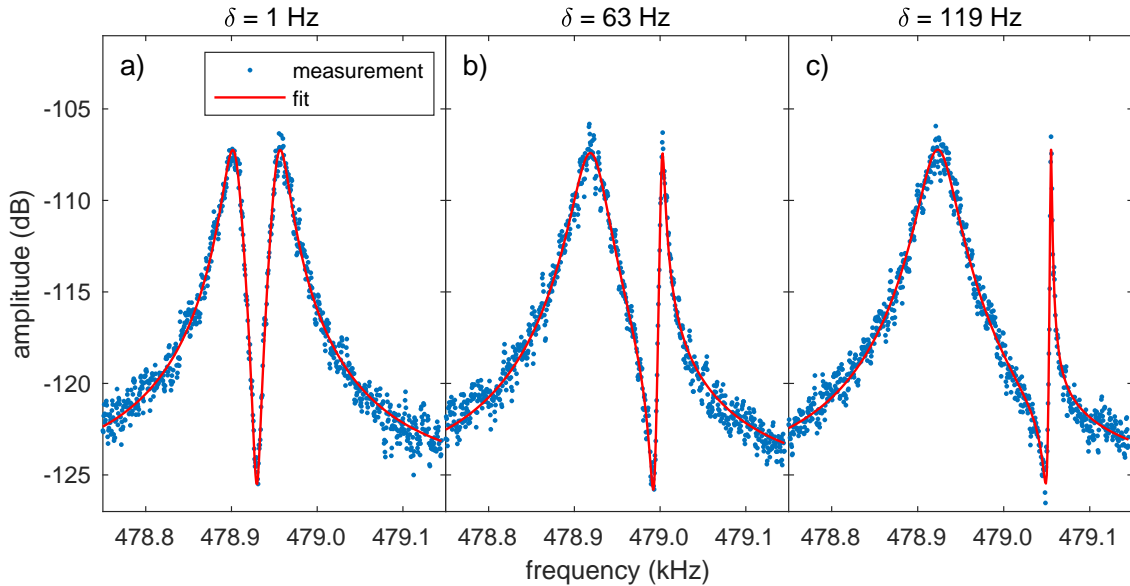

Figure 5.4: FFT spectra of the voltage amplitude shown in figure 5.3a for three selected trap voltages V_0. (a) $V_0 = -7.634\,556\,\text{V}$, (b) $V_0 = -7.636\,385\,\text{V}$, (c) $V_0 = -7.638\,061\,\text{V}$.
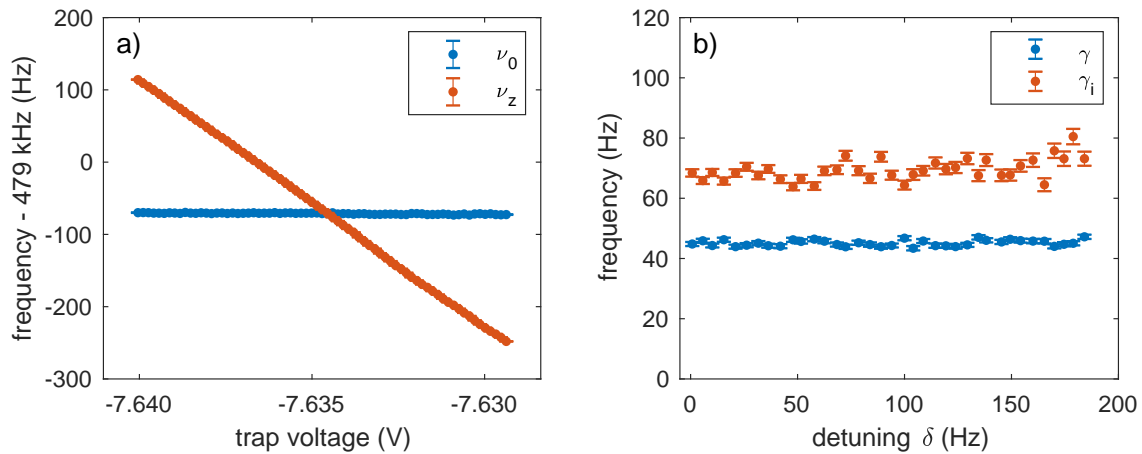
Figure 5.5: Results from fits to the data in figure 5.3a: (a) resonance frequencies of RLC oscillator ν_0 and ion oscillator ν_z as function of trap voltage. (b) RLC circuit damping factor γ and ion-resonator coupling constant γ_i as function of detuning.

use of the fit function

$$S(\nu) = 10 \times \log_{10}\left(A\chi(\nu) + A_{bkg}\right) \tag{5.38}$$

with the frequency-dependent lineshape parameter $\chi(\nu)$, and the frequency-independent amplitude A, and background amplitude A_{bkg}. The lineshape parameter $\chi(\nu; \nu_0, \gamma, \nu_z, \gamma_i)$ is a function of the oscillator properties. Fits for selected trap voltage settings are shown in figure 5.4, and the resulting fit parameters are plotted in figure 5.5. We observe that the fit yields the resonance frequencies of the unperturbed oscillators, as expected from the model. We further observe that both the damping factor of the RLC circuit γ and the ion-to-resonator coupling constant γ_i are independent of the detuning $\delta = \nu_z - \nu_0$.

Finally, we plot the lineshape model as a function of trap voltage and frequency, see figure 5.3b, and compare it to the data in figure 5.3a. Here, the fit parameters from the individual fits, see figure 5.5, are used as input to the model. Fit parameters which are constant as a function of trap voltage are averaged, while a linear regression is used for the parameter ν_z which varies with the trap voltage. Comparing figure 5.3a and 5.3b, we find that the experimental data are well described by our model.

To further refine the model, the effects of the FFT window function should be considered, as well as the effects of a $1/f$-noise component. However, both contributions are negligible here.

The situation for an even stronger ion-resonator coupling with $\gamma_i/\gamma \approx 19$ is shown in figure 5.6 and 5.7. The avoided crossing of the normal modes is more clearly visible, as the damping becomes comparably weaker. Also both normal modes are visible for larger detunings compared to above because at the same detuning the modes contain a relatively larger voltage amplitude component. Compare also to

the lineshapes in figure 5.2b and 5.2d.

For large ion clouds, as in this situation, we typically observe that heating effects become apparent a few minutes after the laser cooling is stopped. This manifests itself in a reduced dip depth as apparent in figure 5.7b and 5.7c. Additionally, sometimes axial frequency jumps are observed, as in figure 5.6a. We attribute these to a rearrangement of the non-center-of-mass modes. These effects can be mitigated by re-cooling the ^{9}Be$^+$ ion cloud before recording each FFT spectrum. However, this was not done for the data presented here, where all FFT spectra were recorded in one go. For small ion clouds, these effects are typically absent, or become apparent only after longer timescales. Taking into account these heating effects, the experimental data are well described by our model.

The situation for weak ion-resonator coupling is shown in figure 5.8 and 5.9 where $\gamma_i/\gamma \approx 0.12$. In the voltage amplitude, the normal modes still show an avoided crossing, and are separated by the antiresonance. The maxima of both modes follow equation (5.18). However, the ion displacement amplitude is only composed of one mode, as can be seen e.g. in the lineshape in figure 5.2a.

For precision measurements of the motional frequencies of the stored ion, a narrow linewidth is advantageous. Therefore, one generally works in the weak coupling regime. The spectrum shown in figure 5.9c where $\gamma_i \ll \gamma$ and $\delta \approx 0$ is typical for these type of measurements. The precision with which the frequency can be determined further depends on the signal-to-noise ratio, the bin width, and the averaging time. Note that the amplitude in each bin is a stochastic quantity. In addition, when the linewidth of the dip becomes comparable to the bin width, the distortion of the lineshape due to the FFT window function becomes relevant and needs to be taken into account in the fit function.

In contrast, for experiments on hybrid quantum systems [96], e.g. RF oscillators coupled to laser-cooled ions, working in the strong coupling regime is desirable. Here, dressed states can be observed such as in figure 5.7c.
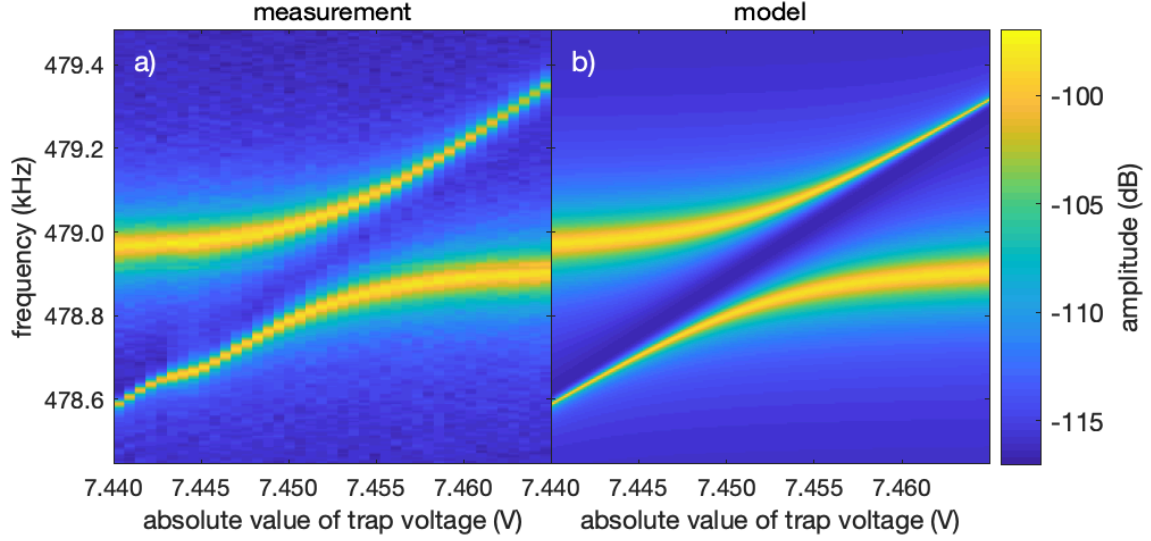
Figure 5.6: Voltage amplitude of the coupled ion-RLC oscillator system as function of frequency and trap voltage. The ion number is chosen such that $\gamma_i/\gamma \approx 19$. (a) measurement, (b) model. For large ion clouds, sometimes axial frequency jumps, such as the one visible in (a) at $|V_0| = 7.445\,\text{V}$, are observed a few minutes after the laser cooling is stopped. We attribute these to a rearrangement of the non-center-of-mass modes.
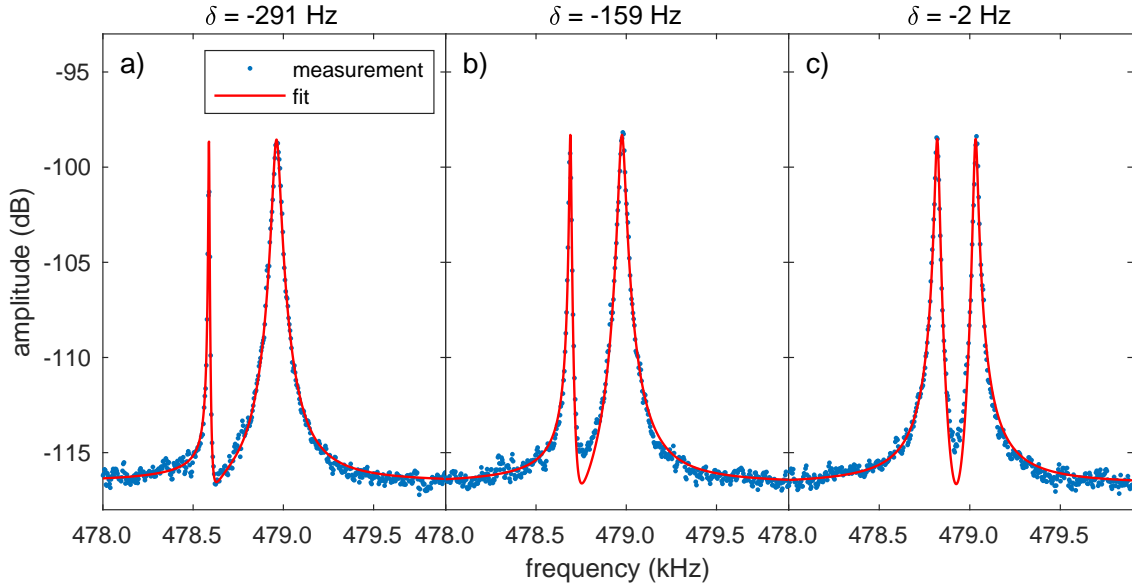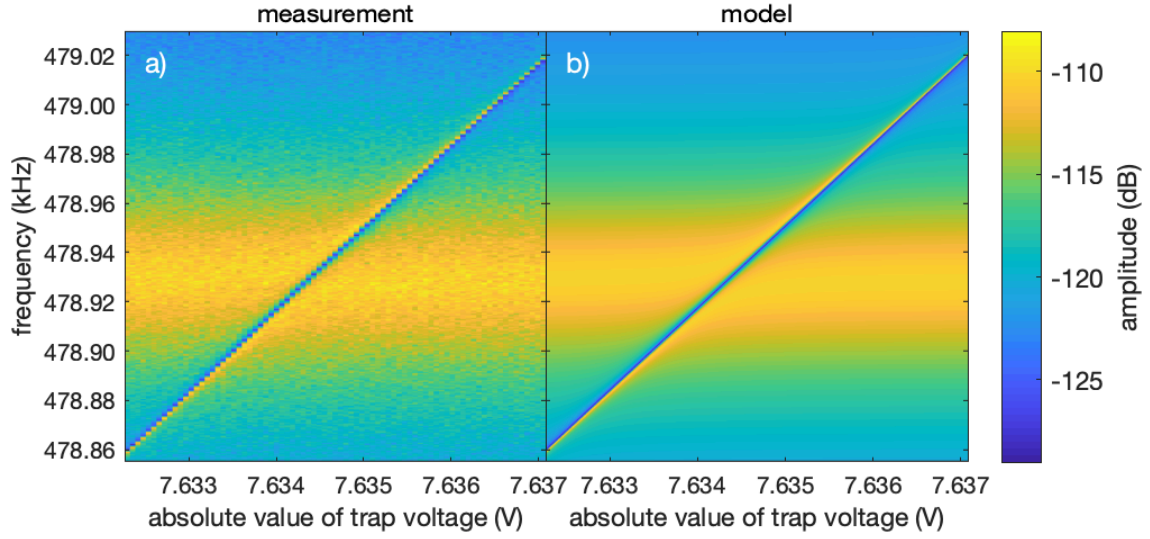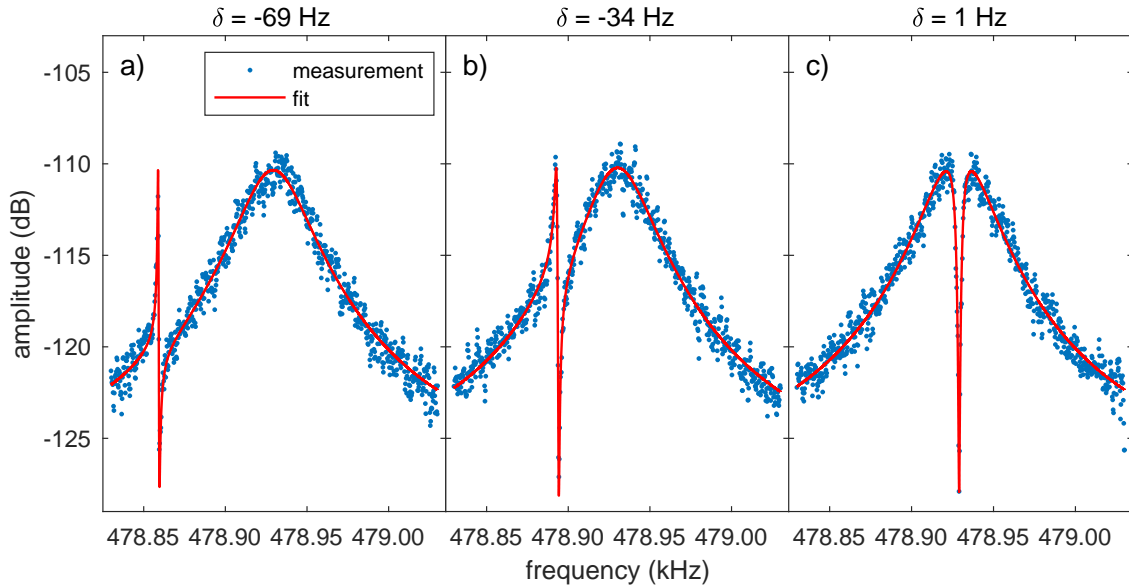

Figure 5.7: FFT spectra of the voltage amplitude shown in figure 5.6a for three selected trap voltages V_0. (a) $V_0 = -7.439\,986\,\text{V}$, (b) $V_0 = -7.445\,473\,\text{V}$, (c) $V_0 = -7.451\,569\,\text{V}$. The reduced dip depth visible in (b) and (c) is typically observed for large ion clouds and for FFT spectra recorded several minutes after the laser cooling is stopped. The FFT spectra recorded in the first few minutes, such as in (a), do not show reduced dip depth. We attribute this to a heating of the center-of-mass mode by the other modes.

Figure 5.8: Voltage amplitude of the coupled ion-RLC oscillator system as function of frequency and trap voltage. The ion number is chosen such that $\gamma_i/\gamma \approx 0.12$. (a) measurement, (b) model.

Figure 5.9: FFT spectra of the voltage amplitude shown in figure 5.8a for three selected trap voltages V_0. (a) $V_0 = -7.632\,265\,\text{V}$, (b) $V_0 = -7.633\,301\,\text{V}$, (c) $V_0 = -7.634\,337\,\text{V}$.

5.8 Readout

An overview of the readout chain used to record the signals on the RLC oscillator is shown in figure 5.10. The superconducting coil is connected to a cryogenic GaAs-based field-effect transistor (FET) amplifier via an autotransformer. This is realized via a tap at the coil with a tap ratio κ. This tap is connected to the amplifier via a coupling capacitance C_a on the order of $10\,\mathrm{pF}$. DC-biasing of the detection electrode is achieved through a low-pass filter which grounds the superconducting coil AC-wise. The FET amplifier provides a very high input resistance to the coil and approximately $50\,\Omega$ to the output. At room temperature, the signal is further amplified by a ZFL-1000-LN+ low-noise amplifier from *Mini-Circuits*. A single-sideband (SSB) mixer from *Stahl Electronics* is used to shift the signal in the frequency range of typically 300 to $600\,\mathrm{kHz}$ to the input range of the fast Fourier transform (FFT) analyzer at 0 to $100\,\mathrm{kHz}$. The local oscillator frequency that defines the frequency offset is provided to the SSB mixer by a frequency generator (FG). An SR780 dynamic signal analyzer from *SRS* is used to record FFT spectra of the amplified and down-mixed signal. This device is connected to the control computer (PC) via GPIB interface. The data is recorded on the PC with LabVIEW software from *NI* which is also used for online data analysis. The frequency generator and FFT analyzer are frequency stabilized to the $10\,\mathrm{MHz}$ output of an FS725 rubidium frequency standard (RFS) from *SRS*.
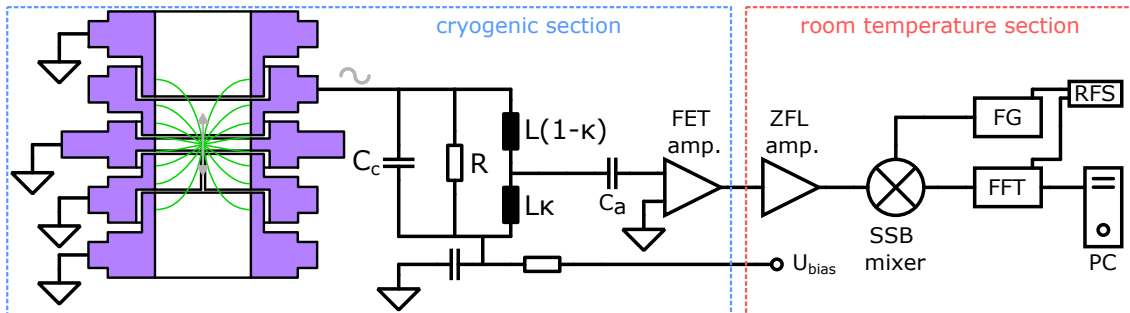

Figure 5.10: Readout chain of image current detectors. RFS: rubidium frequency standard. FG: frequency generator. PC: control computer. FFT: fast Fourier transform analyser. SSB: single-sideband mixer. ZFL: ZFL-1000-LN+ low-noise amplifier. FET: field-effect transistor amplifier. amp.: amplifier.

5.8.1 Superconducting Coils

A crucial component of the image-current detection system is the superconducting coil connected to the detection electrode. To maximize its coupling strength with the stored ion oscillator, the RLC resonator needs a high effective parallel resistance $R = \omega_0 Q L$ and small capacitance $C = C_c + C_e$. Therefore, the coil is wound in a way that maximizes the coil's inductance L while minimising the coil's self-capacitance C_c. The use of superconducting wire with negligible resistance at $4\,\mathrm{K}$ allows to reach

the high Q-factors and, consequently, the high effective parallel resistances necessary for detection of single ions. In this work, we were manufacturing several new coils in order to improve on the Q-factors reached in previous iterations of the experiment. E.g. all-new coils were manufactured for the 2021 trap setup.

The design and dimensions of the used superconducting coils are described in [66, 97]. Each coil consists of a toroidal core made from PTFE on which the superconducting wire is wound. The coils are placed inside a polished OFHC-copper housing and are held in place by PTFE holders. From the 2017 setup onward, three coils are placed in the same copper housing, as shown in figure 5.11. Previously, the two used coils were placed in their own housing. The reason for this design change were space constraints in the electronic section of the experiment setup. Placing the coils in the same housing leads to inductive and capacitive coupling between these coils, however. In order to mitigate coupling effects, the inductance is chosen such that the resonance frequencies of the resonators, once connected to the traps, are separated by at least 50 kHz. The three different values of inductance are realized by varying the number of windings applied to the same core geometry. One advantage of the toroidal geometry is that stray fields are minimized. Consequently, losses induced by eddy currents are reduced. The used superconducting wire is made from niobium-titanium (NbTi), has a diameter of 75 μm, and is coated with PFA insulation. The ribs on the outside of the PTFE core divide the coil into 18 sections, allowing for segmented winding. They also fill the space not occupied by windings. The PTFE core is split into two halves to ease manufacturing. Both halves are wound separately and joined at the end of the manufacturing process.

Winding the coils is a somewhat lengthy and delicate process. We start by wrapping one half of the PTFE core with a layer of 10 mm-wide PTFE tape folded once along the length of the tape such that it is approximately 5 mm wide. Care is taken that the tape is under tension at all times. This layer forms the base where the wires are pressed into and provides good thermal connection between the wiring and the core. In the next step, one layer of the superconducting wire is wound onto the first segment in forward direction. It is critical to keep tension on the wire at all times during the winding process as the wire is rather springy and will tend to move back to its original form. Further it is crucial to avoid kinks in the superconducting wire at all cost, as an abundance of these kinks has been linked to low Q-factors of the respective coil. After winding the first layer of wire, the wire is fixed in place by two to three turns of folded PTFE tape applied in the same direction as the winding. Again, it is crucial to to keep the wire and tape under tension at all times. The PTFE tape is easy to keep in place due to triboelectric effects which make layers of PTFE tape stick to each other. In order to assure good thermal contact it is advisable to press the PTFE tape against the wire layer. The next step is the winding of the second layer of wire, which is now applied in backwards direction,
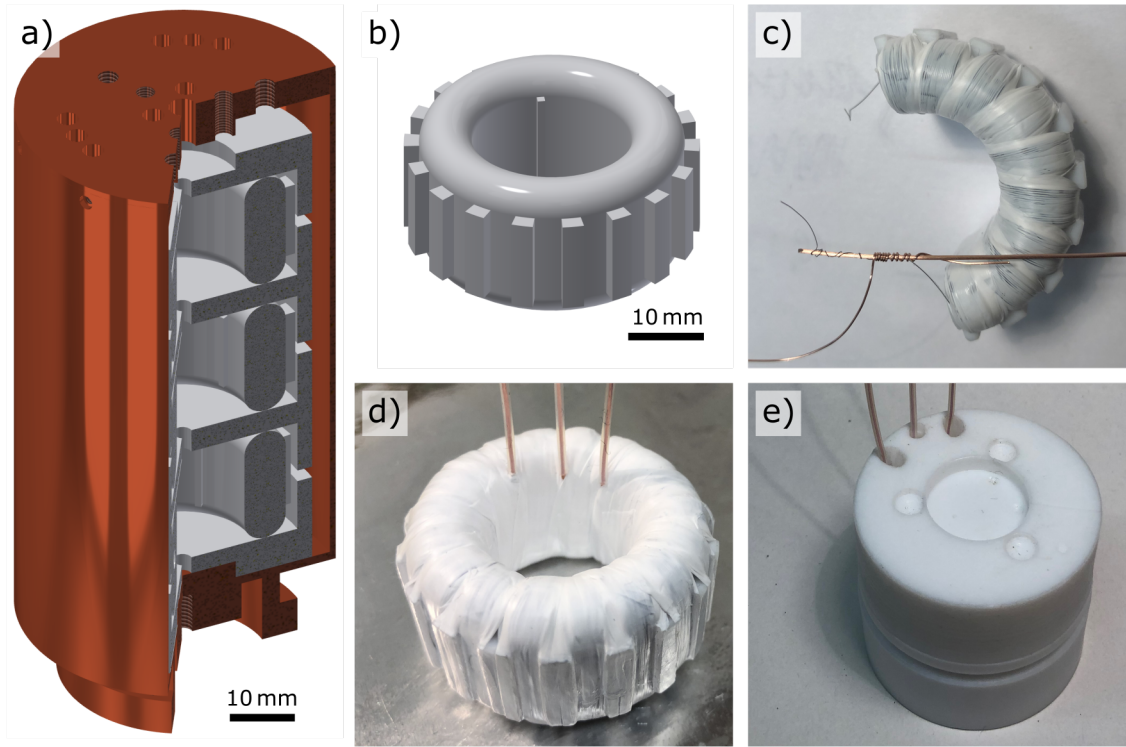
Figure 5.11: Coil housing and superconducting coils. (a) section view of the coil housing, (b) PTFE core, (c) half-core and copper-to-superconductor joint, (d) finished coil, (e) finished coil in coil holder.

followed again by two to three layers of PTFE tape to fix it in place. Depending on the desired inductance, between three and five layers of superconducting wire are wound onto the first segment this way, where the even layers are wound in backwards direction. This process is continued segment by segment until the first half of the PTFE core is done. At the end, all segments are again wrapped in another layer of folded PTFE tape which is applied under stress in order to press the windings tightly to the core. The process is repeated for the second half of the core, taking care that the wire is wound in the same direction as on the first half of the core.

Adding the tap is an even more delicate process. The winding process is paused after approximately $\kappa \times n$ windings to add the tap, here κ is the tap ratio and n is the total number of windings of the coil. Considerations regarding the choice of κ are discussed in the next section. We remove the insulation of an approximately 20 mm-long section of the superconducting wire and tightly wind the superconducting wire around a 0.5 mm-diameter OFHC-copper wire which will become the connection to the amplifier. The superconducting wire forms a helix around the copper wire and is fixed in place by winding a 0.25 mm-diameter OFHC-copper wire around both. It is advisable to choose the position of the tap along the superconducting wire in a way that the connection ends up either inside or outside of the PTFE core but not on the top or bottom of the core. Further care is taken that the superconducting wire is not broken and that kinks are avoided during this process. In the next step,

lead-free solder is applied to the connection to hold everything in place permanently and the connection is wrapped in PTFE tape. In the final step, the winding with the tap attached is laid down on the PTFE core taking care that the superconducting wire is under tension at all times and the winding is fixed in place with two or three turns of PTFE tape. Afterwards, the winding of the half-core continues as described above.

Both halves of the core are assembled and the two ends of the superconducting wire are joined as follows: First, the insulation of the superconducting wire is removed and both wires are twisted around each other until the winding is under tension. Afterwards both twisted wires are wound around a 0.5 mm-diameter OFHC-copper wire and fixed in place by winding a 0.25 mm-diameter OFHC-copper wire around both. Lead-free solder is applied to fix everything in place. Finally, the joint is wrapped in PTFE tape and pressed against the core by winding two or three turns of folded PTFE tape around the joint and the core. The ends of the superconducting wire which will be connected to the ground and trap, respectively, are connected to 0.5 mm-diameter OFHC-copper wire in the same way as the tap described above. Afterwards, all segments of the assembled core are wrapped in several layers of folded PTFE tape which is applied under stress. In the final step, a few layers of PTFE tape are wrapped around the core in poloidal direction and the core is pressed into the PTFE holders. The assembly is now ready to be mounted in the coil housing.

For characterisation measurements in the cryocooler-based test setup[2], three coils are mounted in the coil housing simultaneously. The ground end of each coil is connected to ground via the biasing low-pass filter. The tap and hot end of each coil are connected capacitively to a cryo-coax cable. After cool-down, the resonance of each coil is recorded on a vector network analyzer (VNA). The resulting resonance has, in principle, a Lorentzian lineshape. However, due to direct capacitive coupling between the input and output of the VNA, the lineshape is distorted. We found that these resonances are well reproduced by a Fano-lineshape, which we subsequently used to fit the data. The resulting Q-factors and resonance frequencies ν_0 are shown in figure 5.12. Further cool-downs with an added external capacitance of 10 pF, 20 pF, and 30 pF were performed. Here, a piece of semi-rigid coaxial cable was used as capacitance, as this type of capacitance has extremely low dielectric loss. The data is also shown in figure 5.12. For all coils we measure Q-factors of 100 000 or above, leading to effective parallel resistances above 1 GΩ. These Q-factors are more than sufficient for the purpose of our experiment, where the goal is $Q \geq 20\,000$. In fact, the Q-factor of the complete image-current detection system will be limited by the input resistance of the amplifier, as discussed in the next section. The slightly lower Q-factors for no external capacitance are attributed to insufficient thermalization of
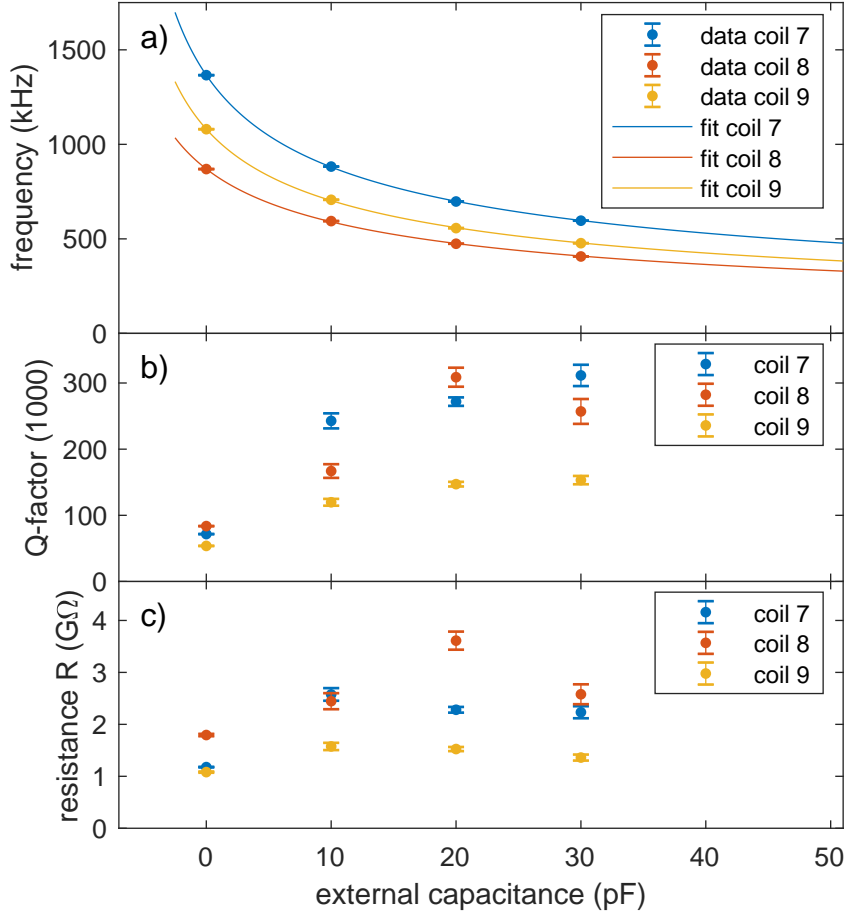
---

[2]See section 6.2.1 and figure 6.3.

Figure 5.12: Properties of the superconducting coils 7 to 9 as function of external capacitance. (a) Resonance frequency ν_0. (b) Quality factor Q. (c) Effective parallel resistance R.

the superconducting wire in this case.

A fit of the resonance frequency as function of the external capacitance allows to determine the inductance L and self-capacitance C_c of the coil, as

$$\nu_0(C_e) = \frac{1}{2\pi} \frac{1}{\sqrt{L(C_c + C_e)}}. \tag{5.39}$$

The fit results for coils 7, 8, and 9 are summarized in table 5.1. During this work, several additional coils previously used in the experiment have been characterized, an overview of the properties of these coils is given in appendix B.

coil	L (mH)	C_c (pF)
7	1.914(10)	7.09(5)
8	3.93(5)	8.53(14)
9	2.96(3)	7.32(10)

Table 5.1: Inductance L and self-capacitance C_c of superconducting coils.

We further compare the measured inductance of all superconducting coils with the number of windings in figure 5.13. We confirm the expected quadratic dependence of the inductance on the number of windings. A fit to the inductance $L(w)$
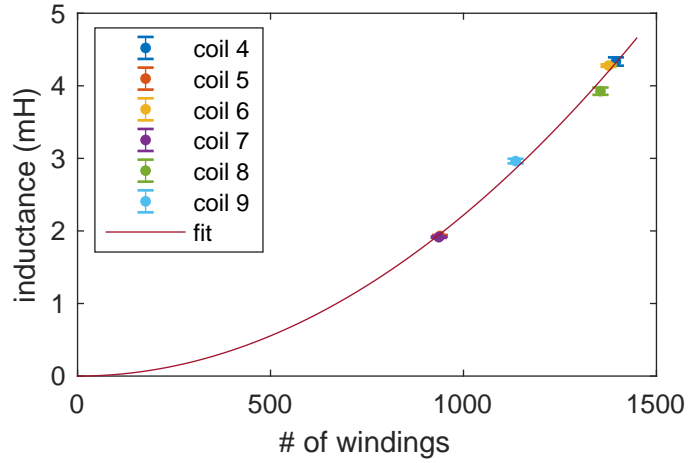
Figure 5.13: Inductance of the superconducting coils 4 to 9 as function of the number of windings. In addition, a quadratic fit to the data is shown.

using

$$L(w) = aw^2 \tag{5.40}$$

where w is the number of windings results in $a = 2.22(2) \times 10^{-6}\,\mathrm{mH}$. The parameter a being characteristic of the used core geometry.

5.8.2 Cryogenic Amplifier

Another crucial component of the image-current detection system is the cryogenic field effect transistor (FET) amplifier which consists of two stages. The first stage is a dual-gate FET where the first gate provides a high input resistance to the coil and the second gate acts as a cascode. The 3SK164 gallium arsenide (GaAs) FET is used for this stage. The second stage is another FET in common drain (source follower) configuration and provides roughly $50\,\Omega$ to the output. For this stage, the CF739 FET is used. The layout of the amplifiers is a standard design that has been used in previous proton g-factor measurements and is described in [66]. Further details on the image-current detection systems in general are also described in [98, 97].

For the 2021 setup we produced three new amplifiers made from PTFE-based circuit board to replace the amplifiers made from FR4, see figure 4.1. Crucially, the amplifiers were placed in close proximity to the the coil housing such that the length and the capacitance of the tap wire is minimized.

The signal-to-noise ratio (SNR) of the detection system is given by

$$S/N = \frac{4k_B T R \kappa^2}{u_n^2} \tag{5.41}$$

where R is the total effective parallel resistance of the image-current detector, and u_n is the voltage noise on the amplifier input. There are two contributions to R: the
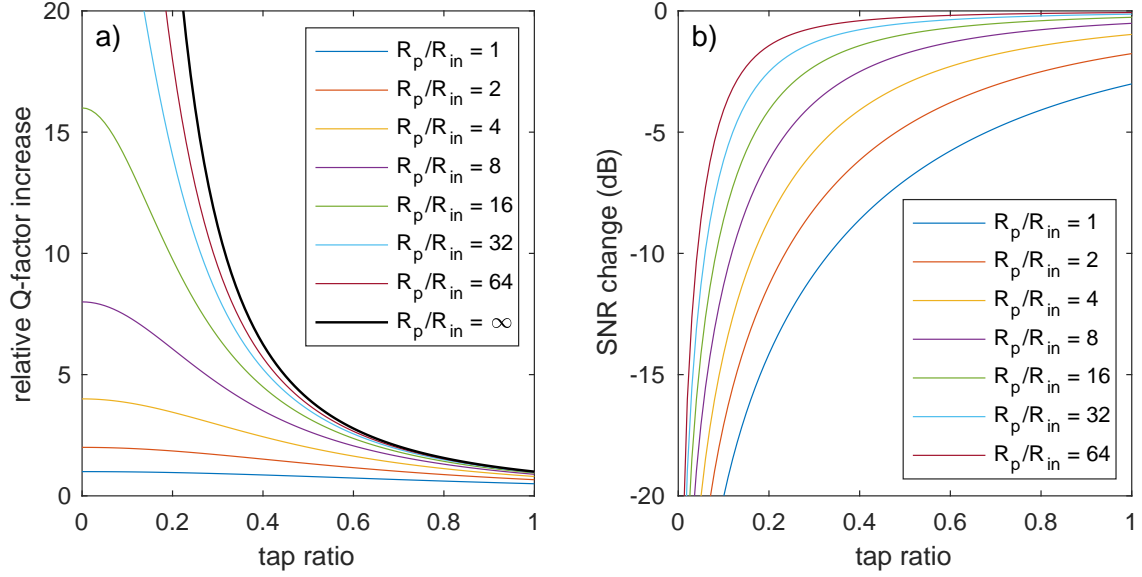
Figure 5.14: Q-factor and SNR as function of the tap ratio κ and the ratio R_p/R_{in}. (a) relative Q-factor increase. (b) change in SNR.

effective parallel resistance of the superconducting coil R_p, and the input resistance of the amplifier R_{in} which is decoupled by the factor κ^2. Typically, $R_{in}/R_p \ll 1$. Since both resistances are connected in parallel,

$$\frac{1}{R} = \frac{1}{R_p} + \frac{1}{R_{in}/\kappa^2}. \tag{5.42}$$

Expressing R as function of R_{in} and the ratio R_p/R_{in}, the SNR becomes

$$S/N = \frac{4k_B T R_{in}}{u_n} \left(\frac{\kappa^2}{\kappa^2 + R_{in}/R_p} \right). \tag{5.43}$$

The choice of the tap ratio κ is influenced by the following considerations: If the superconducting coil would be connected directly to the FET amplifier ($\kappa = 1$), the input resistance of the amplifier limits the Q-factor of the detection system, and defines the maximum attainable SNR. Decoupling the coil via a tap ($\kappa < 1$) allows for higher Q-factors of the detection system to be achieved. This boost in Q-factor of the overall detection system as a function of the tap ratio κ and the ratio R_p/R_{in} is shown in figure 5.14a. Additionally, decoupling the coil reduces the signal-to-noise ratio, as shown in figure 5.14b. There is no optimal solution for the tap ratio. Rather, a judicious choice of κ needs to be made by the experimenter. Essentially, the choice is how much loss in SNR can be accepted for a given improvement in the Q-factor. For the coils manufactured in this work, we chose $\kappa \approx 0.12$.

5.8.3 Cryogenic Switch

For some of the planned sympathetic cooling experiments it is essential to detune the resonance frequency of the detection system from the axial frequencies of the
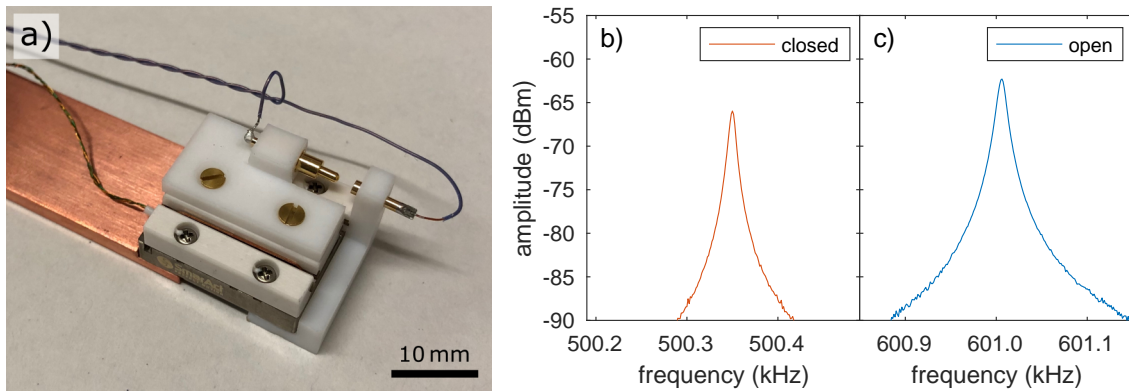
Figure 5.15: Cryogenic switch. (a) Piezo translation stage with spring-loaded pin. (b) Resonance in closed position. (c) Resonance in open position.

stored ions. Attempts to switch an additional capacitance to the detection circuit using varactor diodes or solid-state switches have not achieved the desired results, since the achieved detuning was too small, or since the added losses decreased the Q-factors to unacceptably low levels, see also [74].

In this work, we designed, built, and tested a cryogenic switch actuated by a piezo translation stage for detuning of the detector's resonance frequency. We used the SLC-1720 translation stage from *SmarAct* because it can be operated at cryogenic temperatures and in strong magnetic fields, without degrading the vacuum. Additionally, the device is small enough to be mounted in the 4 K-section of the experiment. The translation stage moves a spring-loaded pin connected to a 5 pF capacitance that is pressed onto a plate connected to the image-current detection system. When the switch is closed, the additional capacitance changes the resonance frequency of the detection system. The cryogenic switch, wired for testing, is shown in figure 5.15a.

For testing, we mounted the cryogenic switch in the cryocooler-based test setup and connected it to a dummy capacitance and one of the superconducting coils. We operated the switch and recorded the resonances of the superconducting coil on the VNA. The resulting resonances in the open and closed position are shown in figure 5.15b and 5.15c, respectively. With the cryogenic switch we were able to change the resonance frequency by approximately 100 kHz. With the freedom to connect any capacitance, the frequency difference can be set to any desired value and is not limited by capacitance constraints such as for varactor diodes. The Q-factor of the RLC circuit was larger than 50 000 in both positions, in this case limited by the losses in the superconducting coil. In the experiment the final Q-factor of the detection system is typically between 10 000 and 20 000 because of losses in the trap capacitance and the biasing network, as discussed in the next section. Therefore, the components of the switch do not limit the performance of the image-current detection system. Assuming a final Q-factor larger than 10 000 this corresponds to a detuning of at least 2000 line widths. At this detuning the resistive heating rate

66

is at least 1×10^7 times smaller than on resonance.

For the 2021 setup, the cryogenic switch was modified with an additional variable capacitance in parallel to the switch. The variable capacitance is realized by moving a gold-plated wire into a copper cylinder lined with PTFE for isolation. The resulting setup allows for fine tuning of the frequency in the open and closed position and provides a large jump in frequency when the contact of the switch is broken. This combines the advantages of both the switch and the variable capacitance.

5.8.4 Q-factor Optimization

We characterized the newly manufactured image-current detectors in the cryocooler-based test setup, where we reached Q-factors in the range of $30\,000$ to $40\,000$. In this test configuration, the image-current detectors, consisting of the superconducting coil connected to the FET amplifier, were connected to dummy trap electrodes. Other than the absence of a strong magnetic field, the setup reproduced the conditions found in the $4\,\mathrm{K}$-section of the experiment.

Later in the magnet we measured Q-factors of 1600 or lower, however. For these low Q-factors the image-current signal of a single particle is too narrow to be detected reliably. We went on to test the complete $4\,\mathrm{K}$-section in the cryocooler-based test setup in order to identify the origin of the additional losses. The reason to use the cryocooler-based test setup was that a cool-down took one or two days, compared to about one week in the magnet. We performed lots of cool-down cycles to check how changes to the setup would influence the Q-factors of the image-current detectors. In the following we summarize our findings and list the changes that affected the Q-factors positively:

- Clean feedthroughs: By connecting only the feedthroughs and disconnecting the wire to the detection electrodes we checked the influence of the feedthroughs on the Q-factors. We found that thoroughly cleaning the feedthroughs improved the Q-factors. However, the Q-factors of the same image-current detector varied considerably by connecting to different feedthroughs. There was no correlation with the used insulator material, as one might expect. Originally, sapphire feedthroughs were foreseen for biasing the electrodes connected to the image-current detectors and alumina feedthroughs were foreseen for biasing the other electrodes. Eventually, we selected the feedthroughs leading to the highest Q-factors for biasing the detector electrodes.

- Solder connection to electrodes: Before gold plating, typically two copper wires are soldered to the electrode in order to connect it to the biasing circuit later. By connecting the image-current detectors to different wires soldered to the same electrode, we found that some of the solder connections reduced the Q-factors to below 500. Examining the solder connection, we found a crystalline

substance below the gold layer. This finding is consistent with tin pest in lead-free solder at low temperatures. Normally, lead-tin solder is used in our lab, but accidental use of lead-free solder cannot be ruled out completely. At last, the problem was solved by wrapping copper wire tightly around the electrodes and connecting the image-current detectors to this wire.

- Blocking resistor: Since the image-current detectors are connected to two detection electrodes, but these electrodes are biased independently, the biasing network of one of these electrodes features a blocking resistor which needs to be larger than the effective parallel resistance of the RLC circuit. In our tests we found that the effective resistance of these resistors is typically smaller than nominal value. Therefore, the resistance was increased appropriately.

- Biasing network: At certain points in the biasing network, such as the biasing of split electrodes, the use of resistors cannot be avoided. However, coupling of any resistance to the image-current detector would lead to additional losses. Therefore, care needs to be taken that these resistances do not couple capacitively to components of the image-current detector, e.g. the wire connecting the coil and the detection electrode. It is also useful to ground the electrodes adjacent to the detection electrode directly next to the electrode with a capacitance, as the resistance of the wire supplying the bias voltage can also lead to losses.

In the end, we stopped further optimisation in the cryocooler-based test setup at the point where the Q-factors of all image-current detectors were in the range of 20 000 to 30 000. Afterwards, with the 4 K-section installed in the magnet again, we found that the Q-factors of the image-current detectors were in the range of 12 000 to 20 000. So the magnetic field of 1.9 T reduced the Q-factors by only about 30 %. As a result of this optimization, for the first time, the Q-factors of all image-current detectors were in a useful range simultaneously.

Chapter 6

Fluorescence Detection

Detection of fluorescence photons is an essential tool in experiments with laser-cooled trapped ions. In early experiments with single trapped ions it allowed the first observation of quantum jumps [99, 100, 101]. In state-of-the-art trapped-ion quantum computers it facilitates high-fidelity qubit readout [102]. In fundamental physics experiments it enables the application of sympathetic ground-state cooling and quantum logic spectroscopy and, therefore, the extension of laser-cooling techniques to ions without suitable laser-cooling transitions [103, 104]. So far, all these experiments rely on collection of fluorescence light with high numerical aperture optics and detection with a photomultiplier tube or camera at room temperature.

Despite Penning traps being indispensable tools for fundamental physic experiments where high magnetic fields are essential, e.g. for g-factor or mass measurements of single trapped ions [13, 14, 15, 105, 106, 107], they typically lack fluorescence detectors. Generally, optical access is at a premium because a Penning trap is usually located inside the bore of a superconducting magnet, and in some cases cooled to cryogenic temperatures. Where fluorescence detection has been used, complicated optical paths have been required to bring the fluorescence photons to the detection system located outside the magnet bore. Examples of such Penning-trap setups are experiments on motional ground-state cooling of calcium ions [28, 29], experiments with two-dimensional ion crystals for quantum simulation [27], mass measurements of heavy ions [108], and laser spectroscopy of highly charged ions [109].

In this chapter, we present a fluorescence detection system based on silicon photomultipliers (SiPM) integrated into the electrode structure of our cryogenic Penning-trap system. Our approach does not require an optical path to the outside of the magnet bore. This is especially useful for experiments where the Penning-trap system is enclosed in a hermetically-sealed vacuum chamber, and is cooled to cryogenic temperatures in order to utilize cryogenic pumping to achieve extreme-high vacuum, for instance allowing for antiproton storage times of years [71]. Due to their compact dimensions and expected insensitivity to magnetic fields SiPM are ideally suited for

operation in this environment. Furthermore, it has been shown that some SiPM are also compatible with cryogenic temperatures down to $4\,\mathrm{K}$ [110, 111, 112]. While the dark count rate of SiPM is typically several $1 \times 10^4\,\mathrm{s}^{-1}\,\mathrm{mm}^{-2}$ at room temperature, at cryogenic temperatures this problem is greatly reduced leading to extremely low dark count rates below a few counts per second. Further, it should be noted that SiPM are a relatively inexpensive commercial product, available in a variety of models, thus avoiding the development of custom-made devices. Related approaches of trap-integrated fluorescence detection use custom micro-fabricated superconducting sensors in a cryogenic radio-frequency trap [113] or custom chip-integrated avalanche photodiodes in a room temperature radio-frequency trap [114].

In our experiment, the fluorescence detection system will be used for the determination of the resonance frequency of the cooling transition in our magnetic field, for optimization of the cooling-laser parameters regarding intensity, position, and polarization, and for determining the axial temperature of the laser-cooled $^9\mathrm{Be}^+$ ion cloud. Ultimately, fluorescence-based state readout of a $^9\mathrm{Be}^+$ ion coupled to a proton or antiproton can be used for sympathetic cooling and implementation of quantum logic spectroscopy for Larmor and cyclotron frequency measurements on the (anti-)proton [30, 115].

This chapter is organized as follows: In the next section we describe the design of the Penning-trap system used in our experiments, in section 6.2 we characterize and compare the SiPM properties at room temperature and at $T = 4\,\mathrm{K}$, in section 6.3 we show measurements of fluorescence photon counts from a cloud of Doppler laser-cooled $^9\mathrm{Be}^+$ ions and determine the axial temperature of the trapped ion cloud. We summarize the results in section 6.4.

6.1 Experimental Setup

Since our Penning-trap system is enclosed in a hermetically-sealed cryogenic vacuum chamber which is located inside the bore of a superconducting magnet, optical and laser access is extremely limited and only possible along the axial direction through small fused-silica windows in the trap chamber. Therefore, instead of routing the fluorescence light to room temperature, which would require complicated optical paths, we pursue trap-integrated detection of fluorescence.

Trap-integrated detection of fluorescence is performed in the beryllium trap (BT) where laser-cooled $^9\mathrm{Be}^+$ ions are stored. The ions are loaded from a beryllium foil in the LT using $5\,\mathrm{ns}$-long pulses of a frequency-doubled Nd:YAG laser at $\lambda = 532\,\mathrm{nm}$ with $0.2\,\mathrm{mJ}$ to $0.6\,\mathrm{mJ}$ pulse energy and are adiabatically transported into the BT by voltage ramps. The BT is a cylindrical open-endcap five-electrode Penning trap with $4\,\mathrm{mm}$ inner diameter designed to be orthogonal and compensated [72]. A crucial additional feature of the BT is the six-fold segmented ring electrode shown in
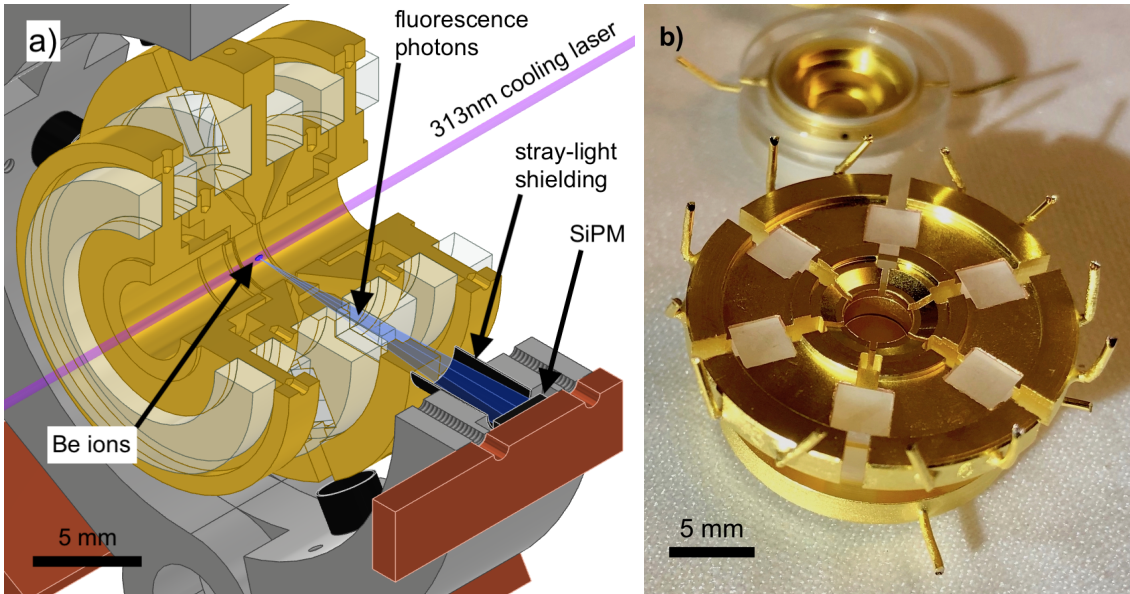
Figure 6.1: BT: (a) Section view of the BT setup. The solid angle of detected fluorescence photons is shown in light blue. (b) Photograph of the BT electrodes. The two topmost electrodes have been removed to show the segmented ring electrode. Note that the sapphire blocks are polished only on the faces through which fluorescence light passes.

figure 6.1. The benefits are two-fold: first, it allows for the application of rotating-wall potentials to compress the stored ion cloud, and second, it allows scattered fluorescence photons from the ^{9}Be$^+$ ion cloud to escape the trapping volume. Each of the six slits covers 6° in azimuth angle, and 0.785 mm in axial direction. Every slit allows about 0.3 % of the fluorescence light to escape the trap, and about 0.087(17) % of the fluorescence light reaches the SiPM. The electrodes are made from gold-plated oxygen-free electrolytic (OFE) copper with spacers made from sapphire. The six segments of the ring electrode are held in place by optically polished sapphire blocks. A tube made of black anodized aluminum mounted in the holder next to the SiPM suppresses stray light from directions other than the center of the trap. In addition, tubes with UV-absorbent coating are placed at the top and bottom of the trap stack for stray-light shielding, clipping the laser beam such that it does not hit the gold-plated electrodes [116].

Fluorescence photons from the trapping region pass the sapphire blocks and are detected by several SiPM mounted outside the six slits of the BT ring electrode. The distance from the SiPM detectors to the trapping region is approximately 17 mm. Each SiPM is read out individually in photon counting mode. The SiPM model MicroFJ-30035-TSV from *onsemi* has been selected because a similar model from the same manufacturer was operated at $T = 4$ K in previous work [111]. Another reason was that it features a glass window. Compared to plastic windows, this makes the device more sensitive to the ultraviolet light of the ^{9}Be$^+$ laser-cooling transition near 313 nm. According to the data sheet, at 313 nm, the photon detection efficiency
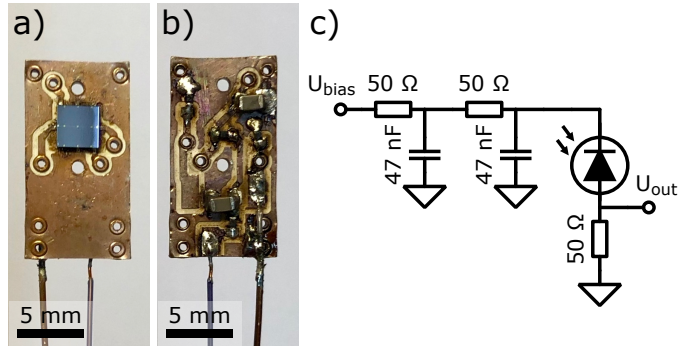
Figure 6.2: Photograph of the SiPM biasing and readout board front (a) and back (b). SiPM biasing and readout board circuit diagram (c).

(PDE) of the SiPM is 23 % at 2.5 V overvoltage and 28 % at 6.0 V overvoltage when operated at room temperature [117]. The SiPM features an active area of $3 \times 3\,\mathrm{mm}^2$ covered by a total of 5676 microcells, each 35 μm in size. The fill factor is 75 %. Due to its insensitivity to magnetic fields, the SiPM is able to operate in the 1.9 T magnetic field of our Penning-trap system.

Each SiPM is soldered onto a small biasing and readout board which contains low-pass filters for the biasing voltage and a 50 Ω output resistance, as shown in figure 6.2. The board material, *Rogers* RO4350B, has a low dielectric loss tangent and is suitable for cryogenic operation. The cabling from room temperature to $T = 4\,\mathrm{K}$ requires a compromise between low thermal conductivity to avoid excessive heat load to the cryogenic experiment and high signal transmission up to frequencies of approximately 1 GHz. For the readout cable an ultra-small diameter semi-rigid coaxial cable of type PE-020SR from *Pasternack* has been chosen. The small diameter keeps the heat flow small while the silver plating of the inner conductor provides sufficient signal transmission. Using a 1 m-long cable, which is also thermally anchored at the liquid nitrogen stage of the cryostat, keeps the heat load to the 4-K stage below 10 mW. Two ZFL-1000LN+ low-noise amplifiers mounted directly onto the SMA vacuum-feedthrough are used to amplify the signal before it is recorded with an oscilloscope, waveform digitizer or photon counter. To supply the biasing voltage to the SiPM, small-diameter manganin wires are used.

The cooling laser is a commercial TA-FHG pro diode laser system from *Toptica*. An external cavity diode laser generates light near 1252 nm which is amplified in a tapered amplifier and frequency doubled twice in two cascaded second harmonic generation (SHG) cavities. The frequency is stabilized with a WSU8-2 wavelength meter from *HighFinesse* using light near 626 nm coupled out after the first SHG stage. The 313 nm light is transferred from the optical table to the magnet via a hydrogen-loaded single-mode photonic crystal fiber [118]. An optical breadboard bolted to the magnet below the entrance window to the horizontal bore contains the beam delivery optics. The beam emerging from the fiber is collimated and then polarized by an alpha-BBO Glan-laser polarizer. The reflection off the polarizer is

used to monitor the power of the delivered 313 nm light. The polarization of the beam directed into the trap is adjusted using motorized half-wave and quarter-wave plates. The beam position and angle are adjusted using a pair of motorized mirrors in front of the entrance window.

6.2 SiPM Characterization at Room Temperature and 4 K

6.2.1 Cryocooler-based Test Setup

A cryocooler-based test setup is used to characterize and compare the properties of the SiPM at room temperature and at $T = 4$ K. For these measurements, a MicroFJ-SMA-30035 evaluation board containing the MicroFJ-30035-TSV SiPM and its biasing and readout circuitry, is mounted to the 4-K stage of the pulse-tube cryocooler. The 4-K section of the cryocooler is completely enclosed by a copper heat shield kept at 4 K in order to eliminate heat load on the evaluation board due to thermal radiation. A second aluminium heat shield mounted to the 50-K stage of the cryocooler reduces the heat load to the 4-K heat shield. A schematic of the setup is shown in figure 6.3. Two Cernox thin-film resistance temperature sensors are mounted on the 4-K stage for temperature measurements. The cabling for biasing and readout of the SiPM evaluation board is the same as in the Penning-trap setup described above. The cables are thermally anchored at the 4-K and 50-K stages of the cryocooler to avoid heat load on the evaluation board due to thermal conduction through the cables.

Light pulses are delivered to the SiPM through a multi-mode fiber. One end of the fiber is mounted to the 4-K stage at a distance of approximately 10 mm from the SiPM. The fiber is routed outside the vacuum chamber using a fiber feedthrough. A LED315W ultraviolet light-emitting diode (UV-LED) from *Thorlabs* with emission around 315 nm is used to generate short pulses of light containing only a few photons which are coupled into the other end of the fiber. The UV-LED is operated by applying rectangular pulses with a fixed pulse length of 20 ns and varying voltage and repetition rate from a waveform generator. Care was taken to install the UV-LED and the fiber coupler inside a lens tube in a light-tight way. The section of the fiber outside of the vacuum chamber had to be enclosed in light-tight black shrink tubing as well in order to suppress light entering the fiber from light sources in the laboratory. Light-tightness of the setup is checked by utilizing the extremely low dark count rate of the SiPM at $T = 4$ K allowing to detect stray-light-photon count rates as low as $1\,\mathrm{s}^{-1}$.

Our test setup allows to cool down the SiPM without affecting the single-photon source, such that the number of photons delivered to the SiPM is independent of
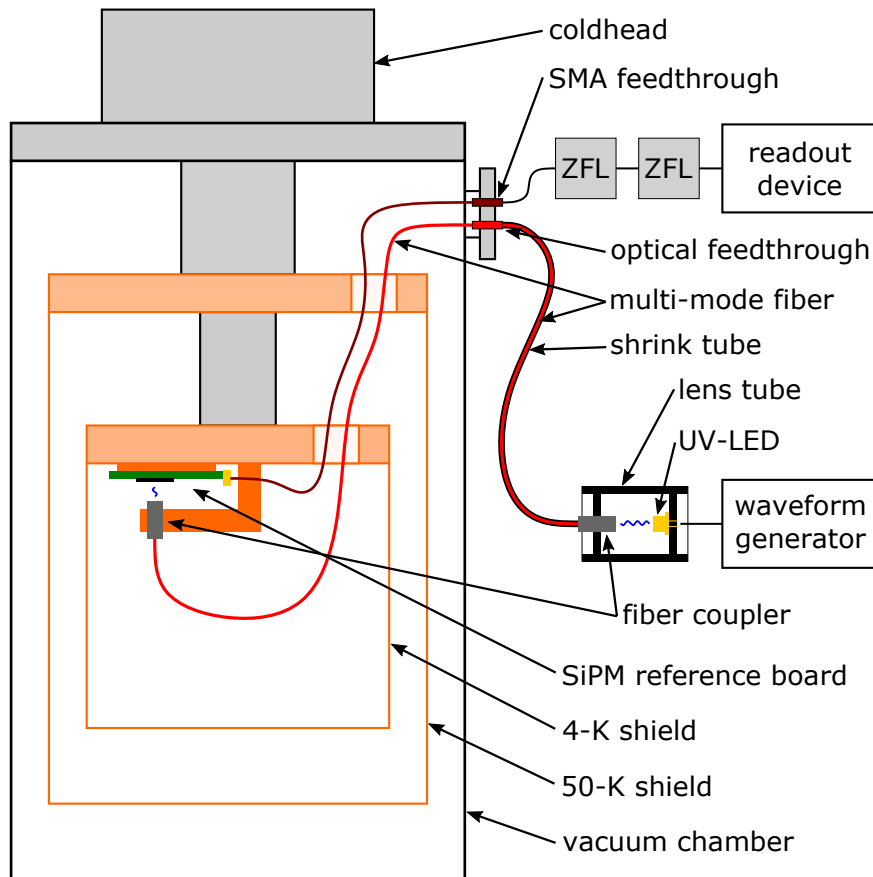
Figure 6.3: Cryocooler-based test setup for SiPM characterization at cryogenic ($T = 4\,\mathrm{K}$) and room temperature. Cables for SiPM biasing are omitted. Readout device: either oscilloscope, waveform digitizer, or photon counter. ZFL: low noise amplifier ZFL-1000LN+ from *Mini-Circuits*.
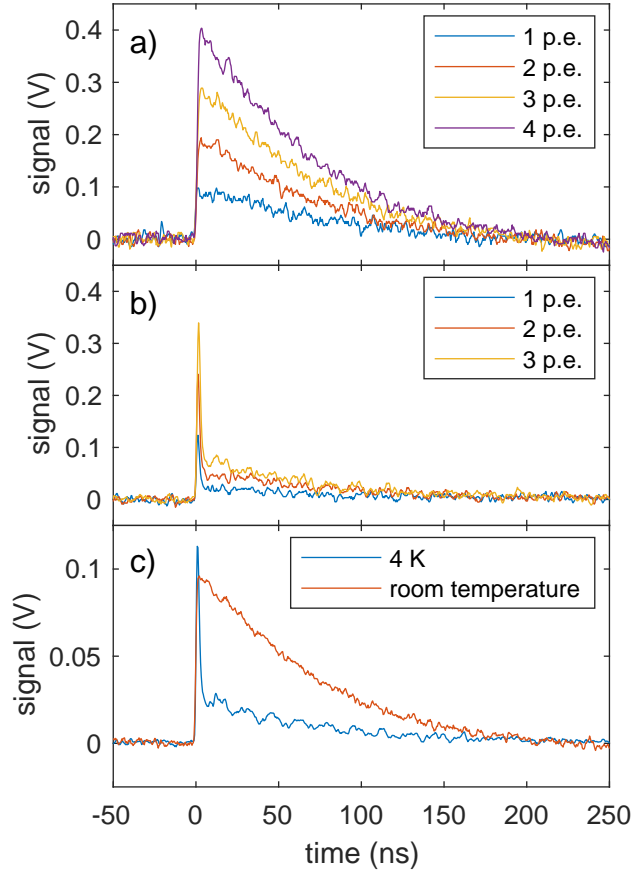
Figure 6.4: Oscilloscope traces of SiPM pulses at room temperature and bias voltage 26.5 V (a) and at $T = 4\,\mathrm{K}$ and bias voltage 24.0 V (b). One graph for each n-photoelectron pulse is shown. (c) Direct comparison of the SiPM pulse shape at $T = 4\,\mathrm{K}$ and room temperature. The average of 27 one-photoelectron pulses is plotted for both temperatures. p.e.: photoelectron.

temperature. This enables a direct comparison of the detection efficiency at room temperature and at $T = 4\,\mathrm{K}$.

6.2.2 Pulse Shape

The output signal of the SiPM is the sum of the contribution from all microcells. The signal is therefore quantized with respect to the number of avalanching microcells and is a multiple of the signal of the one-photoelectron pulse. Graphs of such multi-photoelectron pulses are shown in figure 6.4a for room temperature and in figure 6.4b for $T = 4\,\mathrm{K}$. The shape of the one-photoelectron pulse at room temperature and at $T = 4\,\mathrm{K}$ is compared in figure 6.4c.

The typical pulse shape at room temperature is characterized by a fast rise with a rise-time on the order of 1 ns and an exponential decay. The time constant of the exponential decay is determined by the microcell recharge time constant $\tau_{RC} = R_q C_d$, where R_q is the quench resistance and C_d is the effective microcell capacitance [119]. From a fit to the exponential decay we determine $\tau_{RC} = 70.1(5)\,\mathrm{ns}$.

At cryogenic temperature the fast rise is unchanged. However, the exponential

	τ_{RC} (ns)	C_d (fF)	R_q (MΩ)
Room temperature	70.1(5)	158(2)	0.444(6)
$T = 4\,\mathrm{K}$	74(1)	35(2)	2.1(1)

Table 6.1: Measured values of recharge time constant τ_{RC}, and microcell capacitance C_d, as well as calculated value of quench resistance R_q for the MicroFJ-30035-TSV SiPM.

decay is composed of two components. A fast component decaying with a time constant of $1.9(4)\,\mathrm{ns}$ to a level of about one quarter of the maximum and a slow component decaying with a time constant of $74(1)\,\mathrm{ns}$. Similar pulse shapes have been observed at cryogenic temperatures in [120] and modelled in [121]. The reason for the different pulse shape at cryogenic temperatures is an increased quench resistance. When the quench resistance becomes too large, the quenching occurs partly via the stray capacitance of the quench resistor instead, which explains the fast component.

To quantify the change in quench resistance of our SiPM, its value is calculated from the measured values of the recharge time constant τ_{RC} and the microcell capacitance C_d evaluated in section 6.2.4. The resulting values are listed in table 6.1. At cryogenic temperatures we indeed observe that the quench resistance is increased. In addition, the microcell capacitance is reduced, while the recharge time constant shows only a minor change. We attribute both the change in quench resistance and the change in microcell capacitance to temperature-dependent effects in silicon.

6.2.3 Charge and Pulse Height

A SiPM pulse is characterized by two measures: its pulse height and its charge. The pulse height is defined as the maximum amplitude of the pulse with respect to the baseline. The charge Q of the pulse is defined as the numerical integral over the pulse waveform.

$$Q = \frac{1}{G_A R} \int V(t) \, \mathrm{d}t, \tag{6.1}$$

where G_A is the voltage gain of the ZFL-amplifier chain, and $R = 25\,\Omega$ (the $50\,\Omega$ output resistance of the SiPM biasing and readout circuit in parallel to the $50\,\Omega$ impedance of the transmission line).

The baseline of the pulse is defined as the mean of the signal level in the time window ranging from $1000\,\mathrm{ns}$ to $10\,\mathrm{ns}$ before the trigger, and is determined for each pulse individually in order to take into account baseline fluctuations. Traces containing dark-count pulses in this time window are excluded from the analysis. For the subsequent determination of pulse height and charge, the baseline is subtracted from the signal level. The data in the time window from $10\,\mathrm{ns}$ before the trigger to $200\,\mathrm{ns}$ after the trigger are then used to calculate the pulse height and the charge of an individual pulse.

In the following, we characterize the dependence of pulse height and charge on
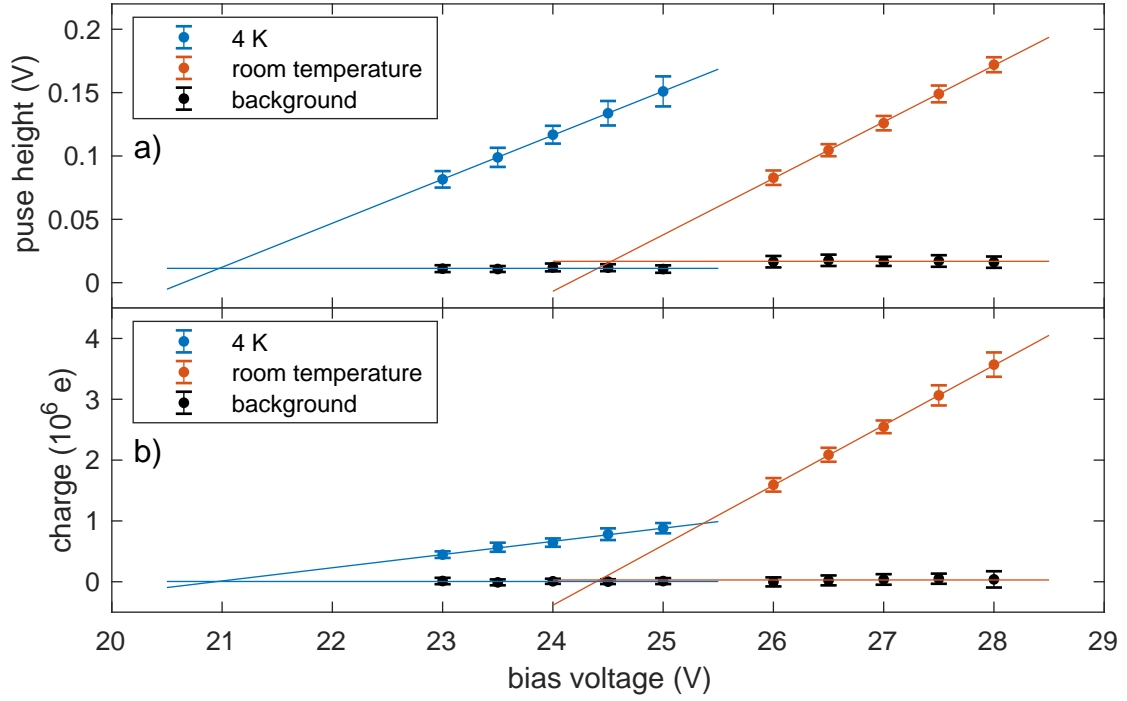
Figure 6.5: Pulse height (a) and charge (b) of one-photoelectron SiPM pulse waveforms as a function of bias voltage. Each datapoint is the average of approximately 50 wavefroms, the errorbars indicate the 1-σ standard deviation.

the bias voltage by analyzing oscilloscope traces of SiPM pulse waveforms. For simplicity, we consider only one-photoelectron waveforms. The resulting values are shown in figure 6.5 where, in each panel, measurements at room temperature and at $T = 4\,\mathrm{K}$ are compared. We observe a linear dependence of both pulse height and charge on bias voltage for both temperatures.

From a linear fit to the data in figure 6.5a we determine the dependence of pulse height on bias voltage to $0.0347(2)\,\mathrm{V/V}$ at $T = 4\,\mathrm{K}$. This is $22\,\%$ lower compared to the value at room temperature of $0.0445(5)\,\mathrm{V/V}$. Based on a linear fit to the data in figure 6.5b we find that the dependence of charge on bias voltage is $0.217(11) \times 10^6\,e/\mathrm{V}$ at $T = 4\,\mathrm{K}$. This is a reduction by a factor of 4.5 compared to the value at room temperature of $0.986(13) \times 10^6\,e/\mathrm{V}$.

6.2.4 Breakdown Voltage, Microcell Capacitance, and Gain

The breakdown voltage U_0 of the SiPM is determined by a linear extrapolation of the pulse height and charge to zero. Since noise is superimposed onto the SiPM pulse, the measured pulse height and charge are modified, which needs to be taken into account. We evaluate noise with the same algorithms as used for the evaluation of SiPM pulses, and arrive at the background values shown in figure 6.5. A finite value for the background pulse height is determined, while the value for the background charge is consistent with zero. Note that the noise pulse height differs between room temperature and 4 K. Consequently, we extrapolate the pulse height to the value

given by the background pulse height and the charge to zero.

The resulting extrapolations are shown in figure 6.5 as well. The estimates of the breakdown voltage based on pulse height and based on charge agree within the error of the measurement, and the resulting combined values are $U_0 = 24.5(1)\,\mathrm{V}$ at room temperature and $U_0 = 21.0(1)\,\mathrm{V}$ at $T = 4\,\mathrm{K}$. Furthermore, the determined breakdown voltage at room temperature is in agreement with the value given in the data sheet [117].

The microcell capacitance C_d is determined by the slope of the charge Q_1 of a one-photoelectron pulse as a function of bias voltage since it is defined as

$$C_d = \frac{Q_1}{\Delta U} = \frac{Q_1}{U - U_0}, \tag{6.2}$$

where $\Delta U = U - U_0$ is the overvoltage. A linear fit to the data in figure 6.5b gives a microcell capacitance of $C_d = 158(2)\,\mathrm{fF}$ at room temperature and $C_d = 35(2)\,\mathrm{fF}$ at $T = 4\,\mathrm{K}$. Compared to room temperature, the microcell capacitance is reduced by a factor of 4.5 at $T = 4\,\mathrm{K}$.

The gain G of the SiPM is determined by the relationship

$$G = \frac{Q_1}{e}, \tag{6.3}$$

where e is the elementary charge, and Q_1 is the charge of a one-photoelectron pulse. The gain measured at room temperature is consistent with the values given in the data sheet [117]. Since the gain is proportional to the microcell capacitance it is also reduced by a factor of 4.5 at $T = 4\,\mathrm{K}$.

6.2.5 Crosstalk

The crosstalk probability q is the probability that a triggered microcell causes an additional and simultaneous avalanche in another microcell. This probability can be determined based on a measurement of the dark count rate as function of the trigger threshold. For dark counts, the ratio of the count rates of two-photoelectron pulses to one-photoelectron pulses is an estimate of the crosstalk probability. For this measurement, the SiPM is installed in the Penning-trap setup, and a SR400 photon counter from *SRS* is used to record the count rate. Stray-light is suppressed, such that dark counts dominate. The recorded dark count rate at room temperature is shown in figure 6.6a for various overvoltages. The resulting crosstalk probability is shown in figure 6.6b. The data show the typical increase of the crosstalk probability with overvoltage.

At $T = 4\,\mathrm{K}$, the dark count rate is too low to determine the crosstalk probability based on dark counts. Instead, fluorescence light from ${}^9\mathrm{Be}^+$ ions is used. The fluorescence light level is chosen so low that the probability of two photons arriving
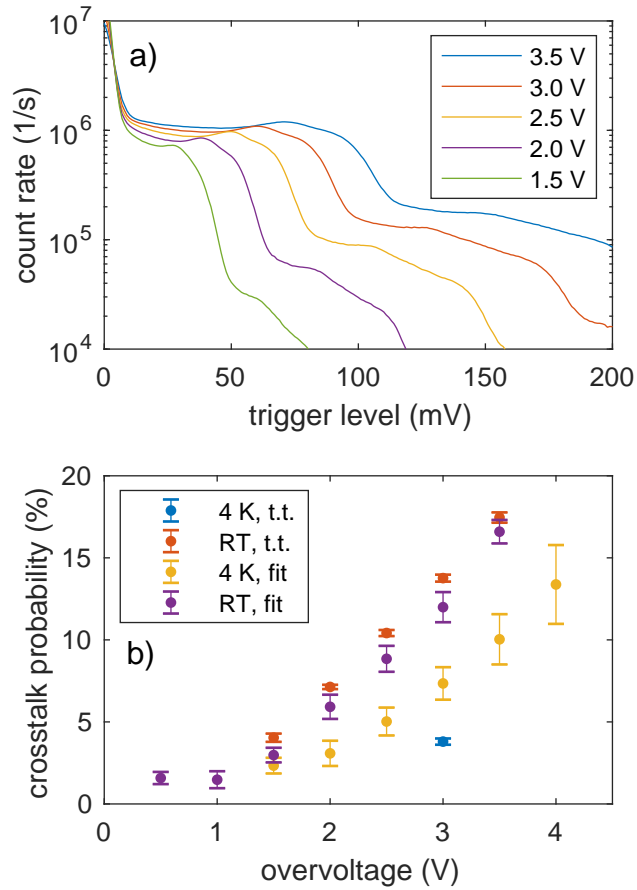
Figure 6.6: Dark count rate at room temperature (RT) as a function of trigger level for various overvoltages (a) and crosstalk probability as function of overvoltage (b). t.t.: trigger-threshold method. fit: fit method.
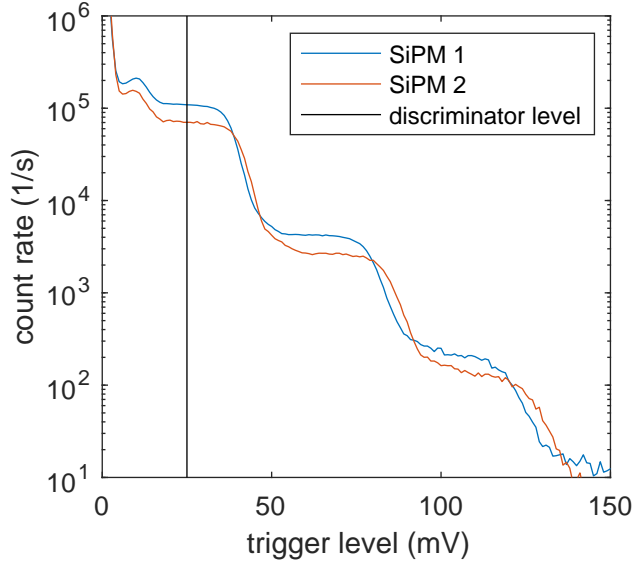
Figure 6.7: Count rate as a function of trigger level for two SiPM installed in the BT and biased with 24.0 V. The data is recorded with a SR400 photon counter. The threshold chosen to discriminate background and one-photoelectron pulses is marked with a black vertical line at 25 mV, as further discussed in section 6.3.

at the same time is negligible. The recorded count rate is shown in figure 6.7 and the resulting crosstalk probability in figure 6.6b. For the typical bias voltage of $U = 24.0$ V used at $T = 4$ K, the crosstalk probability is $3.8(2)$ %. This is a factor of 3 lower than at room temperature at the same overvoltage.

In addition to the trigger-threshold method described above, the crosstalk probability is also determined from a fit to the photoelectron distribution, as introduced in the next section. For this measurement, the SiPM is installed in the cryocooler-based test setup, and is read out by a waveform digitizer. The values resulting from the fit are shown in figure 6.6b as well. This method gives a crosstalk probability at $T = 4$ K which is about a factor of two lower than at room temperature.

Overall, the crosstalk probability at $T = 4$ K is significantly reduced compared to room temperature. At room temperature, the values from both methods show only small deviations. However, at $T = 4$ K the trigger-threshold method results in a factor of 2 lower estimate than the fit method. The discrepancies might be explained by the different processes which are used to trigger the microcells. For the trigger-threshold method dark counts are used at room temperature and 313 nm fluorescence photons at $T = 4$ K, while for the fit method UV-LED light pulses near 315 nm are used at both room temperature and $T = 4$ K. The trigger-threshold measurements and fit measurements have been performed using different SiPM in different environments, so that the discrepancy may also arise from batch variation or the environmental conditions.
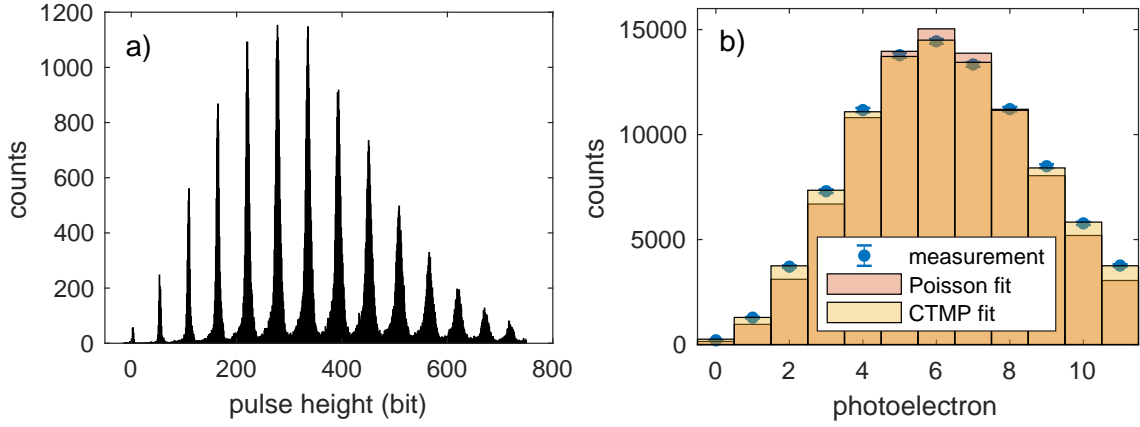
Figure 6.8: (a) SiPM pulse-height distribution for a bias voltage of $27.0\,\mathrm{V}$ at room temperature and UV-LED light intensity setting 1. (b) The photoelectron distribution resulting from 6.8a is fitted with a Poisson distribution and a crosstalk-modified Poisson (CTMP) distribution. The better fit is achieved by the CTMP distribution with $\lambda = 5.96(2)$ and $q = 0.081(4)$.

6.2.6 Photon Detection Efficiency

To characterize the photon detection efficiency (PDE) near $313\,\mathrm{nm}$, UV-LED light pulses containing only a few photons are applied to the SiPM installed in the cryocooler-based test setup. Subsequently, the mean number of detected photons λ per UV-LED light pulse is determined from photoelectron distributions. Finally, a relation between λ and the PDE is established by comparing λ with known values of the PDE given in [117].

Here, we record SiPM pulse waveforms using a DT 5761 waveform digitizer from *CAEN* which is triggered synchronously with the applied UV-LED light pulses. A repetition rate of $10\,\mathrm{kHz}$ assures suppression of accidental recordings of afterpulses and dark counts. All synchronous responses of the SiPM to UV-LED light pulses are recorded, including waveforms that generate a zero-photoelectron response on the SiPM.

The pulse-height distribution from such a measurement is shown in figure 6.8a for room temperature, a SiPM bias voltage of $27.0\,\mathrm{V}$, and a specific UV-LED light intensity termed setting 1. The peaks in the pulse-height distribution correspond to n-photoelectron pulses. In order to improve the resolution of these peaks, a $22\,\mathrm{MHz}$ low-pass filter has been installed at the input of the waveform digitizer. This slightly distorts the pulse shape, but increases the resolving power of the individual peaks considerably. For further evaluation, all counts within the corresponding peaks of the pulse-height distribution are summed up, resulting in the photoelectron distribution shown in figure 6.8b.

The UV-LED light source can be described as a thermal light source with a Poissonian photon distribution. However, crosstalk modifies the measured photo-electron distribution, since for each avalanching microcell an additional microcell

81
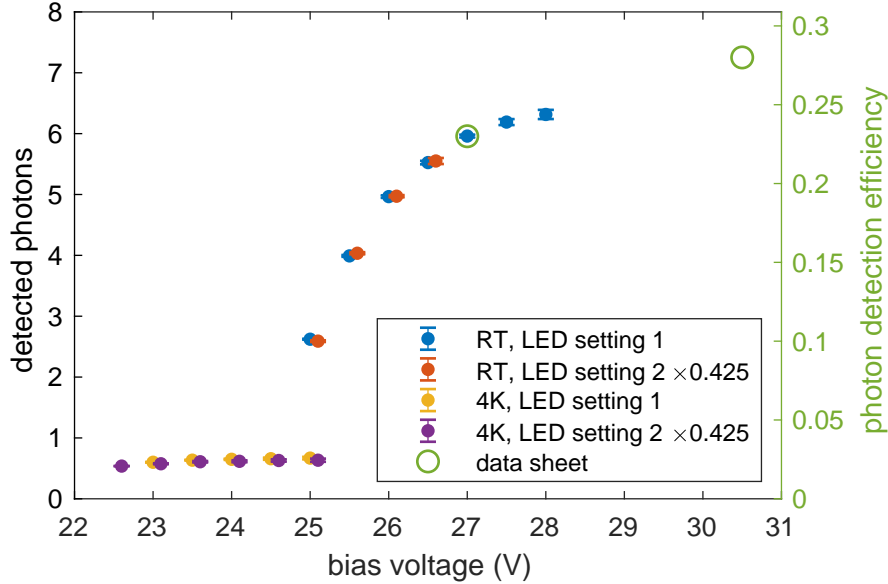
Figure 6.9: Mean number of detected photons λ and photon detection efficiency (PDE) as function of bias voltage, at room temperature (RT) and 4 K, and for two settings of the UV-LED light intensity. The measurements for setting 2 have been scaled by a factor of 0.425 and shifted by 0.1 V for better visualization. The value at RT and 27.0 V bias voltage is used to calibrate the PDE to λ.

is triggered with crosstalk probability q. This effect is taken into account using a crosstalk-modified Poisson (CTMP) distribution, described in [110], with parameters λ and q. For $q \to 0$ this distribution converges to the Poisson distribution with parameter λ. We fit one of the photoelectron distributions with both a Poisson distribution and the CTMP distribution, and compare the results in figure 6.8b. While the Poisson distribution systematically deviates from the measured data, the data is well described by the CTMP distribution. The CTMP distribution further allows to extract an independent value for the crosstalk probability q, shown in figure 6.6b.

The mean number of detected photons λ from fits to photoelectron distributions is plotted in figure 6.9 for two UV-LED light intensity settings, with the SiPM at room temperature and $T = 4$ K, and as a function of bias voltage. The graph shows that λ increases with bias voltage at room temperature. At $T = 4$ K, the dependence on bias voltage is reduced, and λ is smaller by a factor of 5 to 10.

The PDE of the SiPM is shown on the vertical axis on the right in figure 6.9. It has been calibrated by relating λ to the PDE at 313 nm of 23 %, given in the data sheet [117] for room temperature and an overvoltage of 2.5 V. Since the number of applied photons only depends on the UV-LED setting, this calibration is valid for all bias voltages and both temperatures and establishes a relation between λ and the PDE. Two calibrations based on two different UV-LED light intensity settings agree. For the bias voltage of 24.0 V, typically used in the Penning-trap setup at $T = 4$ K, we determine a PDE of 2.5(1) %.

6.3 Trap-integrated Detection of ^{9}Be$^+$ Fluorescence

We demonstrate our SiPM-based detection method with a cloud of ^{9}Be$^+$ ions stored in the BT and brought into resonance with the RLC circuit at $T = 4$ K. The ion number N is determined from the line shape of the frequency spectrum of the RLC circuit [71], and is $N = 540(40)$ in run 1 and $N = 5100(200)$ in run 2. Circularly polarized laser light near 313 nm with laser power between 60 µW and 1800 µW is used to cool the ^{9}Be$^+$ ions. In the 1.9 T magnetic field of the BT, ^{9}Be$^+$ ions can be cooled either on the ^{2}S$_{1/2}$ ($m_J = 1/2$) $\rightarrow$ ^{2}P$_{3/2}$ ($m_J = 3/2$) transition using σ^+ polarized light or on the ^{2}S$_{1/2}$ ($m_J = -1/2$) $\rightarrow$ ^{2}P$_{3/2}$ ($m_J = -3/2$) transition using σ^- polarized light. Both options are closed cycling transitions with an intrinsic off-resonant repumping mechanism [122, 123]. We have cooled ^{9}Be$^+$ ions on and observed fluorescence signals for both transitions using appropriately polarized laser light. In the following we use the ^{2}S$_{1/2}$ ($m_J = -1/2$) $\rightarrow$ ^{2}P$_{3/2}$ ($m_J = -3/2$) transition.

The SiPM is operated with a bias voltage of 24.0 V and SiPM pulses are counted on the SR400 photon counter set to a trigger threshold of 25 mV and a counting window of 1000 ms. The ideal trigger threshold to discriminate one-photoelectron pulses from the noise was determined from a measurement of the background count rate as a function of threshold, as shown in figure 6.7. Note that additional light was introduced into the trap to compensate for the low dark count rate at $T = 4$ K.

We scan the laser frequency across the resonance from low to high frequencies with a scan rate of 2 MHz s^{-1} and record the count rate of fluorescence photons. These scans are repeated for several values of laser power. The resulting background-removed data are shown in figure 6.10. The fluorescence signal slowly rises with increasing laser frequency and follows a Voigt line profile. At the moment the laser frequency reaches the resonance frequency of the cooling transition the fluorescence intensity sharply drops to zero as the ions are heated out of resonance. We further observe power broadening of the linewidth and saturation of the fluorescence count rate with increasing laser power.

The line shape of the fluorescence count rate is modelled as a Voigt profile $V(\nu, P)$ which is cut off at the resonance frequency ν_0. The Voigt profile is the convolution of a Lorentzian profile $L(\nu, P)$ and a Gaussian distribution $G(\nu)$ with standard deviation σ. The Lorentzian profile is defined as

$$L(\nu, P) = \eta I_C \frac{(\gamma/2)^2}{(\gamma/2)^2 + (\nu - \nu_0)^2} \tag{6.4}$$

with the power-broadened line width (FWHM) $\gamma = \gamma_0 \sqrt{1 + P/P_0}$, the on-resonance scattering rate $I_C = \frac{2\pi\gamma_0}{2} \frac{P/P_0}{1 + P/P_0}$, the natural linewidth (FWHM) $\gamma_0 = 19.6(10)$ MHz [124], the saturation power P_0, and the laser power P. The parameter η is the
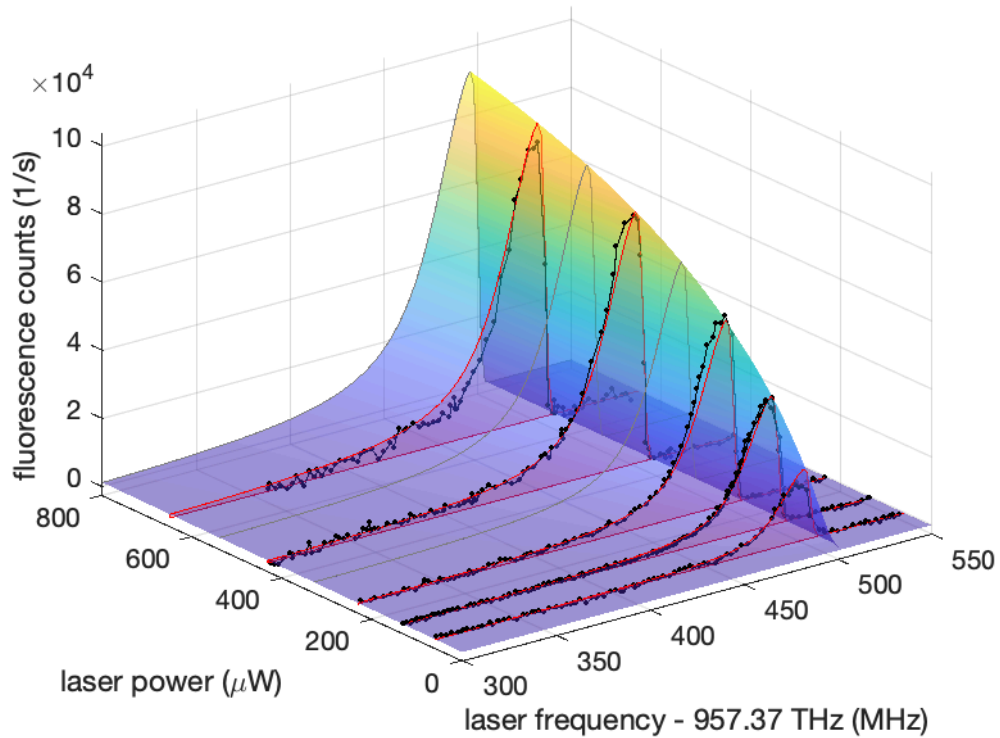
Figure 6.10: Fluorescence spectra of run 1. Black data points show the count rate of fluorescence photons as a function of the cooling-laser frequency and power. The laser frequency is scanned across the resonance from low to high frequencies for different values of the laser power. The sharp drop in fluorescence counts is caused by heating the ions out of resonance when the laser detuning becomes positive. Red curves show the result of the 2-dimensional fit at the laser power of the frequency scans. The color-coded surface shows the 2-dimensional fit, color-coded with respect to the fluorescence count rate. Grey line profiles are added to guide the eye.
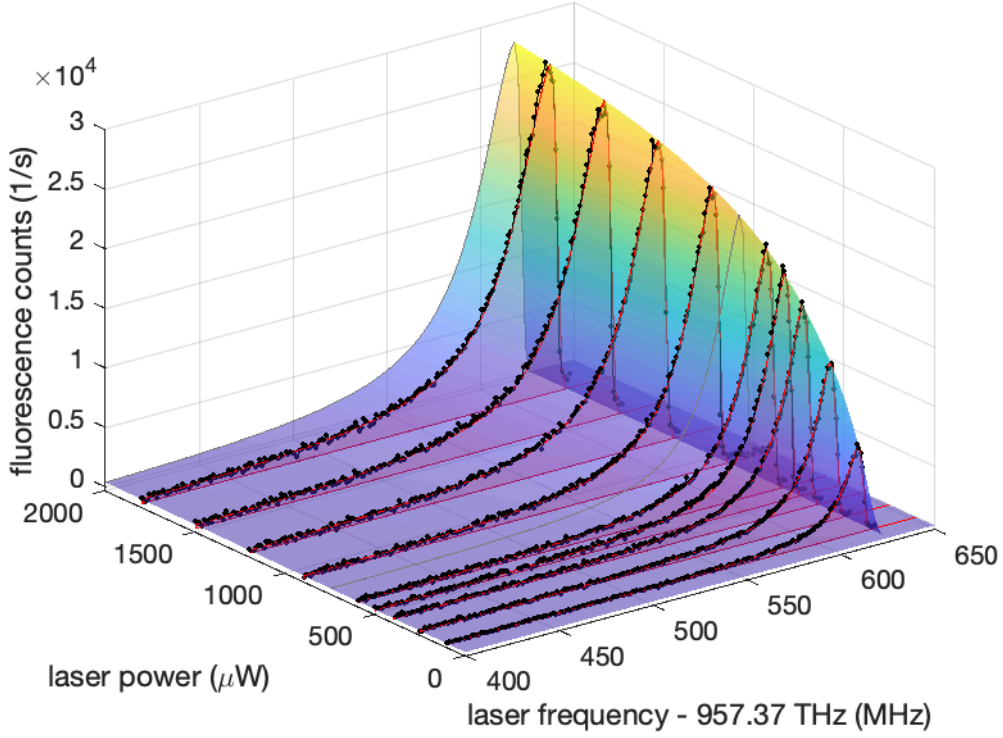
Figure 6.11: Fluorescence spectra of run 2. Description as in figure 6.10.

product of the total detection efficiency and the ion number, expressing the count rate of detected photons in terms of the scattering rate of a single ion. While power broadening and saturation is included in the Lorentzian part of the Voigt profile, Doppler broadening and other broadening effects are included in the Gaussian width of the Voigt profile.

First, the resonance curves for each laser power are fitted individually with the Voigt line profile added to a linear background to determine the background count rate. The resulting background-removed data are shown in figure 6.10 and 6.11. Note that the laser power in run 2 was stabilized to better than 0.3% while in run 1 the laser power fluctuates and drifts up to 10%. The background-removed data are then simultaneously fitted with the Voigt line profile as function of frequency and laser power. This 2-dimensional fit simultaneously accounts for power broadening and saturation which both depend on the ratio P/P_0. The resulting fit surface is plotted in figure 6.10 and 6.11 as well. The fit parameters for run 1 are $\eta = 0.00224(6)$, $P_0 = 212(10)\,\mu\text{W}$, and $\sigma = 9.3(4)\,\text{MHz}$. For the approximately 10 times larger ion cloud in run 2 the fit parameters are $\eta = 0.000546(2)$, and $P_0 = 326(2)\,\mu\text{W}$. The fit parameter σ of the 2-dimensional fit converges to zero, therefore, $\sigma = 3.3(3)\,\text{MHz}$ is determined from the weighted mean of the individual fits.

Considering equation 6.4 for $\nu = \nu_0$ and $P/P_0 \to \infty$, as would be the case for a

saturated transition, the count rate of detected photons n_d is maximum and becomes

$$n_d = \eta_e \eta_g \eta_a \eta_d N \frac{2\pi\gamma_0}{2} = \eta \frac{2\pi\gamma_0}{2} \qquad (6.5)$$

where $\eta_e = 0.75$ is a correction factor due to non-isotropic emission from $\sigma^{\pm}$ transitions in a magnetic field [34], $\eta_g = 0.00087(17)$ is the geometrical acceptance of the SiPM, $\eta_a = 0.84(2)$ takes into account the absorption in the sapphire blocks, η_d is the detection efficiency of the SiPM, and N is the ion number. Under these conditions the ion cloud has a well-defined photon scattering rate $N\pi\gamma_0$. This photon source is then used to independently characterize the detection efficiency of the SiPM. Taking the value of η from the fit of run 1, we evaluate the detection efficiency of the SiPM to $\eta_d = \frac{\eta}{N\eta_e\eta_g\eta_a} = 0.0075(16)$. This value is a factor of 3.3(7) lower than the detection efficiency resulting from the characterization in the cryocooler of $\eta_d = 0.025(1)$. In run 2 we evaluate the detection efficiency of the SiPM to $\eta_d = 0.00019(4)$, which is a factor of 128(27) smaller than the detection efficiency in the cryocooler and a factor of 40(12) smaller than in run 1. In run 3 we measured again a value for the detection efficiency which is consistent with run 1. The reduced detection efficiency, compared to the characterization measurements in the cryocooler, might be explained by the effects of the $1.9\,\mathrm{T}$ magnetic field in the Penning trap, which is not present in the cryocooler. Further, we observed cracks in the glass windows of some of the installed SiPM after repeated cooling cycles. Attenuation due to these cracks could also explain the reduced detection efficiency and the variation in detection efficiency between different examples of SiPM. The best total detection efficiency of our SiPM-based detection method was achieved in run 1 where $\eta/N = 4.2(3) \times 10^{-6}$.

The count rate of detected photons per ion is $n_1 = n_d/N = \frac{P/P_0}{1+P/P_0} \times 256(24)\,\mathrm{s}^{-1}$ on resonance in run 1. This count rate is to be discriminated from the background count rate $n_b = P/P_0 \times 5 \times 10^4\,\mathrm{s}^{-1}$ which is dominated by stray light and increases linearly with laser power. The dark count rate is independent of laser power and contributes less than $1\,\mathrm{s}^{-1}$ to the background count rate. Therefore, the signal-to-background ratio is maximum at low laser power and decreases as the transition is saturated at high laser power. Assuming signal-to-background ratios ≤ 1 and considering counting statistics, the ion sensitivity, defined as the fluorescence count rate divided by the uncertainty of the total count rate, is maximum near $P/P_0 = 1$. At this laser power the signal-to-background ratio for a small ion cloud with $N = 10$ is approximately 0.025, and the ion cloud can be discriminated from the background with five standard deviations within an averaging time of $0.8\,\mathrm{s}$. For smaller ion clouds this time increases proportional to $1/N^2$. If the background count rate due to stray light can be eliminated, the background would be dominated by the dark count rate of the SiPM, and single-ion sensitivity can be achieved with averaging times below $100\,\mathrm{ms}$. Besides reducing stray light, the single-ion sensitivity can be improved by increasing the geometrical acceptance η_g, or by using a sensor with higher detection

efficiency.

The temperature of the laser-cooled $^9\text{Be}^+$ ions is determined from the Gaussian broadening of the Voigt line profile. The fit results in a Gaussian broadening of 9.3(4) MHz in run 1 and 3.3(3) MHz in run 2, which, for $^9\text{Be}^+$ ions, corresponds to a temperature of 9(1) mK and 1.1(2) mK, respectively. The evaluated temperature in run 1 is significantly larger than the Doppler limit of 0.5 mK, while in run 2 the evaluated temperature is close to the Doppler limit. In both cases the ions are heated due to the coupling to the RLC circuit which acts as a thermal bath at a temperature of 4 K. But in run 1 an additional radio-frequency (RF) drive was used for mode coupling, leading to broadening similar to micromotion-induced broadening in RF traps [125]. The temperature estimate above is derived assuming that thermal Doppler broadening is the only broadening effect. Therefore, in case there are other broadening effects present, the estimated temperature constitutes an upper limit for the ion temperature. Consequently, this result demonstrates our ability to cool $^9\text{Be}^+$ ions to the low temperatures necessary for sympathetic cooling of protons for ultra-high precision g-factor measurements.

As an additional consistency check, the beam radius at the position of the ions was measured to $w = 268(2)\,\mu\text{m}$. This allows to relate the total power P in our Gaussian beam to the intensity at the center I as

$$P = \frac{\pi}{2} w^2 I. \qquad (6.6)$$

Setting I to the saturation intensity for $^9\text{Be}^+$ of $I_0 = 840(40)\,\text{W m}^{-2}$ and taking into account anisotropic absorbtion for $\sigma^\pm$-transitions, we calculate the saturation power to $P_0 = 63(3)\,\mu\text{W}$. In the experiment, we observe saturation at $P = 212(10)\,\mu\text{W}$ in run 1 and $P = 326(2)\,\mu\text{W}$ in run 2, which is a factor of 3.4(2) and 5.2(3) higher than the estimate. This deviation is consistent with the ions being positioned off-center where the intensity is lower and higher power is necessary to achieve saturation. Positioning the ions off-center is necessary because then there is an intensity gradient across the ion cloud which is necessary for cooling the radial modes [34]. Part of the deviation could also be explained by absorption in the windows of the vacuum chamber, by polarization impurities of the laser light, and by finite ellipticity of the laser beam.

6.4 Conclusions

In this chapter, we presented a SiPM-based fluorescence detection system for use in our next-generation proton g-factor measurement setup, provided a detailed characterization of the SiPM properties at room temperature and at 4 K, and demonstrated its applicability for the detection of fluorescence photons from laser-cooled $^9\text{Be}^+$ ions stored in our cryogenic Penning-trap system.

Fluorescence detection provides direct information about the cooling rate during Doppler cooling and the final temperature of the laser-cooled ions. This information is not accessible with the regularly used image current detection systems, especially for large cooling rates where the $^9\text{Be}^+$ ions decouple from the RLC circuit.

The presented SiPM setup provides a compact cryogenic fluorescence detection system, that eliminates the need for optical detection pathways into the hermetically-sealed cryogenic trap chamber. This is a considerable advantage as this reduces the radiative heat load on the liquid helium stage and allows for a compact trap design. A further appreciable advantage of our approach is the use of a low-cost and readily-available commercial SiPM sensor, avoiding production of custom micro-fabricated devices.

Characterizing the SiPM, we found that it can be operated reliably at $4\,\text{K}$, and observed detection efficiencies up to $0.75(16)\,\%$ in the magnetic field of $1.9\,\text{T}$ and $2.5(1)\,\%$ without magnetic field in the cryocooler. Dark count rates were below $1\,\text{s}^{-1}$ in both cases. The pulse shape is modified due to a reduced microcell capacitance and increased quench resistance at $4\,\text{K}$ which manifests in a reduced charge of the SiPM pulses while the pulse height is unchanged. Further, the breakdown voltage is reduced by $3.5\,\text{V}$ and the crosstalk probability is a factor of two to three smaller than at room temperature.

Axial temperatures of the laser-cooled $^9\text{Be}^+$ ion cloud as low as $1.1(2)\,\text{mK}$ have been observed with our trap-integrated fluorescence detection system. Using such a laser-cooled $^9\text{Be}^+$ ion cloud as cooling medium for the proton axial mode, e.g. by energy exchange via a common-endcap electrode or shared RLC circuit [126], can potentially reduce the proton axial temperature by a factor of up to 4000, compared to state-of-the-art experiments [15, 14, 13].

Regarding ion sensitivity, our fluorescence detection system provides a total detection efficiency of $4.2(3) \times 10^{-6}$, corresponding to a photon count rate of $\frac{P/P_0}{1+P/P_0} \times 256(24)\,\text{s}^{-1}$ per ion. This allows to unambiguously detect ion clouds with more than 10 ions with averaging times above $0.8\,\text{s}$. The ion sensitivity is predominantly limited by stray light. Therefore, additional straylight suppression measures, e.g. focusing the fluorescence light through a narrow aperture onto the SiPM, can greatly improve the signal-to-background ratio and ion sensitivity. If a reduction by a factor 100 can be achieved the system can be used to resolve fluorescence from a single $^9\text{Be}^+$ ion within an averaging time shorter than $1\,\text{s}$.

Cooling of charged particles below the liquid helium temperature is becoming essential in various precision physics applications, e.g. for precision measurements on $^3\text{He}^{2+}$ [107], highly-charged ions [75], and protons and antiprotons [15, 14, 13]. In particular, high-precision measurements of proton and antiproton g-factors require ultra-low temperatures for high-fidelity readout of the spin state [22], and would immensely profit from the low temperatures reached with laser-cooled $^9\text{Be}^+$ ions.

Fluorescence-based detection using compact cryogenic SiPM detectors with the presented performance, will facilitate sympathetic cooling by laser-cooled ions [127, 126], which will allow to cool single ions to temperatures in the mK regime in future multi-Penning trap experiments.

Further interesting applications for such a SiPM based detection system are fast non-destructive measurements of the motional frequencies of the trapped ion based on the detection of a reduced photon scattering rate due to the Doppler shift induced by a resonant excitation of the trapped ion motion [128, 129]. Also, a two-ion crystal, in our case composed of a proton and a $^9Be^+$ ion, would compose an interesting system for measurements of the motional frequencies or charge-to-mass ratios [130, 131].

Ultimately, using advanced laser-cooling techniques to bring a $^9Be^+$ ion into the motional ground state, e.g. by Raman sideband cooling [30] or EIT cooling [25], the presented SiPM-based detection system can be used to perform state readout for quantum-logic detection of the Larmor frequency and motional frequencies, either for co-trapped ions or coupled ions stored in separate traps [30, 126, 115].

Chapter 7

Laser Cooling of $^9\text{Be}^+$ Ions

Some aspects of laser cooling have been mentioned in the previous chapter already. Here we provide some more details on laser cooling in the Penning trap, on the level structure of the $^9\text{Be}^+$ ion, and on the used cooling-laser setup.

7.1   Laser Cooling in Phase Space

Laser cooling of stored ions in Penning traps is discussed in detail e.g. in [34, 132]. A simple picture of laser cooling is provided if the axial oscillation is viewed in phase space. We look at the axial mode, cooled by a laser with frequency ν_L and wave vector $\vec{k} = k_z \hat{e}_z$. In absence of the cooling laser, the ion moves on ellipses in phase space, as shown in figure 7.1.

If the cooling laser is on, there is a velocity-dependent absorption probability, see the shaded region in figure 7.1. The velocity dependence is due to the Doppler shift $\Delta\nu = 2\pi\vec{k} \cdot \vec{v} = 2\pi k_z v_z$. The detuning of the laser frequency from the atomic transition with center frequency ν_0 and FWHM linewidth γ is defined as $\delta_L = \nu_L - \nu_0$. For cooling, the detuning needs to be negative. Consequently, the absorption probability is maximum for negative velocities. Further, we assume that the absorption probability does not depend on the position of the ion.

Upon absorption of a photon from the cooling laser, the ion recoils and receives the momentum $\vec{p} = \hbar\vec{k}$. The resulting change in velocity is given by the recoil velocity $v_{rec} = \hbar k_z/m$ and directed parallel to $\vec{k}$. If v_z is negative, absorption of a photon moves the ion to a smaller ellipse in phase space, see figure 7.1. Upon spontaneous emission of a photon, the ion receives a recoil again. This time, the direction of the recoil is random, leading to a random walk in phase space. Crucially, the change of velocity due to emission of photons averages to zero.

Subsequently, over many of these absorption and emission events, the ion will be cooled to the region near the origin. The final temperature is determined by the balance of cooling through absorption and heating through emission of photons. The ion is cooled as long as the absorption probability in the negative velocity region
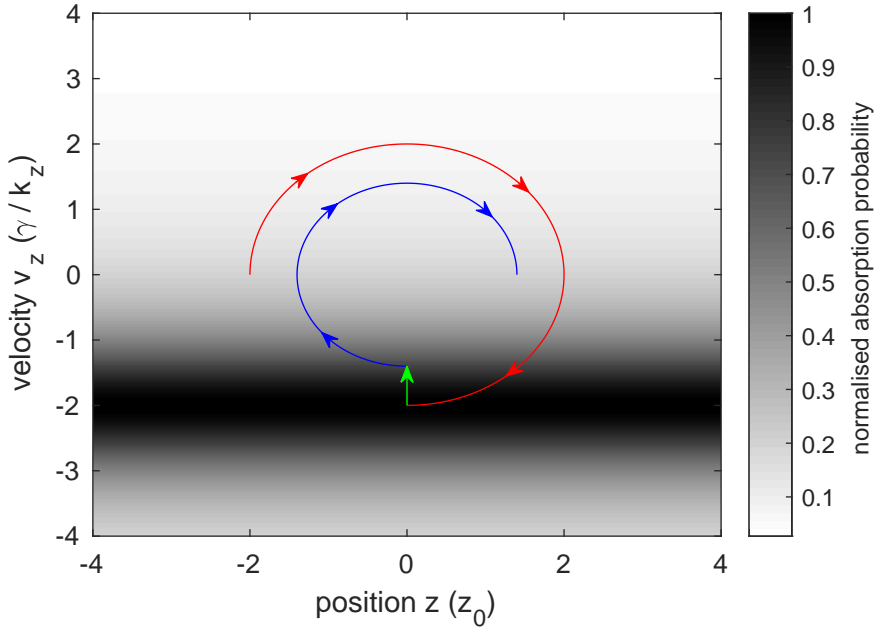
Figure 7.1: Laser cooling in phase space: absorption probability and ion trajectory. The relative absorption probability for $\delta_L = -2\gamma$ is shown as a function of position z and velocity v_z of the ion. $z_0 = \gamma/\omega_z k_z$. The trajectory of an ion before (red) and after (blue) an absorption event is plotted. The velocity change due to recoil is shown in green (not to scale).

is larger than in the positive velocity region. The lowest temperature, the Doppler temperature $T_D = h\gamma/2k_B$, is reached for a detuning of $\delta_L = -\gamma/2$.

Here, we treated the $^9\mathrm{Be}^+$ ion as simple two level system. In general, this is not a good approximation due to its more complicated level structure. In the following, we will discuss the full energy level structure and how optical pumping leads to a situation where the two level system is a good approximation.

7.2 $^9\mathrm{Be}^+$ Level Structure

The choice of the laser-cooling ion for our experiment is constrained by two requirements: First, the laser-cooling ion should have a similar q/m ratio and a similar q^2/m ratio compared to the proton in order to facilitate energy exchange between the motional modes of both ions. Second, suitable lasers must be available at the wavelength of the laser-cooling transition.

The ideal electron configuration for laser cooling of light atoms or ions features the valence electron in an s-orbital. Then, the ground state is an s-state and the transition from the s-state to the next-higher-energy p-state is dipole allowed, easily driven with low laser power, and the electron decays back to the s-state on a timescale of a few nanoseconds. For light atoms or ions the s-to-p transition is a closed cycling transition. For heavier atoms or ions there is a d-state between the s-state and the higher energy p-state and repumping from the d-state to the p-state

is necessary [133].

The discussed electron configuration is realized in group I (alkali metal) atoms and group II (alkaline earth metal) singly-charged ions, most of which are used in laser-cooling experiments. An ideal candidate for our experiment would be ^{4}He$^+$ with $q/m = 1/4$. However, the wavelength of the cooling transition would be in the extreme ultraviolet (EUV) at 30.4 nm. The next best candidate is the lightest alkaline earth metal ion ^{9}Be$^+$ with $q/m = 1/9$ and a wavelength of the cooling transition of 313.2 nm. Commercial tuneable lasers with sufficient output power are available in this wavelength range. Consequently, ^{9}Be$^+$ is chosen as laser-cooling ion, being the best compromise between both requirements.

The lowest energy levels of the three-electron system ^{9}Be$^+$ are the $1s^2\,2s\,2^2S_{1/2}$ ground state, followed by the $1s^2\,2p\,2^2P_{1/2}$, $1s^2\,2p\,2^2P_{3/2}$, and $1s^2\,3s\,3^2S_{1/2}$ states. The zero-field transition frequencies from the ground state to the states $2^2P_{1/2}$, $2^2P_{3/2}$, and $3^2S_{1/2}$ are 957.2 THz, 957.4 THz, and 2645.1 THz. The lifetime τ of the 2^2P excited state is 8.1(4) ns leading to a natural linewidth of $\gamma = \frac{\Gamma}{2\pi} = \frac{1}{\tau}\frac{1}{2\pi} = 19.6(10)$ MHz [124]. In the strong magnetic field of the Penning trap the Zeeman effect has significant influence on the energy levels and will be discussed in the following.

The zero-field fine-structure splitting between the $2^2P_{1/2}$ state and the $2^2P_{3/2}$ state is 197.063 47(53) GHz [134]. In a magnetic field $\vec{B}$ the fine-structure splitting of the 2^2P state is described by the Hamiltonian

$$H_{FS} = A_{FS}\vec{L}\cdot\vec{S}/\hbar^2 - \vec{\mu}_L\cdot\vec{B} - \vec{\mu}_S\cdot\vec{B} \tag{7.1}$$

where $A_{FS} = 2/3\cdot197$ GHz is the fine-structure interaction constant, $\vec{\mu}_S = g_S\mu_B\vec{S}/\hbar$ is the magnetic moment from the electron spin $\vec{S}$, and $\vec{\mu_L} = g_L\mu_B\vec{L}/\hbar$ is the magnetic moment from the orbital angular momentum $\vec{L}$. In this notation $g_L = -1$ and $g_S \approx -2$. The first term describes the spin-orbit coupling and the second and third terms describe the Zeeman effect of $\vec{L}$ and $\vec{S}$, respectively. The electron spin $\vec{S}$ and orbital angular momentum $\vec{L}$ are coupled into the total angular momentum $\vec{J} = \vec{L} + \vec{S}$ at low magnetic fields and will decouple at high magnetic fields when $\mu_B B \gtrsim A_{FS}$. This decoupling is called the Paschen-Back effect and for the 2^2P state in ^{9}Be$^+$ it becomes relevant at magnetic fields comparable to the characteristic field $B_c = A_{FS}/\mu_B \approx 9.4$ T. For lower magnetic fields the Hamiltonian can be approximated as

$$H_{FS}(J, m_J) = A_{FS}\frac{1}{2}\left(J(J+1) - L(L+1) - S(S+1)\right) - g_J\mu_B m_J B \tag{7.2}$$

where $\vec{\mu}_J\cdot\vec{B}$ is replaced by $\mu_{J,z}B = g_J\mu_B m_J B$ which is justified for low magnetic fields. $\vec{\mu}_J = \vec{\mu}_L + \vec{\mu}_S = g_J\mu_B\vec{J}/\hbar$ is the magnetic moment of the orbital angular momentum $\vec{J}$ and g_J is the Landé g-factor.
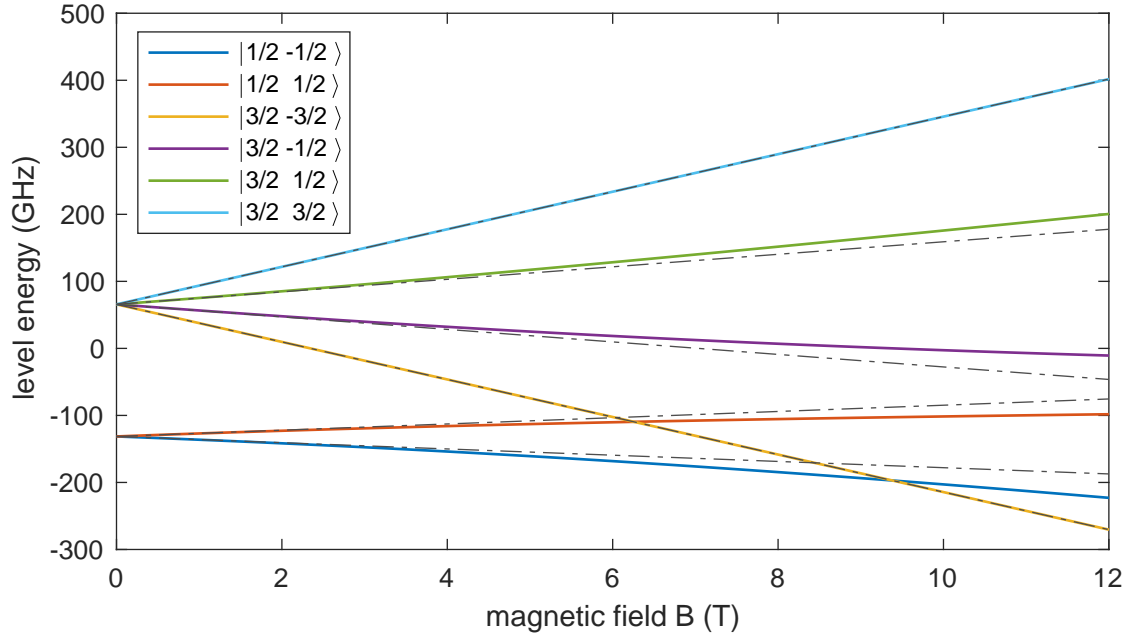
Figure 7.2: Energy levels of the 2^2P state of $^9\mathrm{Be}^+$ as a function of magnetic field. The dash-dotted lines are the level energies in the low-field approximation. The states are labeled as $|J, m_J\rangle$.

In our experiment laser-cooling is performed in a magnetic field of $1.9\,\mathrm{T}$ which is much lower than the above mentioned characteristic field. Therefore, J and m_J are good quantum numbers and the energy levels are well approximated by equation (7.2) to first order. However, for a precise determination of the energy levels and transition frequencies, the Paschen-Back effect must be taken into account. This is achieved by solving the eigenvalue problem with the Hamiltonian from equation (7.1) numerically. In figure 7.2 the true energy levels are compared to the energy levels of the approximate solution where $\vec{L}$ and $\vec{S}$ are coupled into $\vec{J}$. The deviation vanishes for magnetic fields much smaller than the characteristic field.

The hyperfine structure for each of the states $2^2S_{1/2}$, $2^2P_{1/2}$, and $2^2P_{3/2}$ in a magnetic field $\vec{B}$ is described by the Hamiltonian

$$H_{HFS} = A_{HFS}\vec{I} \cdot \vec{J}/\hbar^2 - \vec{\mu}_I \cdot \vec{B} - \vec{\mu}_J \cdot \vec{B} \tag{7.3}$$

where A_{HFS} is the hyperfine interaction constant for the respective state, $\vec{\mu}_I = g_I \mu_N \vec{I}/\hbar$ is the magnetic moment of the nuclear spin $\vec{I}$ with quantum number I, and μ_N is the nuclear magneton. For $^9\mathrm{Be}^+$ $I = 3/2$. The first term describes the coupling between nuclear spin $\vec{I}$ and total angular momentum $\vec{J}$ and the second and third terms describe the Zeeman effect of $\vec{I}$ and $\vec{J}$, respectively. Similar to above, $\vec{I}$ and $\vec{J}$ are coupled into the total angular momentum $\vec{F} = \vec{I} + \vec{J}$ at low magnetic fields and will decouple at high magnetic fields when $\mu_B B \gtrsim A_{HFS}$. This decoupling is called the hyperfine Paschen-Back effect and becomes relevant at a characteristic field $B_c = A_{HFS}/\mu_B$. The magnetic-dipole hyperfine constants A_{HFS}

Table 7.1: Hyperfine constants of ^{9}Be$^+$. The zero-field splitting for the $2^2S_{1/2}$ and the $2^2P_{1/2}$ states is $2A_{HFS}$.

state	A_{HFS} (MHz)	B_c (mT)	reference
$2^2S_{1/2}$	$-625.008\,837\,048(10)$ MHz	45	[128]
$2^2P_{1/2}$	$-118.00(4)$ MHz	8.5	[136]
$2^2P_{3/2}$	$-1.026(3)$ MHz	0.07	[135]

and characteristic field strength B_c for the states $2^2S_{1/2}$, $2^2P_{1/2}$, and $2^2P_{3/2}$ are listed in table 7.1. For the $2^2P_{3/2}$ state there is in addition to the magnetic-dipole contribution an electric-quadrupole contribution which shifts the energy of the states up to 3 MHz [135], but this contribution is neglected here.

The magnetic field of 1.9 T in our experiment is much higher than the characteristic field strength for all three states. Therefore, the nuclear spin $\vec{I}$ and total angular momentum $\vec{J}$ are decoupled and a high-field approximation of equation (7.3) is justified. In this high-field limit of the hyperfine Paschen-Back effect angular momenta $\vec{I}$ and $\vec{J}$ independently precess about the magnetic field axis and the Hamiltonian in equation (7.3) becomes

$$H_{HFS}(J, m_J, I, m_I) = A_{HFS}m_I m_J - g_I \mu_N m_I B - g_J \mu_B m_J B \qquad (7.4)$$

were $\vec{I} \cdot \vec{J}$ is replaced by $\vec{I} \cdot \vec{e}_z\ \vec{J} \cdot \vec{e}_z = \hbar^2 m_I m_J$, $\vec{\mu}_I \cdot \vec{B}$ is replaced by $\mu_{I,z}B = g_I \mu_N m_I B$, and $\vec{\mu}_J \cdot \vec{B}$ is replaced by $\mu_{J,z}B = g_J \mu_B m_J B$.

To calculate the exact energy levels and transition frequencies, both fine structure and hyperfine structure effects must be taken into account. The energy of the sublevels of the $2^2S_{1/2}$, $2^2P_{1/2}$ and $2^2P_{3/2}$ states is calculated according to

$$E = E_0 + \Delta E = E_0 + H_{HFS}(J, m_J, I, m_I) + H_{\Delta,FS}(J, m_J) \qquad (7.5)$$

where E_0 is the zero-field energy of the states $2^2P_{1/2}$ and $2^2P_{3/2}$ with respect to the ground state $2^2S_{1/2}$, and $H_{\Delta,FS}$ is the difference between the full solution from equation (7.1) and the approximation in equation (7.2), taking into account the Paschen-Back effect for the $2^2P_{1/2}$ and $2^2P_{3/2}$ levels. The advantage of this approach is that only the last term needs to be calculated numerically, while all other terms are calculated analytically, which allows for straightforward error propagation. In addition, the last term vanishes for stretched states (where m_J is maximal or minimal), so the energy of these states are calculated analytically.

The values used for evaluating equation (7.5) are listed in table 7.2. The most precise determination of the transition frequencies has been performed in [134]. The magnetic moment of the bare nucleus is affected by nuclear magnetic shielding. Shielding factors for ^{9}Be$^+$ have been calculated in [137]. Here, the experimental

Table 7.2: Constants of $^9\text{Be}^+$.

quantity	value	reference
$\nu_0(2^2S_{1/2} \to 2^2P_{1/2})$	$957\,199\,553.28(52)$ MHz	[134]
$\nu_0(2^2S_{1/2} \to 2^2P_{3/2})$	$957\,396\,616.6(15)$ MHz	[134]
$\mu_I(^9\text{Be}^+)$	$-1.177\,265(3)\mu_N$	[138]
$g_I(^9\text{Be}^+)$	$-0.784\,843(2)$	
$g_S(^9\text{Be}^+)$	$-2.002\,262\,06(42)$	[128]

value of the shielded nuclear magnetic moment from [138] is used. The bound-state g-factor of the electron in the ground state of $^9\text{Be}^+$ has been calculated in [139]. The value is consistent with the measured value from [128], which is used here. The g-factor of the excited states is given by the Landé g-factor

$$g_J = g_L \frac{J(J+1) + L(L+1) - S(S+1)}{2J(J+1)} + g_S \frac{J(J+1) - L(L+1) + S(S+1)}{2J(J+1)}$$

(7.6)

where g_S is the bound-state g-factor of the electron and $g_L = -1$.

The resulting energy-level diagram for $^9\text{Be}^+$ in a magnetic field of $1.9\,\text{T}$ is shown in figure 7.3. The biggest contributions to the uncertainty in the calculated energy levels stem from the zero-field transition frequencies of the $2^2S_{1/2} \to 2^2P_{1/2}$ and $2^2S_{1/2} \to 2^2P_{3/2}$ transitions with an uncertainty on the order of $1\,\text{MHz}$ and from neglecting the electric quadrupole contribution to the hyperfine interaction in the $2^2P_{3/2}$ state which is up to $3\,\text{MHz}$. Each level in figure 7.3 consists of four hyperfine sub-levels. For the $2^2S_{1/2}(m_J = 1/2)$ and $2^2P_{1/2}(m_J = 1/2)$ levels the ordering of hyperfine sub-levels is $m_I = -3/2, -1/2, +1/2, +3/2$ from high to low energy. For all other levels the ordering is $m_I = +3/2, +1/2, -1/2, -3/2$ from high to low energy.

Note that in case the levels with higher m_I start at lower energy, the energy levels cross at a certain magnetic field given by $\mu_N B \approx A_{HFS}$. This is relevant in the case of the $2^2P_{3/2}(m_J = 3/2)$ state for example. To show this effect, the deviation of the energy of the hyperfine sub-levels in the $2^2P_{3/2}(m_J = 3/2)$ state from the mean energy of all hyperfine sub-levels in the $2^2P_{3/2}(m_J = 3/2)$ state is plotted in figure 7.4. Level crossings occur at a magnetic field of $257\,\text{mT}$.

Laser cooling requires a closed cycling transition, such that, after excitation, the ion decays back to the initial state by spontaneous emission with 100% probability. For the $^9\text{Be}^+$ ion there are two possibilities to realize such a closed cycling transition: exciting the ion on the $2^2S_{1/2}(m_I = 3/2, m_J = 1/2) \to 2^2P_{3/2}(m_I = 3/2, m_J = 3/2)$ transition driven by σ^+ polarized light, or exciting the ion on the $2^2S_{1/2}(m_I = -3/2, m_J = -1/2) \to 2^2P_{3/2}(m_I = -3/2, m_J = -3/2)$ transition driven by σ^- polarized light. In addition to being closed, both transitions feature
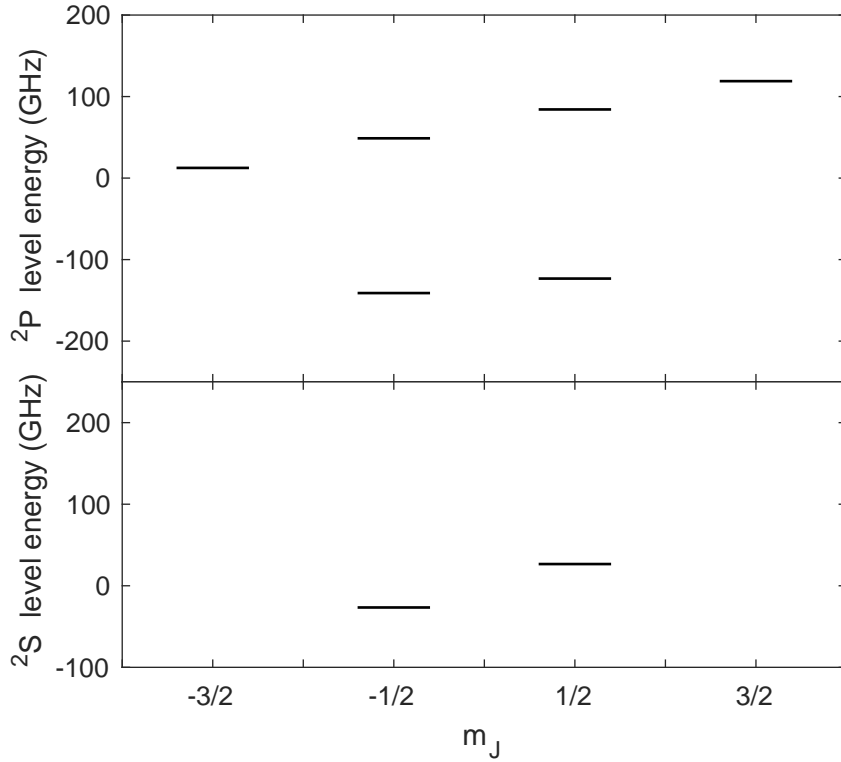
Figure 7.3: Energy-level diagram of $^9\mathrm{Be}^+$ in a magnetic field of 1.9 T. Levels of the 2^2P excited state (top) and $2^2S_{1/2}$ ground state (bottom) are shown. The level energies are given with respect to the center of the $2^2S_{1/2}$ and 2^2P manifolds, respectively. Each level is composed of four hyperfine sub-levels which are not resolved on this scale.
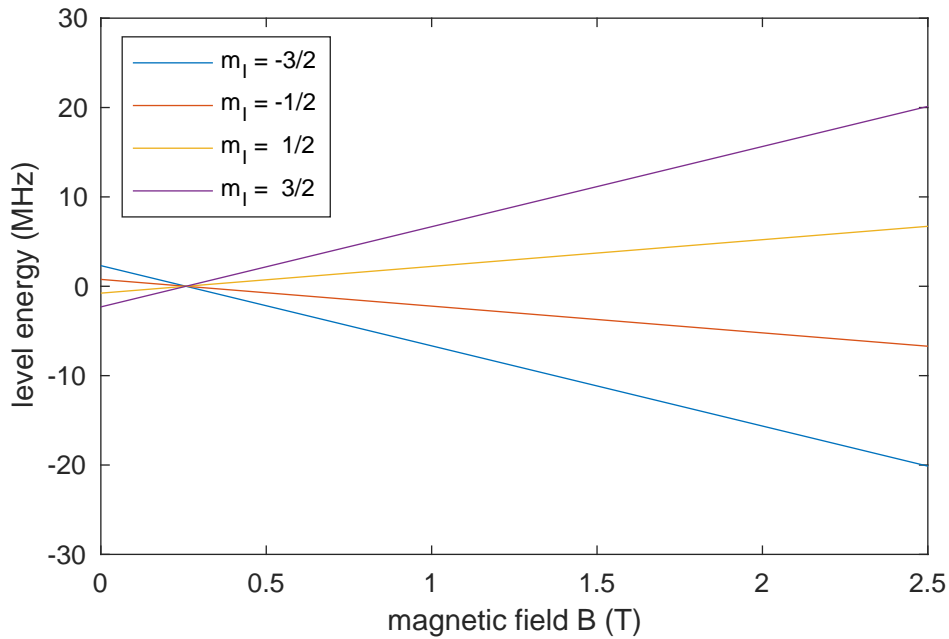

Figure 7.4: Hyperfine contribution to energy-levels in the $2^2P_{3/2}(m_I, m_J = 3/2)$ state of $^9\mathrm{Be}^+$ as a function of magnetic field.

an intrinsic repumping mechanism when driven with appropriately polarized light. Due to this mechanism, the population in the ground state is optically pumped into the $2^2S_{1/2}(m_I = 3/2, m_J = 1/2)$ sub-level in case of the σ^+ transition and optically pumped into the $2^2S_{1/2}(m_I = -3/2, m_J = -1/2)$ sub-level in case of the σ^- transition.

In the coordinate system defined by the quantization axis of the ion, the polarization of the cooling-laser light can be decomposed into three components: σ^+, σ^-, and π. Each component only drives transitions where $\Delta L = +1$, -1, or 0, respectively. A plot of the transition probability for all allowed transitions from the $2^2S_{1/2}$ ground state to the 2^2P excited state in $^9\mathrm{Be}^+$ is shown in figure 7.5. The transitions driven by σ^+, σ^-, and π polarized light are plotted in blue, red, and black, respectively. The lineshape is given by a Lorentzian

$$P(\nu) = \frac{\gamma^2/4}{(\nu - \nu_0)^2 + \gamma^2/4} \tag{7.7}$$

with full width half maximum γ where the natural linewidth $\gamma = 19.6(10)\,\mathrm{MHz}$ is power broadened to $\gamma = 50\,\mathrm{MHz}$. Power broadening of this size is typical for the cooling-laser light intensities used in the experiment. Thermal Doppler broadening is neglected here.

Laser cooling on the $2^2S_{1/2}(m_J = 1/2) \rightarrow 2^2P_{3/2}(m_J = 3/2)$ transition requires the ion to be initially in the $2^2S_{1/2}(m_J = 1/2)$ ground state. After excitation to the $2^2P_{3/2}(m_J = 3/2)$ excited state the ion will only decay back to the $2^2S_{1/2}(m_J = 1/2)$ ground state, due to selection rules. The cycle is closed and photons are scattered continuously. Therefore, the involved ground state is called the bright ground state. The population initially in the $2^2S_{1/2}(m_J = -1/2)$ ground state does not participate in the cooling cycle and, therefore, the state is called the dark ground state. The degree to which the electron spin is optically pumped into the bright ground state depends on the polarization of the cooling-laser light:

σ^+ polarized light drives the cooling transition on resonance and in addition drives the $2^2S_{1/2}(m_J = -1/2) \rightarrow 2^2P_{3/2}(m_J = 1/2)$ transition offresonantly. The $2^2P_{3/2}(m_J = 1/2)$ excited state decays back to the $2^2S_{1/2}(m_J = 1/2)$ ground state with a probability of 2/3, populating the bright ground state. Therefore, this offresonant transition constitutes an intrinsic repumping mechanism which transfers population from the dark ground state into the bright ground state.

π polarized light drives both a repuming and a depopulation transition. The offresonantly driven $2^2S_{1/2}(m_J = -1/2) \rightarrow 2^2P_{3/2}(m_J = -1/2)$ transition followed by a decay from the $2^2P_{3/2}(m_J = -1/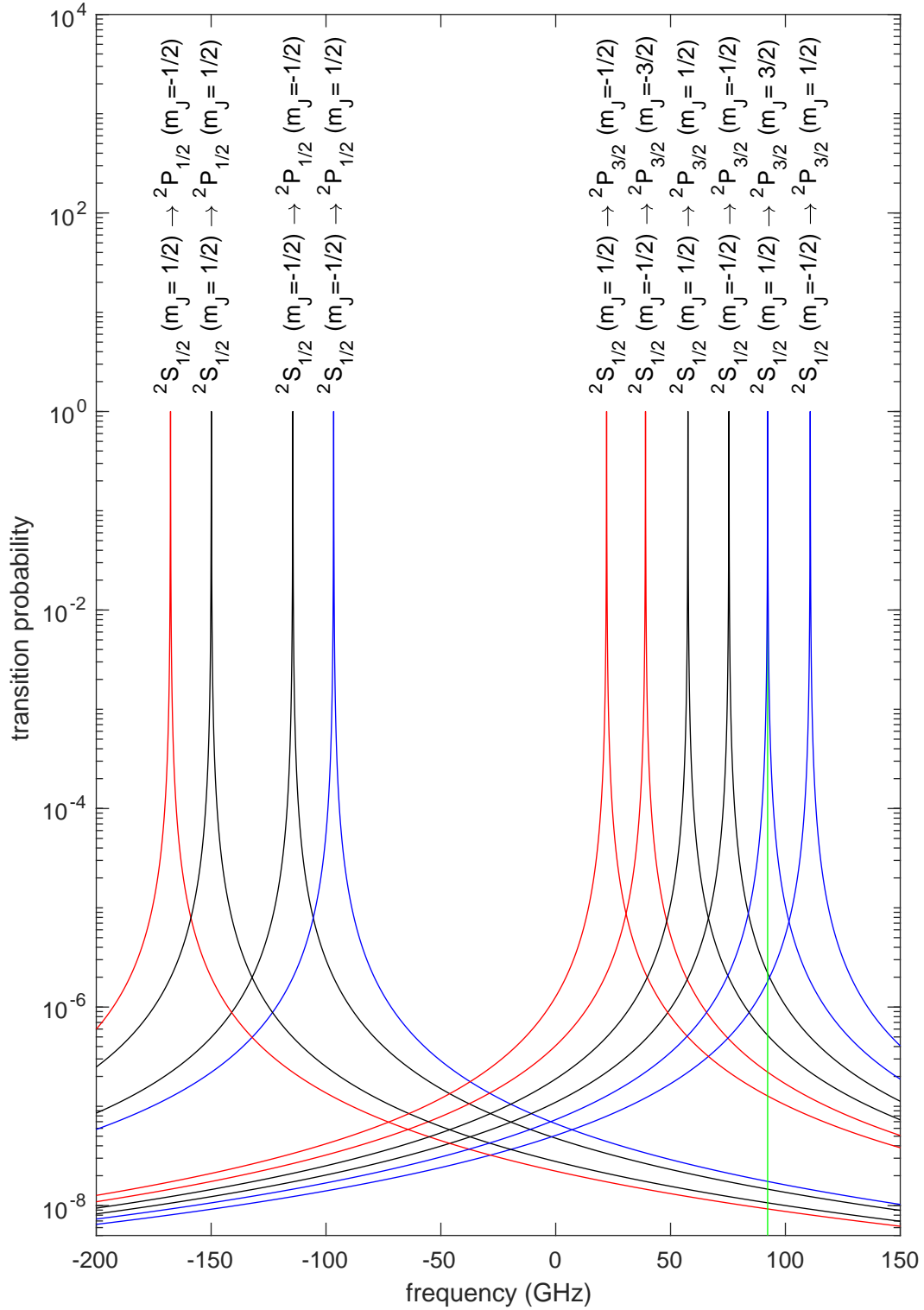2)$ excited state to the $2^2S_{1/2}(m_J = 1/2)$ ground state with a probability of 1/3 populates the bright ground state. The offresonantly driven $2^2S_{1/2}(m_J = 1/2) \rightarrow 2^2P_{3/2}(m_J = 1/2)$ transition followed by a decay from the $2^2P_{3/2}(m_J = 1/2)$ excited state to the $2^2S_{1/2}(m_J = -1/2)$ ground

Figure 7.5: Excitation probability for transitions from the $2^2S_{1/2}$ ground state to the 2^2P excited state in $^9Be^+$ as a function of frequency offset from the transition frequency between the $2^2S_{1/2}$ and 2^2P centers. For a magnetic field of 1.9 T. Transitions driven by σ^+, σ^-, and π polarized light are plotted in blue, red, and black, respectively. The linewidth is power broadened to 50 MHz. The optimal cooling laser frequency for cooling on the $2^2S_{1/2}(m_J = 1/2) \rightarrow 2^2P_{3/2}(m_J = 3/2)$ transition is marked in green.

state with a probability of $1/3$ depopulates the bright ground state.

σ^- polarized light cycles the population in the dark ground state since it drives the $2^2S_{1/2}(m_J = -1/2) \rightarrow 2^2P_{3/2}(m_J = -3/2)$ transition offresonantly. In addition, σ^- polarized light drives the $2^2S_{1/2}(m_J = 1/2) \rightarrow 2^2P_{3/2}(m_J = -1/2)$ transition offresonantly. The $2^2P_{3/2}(m_J = -1/2)$ excited state decays back to the $2^2S_{1/2}(m_J = -1/2)$ ground state with a probability of $2/3$, depopulating the bright ground state.

Consequently, the population in the bright and dark ground state is the result of a balance of competing repumping and depopulation processes. The transition rates as function of laser frequency can be read from figure 7.5. The timescale of the repumping process is about 10^{-6} times the timescale defined by the inverse scattering rate when the laser is tuned to the optimal frequency for laser cooling. The timescale of the depopulation process depends on the π and σ^- polarization components of the cooling-laser beam. For pure σ^+ polarized light there is no depopulation process and the population in in the bright ground state is 100 %. In the experiment the laser might have a σ^- polarized component up to a few % and a π polarized component of $\leq 1\%$. Therefore, the depopulation process is at least 100 times slower than the repumping process and the population in the bright ground state is $> 99\%$.

Optical pumping of the nuclear spin into the $m_I = 3/2$ state occurs due to hyperfine coupling within the excited state [122, 123]. The sub-levels in the $2^2P_{3/2}(m_J = 3/2)$ state which are labeled here as (m_I, m_J) actually have some small components with larger m_I except for the $2^2P_{3/2}(m_I = 3/2, m_J = 3/2)$ state which is pure. The sub-levels can be written as

$$(m_I = 3/2, m_J = 3/2) = |3/2, 3/2\rangle \tag{7.8}$$

$$(m_I = 1/2, m_J = 3/2) = \sqrt{1 - |\alpha|^2} \, |1/2, 3/2\rangle \tag{7.9}$$
$$+ \alpha \, |3/2, 1/2\rangle$$

$$(m_I = -1/2, m_J = 3/2) = \sqrt{1 - |\alpha|^2 - |\beta|^2} \, |-1/2, 3/2\rangle \tag{7.10}$$
$$+ \alpha \, |1/2, 1/2\rangle$$
$$+ \beta \, |3/2, -1/2\rangle$$

$$(m_I = -3/2, m_J = 3/2) = \sqrt{1 - |\alpha|^2 - |\beta|^2 - |\gamma|^2} \, |-3/2, 3/2\rangle \tag{7.11}$$
$$+ \alpha \, |-1/2, 1/2\rangle$$
$$+ \beta \, |1/2, -1/2\rangle$$
$$+ \gamma \, |3/2, -3/2\rangle$$

where the eigenstates of the uncoupled basis are labeled $|m_I, m_J\rangle$ and the coefficients α, β, and γ are small in the sense that $|\alpha|, |\beta|, |\gamma| \ll 1$. Due to this hyperfine coupling the excited states with $m_I < 3/2$ have small probabilities to decay to a ground state with larger m_I. This process continues until all population is trapped in the $m_I = 3/2$ state. The timescale of this process is defined by the size of the mixing and by the timescale of the repumping process for the $m_J = -1/2$ state. The hyperfine coupling in the ground state is much larger than in the excited state, but is not relevant for this process.

An analogous discussion of the optical pumping of the electron and nuclear spin is valid for the $2^2S_{1/2}(m_I = -3/2, m_J = -1/2) \rightarrow 2^2P_{3/2}(m_I = -3/2, m_J = -3/2)$ cooling transition where the population is pumped into the $2^2S_{1/2}(m_I = -3/2, m_J = -1/2)$ ground state.

The magnetic field dependence of the transition frequency is linear for both cooling transitions. This is due to the fact that for stretched states the correction due to fine structure interaction vanishes, as discussed above. The transition frequency becomes

$$\nu(B) = \nu_0 + a \pm bB \text{ with} \tag{7.12}$$

$$a = \frac{9}{4}A_{HFS}(2^2P_{3/2}) - \frac{3}{4}A_{HFS}(2^2S_{1/2}) \text{ and} \tag{7.13}$$

$$b = -\frac{3}{2}g_J(2^2P_{3/2})\mu_B + \frac{1}{2}g_J(2^2S_{1/2})\mu_B = 1\mu_B. \tag{7.14}$$

The upper sign is for the $2^2S_{1/2}(m_I = 3/2, m_J = 1/2) \rightarrow 2^2P_{3/2}(m_I = 3/2, m_J = 3/2)$ transition and the lower sign for the $2^2S_{1/2}(m_I = -3/2, m_J = -1/2) \rightarrow 2^2P_{3/2}(m_I = -3/2, m_J = -3/2)$ transition. The constants $a = 466.448(7)\,\text{MHz}$ and $b = 13\,996.244\,936(4)\,\text{MHz}\,\text{T}^{-1}$. Determination of the magnetic field B from the measured transition frequency will be limited by the uncertainties of ν_0 and $\nu(B)$, allowing magnetic field estimates with up to $0.1\,\text{mT}$ precision. Note that the magnetic field dependence of both transitions is equal in magnitude but has opposite sign. This might be relevant for the choice of the laser-cooling transition when laser-cooling experiments are performed in magnetic bottles. Effects similar to those in Zeeman slowers might be observed.

The hyperfine structure of the $2^2S_{1/2}(m_I = 3/2, m_J = 1/2) \rightarrow 2^2P_{3/2}(m_I = 3/2, m_J = 3/2)$ cooling transition is shown in figure 7.6. The hyperfine splitting in the ground state is resolved while the hyperfine splitting in the excited state is smaller than the linewidth of the transition. The ideal frequency for laser cooling is shown in green. Note that for the population which has not been pumped to the $m_I = 3/2$ state the cooling-laser frequency is blue detuned which will lead to heating. This problem arises for example in a newly loaded ion cloud where all hyperfine levels are approximately equally populated. It is therefore advisable to pre-cool the ion cloud using a cooling-laser frequency which is red detuned by at
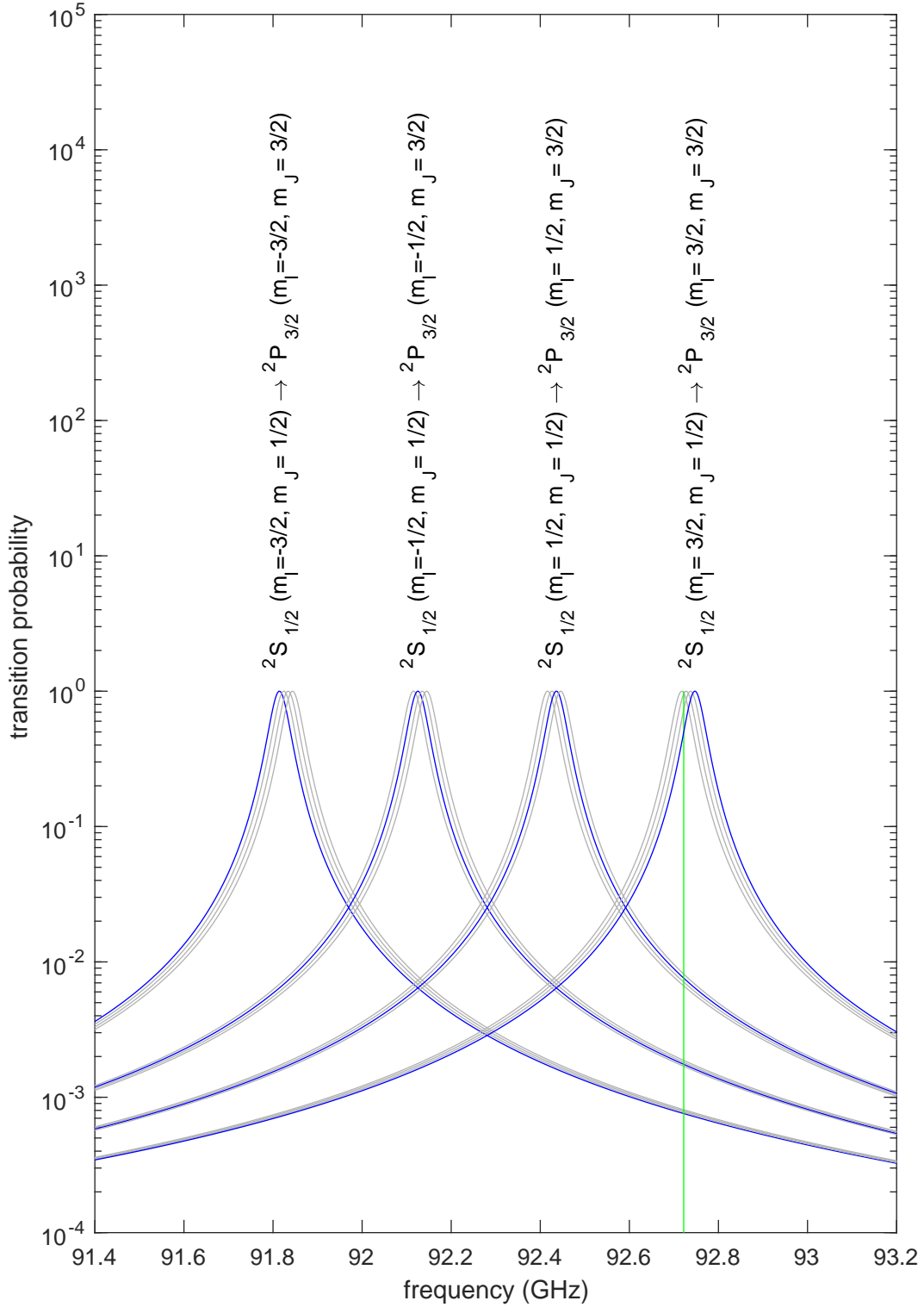
Figure 7.6: Excitation probability for the $2^2S_{1/2}(m_J = 1/2) \to 2^2P_{3/2}(m_J = 3/2)$ transitions as a function of frequency offset from the transition frequency between the $2^2S_{1/2}$ and 2^2P centers. For a magnetic field of $1.9\,\mathrm{T}$. Transitions driven by σ^+ polarized light are plotted in blue. Forbidden transitions are plotted in grey. The linewidth is power broadened to $50\,\mathrm{MHz}$. The optimal cooling laser frequency for cooling on the $2^2S_{1/2}(m_I = 3/2, m_J = 1/2) \to 2^2P_{3/2}(m_I = 3/2, m_J = 3/2)$ transition is marked in green.

least $1\,\mathrm{GHz}$ in order to pump the nuclear spin of a newly loaded ion cloud to the $m_I = 3/2$ state.

For the $2^2S_{1/2}(m_I = -3/2, m_J = -1/2) \to 2^2P_{3/2}(m_I = -3/2, m_J = -3/2)$ cooling transition the discussion is analogous.

Once the population is trapped in the closed cycling transition, a simplified theoretical treatment as two-level system is possible. Imperfect polarization of the cooling laser may lead to a leakage of population into dark states. If the polarization is not properly controlled, this may impact the cooling performance, in particular for small ion clouds or single ions.

7.3 Laser Heating of $^9\mathrm{Be}^+$ Ions

Besides laser-cooling, the $^9\mathrm{Be}^+$ ions can also be laser-heated. This technique is very useful for setting up the experiment, as the signal for heating is easier interpreted as the one for strong cooling, which is identical to the signal of particle loss, see also chapter 8. To utilize laser-heating, we shine low-intensity blue-detuned ($\delta_L \geq 0$) laser light onto the stored ions. Since the wave vector points in axial direction, the axial component of the motion of the stored ion is excited.

We detect the axial motion by tuning the axial frequency to resonance with the image-current detector. Further, we use a sideband drive at $\omega_{RF} = \omega_z + \omega_-$ to couple the magnetron motion to the axial motion, in order to cool the radial modes. As a result, the maxima of the two coupled modes are visible in the spectra in figure 7.7.

When the cooling-laser light is blue detuned, the axial component of the motion is excited, and the FFT spectrum shows peaks instead of dips. This is due to the excited motion being damped by the image-current detector, transferring energy to the detector. The frequency shift of both peaks relative to the dips is caused by electric field anharmonicities, as given in equation (2.20), which lead to amplitude dependent frequency shifts. In fact, these spectra were one of the first signals of laser-ion interaction we recorded in our apparatus.

7.4 Off-Resonant RF Excitation of Laser-Cooled $^9\mathrm{Be}^+$ Ions

An undesired heating effect on the ions during laser cooling can result from the simultaneous application of RF drives. The RF drives we used were intended for coupling the radial modes to the laser-cooled axial mode, thereby also cooling the radial modes. However, the driving field lead to an RF amplitude-dependent distortion of the line-shape of the cooling transition. This is observed in the fluorescence spectrum of the trapped $^9\mathrm{Be}^+$ ions, as shown in figure 7.8.
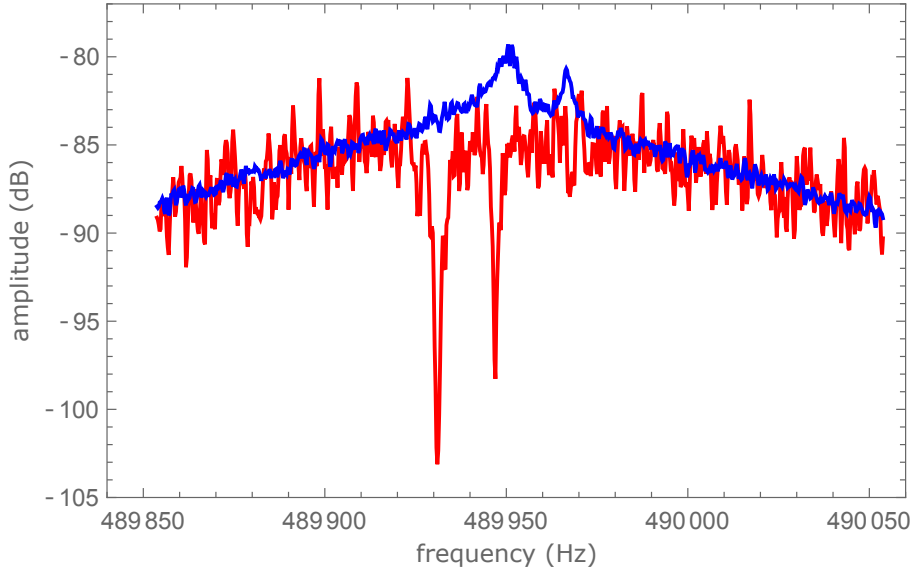
Figure 7.7: Laser heating of $^9\text{Be}^+$ ions. The axial frequency of a $^9\text{Be}^+$ ion cloud is tuned to resonance with the RLC resonator and a sideband drive at $\omega_{RF} = \omega_z + \omega_-$ is applied, coupling the magnetron to the axial mode. As a result two dips are visible in the FFT spectrum (red curve). When, in addition, blue-detuned $313\,\text{nm}$ laser light is applied, two peaks appear instead of the two dips (blue curve). Data obtained commonly with [33].

The observed lineshape results from the motion of the ion in the oscillating field of the applied RF drive. Consider the axial dipole component of the RF field which is superimposed onto the static trap field: The linear potential superimposed onto the static harmonic potential modifies the position of the trap minimum. Since the RF field oscillates at ν_{RF}, the position of the trap minimum also oscillates with frequency ν_{RF} and an amplitude which depends on the amplitude of the drive. The stored ion follows the motion of the trap minimum and the resulting Doppler shift leads to the observed lineshapes. Note that the lineshape is the same whether the RF drive is resonant or not.

These lineshapes have been discussed before in context of RF induced micromotion in Paul traps [125]. As an important consequence, due to the negative gradient for some negative detunings, local heating occurs. This can lead to significant deviations of the final temperature from the Doppler temperature. Especially for the strong drives that are needed to cool larger $^9\text{Be}^+$ ion clouds, this can become a problem.

This effect should in principle also occur when the RF field originates from an RLC oscillator at frequencies far off-resonant from the axial frequency of the stored ion. But its magnitude is small.

103
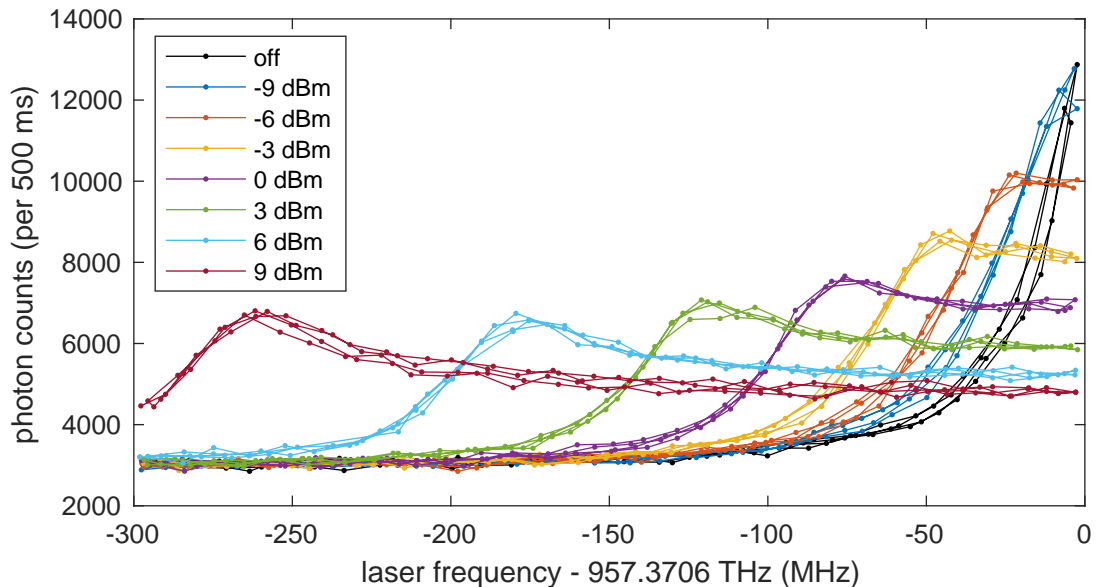
Figure 7.8: Lineshape of the $^9\text{Be}^+$ resonance as function of the RF drive amplitude. For each RF drive amplitude setting, four scans are shown: two where the laser frequency is ramped upwards, and two where the laser frequency is ramped downwards. This shows the excellent reproducibility of the data. The background of approximately 3000 counts is due to stray light.

7.5 Cooling the Radial Modes

A considerable complication of the simple scheme discussed in section 7.1 is the cooling of the radial modes in a Penning trap. This is due to the fact that the magnetron and cyclotron modes are both circular motions. In addition, the energy of the magnetron mode is negative, such that reducing the energy increases the magnetron radius. The physics of cooling the radial modes is discussed in [34]. Essentially, in order to cool the radial modes, there needs to be a radial component of the cooling laser that additionally features an intensity gradient, such that absorption is more likely when the ions radial velocity is parallel to the wave vector of the cooling laser.

To realize this configuration in the experiment, we make sure that the wave vector of the cooling laser has a small radial component. This is achieved by irradiating the beam at an angle, typically 1°, relative to the magnetic field axis. Further, we offset the cooling laser beam from the trap center such that there is an intensity gradient in the trap center. In practice, we perform a two-dimensional scan of the laser pointing and record the fluorescence of the stored $^9\text{Be}^+$ ions. We typically observe fluorescence in one half of the parameter space, and heating in the other, which we attribute to the regions where the ion velocity is in parallel with the wave vector and anti-parallel to the wave vector, respectively. For further experiments we typically chose the parameters where the fluorescence is maximum. This way the radial modes can be cooled reliably.

In parallel to our work, another group studied cooling of the radial modes in the Penning trap [29]. They used $^{40}\text{Ca}^+$ ions which feature a narrow transition that

enables sideband cooling to the ground state. For Doppler cooling they used essentially the same offset-geometry as discussed above, and also highlight the difficulty of laser cooling in the Penning trap. In addition to using a separate radial beam for radial cooling, they also apply an axialization drive, and reach temperatures close to the Doppler limit.

7.6 Cooling-Laser Setup

The cooling-laser setup has been briefly mentioned in section 6.1. Here, we provide more details on the beam delivery into the magnet. The fiber-based delivery used initially has been replaced by a free-space beam in the 2018 setup. The optics are mounted on an aluminum breadboard that is bolted directly to the magnet, which minimizes drifts of the laser position relative to the position of the ions stored in the Penning traps inside the magnet. The beam is routed from the laser table to the breadboard via a photonic crystal fiber [33]. Before coupling into the fiber, on the laser table, a motorized variable attenuator allows to adjust the power over two orders of magnitude. Then, on the breadboard, a Glan-laser polarizer is used to define the initial polarization with high purity. Afterwards the beam passes a motorized rotatable half-wave plate and quarter-wave plate which control the polarization. Finally, the beam position and angle is set with a pair of motorized mirrors with absolute position readout.

A crucial improvement of this setup, which has been implemented in this thesis, is that it allows to control all parameters via control computer. The drivers for all components have been written in LabVIEW. This makes optimization of parameters such as the beam position and angle, laser polarization, laser power, and laser frequency possible. In addition, it allows to return to parameters optimized for laser cooling in one trap after laser cooling in another trap. The laser-system used in the 2018 setup is also described in [33] and the laser-system used in the 2021 setup in [31].

Chapter 8

Sympathetic Cooling of RF Resonators

Coupling laser-cooled ions to a radio-frequency RLC resonator allows for sympathetic cooling of the RLC resonator. In order for the sympathetic cooling to be efficient, the ions need to be cooled at a specific cooling rate, depending on the coupling strength of the laser-cooled ions to the RLC resonator.

The coupled oscillator system is depicted in figure 8.1. In our implementation we use the RLC resonator connected to the BT and the center-of-mass motion of a cloud of $^9\text{Be}^+$ ions stored ibidem. The RLC resonator is thermalized with the environment on a timescale of $\tau = 1/\Gamma = 1/2\pi\gamma$ determined by the damping factor γ which is in the range of $30\,\text{Hz}$ to $50\,\text{Hz}$ for our resonators. The strength of the coupling of the $^9\text{Be}^+$ ion cloud to the RLC resonator is described by $\Gamma_i = 2\pi\gamma_i$, given in equation (5.22). The damping by the laser can be expressed as series resistance in the circuit model [30].

The circuit model and the resulting lineshape $\chi(\nu)$ of the voltage on the RLC resonator are shown in figure 8.2 and 8.3, respectively. The analytic expression for
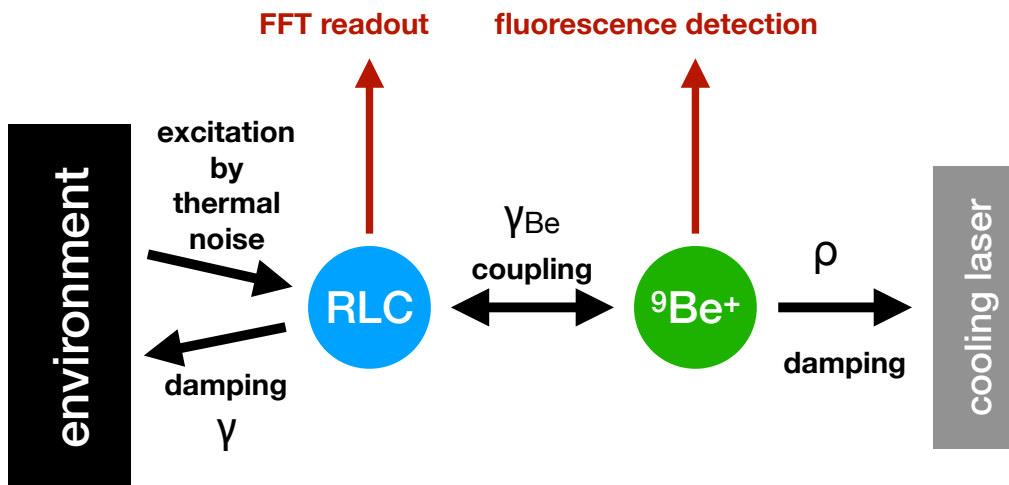
Figure 8.1: Overview of the coupled oscillator system.
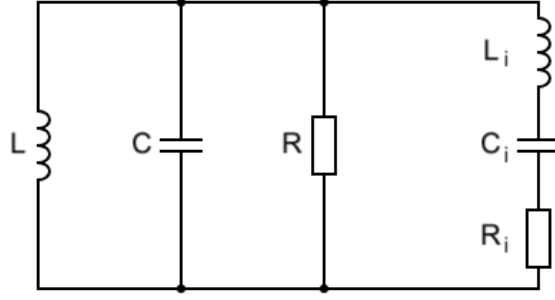
Figure 8.2: Circuit model. The RF resonator is described as parallel RLC circuit and the laser-cooled $^9\text{Be}^+$ ions as series RLC circuit in parallel to the RF resonator. The damping resistance R_i depends on the laser parameters.
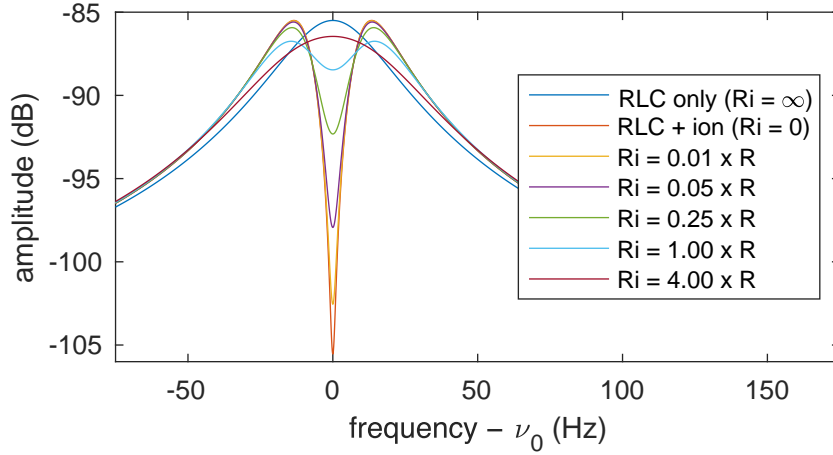
Figure 8.3: Lineshape for various ratios R_i/R.

the lineshape is given in appendix A, equations (A.1) and (A.12). In case of small $\rho = R_i/R$, the lineshape converges to the lineshape of an ion coupled to the RLC resonator, and in case of large ρ, the lineshape converges to the lineshape of an RLC without ions coupled to it. The lineshape is parameterized such that the integral over the lineshape

$$\int_0^\infty \chi(\nu)\partial\nu = \frac{1}{4RC} = \frac{\pi}{2}\gamma \tag{8.1}$$

is independent of ρ. Consequently, the prefactor $4k_BTR\Delta\nu$ can be used to determine the temperature T of the RLC oscillator under the assumption that R does not change.

Experimentally, we simultaneously record FFT spectra and fluorescence counts as we scan the laser frequency across the resonance. The resulting data of a typical scan is shown in figure 8.4. Here, the laser power was stabilized to better than 0.3 %. Selected spectra are shown in figure 8.5. We observe that, from large to small detuning, fist the dip disappears and then the maximum amplitude – which is proportional to the temperature – becomes smaller. As the detuning approaches resonance – where the $^9\text{Be}^+$ ions are strongly cooled – the dip has vanished and the

amplitude recovers to the initial amplitude.

8.1 Temperature of the RF Resonator

For weak laser cooling, the ions have negligible effect and the RLC resonator temperature tends towards the environment temperature. For strong laser cooling, the ions are essentially fixed in position and decouple from the RLC resonator. Also in this case the RLC resonator temperature converges to the environment temperature. In between, there is an optimal damping resistance where the RLC oscillator is most efficiently cooled. We show this in figure 8.6 by plotting the RLC resonator temperature as a function of laser frequency. The plotted temperature has been obtained from a fit to FFT spectra such as the ones in figure 8.4. In addition to the dependence on the laser frequency there is also a power dependence, but the minimum temperature reached is independent of laser power. By relating the temperature to the damping resistance also obtained from the fit (see next section), we show that the temperature of the RLC resonator is uniquely determined by the damping resistance, see figure 8.7.

The lowest achievable temperature depends on the strength of the coupling between the stored ions and the RLC resonator. A measure of the coupling strength is the dip width of the ions, as obtained from a fit to the FFT lineshape. We repeat the analysis for several sets with different ion number and show the lowest temperature reached in each case in figure 8.8 as a function of the dip width. We indeed observe experimentally the expected scaling with dip width. However, we observe that the temperature never drops below about 40 % of the environment temperature for our experimental parameters.

8.2 Damping Resistance of Laser-Cooled ^{9}Be$^+$ Ions

The damping resistance is also obtained from fits to the FFT spectra, as the depth of the dip depends on this quantity, see figure 8.3. Since the damping resistance is measured in terms of the effective parallel resistance of the RLC circuit for image current detection, we introduced the ratio $\rho = R_i/R$. The resistance R can be determined from the properties of the RLC resonator and allows to express the damping resistance as an absolute quantity. As shown in figure 8.9, there are many settings of laser frequency and laser power leading to the same damping resistance. Therefore, a map of the damping resistance as shown in figure 8.9 is a very useful tool to set the right damping resistance in the sympathetic cooling experiments described later in chapter 10.
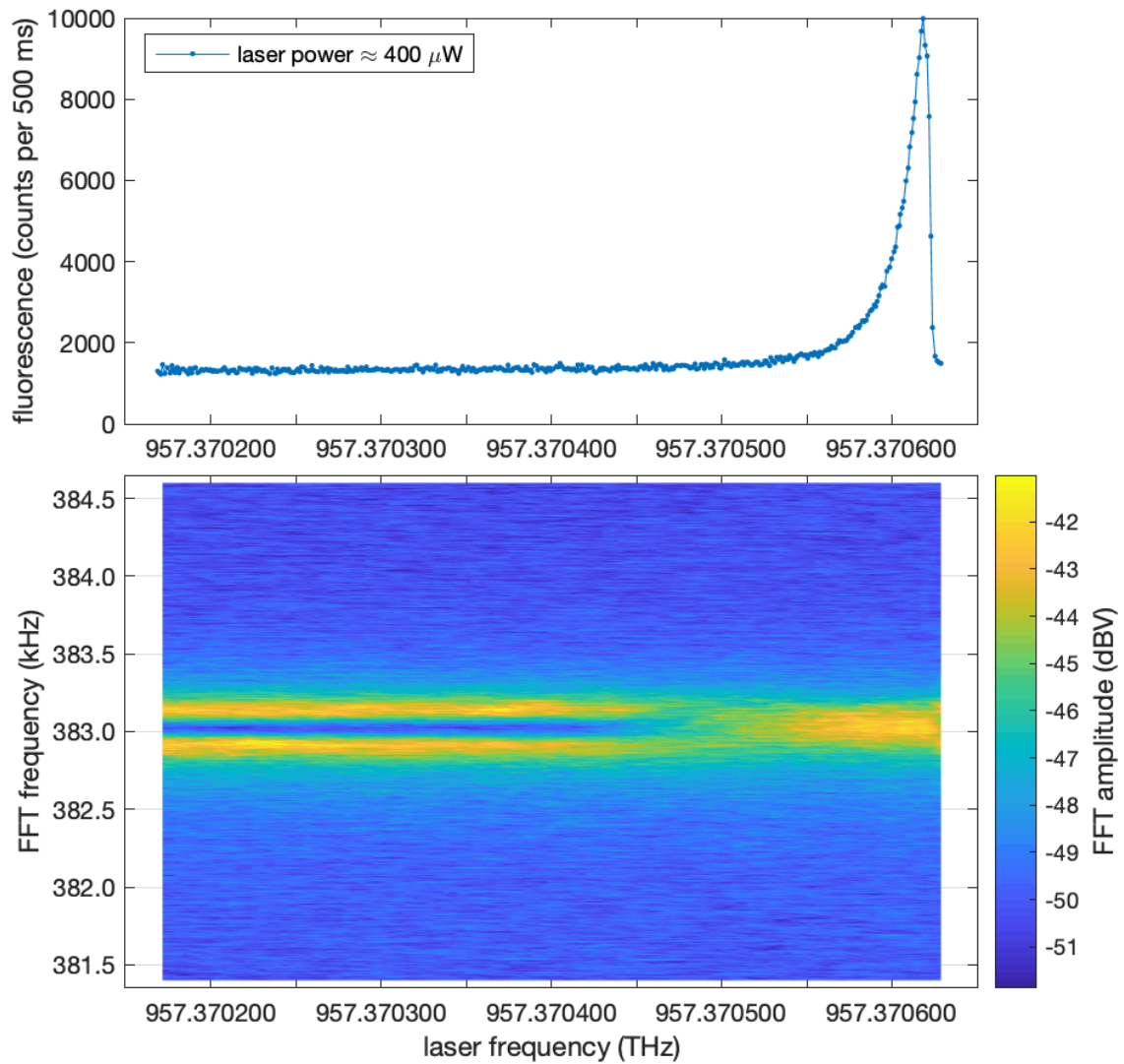
Figure 8.4: Raw data of the scan at $P = 400\,\mu W$ also shown in figure 6.11. Top: photon count rate as function of laser frequency. Bottom: FFT spectra of the RLC oscillator amplitude as function of laser frequency.
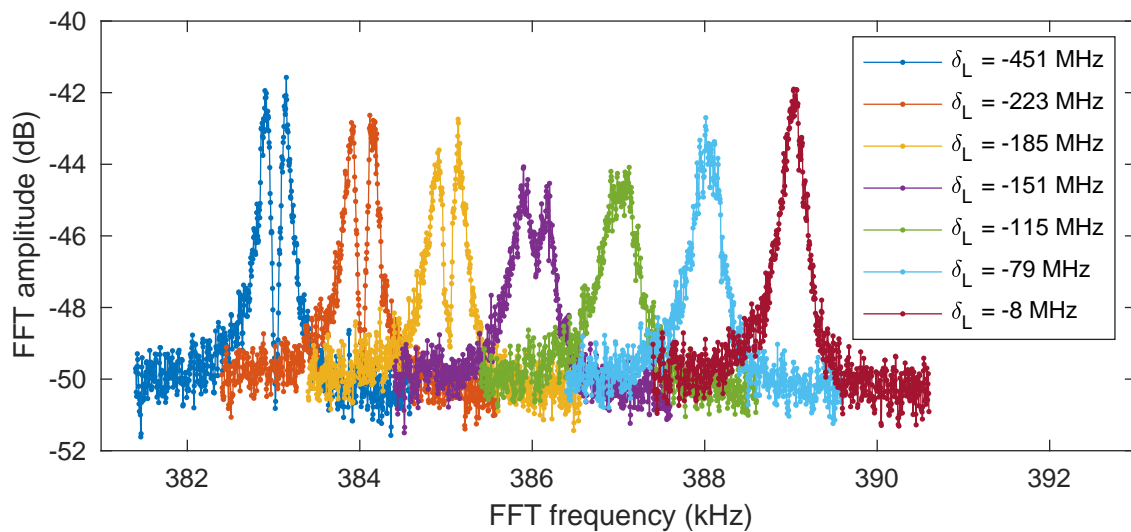
Figure 8.5: Selected FFT spectra from figure 8.4. The fist spectrum is unchanged, and each subsequent spectrum is shifted by $1\,kHz$ for clarity.
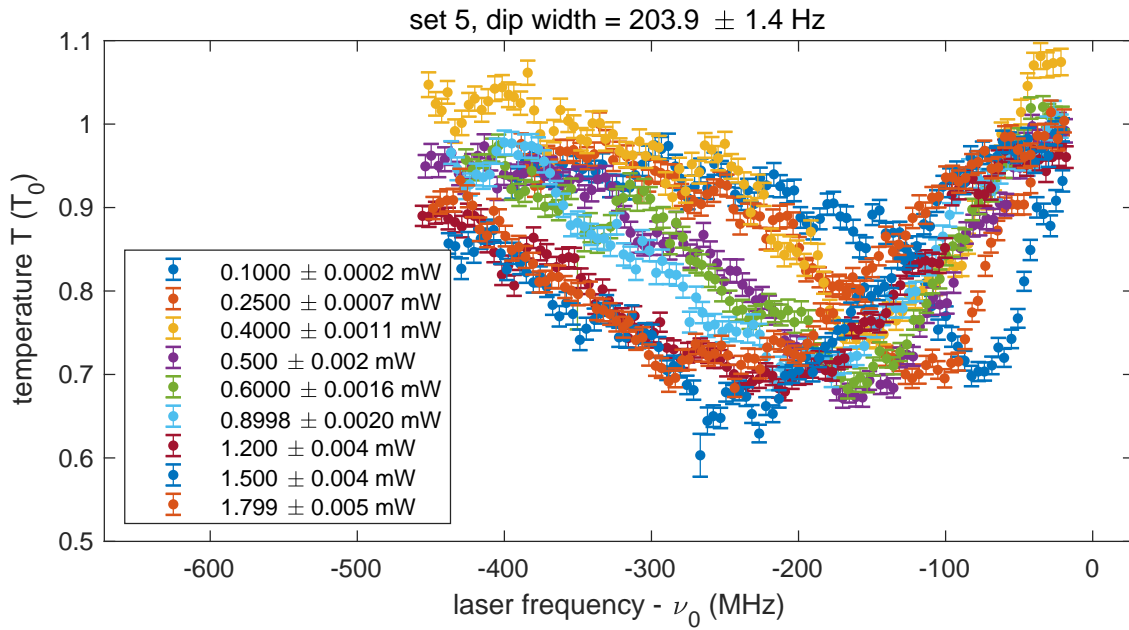
Figure 8.6: RLC oscillator temperature T from fits to the FFT spectra as function of laser frequency. T is given relative to T_0, the RLC oscillator temperature without cooling.
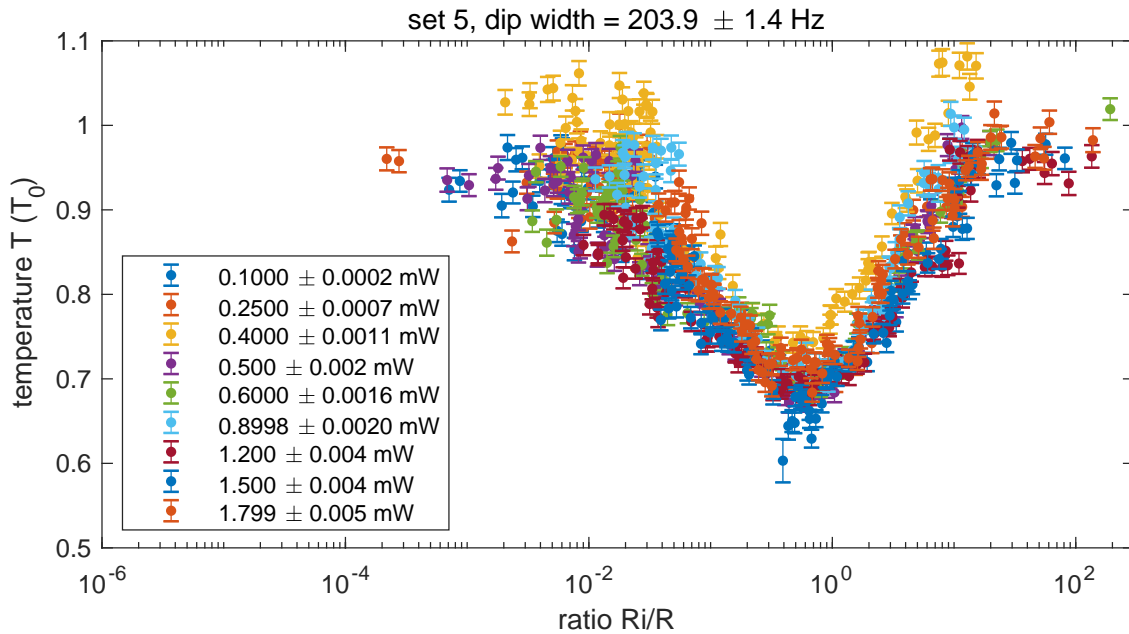
Figure 8.7: RLC oscillator temperature as a function of $\rho = R_i/R$.
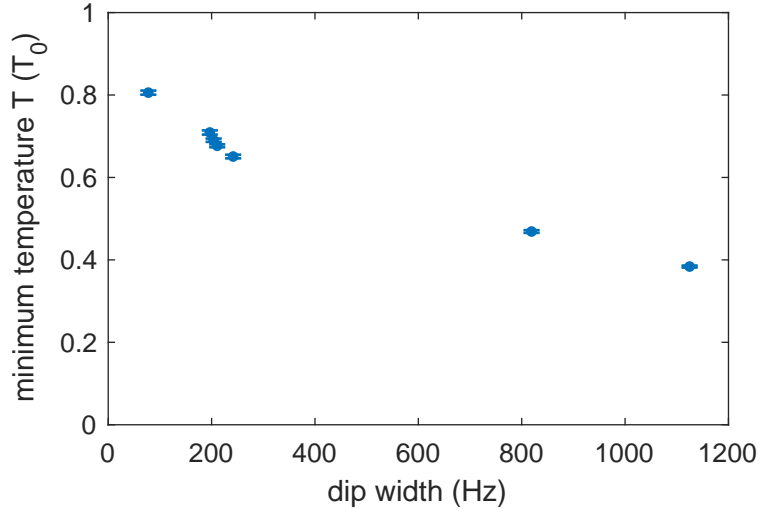
Figure 8.8: Minimum temperature as function of dip width γ_{Be}.
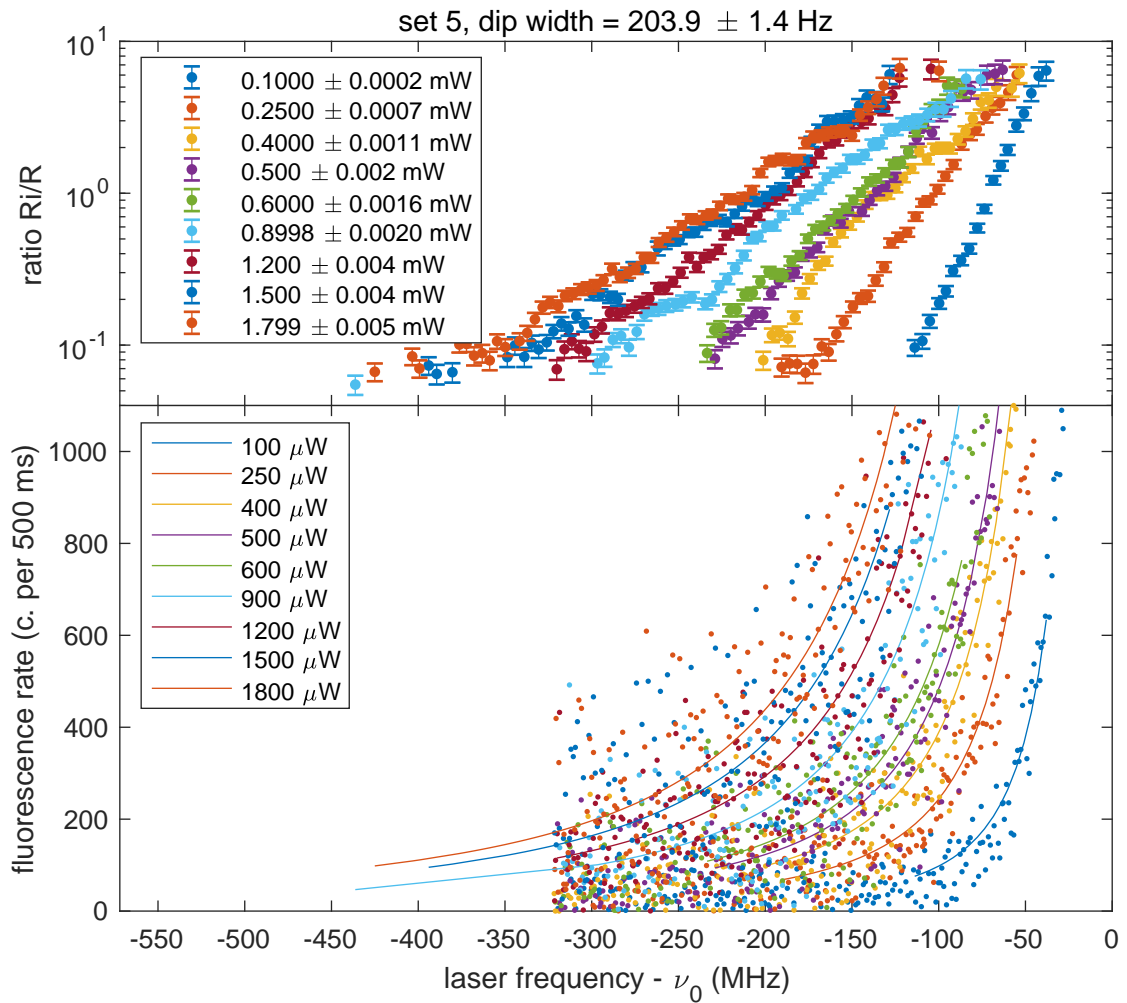
Figure 8.9: Resistance ratio $\rho = R_i/R$ (top) and background-removed fluorescence rate (bottom) as function of the laser frequency. c.: counts.

8.3 Damping Resistance and Photon Scattering Rate

Combining the image-current detection method described in chapter 5, with laser cooling of $^9\text{Be}^+$ ions, and the fluorescence detection system developed in this thesis and described in chapter 6, we were able to measure the laser-induced damping of the $^9\text{Be}^+$ ion cloud and relate it to the photon scattering rate. The damping resistance was calculated in [30] to

$$R_N = 2.2 \times 10^4 \, \Omega \times \frac{\dot{N}(\text{s}^{-1})}{N} \tag{8.2}$$

where $\dot{N}$ is the scattering rate and N is the ion number. The predicted relation between damping resistance and fluorescence rate is linear, but the result may not be directly applicable to our experiment because the assumptions regarding laser parameters are not the same as in our experiment.

In our experiment, we scan the laser frequency across the resonance and simultaneously record the fluorescence count rate and the FFT spectrum. We fit every FFT spectrum with the lineshape described above and extract the ratio R_i/R. We further fit the fluorescence count rate with the model already described in chapter 6. The resulting damping resistance and fluorescence rate are shown in figure 8.9. Crucially, fitting the fluorescence rate allows us to remove the constant stray-light background and to eliminate the scatter of individual measurements. We then plot the damping resistance as a function of fluorescence count rate in figure 8.10a. We observe a quadratic relation between the damping resistance and the fluorescence rate. An order of magnitude increase in the fluorescence rate leads to a two orders of magnitude increase in the damping resistance. In contrast, the is a linear relation between the damping rate and the gradient, defined as the change of fluorescence rate with laser frequency, see figure 8.10b. Further analysis, and a model of the damping process taking into account the parameters in our experiment, is required to explain the scaling observed here. Further analysis of our dataset will also allow to reveal the relation between the damping resistance and the ion number. Finally, to the best of our knowledge, this result constitutes the first measurement of the damping resistance induced by laser light on laser-cooled ions based on image-current detection.
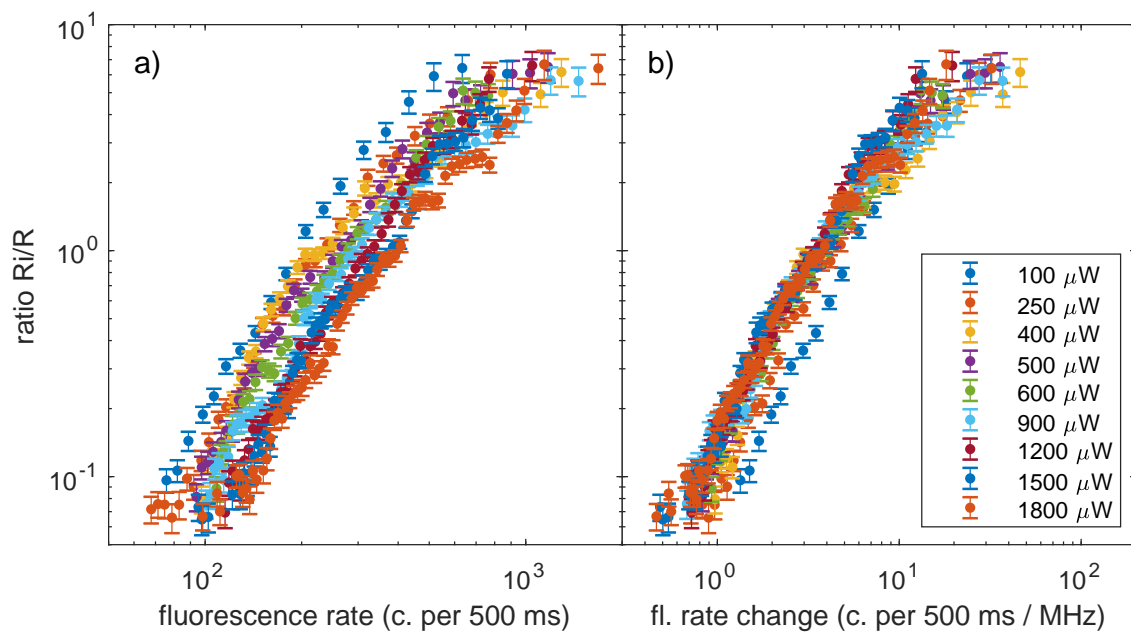
Figure 8.10: Resistance ratio $\rho = R_i/R$ as function of fluorescence rate in (a) and as function of the change in fluorescence rate with frequency in (b). fl.: fluorescence. c.: counts.

Chapter 9

Mode Coupling in the Penning Trap

Coupling of motional modes is an essential part of many measurement methods used in Penning traps, but it can also have negative consequences. In this chapter, coupling of two motional modes of a single ion stored in a Penning trap is briefly discussed. In contrast, coupling of the motional modes of two ions stored in different traps is the topic of the next chapter.

In the quantum mechanical description, coupling of motional modes is described in terms of an interaction Hamiltonian [30]. The overall Hamiltonian is then

$$H = \hbar\omega_1 \left(N_1 + 1/2\right) + \hbar\omega_2 \left(N_2 + 1/2\right) + H_{int} \tag{9.1}$$

where 1 and 2 are two of the motional modes. In the Penning trap $\{1, 2\} \in \{+, z, -\}$. In general, there are two ways to couple these motional modes: Parametric coupling and resonant coupling.

Parametric coupling is described by

$$H_{int} = gx_1x_2 \cos\left(\omega_{12}t\right) \tag{9.2}$$

where $\omega_{12} = \omega_1 - \omega_2$ is the difference frequency, x_1 and x_2 are the position operators of oscillators 1 and 2, respectively, and g is the coupling strength. Parametric coupling in the Penning trap is typically achieved by application of time-varying electric fields with frequency $\omega_{RF} = \omega_{12}$, such as in equation (2.30).

Resonant coupling is described by

$$H_{int} = gx_1x_2 \tag{9.3}$$

where g is a coupling constant. Alternatively, higher orders might also lead to coupling. In this case

$$H_{int} = gx_1 \left(x_2\right)^n \tag{9.4}$$

where n is an integer. The fields leading to these interaction Hamiltonians are typically static and unavoidable in a real Penning trap. Coupling effects include frequency shifts and energy exchange, which becomes relevant when $\omega_1 \approx \omega_2$ or $\omega_1 \approx n \times \omega_2$. This type of coupling can also lead to ion loss, as observed in Paul traps [140, 141, 142] and in Penning traps [143, 144, 145].

The most desirable effect of coupling two oscillators is oscillatory exchange of action. In case of $\omega_1 = \omega_2$, this is equivalent to oscillatory exchange of energy. This manifests itself in (classical) Rabi oscillations of the amplitudes of both involved oscillators and allows, e.g., to swap the amplitudes.

9.1 In-Trap Parametric Coupling

As mentioned before, parametric coupling is used extensively in Penning traps [35, 43] where the technique is also called sideband coupling or mode interconversion. It allows e.g. to couple the radial modes to the axial mode without adding noise [30]. The coupling leads to the formation of two normal modes, both of which have a component of motion in the original direction. For example, when coupling the magnetron mode to the axial mode, two modes can be observed in the axial spectrum, as shown in figure 7.7.

9.2 In-Trap Resonant Coupling

In the ideal Penning trap, the three motional modes are independent of each other. However, in the presence of electric field anharmonicities or magnetic field inhomogeneities, the motional modes can couple to each other. The resulting frequency shifts of some coupling terms have been discussed in section 2.2. A further consequence of these (and other) coupling terms is that they enable resonant energy exchange. To fulfill the resonance condition, the frequency ratio of the involved motional modes needs to be an integer. In the Penning trap, this situation occurs when

$$\omega_+ = n \times \omega_z \Rightarrow \omega_z = 2n \times \omega_-, \tag{9.5}$$

$$\omega_+ = n \times \omega_-, \tag{9.6}$$

or

$$\omega_z = n \times \omega_- \tag{9.7}$$

where n is an integer. Note that, due to equation (2.15), whenever ω_+/ω_z is integer, ω_z/ω_- is integer also, but not vice versa. Consequently, the magnetron mode is involved in all cases. In addition, the role of the inverted level structure of the magnetron mode is important: When the magnetron mode is coupled to another mode resonantly, the amplitude of both modes can grow while keeping the energy
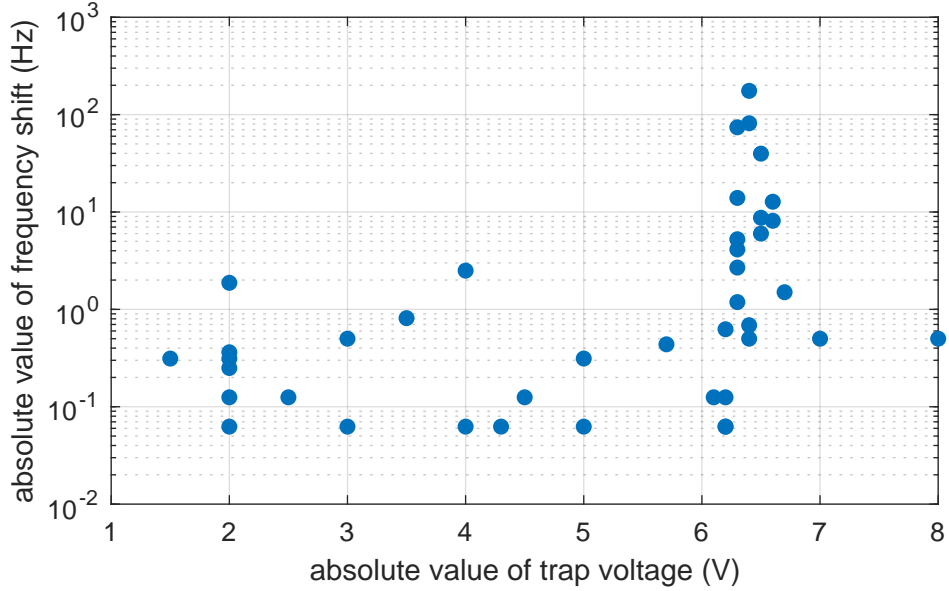
Figure 9.1: Absolute value of frequency shift after ramping to indicated trap voltage.

of the system constant.

To demonstrate the effect of resonant coupling, we tune the axial frequency by means of the applied trap voltage to a value where resonant behaviour is expected and observe the resulting energy change in the motional modes. For this experiment we use a single $^9\text{Be}^+$ ion in the AT. In this trap, the magnetic field is reduced to approximately $1.17\,\text{T}$ due to the ferromagnetic ring electrode. This leads to a lower cyclotron frequency of the $^9\text{Be}^+$ ion of $\omega_c \approx 2.0\,\text{MHz}$. Consequently, the ratios ω_+/ω_z and ω_z/ω_- are relatively small. In addition, the large magnetic bottle of $300\,\text{kT}\,\text{m}^{-2}$ provides a large magnetic field inhomogeneity. Further, we use the continuous Stern-Gerlach effect of the magnetic bottle in the AT to determine the energy of the radial modes. According to equation (3.4), the axial frequency shift due to the energy in the radial modes is $11\,\text{Hz}\,\text{K}^{-1}/k_B$ for $^9\text{Be}^+$ ions.

The measurement procedure is as follows: First, we measure the axial frequency of the $^9\text{Be}^+$ ion by bringing it into resonance with the image-current detector. Then, we ramp the trap voltage to the desired value. After a waiting period of $\approx 1\,\text{s}$, the voltage is ramped back and the axial frequency is measured again. In figure 9.1 we plot the resulting axial frequency shift as a function of the trap voltage. Indeed, we observe increased fluctuation in the energy of the radial modes when the axial frequency is tuned near the resonance at $V_0 = 6.3\,\text{V}$ where $\omega_+/\omega_z = 3$ and $\omega_z/\omega_- = 6$. The frequency shifts below $\approx 1\,\text{Hz}$ are consistent with fluctuations and long-term drifts of the trap voltage. For comparison, the motional frequencies in the AT and their multiples are shown in figure 9.2 as a function of trap voltage. In addition, the trap voltages where resonant behaviour is expected are indicated. We observe the resonance at $6.3\,\text{V}$, but not at $3.7\,\text{V}$. We attribute this to a reduced coupling strength for higher order resonances.

As a consequence of this coupling, the mode energies are exchanged near res-

onances for which n is small. In practice it is difficult to avoid these completely, especially when transporting ions into and out of the AT. In the first versions of our experiment, this effect prevented us from direct measurements of the energy of a laser-cooled ^{9}Be$^+$ ion using the continuous Stern-Gerlach effect in the AT. In comparison, this is less of a problem for protons since the cyclotron frequency is approximately 9 times larger and, consequently, the ratios ω_+/ω_z and ω_z/ω_- are 9 times larger as well. In the newly implemented ST, these problems are greatly reduced for ^{9}Be$^+$ ions, and a temperature measurement of laser-cooled ions might be attempted in the future.
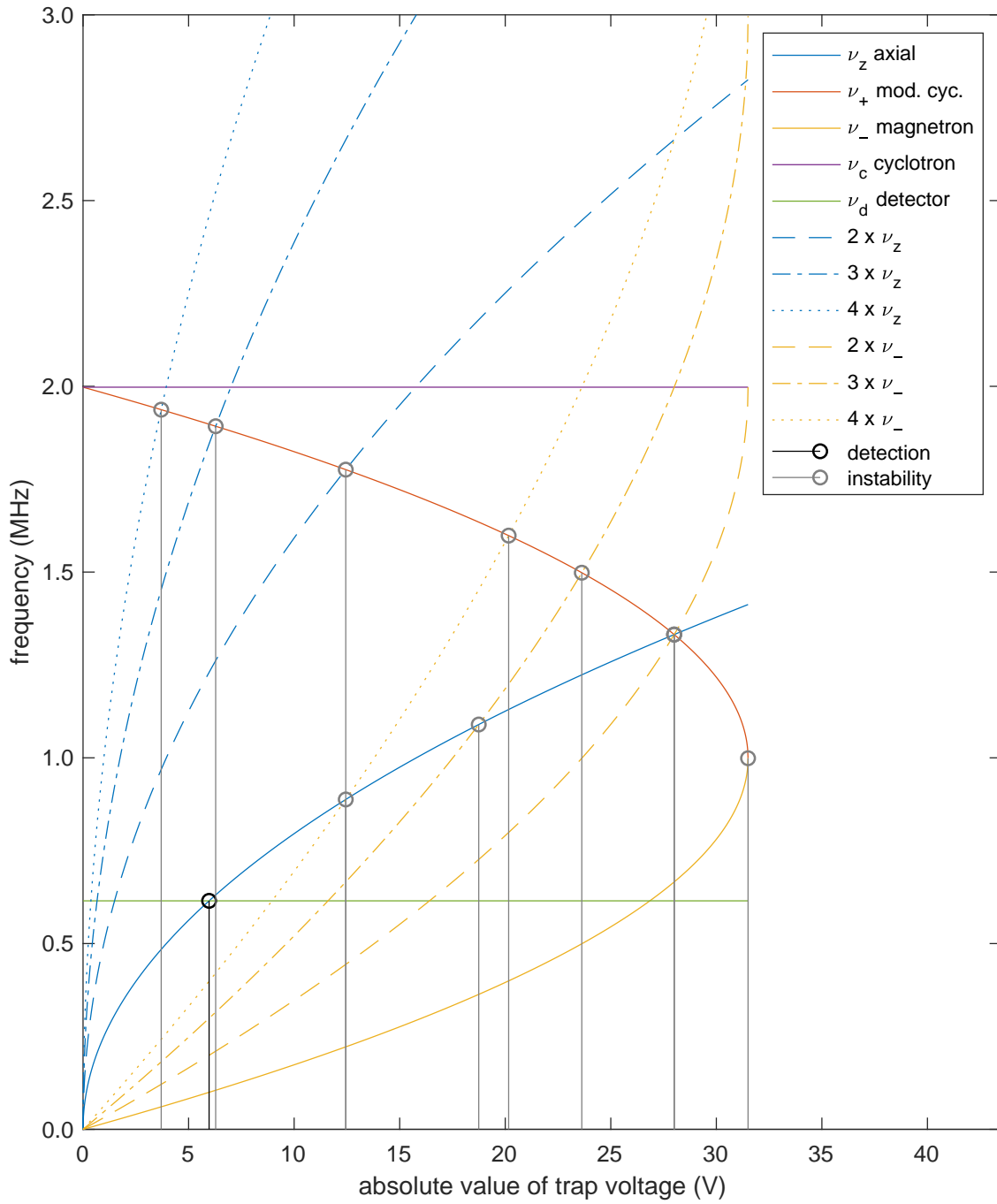
Figure 9.2: Frequencies of a $^9\mathrm{Be}^+$ ion in the AT as a function of trap voltage V_0. The magnetic field in the AT is $B = 1.17\,\mathrm{T}$. For detection, the axial frequency is equal to the detector frequency at $V_0 = 5.97\,\mathrm{V}$. The closest instabilities occur near $V_0 = 3.70\,\mathrm{V}$ and $V_0 = 6.28\,\mathrm{V}$.

Chapter 10

Inter-Trap Coupling and Cooling

Coupling between separated traps is essential for sympathetic cooling of individually-trapped particles. In this chapter, we describe our experiments on sympathetic cooling of a single individually-trapped proton. Originally, the coupling via a common capacitance, also called common endcap or common electrode, was envisioned [30]. This concept was adapted to our proton g-factor experiment [60, 33] and simulations of the cooling performance for parameters typical of our experiment were performed [31]. Essentially, the interaction of the stored ions image currents via the common capacitance leads to a coupling of both stored-ion oscillators. For cooling we make use of a characteristic property of coupled oscillators: the oscillatory exchange of amplitude between the two oscillators. In our case the beryllium-ion oscillator will be laser cooled to mK temperatures. In the following, the proton amplitude is exchanged with the beryllium amplitude. Consequently, when the coupling is stopped after a π-pulse, the proton amplitude will be at mK temperatures. This oscillatory exchange of proton and beryllium amplitudes is shown in figure 10.1.

To derive the coupling strength, consider the equations of motion (EOM) of the axial mode of the proton and the $^9\mathrm{Be}^+$ ion, as in equation (5.3). The image currents
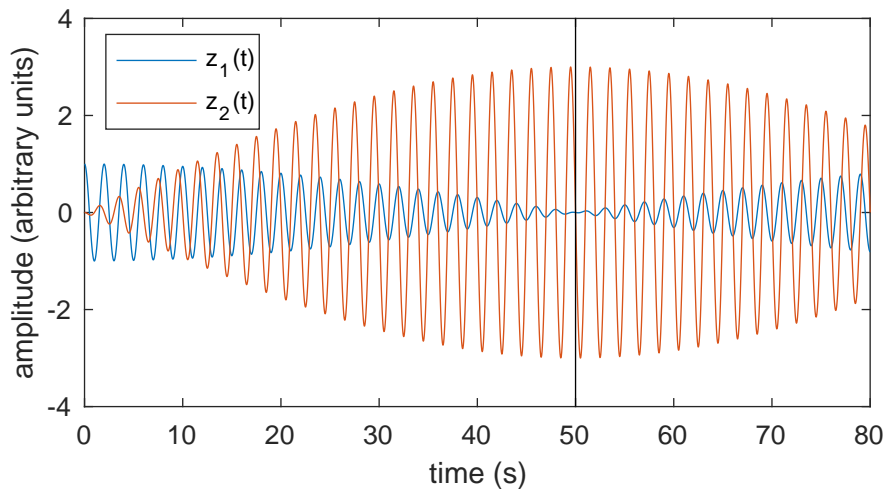
Figure 10.1: Proton and $^9\mathrm{Be}^+$ ion amplitudes during coupling.

of the stored ions induce a voltage V on the common electrode with capacitance C_c as

$$V = \frac{Q}{C_c} = \frac{1}{C_c} \int (i_1 + i_2) \, dt = \frac{1}{C_c} \int \left(\frac{q_1}{D_1} v_1 + \frac{q_2}{D_2} v_2 \right) dt = \frac{1}{C_c} \left(\frac{q_1}{D_1} z_1 + \frac{q_2}{D_2} z_2 \right) \tag{10.1}$$

where the index 1 represents the quantities of the proton, and the index 2 the quantities of the $^9\mathrm{Be}^+$ ion. Consequently, the forces on the ions are

$$F_1 = -\frac{q_1}{D_1} \frac{1}{C_c} \left(\frac{q_1}{D_1} z_1 + \frac{q_2}{D_2} z_2 \right) \tag{10.2}$$

$$F_2 = -\frac{q_2}{D_2} \frac{1}{C_c} \left(\frac{q_1}{D_1} z_1 + \frac{q_2}{D_2} z_2 \right). \tag{10.3}$$

Inserted into equation (5.3), the EOM of the proton and $^9\mathrm{Be}^+$ ion become

$$\ddot{z}_1 + \omega_1^2 z_1 + \frac{q_1 q_2}{m_1 C_c D_1 D_2} z_2 = 0 \tag{10.4}$$

$$\ddot{z}_2 + \omega_2^2 z_2 + \frac{q_1 q_2}{m_2 C_c D_1 D_2} z_1 = 0 \tag{10.5}$$

where the self-interaction has been absorbed into ω_1 and ω_2. The coupled EOM can be solved using the ansatz $z_k = a_k \cos(\omega t + \phi)$, where $k \in \{1, 2\}$. This leads to a system of linear equations where the condition for the determinant of the coefficient matrix is

$$\left(\omega_1^2 - \omega^2 \right) \left(\omega_2^2 - \omega^2 \right) - \frac{q_1^2 q_2^2}{m_1 m_2 C_c^2 D_1^2 D_2^2} = 0 \tag{10.6}$$

with solutions

$$\omega_\pm^2 = \frac{1}{2} \left(\omega_1^2 + \omega_2^2 \right) \pm \sqrt{ \frac{1}{4} \left(\omega_1^2 - \omega_2^2 \right)^2 + \frac{q_1^2 q_2^2}{m_1 m_2 C_c^2 D_1^2 D_2^2} }. \tag{10.7}$$

The resulting normal-mode frequencies $\omega_\pm$ show the avoided crossing typical of coupled oscillators. For $\omega_1 = \omega_2$, the normal-mode frequencies can be approximated by

$$\omega_\pm \approx \omega_1 \pm \Omega/2 \tag{10.8}$$

with the Rabi frequency

$$\Omega = \frac{q_1 q_2}{\omega_1 \sqrt{m_1 m_2} C_c D_1 D_2}. \tag{10.9}$$

If the center-of-mass mode of a cloud of ions is used, $q_k \to N_k \times q_k$ and $m_k \to N_k \times m_k$, where N_k is the ion number, leading to an additional factor of $\sqrt{N_1 N_2}$.

After a duration of

$$t = \frac{\pi}{\Omega} = \pi \omega_1 C_c \frac{\sqrt{m_1 m_2} D_1 D_2}{q_1 q_2 \sqrt{N_1 N_2}} \tag{10.10}$$

the amplitudes of both oscillators are exchanged. The coupling is enhanced when

the capacitance of the common electrode is small. In addition, the involved masses and effective electrode distances should be small, and the involved charges should be large. The coupling can be further enhanced by using an ion cloud with ion number N_k. For the situation in our experiment, a single proton in the CT and approximately 100 ^{9}Be$^+$ ions in the BT, the exchange time is on the order of 50 s [60]. This large exchange time requires frequency matching and frequency stability of both ion oscillators on the level of 10 mHz which is extremely challenging.

The capacitance can also be an effective capacitance, such as the one presented by an RLC circuit off resonance, as proposed in [30] and further discussed in [75]. In the above equations C_c is replaced by C_e which is given by

$$C_e = -\frac{1}{\omega \operatorname{Im}(Z(\omega))}. \tag{10.11}$$

In this case the coupling strength depends on the detuning δ of the ion frequencies ω_k from the resonance frequency of the RLC circuit ω_0 and can be several orders of magnitude larger than the coupling strength achieved with common electrode coupling. Additionally, however, there is a resistive component due to the real part of the impedance, which tends to heat the ions to the resonator temperature.

In the following we distinguish two cases: The first one is the resonant case where $\omega_0 = \omega_1 = \omega_2$. Here, ω_0, ω_1, and ω_2 are the resonance frequencies of the RLC oscillator, the proton oscillator, and the ^{9}Be$^+$ ion oscillator, respectively. In this case there is no oscillatory exchange of energy between the two ion oscillators, but this situation can still be useful for cooling the proton oscillator. All our cooling experiments so far have been performed in this regime. The second case is when $\omega_1 = \omega_2 = \omega_0 + \delta$ where both ion resonators are detuned from the RLC oscillator by the detuning δ. In this case one can observe oscillatory exchange of energy, as reported by another group in [146], but not in the related publication [75]. Alternatively, in thermal equilibrium, the avoided crossing of both ion oscillator modes can be observed.

10.1 Ions On-Resonant with the RF Resonator

On resonance, the imaginary part of the impedance of the RLC circuit is zero. Consequently, $C_e \to \infty$ and there is no coupling between the ion oscillators. However, this situation can still be utilized for cooling.

To see how this comes about, consider the motion of the proton and the ^{9}Be$^+$ ions in terms of their image currents induced on the common electrode. The motion can be decomposed into two modes: the in-phase mode where the image currents add, and the out-of-phase mode where the image currents cancel. Only the in-phase mode interacts with the RLC circuit connected to the common electrode. The
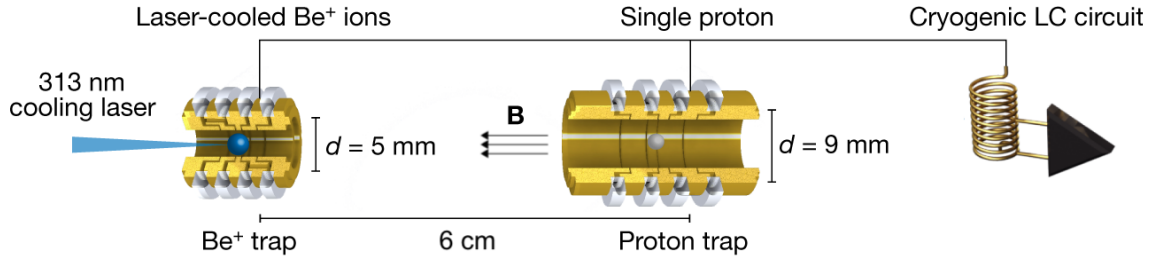
Figure 10.2: Trap configuration used for the C_4-based temperature measurement of the sympathetic cooling experiment. A single proton is individually trapped in the proton trap (PT) and a cloud of laser-cooled $^9\text{Be}^+$ ions is stored in the $^9\text{Be}^+$ trap (ST). The configuration of the ST without magnetic bottle was used, as implemented in the 2018 setup, see also figure 4.8. Both traps are connected to the same RLC circuit for image-current detection. Adapted from [127]. Note that the inter-trap distance is 6 cm instead of the 9 cm stated in [127] and that the direction of the magnetic field is reversed. See also the trap stack configurations in figure 4.8.

other mode is invisible to the RLC circuit and will not be excited by the thermal noise. Crucially, both modes have a $^9\text{Be}^+$ component and can be cooled by laser cooling. Consequently, all modes other than the in-phase mode can be cooled to low temperatures.

The proton content in the in-phase mode is proportional to the proton dip width γ_p, as defined in equation (5.22), and the $^9\text{Be}^+$ content is proportional to the $^9\text{Be}^+$ dip width γ_{Be}. For weak cooling, the temperature of the in-phase mode T_{ip} is still thermalized with the RLC resonator at a temperature of T_0. Consequently, the proton temperature is

$$T_p = \frac{\gamma_p}{\gamma_p + \gamma_{Be}} T_{ip} = \frac{\gamma_p}{\gamma_p + \gamma_{Be}} T_0. \tag{10.12}$$

This temperature model has been confirmed by simulations [126]. To reach low proton temperatures, the coupling of the RLC circuit to the $^9\text{Be}^+$ ions γ_{Be} should be maximized, while the coupling to the proton γ_p should be minimized.

In the experiment, we determine the proton's axial temperature from amplitude-dependent axial frequency shifts. In two separate runs, two different methods, relying on electric field anharmonicities and magnetic field inhomogeneities, respectively, have been used, which are described in the following.

10.1.1 Temperature Measurement via C_4

An initial proof-of-principle measurement was performed in the 2018 setup [127]. Here, a single proton was stored in the PT and a cloud of laser-cooled $^9\text{Be}^+$ ions in the ST. The relevant part of the setup is shown in figure 10.2.

The FFT spectrum of the voltage on the RLC resonator connected to both traps is shown in figure 10.3. The spectrum shows a broad and a narrow dip. The broad dip is due to the laser cooled $^9\text{Be}^+$ ions and does not reach the noise floor due to
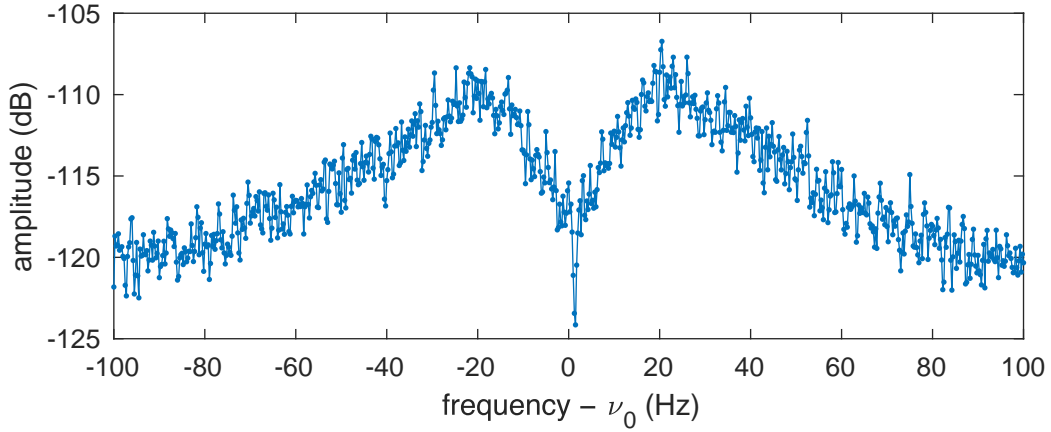
Figure 10.3: FFT spectrum of the voltage on the RLC circuit during the sympathetic cooling experiment. The proton and the laser-cooled $^9\text{Be}^+$ ion cloud are tuned to resonance ($\omega_0 = \omega_1 = \omega_2$). The broad dip is due to the laser-cooled $^9\text{Be}^+$ ions, the narrow dip is due to the single proton. Adapted from [33].

the laser-induced damping, as discussed in chapter 8. The narrow dip is due to the single proton.

For temperature measurement, we introduce a finite tuning ratio offset ΔTR. As discussed in section 4.7, this leads to a temperature dependent axial frequency shift of

$$\Delta\omega_z = \frac{3}{2m\omega_z C_2}\left(D_4 \times \Delta TR\right)E_z \tag{10.13}$$

due to the energy in the axial mode. In practice, several values of ΔTR are applied and the temperature is determined from the slope of the resulting axial frequency shift as a function of ΔTR. One disadvantage of this method is that only temperature differences can be measured. Consequently, the RLC resonator temperature had to be determined independently, with the result $T_0 = 17.0(2.4)\,\text{K}$.

The so-determined proton temperatures are the differences between the RLC resonator temperature and the temperature change measured by equation (10.13), and are shown in figure 10.4 as function of the $^9\text{Be}^+$ ion dip width. In general, the data reproduces the scaling of our temperature model. However, the temperature limits predicted by equation (10.12) could not be reached. This was on the one hand due to the too strong laser cooling which had to be applied in order to be able to resolve the proton dip below the $^9\text{Be}^+$ ion dip in the FFT spectrum, and on the other hand due to the low resolution of this temperature measurement method. The lowest proton temperature measured was $2.6(2.5)\,\text{K}$, almost an order of magnitude below the resonator temperature. More details about this measurement can be found in [33, 127].
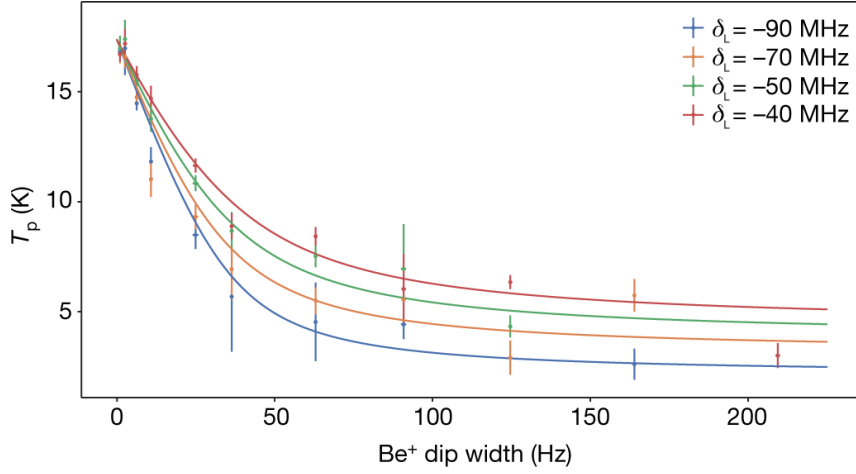
Figure 10.4: Final temperature of the axial mode of the single proton as a function of the laser detuning δ_L and the $^9\text{Be}^+$ ion dip width. Adapted from [127].

10.1.2 Temperature Measurement via B_2

With the upgraded 2021 setup, which featured the ST with magnetic bottle, we performed another proton temperature measurement. Here, a single proton was stored in the PT and a cloud of laser-cooled $^9\text{Be}^+$ ions in the LT. For measurement of the proton temperature, the energy in the axial mode is first transferred to the cyclotron mode by interconversion of modes. Afterwards, the proton is transported from the PT to the ST where the temperature of the cyclotron mode is measured as axial frequency shift. The relevant part of the experimental setup is shown in figure 10.5.

The axial frequency shift in the ST is due to the continuous Stern-Gerlach effect, equation (3.5), and becomes

$$\Delta\omega_z = \frac{B_{0,\text{ST}}}{B_{0,\text{PT}}} \frac{B_{2,\text{ST}}}{B_{0,\text{ST}} m \omega_{z,\text{ST}}} E_{+,\text{PT}} \tag{10.14}$$

where the first factor is due to the adiabatic transport from the PT to the ST. The cyclotron and axial energies are related by

$$E_{+,\text{PT}} = \frac{\omega_{+,\text{PT}}}{\omega_{z,\text{PT}}} E_{z,\text{PT}}. \tag{10.15}$$

In the magnetic bottle of the ST of $B_2 = 27.8(7)\,\text{kT}\,\text{m}^{-2}$ the axial frequency shift of the proton due to energy of the cyclotron mode is $5.7\,\text{Hz}\,\text{K}^{-1}/k_B$. The axial frequencies of an example measurement are shown in figure 10.6a. A histogram of these axial frequency shifts, figure 10.6b, clearly shows that the energies and thus the frequencies are Boltzmann distributed. For analysis, the cumulative distribution is used, see figure 10.6c. Fitting the cumulative distribution provides a more robust value for the temperature than fitting the Boltzmann distribution directly, since binning the data is avoided.
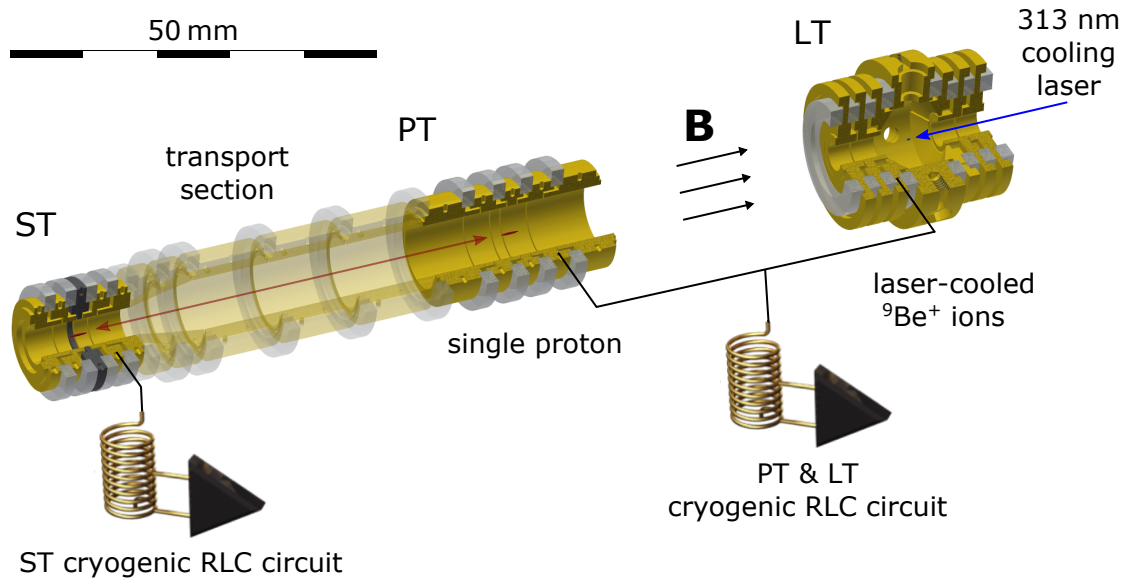
Figure 10.5: Trap configuration used for the B_2-based temperature measurement of the sympathetic cooling experiment. A single proton is individually trapped in the proton trap (PT) and a cloud of laser-cooled $^9Be^+$ ions is stored in the $^9Be^+$ trap (LT). For temperature measurement, the proton is transported to the ST. The PT and LT are connected to the same RLC circuit for image-current detection, while the ST features a separate RLC circuit.
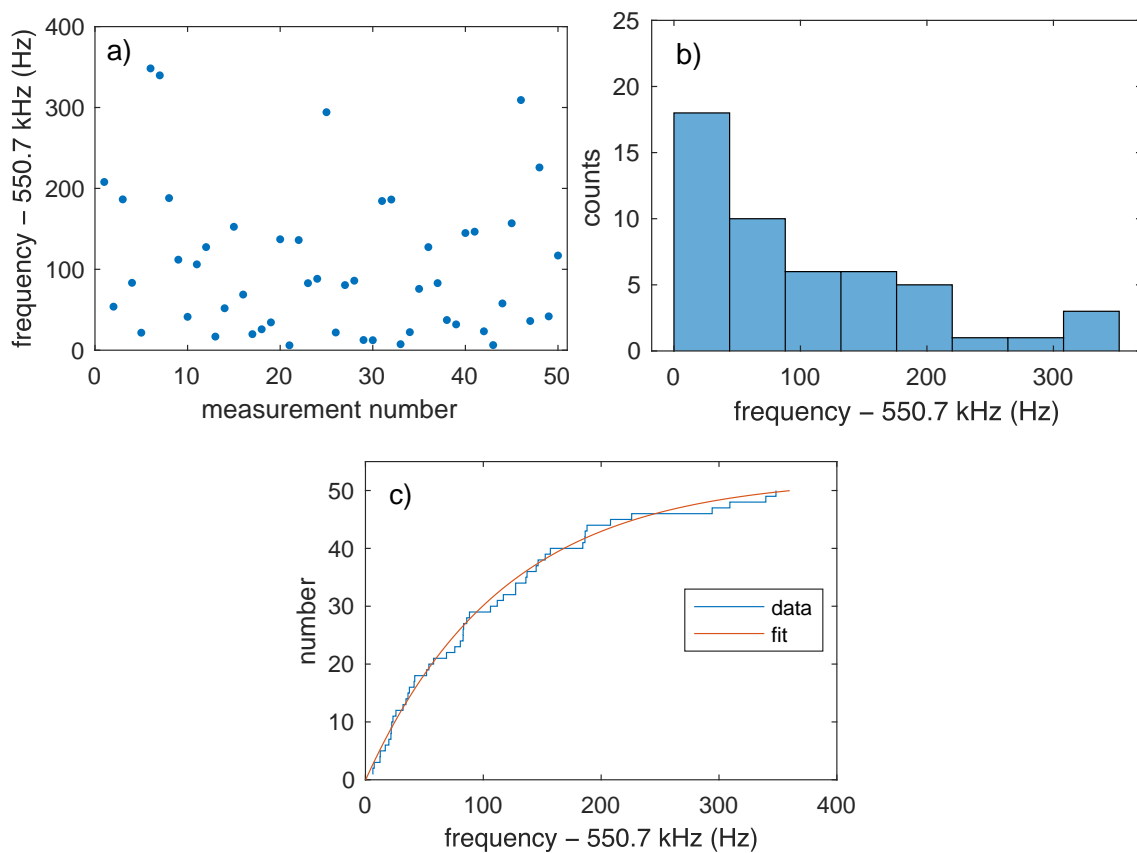
Figure 10.6: Temperature measurement in the magnetic bottle of the ST. (a) measured axial frequencies, (b) frequency histogram, (c) cumulative distribution and fit. Data recorded by [31]. Subfigures (a) and (b) modified from [31].

125
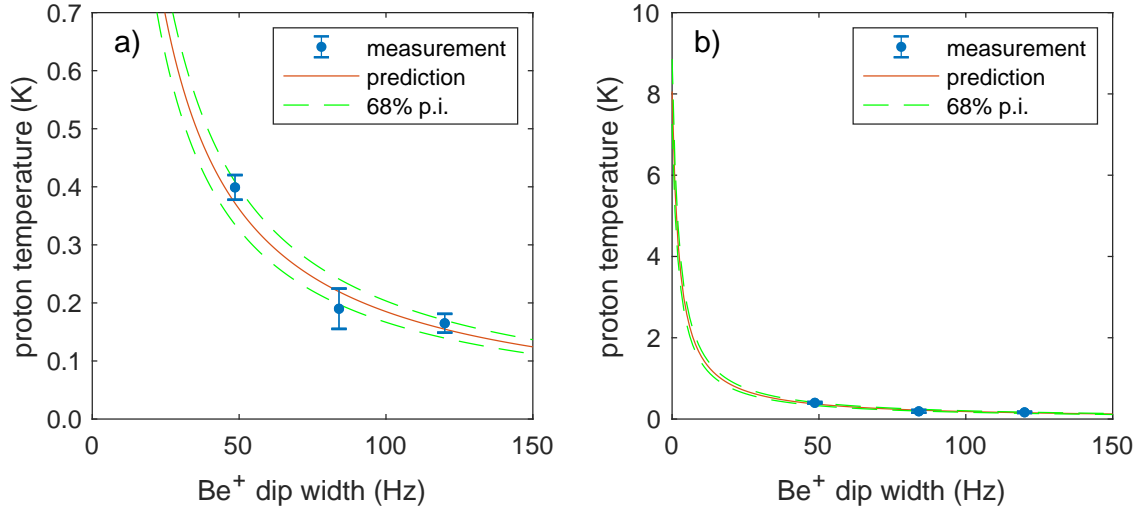
Figure 10.7: Temperature of the axial mode of the single proton in the PT after sympathetic cooling, as measured in the magnetic bottle of the ST after transport. The data in (a) is re-plotted on a larger scale in (b) for comparison to figure 10.4. The prediction is based on an independently determined resonator temperature. p.i.: prediction interval. Data recorded by [31]. Figure modified from [31].

Before transport to the ST, the continuously coupled axial and cyclotron modes were thermalized for $90\,\mathrm{s}$ in the PT. In contrast to the C_4-based temperature measurement, the $^9\mathrm{Be}^+$ ion cloud was only cooled very weakly in this measurement. The laser power and detuning were $P/P_0 = 0.015$ to 0.045 and $\delta_L = -85\,\mathrm{MHz}$ for the $48\,\mathrm{Hz}$-cloud and $P/P_0 \approx 0.33$ and $\delta_L = -200\,\mathrm{MHz}$ for the other two clouds shown in figure 10.7. The resulting damping rate was sufficiently low such that the $^9\mathrm{Be}^+$ ion dip reached the noise floor.

The final temperatures are shown in figure 10.7 as a function of $^9\mathrm{Be}^+$ ion dip width. Each plotted temperature is the average of three or four individual measurements with 25 to 60 data points each. The temperatures of the individual measurements are consistent with each other, which demonstrates the reproducibility of the measurement technique. Further, with this more precise temperature measurement method, we do not only confirm the scaling predicted by our temperature model, but also show that the values of the measured temperatures are all in very good agreement with the prediction. The prediction is based on an independently determined resonator temperature of $8.6(8)\,\mathrm{K}$, and is also shown in figure 10.7. This lower resonator temperature, compared to above, was achieved by turning off the cryogenic amplifier during the measurement, which lowers the noise on the resonator. Finally, the lowest axial proton temperature reached was $160(30)\,\mathrm{mK}$, almost two orders of magnitude lower than the resonator temperature. Another description of this measurement can be found in [31].

The limit of this method, at the moment, is the number of $^9\mathrm{Be}^+$ ions that can be stored in the trap. The reason is that large clouds have increased axial frequency instability, which negatively impacts the ability to match the proton and

^{9}Be$^+$ ion frequency. For improved sympathetic cooling, instead of maximising the ^{9}Be$^+$ ion number, the ratio of the dip widths γ_{Be}/γ_p should be optimized by the other available parameters, see equation (5.22). E.g., the common RLC resonator should be connected to an electrode with large D_p in the PT, and to electrodes with small D_{Be} in the LT. Alternatively, using a small-diameter trap instead of the LT for storing the laser-cooled ^{9}Be$^+$ ions would also minimize D_{Be} and thus maximize γ_{Be}.

10.2 Ions Off-Resonant with the RF Resonator

When the ions are off-resonant from the RLC resonator, and under the conditions that $\Gamma_i \ll \Gamma$ and $\Gamma_i \ll \delta$, the resonator-ion interaction can be treated by solving the EOM of the RLC resonator and the stored ions independently. The situation is then similar to the one discussed in section 5.5, equation (5.14), with the RLC resonator impedance being

$$Z(\omega = \omega_0 + \delta) = R_e + i\frac{-1}{\omega C_e} \tag{10.16}$$

where

$$C_e = \frac{-1}{\omega \operatorname{Im}(Z(\omega))} \approx \frac{\delta C}{-\omega_0} \tag{10.17}$$

and

$$R_e = \operatorname{Re}(Z(\omega)) \approx \frac{R\Gamma^2}{\delta^2}. \tag{10.18}$$

are the effective capacitance and the effective resistance at the detuning δ, respectively. The last term is an approximation that is valid for $\delta \gg \Gamma$ and $\delta \ll \omega_0$.

For coupling, the relevant timescale is given by the exchange time $\tau_{ex} = \pi/\Omega$ which is proportional to C_e and thus to δ. Depending on the detuning, the exchange time can be several orders of magnitude smaller than in the case of common electrode coupling, e.g., in [146] $\tau_{ex} = 0.85$ s was reported. For the heating effect, the relevant timescale is given by the thermalization time constant $\tau_{th} = 1/\Gamma_{i,e}$ which is proportional to δ^2. Here, $\Gamma_{i,e}$ is an effective dip width given by equation (5.22) for $R \to R_e$. Consequently, the ratio τ_{th}/τ_{ex} is proportional to the detuning δ. Therefore, in order to suppress the heating effect as much as possible, it is advantageous to choose the detuning as large as possible. However, the Rabi frequency should still be larger than typical axial frequency fluctuations. Neglecting factors proportional to Nq^2/mD^2, which drop out anyway when the dip widths of both ions are equal, the ratio becomes

$$\tau_{th}/\tau_{ex} = \frac{\delta}{\pi\Gamma}. \tag{10.19}$$

Therefore, it is also essential to maximize the Q-factor of the RLC resonator mediating the coupling, since $Q = \omega_0/\Gamma$.

In the experiment, detunings δ on the order of Γ can be set by adjusting the trap voltages in the respective traps. However, it becomes difficult to set large detunings $(\delta \gg \Gamma)$ this way because the ion signal becomes narrower. It is therefore desirable to detune the resonator frequency instead. In our setup, this is achieved – without degrading the Q-factor – by changing the capacitance using the cryogenic switch discussed in section 5.8.3.

10.2.1 Avoided Crossing in Thermal Equilibrium

Besides coherent energy exchange, the avoided crossing is a characteristic of coupled oscillators. Experimentally, we demonstrate that coupling occurs in the off-resonant case by showing the avoided crossing of the proton and $^9\text{Be}^+$ ion oscillators. The setup is the same as used in section 10.1.1 and shown in figure 10.2, except that both stored ion oscillators are detuned by $60\,\text{Hz}$ from the resonance frequency of the RLC oscillator. The $^9\text{Be}^+$ ion number is chosen such that the dip width is approximately equal to the one of the single proton. To tune the frequency of the $^9\text{Be}^+$ ion oscillator, the trap voltage in the ST is adjusted.

FFT spectra of the voltage on the RLC osicilator are recorded and plotted in figure 10.8. To interpret these spectra, we refer to section 5.3 and 5.4. We have to distinguish between the unperturbed ion frequencies and the frequency at which the ions oscillate when coupled to the RLC oscillator. The former is represented by the antiresonance (the minimum in amplitude in figure 10.8) which does not show an avoided crossing, and the latter by the peak in amplitude, which shows the avoided crossing. Compare also to figure 5.2c, which shows that, in the off-resonant case, the peak in the RLC oscillator voltage coincides with the peak amplitude of the oscillating ion.

The situation shown in figure 10.8, where $\delta/\Gamma \approx 1.3$, is not yet useful for cooling, as the heating by the RLC oscillator dominates. For the heating to become negligible, $\delta/\Gamma \geq 30$ is required.

10.2.2 Coherent Energy Exchange

As an outlook, we show how coherent energy exchange between a single proton and a laser-cooled $^9\text{Be}^+$ ion cloud would work. Neglecting the heating effect of the resonator, we expect classical Rabi oscillations between the proton and the $^9\text{Be}^+$ ions. Initially, the $^9\text{Be}^+$ ion cloud is laser-cooled to the Doppler limit. Since it is much smaller than the proton amplitude, we neglect the initial amplitude of the $^9\text{Be}^+$ ions. Then, the proton amplitude evolves as shown in figure 10.9.

To reach the lowest temperatures, the detuning $\delta_{1,2} = \omega_2 - \omega_1$ and the coupling time t need to be adjusted precisely. However, for the large detuning δ necessary to suppress the heating by the RLC oscillator, it is rather difficult to match the proton
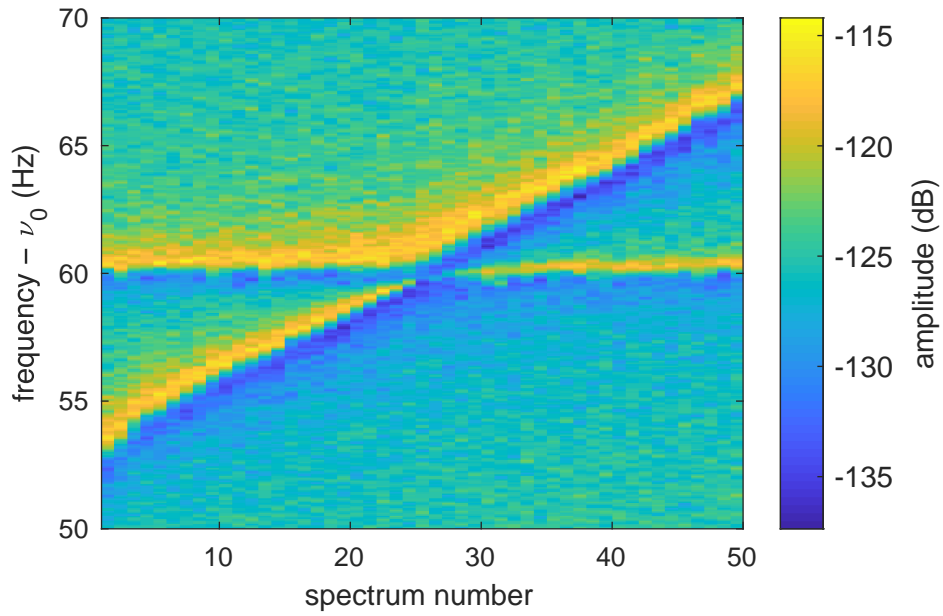
Figure 10.8: Avoided crossing of the proton and the $^9\text{Be}^+$ ion oscillators, $\delta = 2\pi \times 60\,\text{Hz}$ detuned from the resonance frequency of the RLC oscillator $\nu_0 = 478\,930\,\text{Hz}$. The proton is stored in the PT and the $^9\text{Be}^+$ ion in the ST, as in the setup shown in figure 10.2. To scan the frequency of the $^9\text{Be}^+$ ion oscillator, the trap voltage in the ST is increased proportional to the spectrum number.
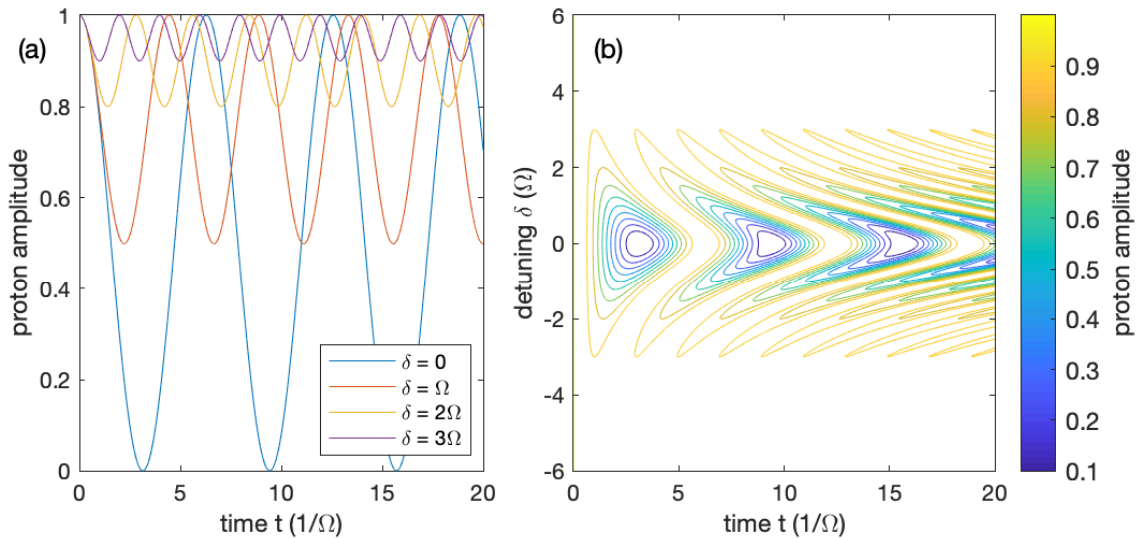

Figure 10.9: Classical Rabi oscillations of the proton amplitude. The amplitude is shown relative to the initial amplitude. Here, δ refers to the detuning $\delta_{1,2} = \omega_2 - \omega_1$, the difference between both ion frequencies.
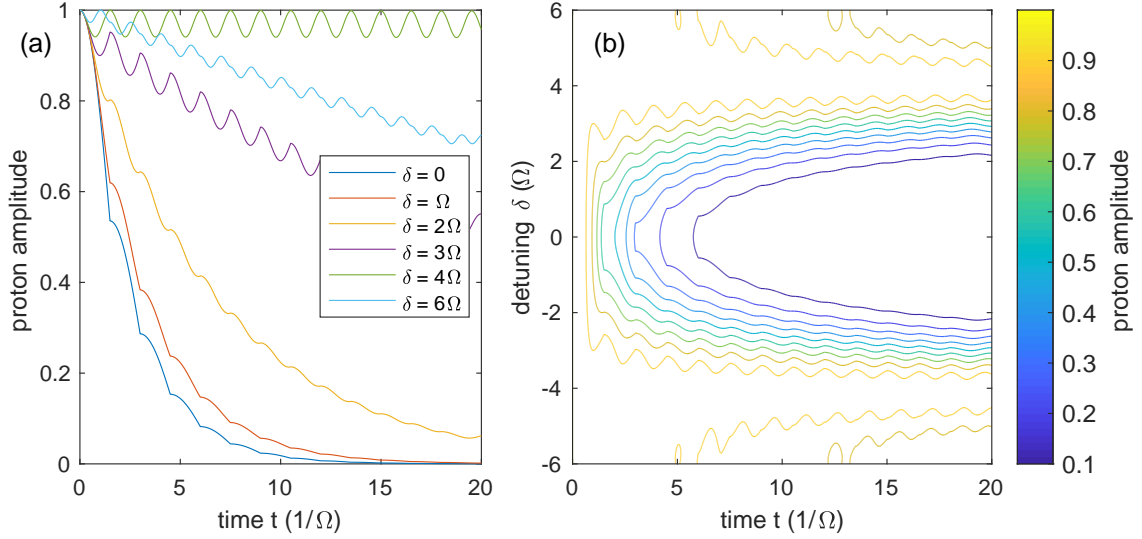
Figure 10.10: Proton amplitude for MICRO cooling. The amplitude is shown relative to the initial amplitude. The cooling interval is $t_c = 1.5/\Omega$. Here, δ refers to the detuning $\delta_{1,2} = \omega_2 - \omega_1$, the difference between both ion frequencies.

and the $^9\text{Be}^+$ ion frequencies to that level. In addition, the final proton amplitude is very sensitive to frequency drifts.

10.2.3 MICRO Cooling

Cooling by Multiple In-Complete Rabi Oscillations can relax the strict requirements on frequency matching. The concept was introduced in [75] and numerical simulations were performed in [126]. The essence of the technique is that the $^9\text{Be}^+$ ions are re-cooled after a time interval t_c. Therefore, at this point in time, the Rabi oscillations restart from a smaller proton amplitude. The resulting proton amplitude is shown in figure 10.10.

A considerable advantage of this technique is the large parameter space where cooling is expected. Compare this to the case of Rabi oscillations, where the detuning $\delta_{1,2} = \omega_2 - \omega_1$ and the coupling time t need to be adjusted precisely in order to achieve a low proton amplitude. In addition, this method is much less sensitive to frequency drifts during the coupling.

Chapter 11

Conclusion and Outlook

Starting from the proton g-factor experiment we inherited from [32], in this work, we set up the next-generation proton g-factor experiment based on sympathetic cooling. The cooling requirement is motivated by the observed scaling of the spin-detection fidelity as function of the radial temperature [22, 55] and is addressed by image-current coupling to laser-cooled $^9\mathrm{Be}^+$ ions. Setting up the new experiment, we learned that new is not better. In fact some of the newly installed components required some persistent convincing in order to perform well. This was especially true for some of the newly installed trap electrodes which interfered with the Q-factors of the image-current detectors, and it took a significant amount of time and work to assure that the detectors are in working order with Q-factors in the range of 10 000 to 20 000. Once the setup was operational, however, we performed very successful experiments on laser-cooling and sympathetic cooling.

Two notable additions to the trap stack, that have been designed, manufactured, implemented, and tested in this work, are the loading trap (LT) and the modified storage trap (ST). In designing the LT, we followed a new approach based on a barrel-shaped trap cavity that features a long ring electrode. This provided ample space for radial access to the trap center, which allowed us to equip the LT with two ablation targets and a fluorescence detector. The new LT turned out to be a very reliable source of protons and $^9\mathrm{Be}^+$ ions – after the right target material for protons was found [76]. In addition, the LT was also used as part of the three-trap sympathetic cooling experiment. Further, we designed a magnetic bottle for the ST, which turned it into a temperature measurement trap. The modified ST performed extremely well regarding temperature measurements and allowed us to characterise our sympathetic cooling technique with much improved precision.

In this work, we also developed a single-photon-sensitive fluorescence detection system based on silicon photomultipliers (SiPM) operated at cryogenic temperatures, and compatible with the magnetic field of the superconducting magnet, and the 1×10^{-17} mbar vacuum inside the trap chamber. The SiPM are integrated into the trap structure and thus avoid optical pathways from the hermetically sealed

trap chamber to detectors outside the magnet bore. We thoroughly characterized the properties of the SiPM at $4\,\mathrm{K}$ and measured detection efficiencies of the SiPM of up to $0.75(16)\,\%$ in the magnetic field of $1.9\,\mathrm{T}$ and $2.5(1)\,\%$ without a magnetic field in the cryocooler. A very desirable feature of SiPM at cryogenic temperatures are the extremely low dark count rates, measured to be $\leq 1\,\mathrm{s}^{-1}$ in both cases. The total detection efficiency of the fluorescence detection system was determined to $4.2(3) \times 10^{-6}$, corresponding to a photon count rate of $\frac{P/P_0}{1+P/P_0} \times 256(24)\,\mathrm{s}^{-1}$ per ion. Based on the fluorescence line-shape, we measured the temperature of the laser-cooled $^9\mathrm{Be}^+$ ions stored in the BT to $1.1(2)\,\mathrm{mK}$. This provided convincing evidence that we were able to cool the $^9\mathrm{Be}^+$ ions to the low temperatures necessary for sympathetic cooling, as temperature measurements in the magnetic bottle of the AT, at the time, were not possible.

Relying on the detection systems set up in this work, the improved image-current detectors and the newly developed fluorescence detection system, we were able to perform experiments on simultaneous detection of fluorescence photons and image currents from laser-cooled $^9\mathrm{Be}^+$ ions. With these detection methods available, we could measure the (relative) temperature of the RLC oscillator and the laser-induced damping resistance of the $^9\mathrm{Be}^+$ ions by means of image-current detection, and the photon scattering rate of the laser-cooled $^9\mathrm{Be}^+$ ions (relative to the scattering rate at saturation) by means of fluorescence detection. This allowed us, to the best of our knowledge, for the first time, to experimentally investigate the relationship between the laser-induced damping and the photon scattering rate. This insight into the laser-cooling process also proved to be useful in the following sympathetic cooling experiments.

Several sympathetic cooling experiments have been performed in different evolution stages of the new experimental apparatus, cooling single individually-trapped protons by laser-cooled $^9\mathrm{Be}^+$ ions. In a first attempt, a single proton was cooled from $17.0(2.4)\,\mathrm{K}$ to $2.6(2.5)\,\mathrm{K}$, limited only by the applied temperature measurement method [127, 33]. With an improved temperature measurement method, enabled by the newly implemented temperature measurement trap, this value was improved to $160(30)\,\mathrm{mK}$ in [31]. The temperatures given here are the temperature of the axial mode of the sympathetically cooled proton, because it is this mode that is thermalized.

For antiproton and proton g-factor measurements, the energy in the cyclotron mode is more relevant, and the quantity to be minimized. We therefore summarize our cooling results in figure 11.1 in terms of the cyclotron temperature and compare it to other experiments that have been performed in Penning traps. The cooling performance of our method (f) is comparable to the performance of the cyclotron resonator in the last proton g-factor measurement (c) [15, 32]. Meanwhile, optimized cyclotron resonators have been developed in parallel to this work [58, 59], outdoing
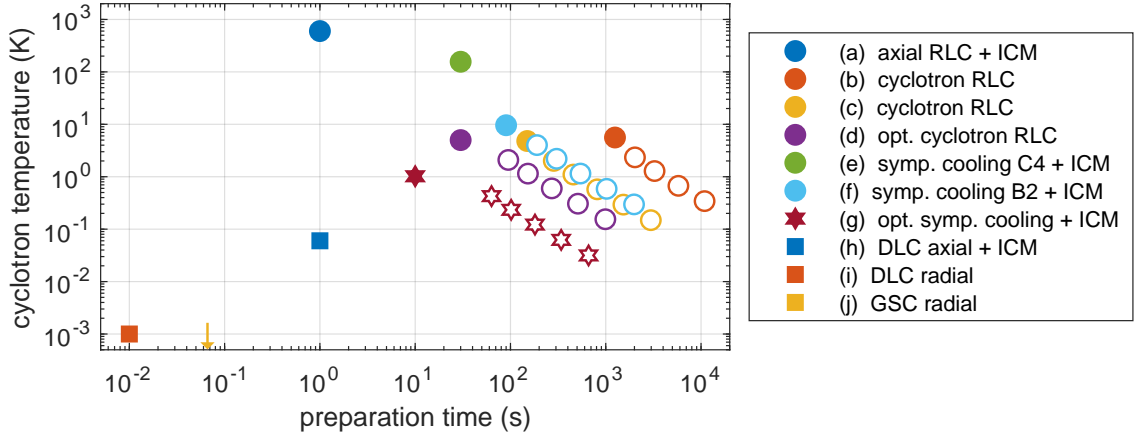
Figure 11.1: Comparison of sympathetic cooling results. Circles: techniques applicable to a single proton and other ions without suitable laser-cooling transitions. Squares: techniques only applicable to ions that can be laser cooled. The star indicates the expected performance of an optimized sympathetic cooling technique. Open symbols show the gain in temperature that can be achieved with sub-thermal cooling. ICM: interconversion of modes (adds about 1 s preparation time); opt.: optimized; symp.: sympathetic; DLC: Doppler laser cooling; GSC: ground state cooling. (a) thermalization with axial resonator as in section 5.7 and ICM [35, 43], (b) thermalization with cyclotron resonator [66], (c) thermalization with cyclotron resonator [32], (d) thermalization with optimized cyclotron resonator [58], (e) sympathetic cooling as in section 10.1.1 and [33, 127], (f) sympathetic cooling as in section 10.1.2 and [31], (g) estimated performance of optimized sympathetic cooling, (h) Doppler laser cooling the axial mode as in section 6.3 and ICM, (i) Doppler laser cooling of the radial modes [29] (j) sideband cooling of the radial modes to the ground state [29] (not shown on this scale, preparation time indicated with arrow).

the cooling performance of our technique. On the other hand these devices are highly optimized and fundamentally limited by the temperature in the cryogenic apparatus, while our cooling technique is just a first attempt.

The cooling performance of our method scales with the ratio γ_{Be}/γ_p and can be improved in three ways: increasing the $^9Be^+$ ion number, increasing the effective electrode distance D_p for the proton, and decreasing the effective electrode distance D_{Be} for $^9Be^+$ ions. While we have probably reached the limit regarding the $^9Be^+$ ion number, the ratio of effective electrode distances could be improved by a factor of 10 with an optimized trap design[1]. Note that the cooling time has not been optimized in our first attempt. Simulations indicate that it can be reduced by almost a factor of 10 also [126, 31]. This would then lead to an optimized sympathetic cooling technique, (g) in figure 11.1, that can outdo even optimized cyclotron RLC resonators in terms of cooling performance. Consequently, the optimized technique would also enable antiproton and proton g-factor measurements with an order of magnitude improved precision.

Further improvements in sympathetic cooling could be reached by coherent cou-

[1]In principle, D_p can be increased arbitrarily, but we limit ourselves to reasonable values.

pling between single protons and laser-cooled ^{9}Be$^+$ ions. In this work, several developments, such as the cryogenic switch, have been implemented and tested, which will allow to explore these techniques in the future. The possible gain in temperature and preparation time is orders of magnitude, as indicated by the squares in figure 11.1, which show the values reached for laser-coolable ions.

A big advantage of our sympathetic cooling technique, compared to cooling by cyclotron resonators, is that it is applicable to all ions without modifications. In contrast, the resonance frequency of the cyclotron resonator needs to be matched to the cyclotron frequency of the to-be-cooled ion, but these resonators can only be tuned in a narrow range. Finally, we think that the presented sympathetic cooling method will be an attractive tool for preparation of arbitrary stored ions with orders-of-magnitude lower temperatures than reached in current experiments. Implementation of this technique into state-of-the-art high-precision Penning trap experiments, therefore, has the potential to greatly improve the measurement precision in these experiments.

Bibliography

[1] Michael Dine and Alexander Kusenko. "Origin of the matter-antimatter asymmetry". In: *Reviews of Modern Physics* 76.1 (2004), pp. 1–30. DOI: `10.1103/revmodphys.76.1`.

[2] Laurent Canetti, Marco Drewes, and Mikhail Shaposhnikov. "Matter and antimatter in the universe". In: *New Journal of Physics* 14.9 (2012), p. 095012. DOI: `10.1088/1367-2630/14/9/095012`.

[3] Peter von Ballmoos. "Antimatter in the Universe: constraints from gamma-ray astronomy". In: *Hyperfine Interactions* 228.1-3 (2014), pp. 91–100. DOI: `10.1007/s10751-014-1024-9`.

[4] M. Aguilar et al. "The Alpha Magnetic Spectrometer (AMS) on the international space station: Part II — Results from the first seven years". In: *Physics Reports* 894 (2021), pp. 1–116. DOI: `10.1016/j.physrep.2020.09.003`.

[5] Simon Dupourqué, Luigi Tibaldo, and Peter von Ballmoos. "Constraints on the antistar fraction in the Solar System neighborhood from the 10-year Fermi Large Area Telescope gamma-ray source catalog". In: *Physical Review D* 103.8 (2021), p. 083016. DOI: `10.1103/physrevd.103.083016`.

[6] M. B. GAVELA et al. "STANDARD MODEL CP-VIOLATION AND BARYON ASYMMETRY". In: *Modern Physics Letters A* 9.09 (1994), pp. 795–809. DOI: `10.1142/s0217732394000629`.

[7] O. Bertolami et al. "CPT violation and baryogenesis". In: *Physics Letters B* 395.3-4 (1997), pp. 178–183. DOI: `10.1016/s0370-2693(97)00062-2`.

[8] Ralf Lehnert. "CPT Symmetry and Its Violation". In: *Symmetry* 8.11 (2016), p. 114. DOI: `10.3390/sym8110114`.

[9] Gerhart Lüders. "Proof of the TCP theorem". In: *Annals of Physics* 2.1 (1957), pp. 1–15. DOI: `10.1016/0003-4916(57)90032-5`.

[10] John Stewart Bell. "Time reversal in field theory". In: *Proceedings of the Royal Society of London. Series A. Mathematical and Physical Sciences* 231.1187 (1955), pp. 479–495. DOI: `10.1098/rspa.1955.0189`.

[11] C S Wu et al. "Experimental Test of Parity Conservation in Beta Decay". In: *Physical Review* 105.4 (1957), pp. 1413–1415. DOI: 10.1103/physrev.105.1413.

[12] J. H. Christenson et al. "Evidence for the 2π Decay of the K_2^0 Meson". In: *Physical Review Letters* 13.4 (1964), pp. 138–140. DOI: 10.1103/physrevlett.13.138.

[13] M. J. Borchert et al. "A 16-parts-per-trillion measurement of the antiproton-to-proton charge–mass ratio". In: *Nature* 601.7891 (2022), pp. 53–57. DOI: 10.1038/s41586-021-04203-w.

[14] C. Smorra et al. "A parts-per-billion measurement of the antiproton magnetic moment". In: *Nature* 550.7676 (2017), p. 371. DOI: 10.1038/nature24048.

[15] Georg Schneider et al. "Double-trap measurement of the proton magnetic moment at 0.3 parts per billion precision". In: *Science* 358.6366 (2017), pp. 1081–1084. DOI: 10.1126/science.aan0207.

[16] Don Colladay and Alan V Kostelecký. "CPT violation and the standard model". In: *Physical Review D* 55.11 (1997), p. 6760. DOI: 10.1103/PhysRevD.55.6760.

[17] Robert Bluhm, V. Alan Kostelecký, and Neil Russell. "CPT and Lorentz tests in Penning traps". In: *Physical Review D* 57.7 (1998), pp. 3932–3943. DOI: 10.1103/physrevd.57.3932.

[18] C. Smorra et al. "Direct limits on the interaction of antiprotons with axion-like dark matter". In: *Nature* 575.7782 (2019), pp. 310–314. DOI: 10.1038/s41586-019-1727-9.

[19] W. A. Bertsche. "Prospects for comparison of matter and antimatter gravitation with ALPHA-g". In: *Philosophical Transactions of the Royal Society A: Mathematical, Physical and Engineering Sciences* 376.2116 (2018), p. 20170265. DOI: 10.1098/rsta.2017.0265.

[20] A. Kellerbauer et al. "Proposed antimatter gravity measurement with an antihydrogen beam". In: *Nuclear Instruments and Methods in Physics Research Section B: Beam Interactions with Materials and Atoms* 266.3 (2008), pp. 351–356. DOI: 10.1016/j.nimb.2007.12.010.

[21] P. Pérez et al. "The GBAR antimatter gravity experiment". In: *Hyperfine Interactions* 233.1-3 (2015), pp. 21–27. DOI: 10.1007/s10751-015-1154-8.

[22] A. Mooser et al. "Resolution of Single Spin Flips of a Single Proton". In: *Physical Review Letters* 110.14 (2013), p. 140405. DOI: 10.1103/physrevlett.110.140405.

[23]   A. Mooser et al. "Demonstration of the double Penning Trap technique with a single proton". In: *Physics Letters B* 723.1-3 (June 2013), pp. 78–81. DOI: `10.1016/j.physletb.2013.05.012`.

[24]   C. Smorra et al. "Observation of individual spin quantum transitions of a single antiproton". In: *Physics Letters B* 769 (2017), pp. 1–6. DOI: `10.1016/j.physletb.2017.03.024`.

[25]   Giovanna Morigi, Jürgen Eschner, and Christoph H. Keitel. "Ground State Laser Cooling Using Electromagnetically Induced Transparency". In: *Physical Review Letters* 85.21 (2000), pp. 4458–4461. DOI: `10.1103/physrevlett.85.4458`.

[26]   C. F. Roos et al. "Experimental Demonstration of Ground State Laser Cooling with Electromagnetically Induced Transparency". In: *Physical Review Letters* 85.26 (2000), pp. 5547–5550. DOI: `10.1103/physrevlett.85.5547`.

[27]   Elena Jordan et al. "Near Ground-State Cooling of Two-Dimensional Trapped-Ion Crystals with More than 100 Ions". In: *Physical Review Letters* 122.5 (2019), p. 053603. DOI: `10.1103/physrevlett.122.053603`.

[28]   J. F. Goodwin et al. "Resolved-Sideband Laser Cooling in a Penning Trap". In: *Physical Review Letters* 116.14 (2016), p. 143002. DOI: `10.1103/physrevlett.116.143002`.

[29]   P. Hrmo et al. "Sideband cooling of the radial modes of motion of a single ion in a Penning trap". In: *Physical Review A* 100.4 (2019), p. 043414. DOI: `10.1103/physreva.100.043414`.

[30]   D. J. Heinzen and D. J. Wineland. "Quantum-limited cooling and detection of radio-frequency oscillations by laser-cooled ions". In: *Physical Review A* 42.5 (1990), pp. 2977–2994. DOI: `10.1103/physreva.42.2977`.

[31]   Christian Will. "Sympathetic Cooling of Trapped Ions Coupled via Image Currents: Simulation and Measurement". to be published. PhD thesis. Ruperto-Carola-University of Heidelberg, July 2023.

[32]   Georg Schneider. "300 ppt Measurement of the Proton g-Factor". PhD thesis. Johannes Gutenberg University of Mainz, Dec. 2017.

[33]   Matthew Bohman. "Sympathetic Cooling of a Proton with Resonant Image Current Coupling". PhD thesis. Ruperto-Carola-University of Heidelberg, Jan. 2021.

[34]   Wayne M. Itano and D. J. Wineland. "Laser cooling of ions stored in harmonic and Penning traps". In: *Physical Review A* 25.1 (1982), pp. 35–54. DOI: `10.1103/physreva.25.35`.

[35] Lowell S Brown and Gerald Gabrielse. "Geonium theory: Physics of a single electron or ion in a Penning trap". In: *Reviews of Modern Physics* 58.1 (1986), pp. 233–311. DOI: 10.1103/revmodphys.58.233.

[36] Lowell S. Brown and Gerald Gabrielse. "Precision spectroscopy of a charged particle in an imperfect Penning trap". In: *Physical Review A* 25.4 (1982), pp. 2423–2425. DOI: 10.1103/physreva.25.2423.

[37] X. Fan and G. Gabrielse. "Circumventing Detector Backaction on a Quantum Cyclotron". In: *Physical Review Letters* 126.7 (2021), p. 070402. DOI: 10.1103/physrevlett.126.070402.

[38] Klaus Blaum. "High-accuracy mass spectrometry with stored ions". In: *Physics Reports* 425.1 (2006), pp. 1–78. DOI: 10.1016/j.physrep.2005.10.011.

[39] Martin Kretzschmar. "Excitation of particle motions in a Penning trap: description in the classical canonical formalism". In: *Physica Scripta* 46.6 (1992), pp. 555–559. DOI: 10.1088/0031-8949/46/6/012.

[40] Martin Kretzschmar. "Theoretical investigations of different excitation modes for Penning trap mass spectrometry". In: *International Journal of Mass Spectrometry* 349 (2013), pp. 227–239. DOI: 10.1016/j.ijms.2013.03.023.

[41] Vasant Natarajan, Frank DiFilippo, and David E. Pritchard. "Classical Squeezing of an Oscillator for Subthermal Noise Operation". In: *Physical Review Letters* 74.15 (1995), pp. 2855–2858. DOI: 10.1103/physrevlett.74.2855.

[42] Stefan Ulmer. "First Observation of Spin Flips with a Single Proton Stored in a Cryogenic Penning Trap". PhD thesis. Ruperto-Carola-University of Heidelberg, July 2011.

[43] Eric A. Cornell et al. "Mode coupling in a Penning trap: π pulses and a classical avoided crossing". In: *Physical Review A* 41.1 (1990), pp. 312–315. DOI: 10.1103/physreva.41.312.

[44] Eric A. Cornell et al. "Single-ion cyclotron resonance measurement of M(CO+)/M(N2+)". In: *Physical Review Letters* 63.16 (1989), pp. 1674–1677. DOI: 10.1103/physrevlett.63.1674.

[45] Sven Sturm. "The g-factor of the electron bound in $^{28}Si^{13+}$: The most stringent test of bound-state quantum electrodynamics". PhD thesis. Johannes Gutenberg-Universität Mainz, Dec. 2011.

[46] Sven Sturm et al. "Phase-Sensitive Cyclotron Frequency Measurements at Ultralow Energies". In: *Physical Review Letters* 107.14 (2011), p. 143003. DOI: 10.1103/physrevlett.107.143003.

[47] M H Holzscheiter. "Cooling of Particles Stored in Electromagnetic Traps". In: *Physica Scripta* T22 (1988), pp. 73–78. DOI: 10.1088/0031-8949/1988/t22/010.

[48] Wayne M Itano et al. "Cooling methods in ion traps". In: *Physica Scripta* T59 (1995), pp. 106–120. DOI: 10.1088/0031-8949/1995/t59/013.

[49] C. Smorra and A. Mooser. "Precision Measurements of the Fundamental Properties of the Proton and Antiproton". In: *Journal of Physics: Conference Series* 1412.3 (2020), p. 032001. DOI: 10.1088/1742-6596/1412/3/032001.

[50] H. Dehmelt and P. Ekstrom. "Proposed g-2 Experiment on Single Stored Electron or Positron". In: *Bulletin of the American Physical Society* 18 (1973). Proposal to use Continuous Stern-Gerlach Effect for a electron g-2 measurement, p. 727.

[51] Hans Dehmelt. "Continuous Stern-Gerlach effect: Principle and idealized apparatus". In: *Proceedings of the National Academy of Sciences* 83.8 (1986), pp. 2291–2294. DOI: 10.1073/pnas.83.8.2291.

[52] Hans Dehmelt. "Continuous Stern-Gerlach effect: Noise and the measurement process". In: *Proceedings of the National Academy of Sciences* 83.10 (1986), pp. 3074–3077. DOI: 10.1073/pnas.83.10.3074.

[53] C C Rodegheri et al. "An experiment for the direct determination of the g-factor of a single proton in a Penning trap". In: *New Journal of Physics* 14.6 (2012), p. 063011. DOI: 10.1088/1367-2630/14/6/063011.

[54] H. Häffner et al. "Double Penning trap technique for precise g factor determinations in highly charged ions". In: *The European Physical Journal D - Atomic, Molecular, Optical and Plasma Physics* 22.2 (2003), pp. 163–182. DOI: 10.1140/epjd/e2003-00012-2.

[55] MJ Borchert et al. "Measurement of Ultralow Heating Rates of a Single Antiproton in a Cryogenic Penning Trap". In: *Physical Review Letters* 122.4 (2019), p. 043201. DOI: 10.1103/physrevlett.122.043201.

[56] D.W. Allan. "Statistics of atomic frequency standards". In: *Proceedings of the IEEE* 54.2 (1966), pp. 221–230. DOI: 10.1109/proc.1966.4634.

[57] M. Schuh et al. "Image charge shift in high-precision Penning traps". In: *Physical Review A* 100.2 (Aug. 2019), p. 023411. DOI: 10.1103/physreva.100.023411.

[58] Markus Fleck. "Towards a Tenfold Improvement on the Measurement of the Antiproton Magnetic Moment". to be published. PhD thesis. University of Tokyo, 2022.

[59] Stefan Ulmer. *BASE - Annual Report 2022*. Tech. rep. BASE collaboration. Geneva: CERN, 2023.

[60] M. Bohman et al. "Sympathetic cooling of protons and antiprotons with a common endcap Penning trap". In: *Journal of Modern Optics* 65.5-6 (2018), pp. 568–576. DOI: 10.1080/09500340.2017.1404656.

[61] D. J. Larson et al. "Sympathetic cooling of trapped ions: A laser-cooled two-species nonneutral ion plasma". In: *Physical Review Letters* 57.1 (1986), pp. 70–73. DOI: 10.1103/physrevlett.57.70.

[62] P. O. Schmidt et al. "Spectroscopy Using Quantum Logic". In: *Science* 309.5735 (2005), pp. 749–752. DOI: 10.1126/science.1114375.

[63] K. R. Brown et al. "Coupled quantized mechanical oscillators". In: *Nature* 471.7337 (2011), pp. 196–199. DOI: 10.1038/nature09721.

[64] M. Harlander et al. "Trapped-ion antennae for the transmission of quantum information". In: *Nature* 471.7337 (2011), pp. 200–203. DOI: 10.1038/nature09800.

[65] A. Mooser et al. "Direct high-precision measurement of the magnetic moment of the proton". In: *Nature* 509.7502 (2014), pp. 596–599. DOI: 10.1038/nature13388.

[66] Andreas Mooser. "Der *g*-Faktor des Protons". PhD thesis. Johannes Gutenberg University of Mainz, Dec. 2013.

[67] Cricia de Carvalho Rodegheri. "Neuartige kryogene Penning-Falle für den Nachweis von Spin-Übergängen eines Protons und Bestimmung seines *g*-Faktors". PhD thesis. Johannes Gutenberg University of Mainz, Dec. 2013.

[68] Susanne Waltraud Kreim. "Direct Observation of a Single Proton in a Penning Trap Towards a Direct Measurement of the Proton g-Factor". PhD thesis. Johannes Gutenberg University of Mainz, June 2009.

[69] Holger Kracke. "Detection of individual spin transitions of a single proton confined in a cryogenic Penning trap". PhD thesis. Johannes Gutenberg University of Mainz, Dec. 2012.

[70] Stefan Ulmer. "Entwicklung eines experimentellen Aufbaus zur Messung des *g*-Faktors des Protons in einer Penning-Falle". MA thesis. Ruperto-Carola-University of Heidelberg, 2006.

[71] S Sellner et al. "Improved limit on the directly measured antiproton lifetime". In: *New Journal of Physics* 19.8 (2017), p. 083023. DOI: 10.1088/1367-2630/aa7e73.

[72] G Gabrielse, L Haarsma, and S L Rolston. "Open-endcap Penning traps for high precision experiments". In: *International Journal of Mass Spectrometry and Ion Processes* 88.2-3 (1989), pp. 319–332. DOI: 10.1016/0168-1176(89)85027-x.

[73] G Gabrielse and J Tan. "Self-shielding superconducting solenoid systems". In: *Journal of Applied Physics* 63.10 (1988), pp. 5143–5148. DOI: 10.1063/1.340416.

[74]   Natalie Schön. "Optimizing catching efficiencies of antiprotons in a Penning trap and Developments towards resonant coupling of single protons and laser cooled beryllium ions". MA thesis. Johannes Gutenberg University of Mainz, Apr. 2018.

[75]   Bingsheng Tu et al. "Tank-Circuit Assisted Coupling Method for Sympathetic Laser Cooling". In: *Advanced Quantum Technologies* 4.7 (2021), p. 2100029. DOI: 10.1002/qute.202100029.

[76]   Hüseyin Yildiz. to be published. PhD thesis. Johannes Gutenberg University of Mainz.

[77]   Christine Böhm. "High-precision mass measurements of neutron-deficient Tl isotopes at ISOLTRAP and the development of an ultra-stable voltage source for the PENTATRAP experiment". PhD thesis. Ruperto-Carola-University of Heidelberg, Jan. 2015.

[78]   C. Smorra et al. "A reservoir trap for antiprotons". In: *International Journal of Mass Spectrometry* 389 (2015), pp. 10–13. DOI: 10.1016/j.ijms.2015.08.007.

[79]   R. S. Van Dyck et al. "Ultrastable superconducting magnet system for a penning trap mass spectrometer". In: *Review of Scientific Instruments* 70.3 (1999), pp. 1665–1671. DOI: 10.1063/1.1149649.

[80]   Jack A. Devlin et al. "Superconducting Solenoid System with Adjustable Shielding Factor for Precision Measurements of the Properties of the Antiproton". In: *Physical Review Applied* 12.4 (2019), p. 044012. DOI: 10.1103/physrevapplied.12.044012.

[81]   Maurice Egan. "The 20-Bit DAC Is the Easiest Part of a 1-ppm-Accurate Precision Voltage Source". In: *Analog Dialogue* 44.2 (Apr. 2010), p. 3.

[82]   H. G. Dehmelt and F. L. Walls. ""Bolometric" Technique for the rf Spectroscopy of Stored Ions". In: *Physical Review Letters* 21.3 (1968), pp. 127–131. DOI: 10.1103/physrevlett.21.127.

[83]   D. Wineland, P. Ekstrom, and H. Dehmelt. "Monoelectron Oscillator". In: *Physical Review Letters* 31.21 (1973). First single electron detection in a Penning trap. Opened the way for g-factor measurements., pp. 1279–1282. DOI: 10.1103/physrevlett.31.1279.

[84]   D J Wineland and H G Dehmelt. "Principles of the stored ion calorimeter". In: *Journal of Applied Physics* 46.2 (1975), pp. 919–930. DOI: 10.1063/1.321602.

[85]   X Feng et al. "Tank circuit model applied to particles in a Penning trap". In: *Journal of Applied Physics* 79.1 (1996), pp. 8–13. DOI: 10.1063/1.360947.

[86] G. Gabrielse et al. "Precision Mass Spectroscopy of the Antiproton and Proton Using Simultaneously Trapped Particles". In: *Physical Review Letters* 82.16 (1999), pp. 3198–3201. DOI: 10.1103/physrevlett.82.3198.

[87] J. Repp et al. "PENTATRAP: a novel cryogenic multi-Penning-trap experiment for high-precision mass measurements on highly charged ions". In: *Applied Physics B* 107.4 (2012), pp. 983–996. DOI: 10.1007/s00340-011-4823-6.

[88] Sven Sturm et al. "The ALPHATRAP experiment". In: *The European Physical Journal Special Topics* 227.13 (2019), pp. 1425–1491. DOI: 10.1140/epjst/e2018-800225-2.

[89] C. Smorra et al. "BASE – The Baryon Antibaryon Symmetry Experiment". In: *The European Physical Journal Special Topics* 224.16 (2015), pp. 3055–3108. DOI: 10.1140/epjst/e2015-02607-4.

[90] J. B. Johnson. "Thermal Agitation of Electricity in Conductors". In: *Physical Review* 32.1 (1928), pp. 97–109. DOI: 10.1103/physrev.32.97.

[91] H. Nyquist. "Thermal Agitation of Electric Charge in Conductors". In: *Physical Review* 32.1 (1928), pp. 110–113. DOI: 10.1103/physrev.32.110.

[92] Herbert B. Callen and Theodore A. Welton. "Irreversibility and Generalized Noise". In: *Physical Review* 83.1 (1951), pp. 34–40. DOI: 10.1103/physrev.83.34.

[93] W Shockley. "Currents to Conductors Induced by a Moving Point Charge". In: *Journal of Applied Physics* 9.10 (1938), pp. 635–636. DOI: 10.1063/1.1710367.

[94] S. Ramo. "Currents Induced by Electron Motion". In: *Proceedings of the IRE* 27.9 (1939), pp. 584–585. DOI: 10.1109/jrproc.1939.228757.

[95] C. Sames et al. "Antiresonance Phase Shift in Strongly Coupled Cavity QED". In: *Physical Review Letters* 112.4 (2014), p. 043601. DOI: 10.1103/physrevlett.112.043601.

[96] Shlomi Kotler et al. "Hybrid quantum systems with trapped charged particles". In: *Physical Review A* 95.2 (2017), p. 022327. DOI: 10.1103/physreva.95.022327.

[97] H. Nagahama et al. "Highly sensitive superconducting circuits at $\sim$700 kHz with tunable quality factors for image-current detection of single trapped antiprotons". In: *Review of Scientific Instruments* 87.11 (2016), p. 113305. DOI: 10.1063/1.4967493.

[98] S Ulmer et al. "The quality factor of a superconducting rf resonator in a magnetic field". In: *Review of Scientific Instruments* 80.12 (2009), p. 123302. DOI: 10.1063/1.3271537.

[99]   Warren Nagourney, Jon Sandberg, and Hans Dehmelt. "Shelved optical electron amplifier: Observation of quantum jumps". In: *Physical Review Letters* 56.26 (1986). First observation of quantum jumps. Two other groups observed this in the same year., pp. 2797–2799. DOI: 10.1103/physrevlett.56.2797.

[100] Th. Sauter et al. "Observation of Quantum Jumps". In: *Physical Review Letters* 57.14 (1986), pp. 1696–1698. DOI: 10.1103/physrevlett.57.1696.

[101] J. C. Bergquist et al. "Observation of Quantum Jumps in a Single Atom". In: *Physical Review Letters* 57.14 (1986), pp. 1699–1702. DOI: 10.1103/physrevlett.57.1699.

[102] A. H. Myerson et al. "High-Fidelity Readout of Trapped-Ion Qubits". In: *Physical Review Letters* 100 (20 May 2008), p. 200502. DOI: 10.1103/PhysRevLett.100.200502.

[103] S. M. Brewer et al. "^{27}Al$^+$ Quantum-Logic Clock with a Systematic Uncertainty below 10^{-18}". In: *Physical Review Letters* 123 (3 July 2019), p. 033201. DOI: 10.1103/PhysRevLett.123.033201.

[104] P. Micke et al. "Coherent laser spectroscopy of highly charged ions using quantum logic". In: *Nature* (2020), pp. 1–6. DOI: 10.1038/s41586-020-1959-8.

[105] R. X. Schüssler et al. "Detection of metastable electronic states by Penning trap mass spectrometry". In: *Nature* 581.7806 (2020), pp. 42–46. DOI: 10.1038/s41586-020-2221-0.

[106] Sascha Rau et al. "Penning trap mass measurements of the deuteron and the HD+ molecular ion". In: *Nature* 585.7823 (2020), pp. 43–47. DOI: 10.1038/s41586-020-2628-7.

[107] A. Schneider et al. "Direct measurement of the 3He+ magnetic moments". In: *Nature* (2022), pp. 1–6. DOI: 10.1038/s41586-022-04761-7.

[108] Manuel J Gutiérrez et al. "The TRAPSENSOR facility: an open-ring 7 tesla Penning trap for laser-based precision experiments". In: *New Journal of Physics* 21.2 (2019), p. 023023. DOI: 10.1088/1367-2630/aafa45.

[109] S. Schmidt et al. "Sympathetic cooling in two-species ion crystals in a Penning trap". In: *Journal of Modern Optics* 65.5-6 (2017), pp. 1–11. DOI: 10.1080/09500340.2017.1342877.

[110] M. Biroth et al. "Silicon photomultiplier properties at cryogenic temperatures". In: *Nuclear Instruments and Methods in Physics Research Section A: Accelerators, Spectrometers, Detectors and Associated Equipment* 787 (2015), pp. 68–71. DOI: https://doi.org/10.1016/j.nima.2014.11.020.

[111] Maik Biroth et al. "Performance of SensL C-Series SiPM with High Photo-electron Resolution at Cryogenic Temperatures". In: *2016 IEEE Nuclear Science Symposium, Medical Imaging Conference and Room-Temperature Semiconductor Detector Workshop (NSS/MIC/RTSD)*. 2016, pp. 1–3. DOI: `10.1109/nssmic.2016.8069771`.

[112] P. Achenbach et al. "Gain stabilization and noise minimization for SiPMs at cryogenic temperatures". In: *Nuclear Instruments and Methods in Physics Research Section A: Accelerators, Spectrometers, Detectors and Associated Equipment* 912 (2018), pp. 110–111. DOI: `https://doi.org/10.1016/j.nima.2017.10.080`.

[113] S. L. Todaro et al. "State Readout of a Trapped Ion Qubit Using a Trap-Integrated Superconducting Photon Detector". In: *Physical Review Letters* 126.1 (2021), p. 010501. DOI: `10.1103/physrevlett.126.010501`.

[114] David Reens et al. "High-Fidelity Ion State Detection Using Trap-Integrated Avalanche Photodiodes". In: *Physical Review Letters* 129.10 (2022), p. 100502. DOI: `10.1103/physrevlett.129.100502`.

[115] Juan M Cornejo et al. "Quantum logic inspired techniques for spacetime-symmetry tests with (anti-)protons". In: *New Journal of Physics* 23.7 (2021), p. 073045. DOI: `10.1088/1367-2630/ac136e`.

[116] Valentin Grunhofer. "Cyclotron cooling of a single proton in a Penning trap and improvements towards sympathetic cooling". MA thesis. Johannes Gutenberg University of Mainz, July 2020.

[117] *J-Series SiPM Sensors*. Rev. 4. ON Semiconductors. Sept. 2018.

[118] Yves Colombe et al. "Single-mode optical fiber for high-power, low-loss UV transmission". In: *Optics Express* 22.16 (2014), p. 19783. DOI: `10.1364/oe.22.019783`.

[119] *Introduction to the Silicon Photomultiplier (SiPM)*. Rev. 8. ON Semiconductors. July 2021.

[120] H. Otono et al. "Study of MPPC at Liquid Nitrogen Temperature". English. In: *Proceedings of International Workshop on new Photon-Detectors PD07, PoS (PD07) 007*. 2007.

[121] H. Otono et al. "On the basic mechanism of Pixelized Photon Detectors". In: *Nuclear Instruments and Methods in Physics Research Section A: Accelerators, Spectrometers, Detectors and Associated Equipment* 610.1 (2009), pp. 397–399. DOI: `https://doi.org/10.1016/j.nima.2009.05.139`.

[122] D J Wineland et al. "Double-resonance and optical-pumping experiments on electromagnetically confined, laser-cooled ions". In: *Optics Letters* 5.6 (1980), p. 245. DOI: `10.1364/ol.5.000245`.

[123] Wayne M. Itano and D. J. Wineland. "Precision measurement of the ground-state hyperfine constant of ^{25}Mg$^+$". In: *Physical Review A* 24.3 (1981). description of optical pumping in 9Be+, pp. 1364–1373. DOI: 10.1103/physreva.24.1364.

[124] T. Andersen, K. A. Jessen, and G. Sørensen. "Mean-Life Measurements of Excited Electronic States in Neutral and Ionic Species of Beryllium and Boron". In: *Physical Review* 188.1 (1969), pp. 76–81. DOI: 10.1103/physrev.188.76.

[125] R. Blümel et al. "Chaos and order of laser-cooled ions in a Paul trap". In: *Physical Review A* 40.2 (1989), pp. 808–823. DOI: 10.1103/physreva.40.808.

[126] C Will et al. "Sympathetic cooling schemes for separately trapped ions coupled via image currents". In: *New Journal of Physics* 24.3 (2022), p. 033021. DOI: 10.1088/1367-2630/ac55b3.

[127] M Bohman et al. "Sympathetic cooling of a trapped proton mediated by an LC circuit". In: *Nature* 596.7873 (2021), pp. 514–518. DOI: 10.1038/s41586-021-03784-w.

[128] D. J. Wineland, J. J. Bollinger, and Wayne M. Itano. "Laser-Fluorescence Mass Spectroscopy". In: *Physical Review Letters* 50.9 (1983), pp. 628–631. DOI: 10.1103/physrevlett.50.628.

[129] D. Rodríguez. "A quantum sensor for high-performance mass spectrometry". In: *Applied Physics B* 107.4 (2012), pp. 1031–1042. DOI: 10.1007/s00340-011-4824-5.

[130] M. J. Gutiérrez et al. "Dynamics of an unbalanced two-ion crystal in a Penning trap for application in optical mass spectrometry". In: *Physical Review A* 100.6 (Dec. 2019), p. 063415. DOI: 10.1103/PhysRevA.100.063415.

[131] J. Berrocal et al. "Formation of two-ion crystals by injection from a Paul-trap source into a high-magnetic-field Penning trap". In: *Physical Review A* 105.5 (2022), p. 052603. DOI: 10.1103/physreva.105.052603.

[132] D. J. Wineland and Wayne M. Itano. "Laser cooling of atoms". In: *Physical Review A* 20.4 (1979), pp. 1521–1540. DOI: 10.1103/physreva.20.1521.

[133] Peter Van der Straten and Harold Metcalf. *Atoms and molecules interacting with light: Atomic physics for the laser era*. Cambridge University Press, 2016.

[134] A. Krieger et al. "Frequency-comb referenced collinear laser spectroscopy of Be+ for nuclear structure investigations and many-body QED tests". In: *Applied Physics B* 123.1 (2016), p. 15. DOI: 10.1007/s00340-016-6579-5.

[135] Mariusz Puchalski and Krzysztof Pachucki. "Fine and hyperfine splitting of the 2P state in Li and Be+". In: *Physical Review A* 79.3 (2009), p. 032510. DOI: 10.1103/physreva.79.032510.

[136] W. Nörtershäuser et al. "Nuclear Charge Radii of Be7,9,10 and the One-Neutron Halo Nucleus Be11". In: *Physical Review Letters* 102.6 (2008), p. 062503. DOI: 10.1103/physrevlett.102.062503.

[137] Krzysztof Pachucki and Mariusz Puchalski. "Accurate determination of Be magnetic moment". In: *Optics Communications* 283.5 (2010), pp. 641–643. DOI: 10.1016/j.optcom.2009.10.058.

[138] Wayne M. Itano. "Chemical shift correction to the Knight shift in beryllium". In: *Physical Review B* 27.3 (1983), pp. 1906–1907. DOI: 10.1103/physrevb.27.1906.

[139] Zong-Chao Yan. "Calculations of Magnetic Moments for Three-Electron Atomic Systems". In: *Physical Review Letters* 86.25 (2001), pp. 5683–5686. DOI: 10.1103/physrevlett.86.5683.

[140] R. Alheit et al. "Observation of instabilities in a Paul trap with higher-order anharmonicities". In: *Applied Physics B* 61.3 (1995), pp. 277–283. DOI: 10.1007/bf01082047.

[141] R. Alheit et al. "Some Observations on Higher-order Non-linear Resonances in a Paul Trap". In: *Rapid Communications in Mass Spectrometry* 10.5 (1996), pp. 583–590. DOI: 10.1002/(sici)1097-0231(19960331)10:5<583::aid-rcm497>3.0.co;2-2.

[142] R. Alheit et al. "Higher order non-linear resonances in a Paul trap". In: *International Journal of Mass Spectrometry and Ion Processes* 154.3 (1996), pp. 155–169. DOI: 10.1016/0168-1176(96)04380-7.

[143] L. Schweikhard et al. "The trapping condition and a new instability of the ion motion in the ion cyclotron resonance trap". In: *International Journal of Mass Spectrometry and Ion Processes* 141.1 (1995), pp. 77–90. DOI: 10.1016/0168-1176(94)04092-l.

[144] K. Hübner et al. "Instabilities of ion confinement in a penning trap". In: *EPL (Europhysics Letters)* 37.7 (1997), pp. 459–464. DOI: 10.1209/epl/i1997-00172-5.

[145] P. Paasche et al. "Instabilities of an electron cloud in a Penning trap". In: *The European Physical Journal D - Atomic, Molecular, Optical and Plasma Physics* 22.2 (2003), pp. 183–188. DOI: 10.1140/epjd/e2002-00239-3.

[146] Felix Hahne. "Investigation of a Novel Method for Sympathetic Laser Cooling of Highly Charged Ions in a Penning Trap". MA thesis. Ruperto-Carola-University of Heidelberg, 2020.

List of Publications

- Sympathetic cooling of protons and antiprotons with a common endcap Penning trap

  M. Bohman, A. Mooser, G. Schneider, N. Schön, M. Wiesinger, J. Harrington, T. Higuchi, H. Nagahama, C. Smorra, S. Sellner, K. Blaum, Y. Matsuda, W. Quint, J. Walz & S. Ulmer

  Journal of Modern Optics 65, 568–576 (2018)

  https://doi.org/10.1080/09500340.2017.1404656

- Direct limits on the interaction of antiprotons with axion-like dark matter

  C. Smorra, Y. V. Stadnik, P. E. Blessing, M. Bohman, M. J. Borchert, J. A. Devlin, S. Erlewein, J. A. Harrington, T. Higuchi, A. Mooser, G. Schneider, M. Wiesinger, E. Wursten, K. Blaum, Y. Matsuda, C. Ospelkaus, W. Quint, J. Walz, Y. Yamazaki, D. Budker & S. Ulmer

  Nature 575, 310–314 (2019)

  https://doi.org/10.1038/s41586-019-1727-9

- Sympathetic cooling of a trapped proton mediated by an LC circuit

  M. Bohman, V. Grunhofer, C. Smorra, M. Wiesinger, C. Will, M. J. Borchert, J. A. Devlin, S. Erlewein, M. Fleck, S. Gavranovic, J. Harrington, B. Latacz, A. Mooser, D. Popper, E. Wursten, K. Blaum, Y. Matsuda, C. Ospelkaus, W. Quint, J. Walz & S. Ulmer

  Nature 596, 514–518 (2021)

  https://doi.org/10.1038/s41586-021-03784-w

- Measurement of Ultralow Heating Rates of a Single Antiproton in a Cryogenic Penning Trap

  M. J. Borchert, P. E. Blessing, J. A. Devlin, J. A. Harrington, T. Higuchi, J. Morgner, C. Smorra, E. Wursten, M. Bohman, M. Wiesinger, A. Mooser, K. Blaum, Y. Matsuda, C. Ospelkaus, W. Quint, J. Walz, Y. Yamazaki & S. Ulmer

  Phys. Rev. Lett. 122, 043201 (2019)

https://doi.org/10.1103/PhysRevLett.122.043201

- Superconducting Solenoid System with Adjustable Shielding Factor for Precision Measurements of the Properties of the Antiproton

  J. A. Devlin, E. Wursten, J. A. Harrington, T. Higuchi, P. E. Blessing, M. J. Borchert, S. Erlewein, J. J. Hansen, J. Morgner, M. A. Bohman, A. H. Mooser, C. Smorra, M. Wiesinger, K. Blaum, Y. Matsuda, C. Ospelkaus, W. Quint, J. Walz, Y. Yamazaki & S. Ulmer

  Phys. Rev. Applied 12, 044012 (2019)

  https://doi.org/10.1103/PhysRevApplied.12.044012

- Constraints on the Coupling between Axionlike Dark Matter and Photons Using an Antiproton Superconducting Tuned Detection Circuit in a Cryogenic Penning Trap

  J. A. Devlin, M. J. Borchert, S. Erlewein, M. Fleck, J. A. Harrington, B. Latacz, J. Warncke, E. Wursten, M. A. Bohman, A. H. Mooser, C. Smorra, M. Wiesinger, C. Will, K. Blaum, Y. Matsuda, C. Ospelkaus, W. Quint, J. Walz, Y. Yamazaki & S. Ulmer

  Phys. Rev. Lett. 126, 041301 (2021)

  https://doi.org/10.1103/PhysRevLett.126.041301

- A 16-parts-per-trillion measurement of the antiproton-to-proton charge–mass ratio

  M. J. Borchert, J. A. Devlin, S. R. Erlewein, M. Fleck, J. A. Harrington, T. Higuchi, B. M. Latacz, F. Voelksen, E. J. Wursten, F. Abbass, M. A. Bohman, A. H. Mooser, D. Popper, M. Wiesinger, C. Will, K. Blaum, Y. Matsuda, C. Ospelkaus, W. Quint, J. Walz, Y. Yamazaki, C. Smorra & S. Ulmer

  Nature 601, 53–57 (2022)

  https://doi.org/10.1038/s41586-021-04203-w

- Sympathetic cooling schemes for separately trapped ions coupled via image currents

  C. Will, M. Bohman, T. Driscoll, M. Wiesinger, F. Abbass, M. J. Borchert, J. A. Devlin, S. Erlewein, M. Fleck, B. Latacz, R. Moller, A. Mooser, D. Popper, E. Wursten, K. Blaum, Y. Matsuda, C. Ospelkaus, W. Quint, J. Walz, C. Smorra & S. Ulmer

  New J. Phys. 24, 033021 (2022)

  https://doi.org/10.1088/1367-2630/ac55b3

- A high-Q superconducting toroidal medium frequency detection system with a capacitively adjustable frequency range > 180 kHz

  F. Völksen, J. A. Devlin, M. J. Borchert, S. R. Erlewein, M. Fleck, J. I. Jäger, B. M. Latacz, P. Micke, P. Nuschke, G. Umbrazunas, E. J. Wursten, F. Abbass, M. A. Bohman, D. Popper, M. Wiesinger, C. Will, K. Blaum, Y. Matsuda, A. Mooser, C. Ospelkaus, C. Smorra, A. Soter, W. Quint, J. Walz, Y. Yamazaki & S. Ulmer

Acknowledgements

There are so many things that conspired to make this thesis possible, it is for sure impossible to name them all.

First of all, I want to thank the Englisch language, for the freedom of expression it provides. In contrast to my native Austrian, there is no single authority governing the rules of writing. So whenever the reader might find an error, we want them to think of this fact.

Let me continue with the most important persons:

Klaus Blaum, thank you for luring me to Mainz, for supervising this thesis and all the support you provided.

A big thank you to Prof. Matthias Weidemüller for agreeing to act as second reviewer.

Many thanks to the people who led the group in Mainz: Andreas Mooser, Christian Smorra and Peter Micke. Without you nothing would get done.

Many thanks to the speaker of the BASE collaboration Stefan Ulmer for many helpful discussions. These thanks also go to Jochen Walz, Wolfgang Quint and Christian Ospelkaus.

To my fellow PhD students: Georg Schneider, Matthew Bohman, Christian Will, and Hüseyin Yildiz. Thank you for the great time we had together in the lab.

To the other ion trappers in Mainz: Sven Sturm, Fabian Heiße, Florian Köhler, Sascha Rau, Sangeetha Sasidharan, Olesia Bezrodnova, Fatma Abbas, and Daniel Popper. Thank you for many interesting conversations and discussions not only during lunch but also elsewhere.

Much love to the AVA fellows, you made the time at many workshops, schools, and conferences memorable.

To the members of the CERN group of BASE I had the honor to get to know better: Matthias Borchert and James Harrington, thank you for a great time in Geneva. Thanks also to Barbara Latacz for being so accommodating.

Finally, since this thesis was carried out during a worldwide pandemic and a major land war in Europe: Thanks to all the people that keep us healthy and safe.

Zum Abschluss möchte ich meinen Eltern Edith und Ewald Wiesinger danken, für die unerschütterliche Unterstützung die Ihr mir gegeben habt. Ohne Euch wäre das alles nicht möglich gewesen.

Appendix A

Resonator Lineshape

The power spectral density (PSD) in units of dBm/Hz is given by

$$S(\nu) = 10 \times \log_{10}\left(A\chi(\nu) + A_{bkg}\right) \tag{A.1}$$

with the amplitude A, frequency-dependent line-shape parameter $\chi(\nu)$, and background amplitude A_{bkg}.

The amplitude is given by

$$A = a\kappa^2 \times 4k_BTR \tag{A.2}$$

where a is the amplification factor, κ the coupling factor, k_B the Boltzmann constant, T the resonator temperature, and R the parallel resistance. The frequency-dependent lineshape parameter $\chi(\nu)$ depends on the properties of the oscillators coupled to the RLC resonator. It has the following properties

$$\max(\chi(\nu)) = 1 \tag{A.3}$$

$$\int_0^\infty \chi(\nu)\partial\nu = \frac{1}{4RC} = \frac{\pi}{2}\gamma \tag{A.4}$$

Lineshape parameters $\chi(\nu)$ are listed for: A resonator on its own

$$\chi(\nu) = \frac{1}{1 + \left(Q\left(\frac{\nu}{\nu_0} - \frac{\nu_0}{\nu}\right)\right)^2} \tag{A.5}$$

a resonator with one ion with frequency ν_z and dip width γ_z

$$\chi(\nu) = \frac{1}{1 + \left(Q\left(\frac{\nu}{\nu_0} - \frac{\nu_0}{\nu}\right) - \frac{\nu\gamma_z}{\nu^2 - \nu_z^2}\right)^2} \tag{A.6}$$

a resonator with two ions with frequencies ν_1 and ν_2 and dip widths γ_1 and γ_2

$$\chi(\nu) = \frac{1}{1 + \left(Q \left(\frac{\nu}{\nu_0} - \frac{\nu_0}{\nu} \right) - \frac{\nu\gamma_1}{\nu^2 - \nu_1^2} - \frac{\nu\gamma_2}{\nu^2 - \nu_2^2} \right)^2} \tag{A.7}$$

a resonator with N ions with frequencies ν_n and dip widths γ_n for $n = 1, ..., N$

$$\chi(\nu) = \frac{1}{1 + \left(Q \left(\frac{\nu}{\nu_0} - \frac{\nu_0}{\nu} \right) - \sum_{n=1}^{N} \frac{\nu\gamma_n}{\nu^2 - \nu_n^2} \right)^2} \tag{A.8}$$

and a resonator with one ion with frequency ν_1 and dip width γ_1 damped with damping resistance R_1

$$\rho = R_1/R \tag{A.9}$$

$$\rho_s = \rho^2 + \left(\left(\nu^2 - \nu_1^2 \right) / \nu\gamma_1 \right)^2 \tag{A.10}$$

$$\rho_l = \rho_s + \rho \tag{A.11}$$

$$\chi(\nu) = \frac{\rho_s \rho_l}{\rho_l^2 + \left(\rho_s Q \left(\frac{\nu}{\nu_0} - \frac{\nu_0}{\nu} \right) - \frac{\nu^2 - \nu_1^2}{\nu\gamma_1} \right)^2} \tag{A.12}$$

where ρ is the resistance ratio, and ρ_s and ρ_l are dimensionless quantities which allow to write the above equation concisely.

Appendix B

Coil Parameters

The parameters of all superconducting coils that were used in the experiment at some point are listed in table B.1. All these coils are made from $0.075\,\mathrm{mm}$ diameter NbTi wire wound on PTFE cores. To determine the coil inductance L_c and self capacitance C_c, external capacitances C_e are connected to the coil and the resulting resonance frequency ν_0 is measured. Fitting the resonance frequency with the function

$$\nu_0(C_e) = \frac{1}{2\pi}\frac{1}{\sqrt{L_c(C_c + C_e)}} \tag{B.1}$$

allows us to determine L_c and C_c. The fit to coils 1 to 9 is shown in figure B.1 and the resulting fit parameters are listed in table B.1.
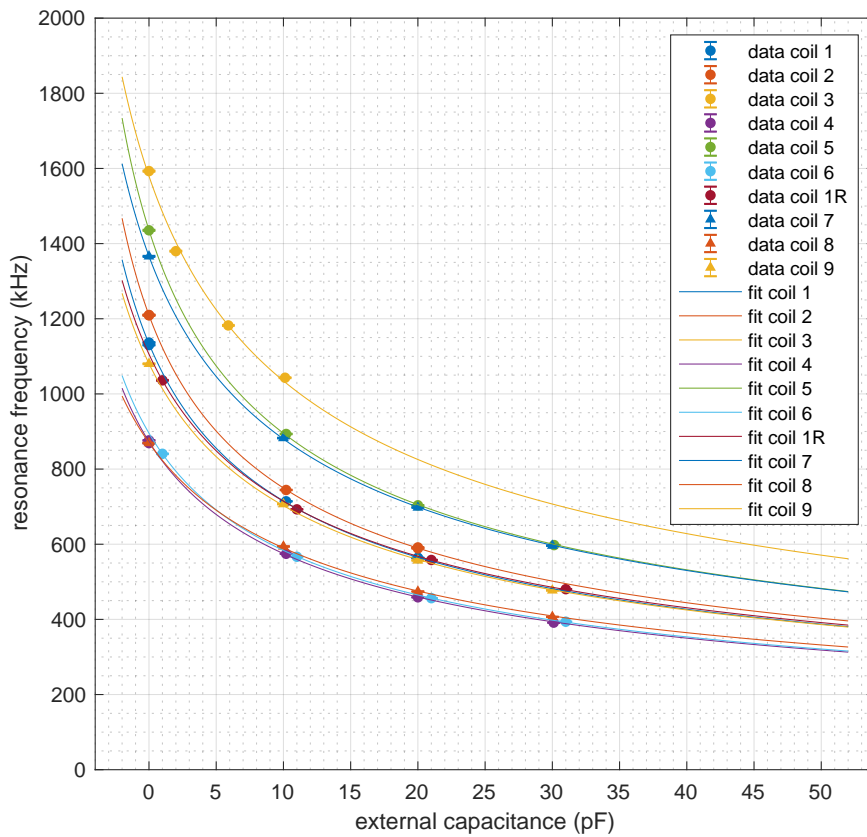

Figure B.1: Resonance frequency as function of external capacitance.

| coil | windings | insulation material | \multicolumn{3}{c}{measured NbTi-wire resistance (Ω)} | tap ratio | \multicolumn{2}{c}{measured} | \multicolumn{2}{c}{used in} |
			$R_{\text{trap - GND}}$	$R_{\text{tap - GND}}$	$R_{\text{tap - trap}}$		L_c (mH)	C_c (pF)	year	trap
1	unk.	PFA	9309	1674	7636	0.180	2.98(3)	6.62(8)	2018	ST PT
									2017	BT CT
									2015	AT
2	unk.	unk.	8077	935	7156	0.116	2.775(9)	6.239(23)	2018	AT
									2017	AT
									2015	PT
3	unk.	unk.	6133	565	5578	0.092	1.35(8)	7.5(6)	2018	BT CT
									2017	PT ST
4	1395	formvar	8782	2176	6605	0.248	4.33(6)	7.67(12)		
5	939	PFA	7827	1001	6826	0.128	1.931(13)	6.36(6)		
6	1376	PFA	11715	1457	10257	0.124	4.279(17)	7.38(4)		
1R	unk.	PFA	9280	1666	7616	0.180	2.891(14)	7.17(5)		
7	936	PFA	7815	831	6984	0.106	1.914(10)	7.09(5)	2021	AT ST
8	1355	PFA	10931	1525	9406	0.140	3.93(5)	8.53(14)	2021	PT LT
9	1135	PFA	8727	979	7748	0.112	2.96(3)	7.32(10)	2021	BT CT

Table B.1: Parameters of superconducting coils. Coils 1, 2, and 3 have been retained from [32, 33, 66]. Coils 4 to 9 have been newly made. Coil 1R is coil 1 with two windings removed and refurbished superconducting joints. L_c is the inductance and C_c the self capacitance of the coil. unk.: unknown. PFA: perfluoroalkoxy.